Numerical homogenization strategies for cellular materials with applications in structural mechanics

Vom Promotionsausschuss der
Technischen Universität Hamburg-Harburg

zur Erlangung des akademischen Grades

Doktor-Ingenieur (Dr.-Ing.)

genehmigte Dissertation

von
Hans-Georg Sehlhorst

aus
Essen

2011

Gutachter:	Prof. Dr.-Ing. habil. Alexander Düster Prof. Dr.-Ing. Stefan Diebels
Tag der mündlichen Prüfung:	11.11.2011

Vorwort

Die vorliegende Arbeit entstand während meiner Tätigkeit als wissenschaftlicher Mitarbeiter am Lehrstuhl für Computation in Engineering (CiE) der TU München (September 2006 bis August 2009) und am Fachgebiet Numerische Strukturanalyse mit Anwendungen in der Schiffstechnik (M-10) der TU Hamburg-Harburg (September 2009 bis August 2011) im Rahmen des DFG-Forschungsprojekts Numerische Homogenisierungsstrategien für erweiterte Kontinua.

Zunächst möchte ich mich herzlich bei meinem Doktorvater, Herrn Prof. Dr.-Ing. habil. Alexander Düster, für die Betreuung und Begleitung meiner Doktorarbeit bedanken. Seit ich bei ihm im Rahmen meines Masterstudiums an der TU München studentische Hilfskraft war, stand seine Türe für mich immer offen. Er ließ mir während der Doktorarbeit viele Freiräume, um mich mit verschiedenen Fragestellungen zu befassen. Besonders dankbar bin ich ihm dafür, dass er mich mit an die TU Hamburg-Harburg genommen hat. Dort konnte ich weitere Anwendungen numerischer Methoden kennenlernen und Lehrveranstaltungen durchführen, die nahe an meinem Thema lagen.

Darüber hinaus danke ich Herrn Prof. Dr.-Ing. Stefan Diebels für die Übernahme der Zweitkorrektur, die gute Zusammenarbeit im Forschungsprojekt sowie die Möglichkeit, den Lehrstuhl für Technische Mechanik an der Universität des Saarlandes bei verschiedenen Seminaren und Projekttreffen kennenzulernen.

Herrn Prof. Dr.-Ing. Thomas Rung danke ich für die Übernahme des Prüfungsvorsitzes.

Meinem ehemaligen Projektpartner, Herrn Dr.-Ing. Ralf Jänicke, möchte ich für die konstruktive Zusammenarbeit danken.

Nun möchte ich mich bei dem Lehrstuhl CiE für die Unterstützung bedanken. Besonders danke ich Herrn Prof. Dr. rer. nat. Ernst Rank, bei dem meine Doktorarbeit begann. Darüber hinaus danke ich Frau Hanne Cornils für die persönliche und administrative Unterstüzung und meinem ehemaligen Zimmerkollegen, Herrn Dr.-Ing. Stefan Kollmannsberger, der mit mir zusammen die Zeit in München angenehm gestaltet hat.

Weiterhin danke ich dem gesamten Institut M-10. Bei Herrn Dr.-Ing. Horst Höft bedanke ich mich für die Unterstützung meiner Berechnungen, bei Herrn Wolfgang Koch für die interessanten Einblicke in die Versuchstechnik sowie bei Frau Jutta Henrici für die Beantwortung organisatorischer Fragen im Rahmen meines Projekts. Bei Frau Sonja Zacke bedanke ich mich für die gute Arbeitsatmosphäre im gemeinsamen Büro.

Meinen Eltern gebührt große Anerkennung für die konstante Förderung und ihr Vertrauen in mich. Schließlich möchte ich mich sehr herzlich bei meiner Familie bedanken. Insbesondere danke ich meiner Frau Cornelia, die immer für mich da war und somit einen großen Beitrag zu dieser Arbeit geleistet hat.

Krefeld, den 11.11.2011

Hans-Georg Sehlhorst

Contents

Notation

The notation of tensors, some operators[1] and matrices are briefly introduced here. Tensors and tensor products are used within the CARTESIAN coordinate system with unit base vectors $\underset{\sim}{E}_1$, $\underset{\sim}{E}_2$ and $\underset{\sim}{E}_3$. Note that the EINSTEIN summation convention is applied.

Tensors

A	Scalar value
$\underset{\sim}{X} = X_i \, \underset{\sim}{E}_i$	First-order tensor (vector)
$\underset{\sim}{\mathrm{S}} = S_{ij} \, \underset{\sim}{E}_i \otimes \underset{\sim}{E}_j$	Second-order tensor
$\overset{3}{\underset{\sim}{\mathrm{Q}}} = Q_{ijk} \, \underset{\sim}{E}_i \otimes \underset{\sim}{E}_j \otimes \underset{\sim}{E}_k$	Third-order tensor
$\overset{4}{\underset{\sim}{\mathrm{C}}} = C_{ijkl} \, \underset{\sim}{E}_i \otimes \underset{\sim}{E}_j \otimes \underset{\sim}{E}_k \otimes \underset{\sim}{E}_l$	Fourth-order tensor

Tensor operations

$\underset{\sim}{u} \otimes \underset{\sim}{v} = u_i \, v_j \, \underset{\sim}{E}_i \otimes \underset{\sim}{E}_j$	Dyadic product
$\underset{\sim}{\mathrm{S}} \cdot \underset{\sim}{\mathrm{F}} = S_{ij} \, F_{ij}$	Inner product
$\underset{\sim}{\mathrm{S}} \, \underset{\sim}{\mathrm{F}} = S_{ij} \, F_{jk} \, \underset{\sim}{E}_i \otimes \underset{\sim}{E}_k$	Tensor product

Matrices

$\boldsymbol{u}$	Local element column vector
$\boldsymbol{J}$	Local element matrix
$\mathbf{r}$, $\mathbf{R}$	Global column vector, global matrix

[1] Additional operators will be discussed when they appear for the first time.

Abstract

Cellular materials are of increasing interest since they offer a unique combination of properties like, for example, high mechanical stiffness or damping features and low weight. However, the modeling and computation of such materials is difficult due to size dependent boundary layer effects and deformation-induced anisotropy caused by reorientations and cell buckling. In order to capture such effects, there exist a variety of analytical and numerical methods. In this thesis numerical approaches are developed and applied, mainly focusing on numerical homogenization techniques. These multiscale techniques are based on the principle of scale separation, where an explicit microstructure is embedded into a macroscopic framework. The scales are coupled together by projection of macroscopic strain-like quantities and homogenization of microscopic stress-like quantities. Therefore, a nested boundary value problem, commonly referred to as the FE^2-problem, has to be solved. Depending on the underlying continuum theory there are first-order and higher-order FE^2-schemes. In earlier FE^2-schemes, the spatial discretization of the microscale was based on (dimensionally reduced) low-order finite elements. This work applies higher-order continuum finite element methods, which are known to be highly efficient and very robust.

In particular, three different homogenization schemes have been developed: A two-dimensional hyperelastic first-order FE^2-scheme using classical continua has been applied on both scales to investigate cellular materials under large deformations focusing on deformation-induced anisotropy. In order to detect size effects, a higher-order FE^2-scheme with restriction to 2D and small deformations has been designed. It is based on the micromorphic continuum theory and includes its subcontinua like, for example, the micropolar theory. The results of these schemes have been verified successfully by microscopically resolved reference computations.

In three dimensions a first-order homogenization approach was developed, which computes effective linear elastic properties of any microstructured material whereby the microstructure is represented by computed tomography (micro CT-scans). The key feature of this approach is the application of a higher-order fictitious domain method allowing for fast and simple discretization of micro CT-scans. The approach has been verified numerically by considering solid- and foam-like materials and validated by comparision to experiments with commercially available foams. In the validation the pure foam material under compression and shear has been investigated and in addition sandwich plates consisting of aluminum faceplates and a foamed core were subjected to bending experiments.

The thesis concludes with microscopic stability investigations of two- and three-dimensional open-cell foam-like structures under large strain compression whereby the discretization has been performed by anisotropic hyperelastic higher-order finite elements. It could be observed that cellular materials under compression do not exhibit any distinct point of instability, since buckling of the individual cell walls does not occur simultaneously. This observation is in accordance with experimental investigations.

Zusammenfassung

Zelluläre Materialien erlangen eine immer größere Bedeutung, da sie eine einzigartige Kombination aus Eigenschaften wie zum Beispiel hoher mechanischer Steifigkeit oder Dämpfungseigenschaften bei gleichzeitig geringem Gewicht bieten. Die Berechnung solcher Materialien ist schwierig, da maßstabsabhängige Randschichteffekte und deformationsgetriebene Anisotropie, welche durch Zellumorientierungen bedingt ist, auftreten können. Um diese Effekte zu erfassen, existieren eine Reihe analytischer und numerischer Verfahren. In dieser Arbeit wird ein numerischer Zugang gewählt, wobei hauptsächlich numerische Homogenisierungsverfahren betrachtet werden. Diese Mehrskalentechniken basieren auf dem Prinzip der Skalenseparation, wobei eine explizite Mikrostruktur in eine makroskopische Berechnung integriert wird. Die Skalen sind gekoppelt über Projektion makroskopischer verzerrungsartiger Größen und Homogenisierung mikroskopischer spannungsartiger Größen, wodurch ein geschachteltes Randwertproblem gelöst werden muss, welches gewöhnlich als FE^2-Problem bezeichnet wird. In Abhängigkeit von den verwendeten Kontinuumstheorien kann man zwischen FE^2-Schemata erster und höherer Ordnung unterscheiden. Im Gegensatz zu existierenden FE^2-Schemata, in denen die räumliche Diskretisierung auf (oftmals dimensionsreduzierten) finiten Elementen niedriger Ordnung basiert, werden in dieser Arbeit finite Kontinumselemente höherer Ordnung, die sich als sehr effizient und robust erwiesen haben, verwendet.

Insgesamt sind drei unterschiedliche Homogensierungsschemata entwickelt worden: Ein zweidimensionales hyperelastisches FE^2-Schema erster Ordnung, welches klassische Kontinua auf beiden Skalen verwendet, ist angewandt worden, um Schaumstrukturen unter großen Verformungen zu untersuchen. Hierbei lag das Hauptaugenmerk auf deformationsgetriebener Anisotropie. Zur Erfassung von Maßstabseffekten ist ein FE^2-Schema höherer Ordnung mit Einschränkung auf zwei Dimensionen und kleine Verformungen entwickelt worden. Es basiert auf der mikromorphen Kontinuumstheorie und schließt deren Unterkontinua, wie beispielsweise die mikropolare Theorie, ein. Die Ergebnisse beider Schemata sind erfolgreich an mikroskopisch voll aufgelösten Referenzrechnungen verifiziert worden.

Im Dreidimensionalen ist ein Homogenisierungsansatz erster Ordnung entwickelt worden, welcher effektive linear elastische Eigenschaften mikrostrukturierter Materialien berechnet, wobei die Mikrostruktur durch Mikrotomographie (CT-Scans) repräsentiert wird. Der Hauptvorteil des Homognisierungsansatzes ist die Anwendung einer Fictitious Domain Methode höherer Ordnung, die eine schnelle und einfache Diskretisierung der mikroskopischen CT-Scans ermöglicht. Der Ansatz ist numerisch an massiven und schaumartigen Materialien verifiziert worden. Eine Validierung erfolgt durch die Modellierung von Experimenten mit kommerziellen Schäumen. Hierbei wurden sowohl der reine Schaum unter Druck und Scherung als auch Sandwichplatten, die aus Aluminium Deckschichten mit geschäumten Kernen bestehen, untersucht.

Die Arbeit schließt ab mit mikroskopischen Stabilitätsuntersuchungen an zwei- und dreidimensionalen offenporigen Schaumstrukturen unter starker Kompression, wobei die Diskretisierung durch hyperelastische finite Elemente höherer Ordnung erfolgt. Hierbei zeigt sich, dass zelluläre Materialien keine ausgeprägten Instabilitätspunkt besitzen, da das Ausknicken der Zellwände nicht gleichzeitig auftritt. Diese Beobachtung deckt sich mit experimentellen Untersuchungen.

Chapter 1

Introduction

1.1 Motivation

There is an increasing interest in cellular materials, since they combine properties like, for example, damping respectively insulation features and high mechanical stiffness with low mass density. One can distinguish between open-cell and closed-cell materials, see Figures 1.1 and 1.2.

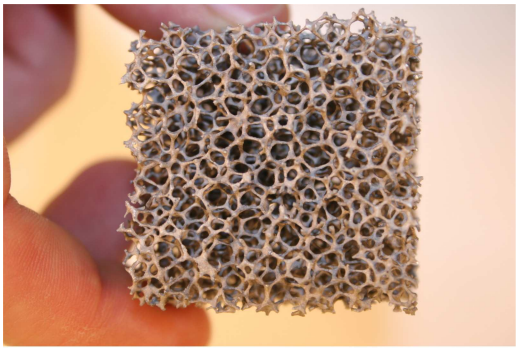

Figure 1.1: Open-cell aluminum foam

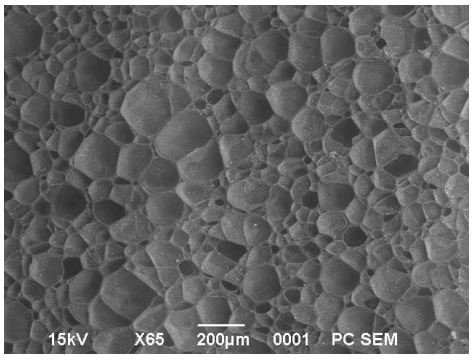

Figure 1.2: Closed-cell polymeric foam

Let us consider a few applications of such materials:

- In vehicle construction, bumpers, girders, catalytic converters and heat exchangers are made of foam-like materials.
- Cellular materials are widely used in civil engineering for thermal protection shields and sound absorbers.
- In mechanical engineering closed-cell aluminum foams are applied to rollers or sliding tables.
- Sandwich structures with foamed cores can be found in ship and aircraft construction.

Cellular materials show a complex mechanical behavior which becomes obvious in the following example: We consider three independent mechanical tests of a foam-like specimen as depicted in Figure 1.3. From these tests one can obtain the mechanical parameters E, K, and G. It is

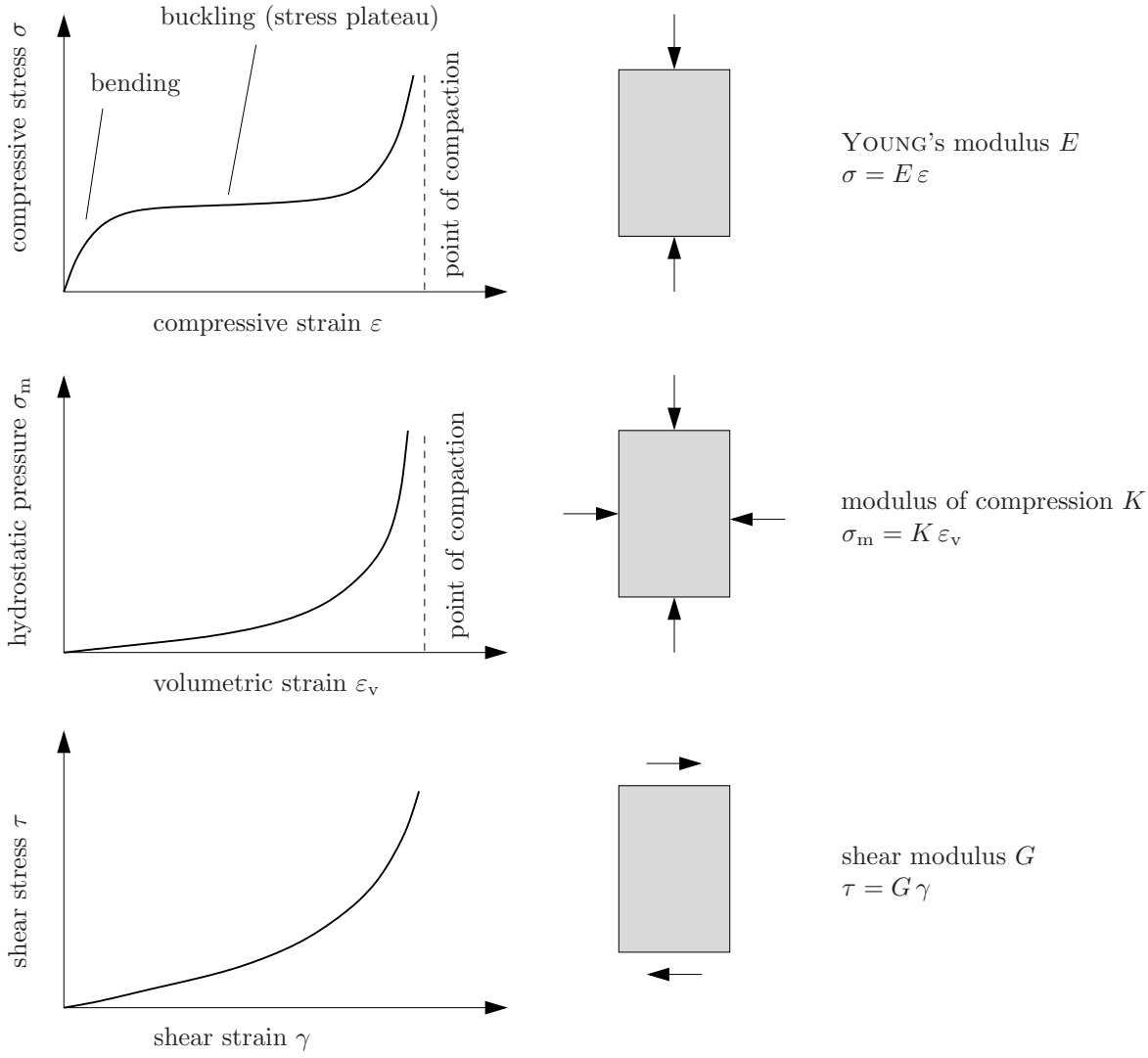

Figure 1.3: Foam-like specimen subjected to three independent tests

well known that for isotropic, homogeneous materials these parameters are not independent, and the following relation

$$G_{\mathrm{theoretical}} \;=\; \frac{3\,E\,K}{9\,K - E} = G_{\mathrm{experimental}} \tag{1.1}$$

should hold. However, in the case of foam-like materials equation (1.1) is not valid. The reason lies in the fact that such materials feature, for example, *deformation-induced anisotropy* due to local reorientations and cell buckling [31, 55, 71, 77, 84, 100, 108] or *size-dependent boundary layer effects* [3, 10, 13, 69, 78, 102].
Size-dependency means that the mechanical properties depend on the specimen's size. Imagine specimens with different height H that are subjected to a shear test, see Figure 1.4. Here, one observes that with increasing height the effective shear modulus G decreases and converges towards a certain bulk value. In the next section methods that allow for modeling of cellular materials are presented.

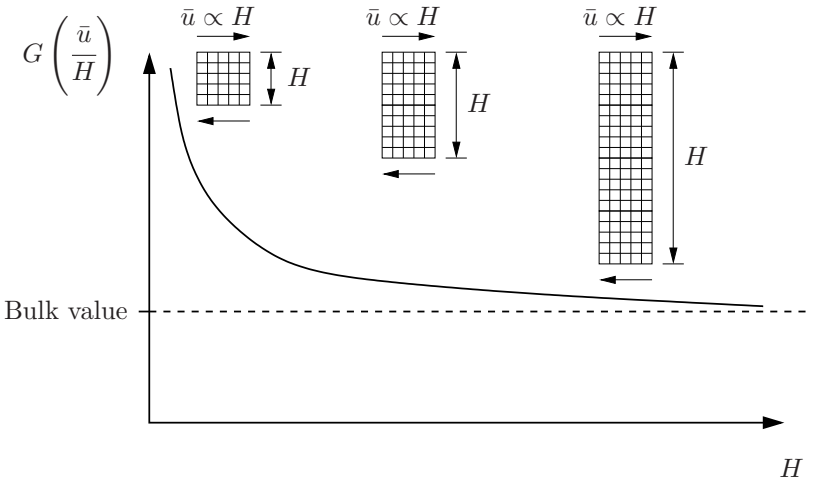

Figure 1.4: Size effect in a shear test with specimens of different heights H; note that prescribed displacements $\bar{u} \propto H$ are applied to the top and bottom and periodic boundary conditions are assumed at the left and right hand side

1.2 Modeling of cellular materials

In this section we give an overview of modeling approaches of (heterogeneous) cellular materials. There are basically two approaches, refer to Figure 1.5: The *microscopic* approach, see Gibson and Ashby [41], Diebels and Steeb [19], Tekoğlu [93] and the *macroscopic* approach, see for example Eringen et al. [29, 65], Anderson and Lakes [4], Diebels and Steeb [20]. In the *microscopic* approach the structure is microscopically resolved by finite

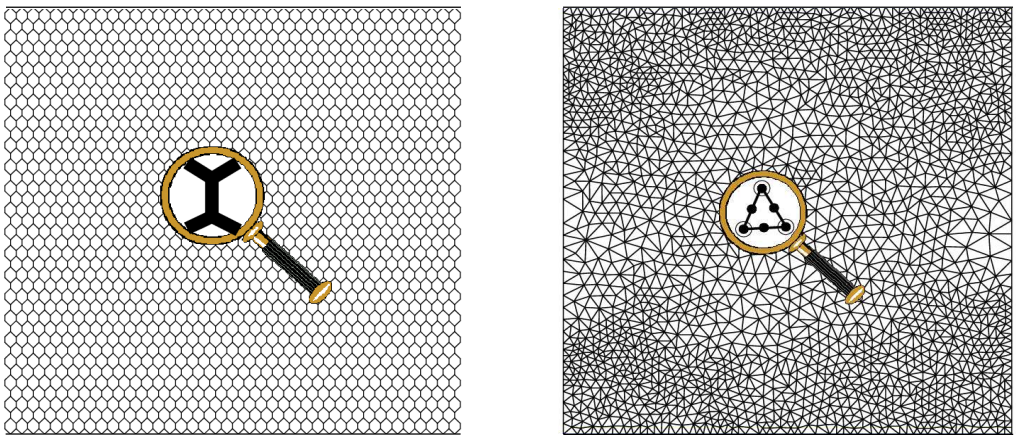

microscopic approach *macroscopic* approach

Figure 1.5: Modeling of cellular materials

elements and allows all microscopic effects to be studied. However, this method involves a high number of degrees of freedom, and it is therefore limited to small problems. A possible

application of this approach is reference computations, which can be applied to verify for example the results obtained by *macroscopic* modeling.

The *macroscopic* approach is based on extended continuum theories and replaces the microheterogeneous material with an *extended* homogeneous macromaterial allowing for higher-order effects, for example size effects. Extended continua can be classified into *higher-order* theories and *higher-grade* theories. In the *first* group additional degrees of freedom are introduced. The most popular representative is the micropolar or COSSERAT theory [15] where microrotations are assumed. This is a subcontinuum of the class of micromorphic continua [30]. The *second* group does not require additional degrees of freedom but higher-order derivatives of the macroscopic displacement field [12, 40]. Although the numerical efficiency of *macroscopic* modeling is much higher as compared to *microscopic* modeling, it is limited by the fact that the material parameters are difficult to obtain as shown by LAKES [70].

A promising combination of both approaches is the FE^2 method. This method is based on the principle of scale separation or *MMM-principle* as stated by HUET [60], refer to Figure 1.6. Here, three different scales are considered: the **m**acro-, **m**eso-, and **m**icroscale. While

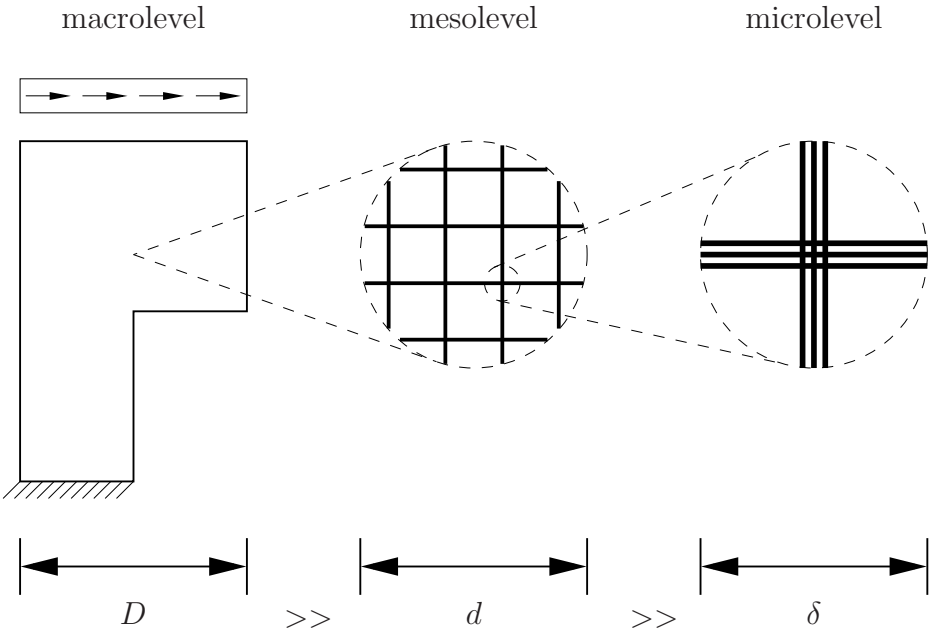

Figure 1.6: MMM-principle: different levels

the macroscale describes the entire structure as a continuum, the mesoscale gives an insight into the microtopology, and finally, the microscale resolves the microstructure on the atomistic level. In this thesis the step between meso- and microscale is assumed to be very large, and not considered further. For simplification of the nomenclature the term meso will be replaced by micro in the sequel. In order to brigde the scales the FE^2-method is applied, compare with Figure 1.7. In this method, a characteristic microstructure with volume V_m is embedded into a macroscopic finite element framework via projection and homogenization rules and thus the complicated macroscopic constitutive equations are replaced by the solution of nested bound-

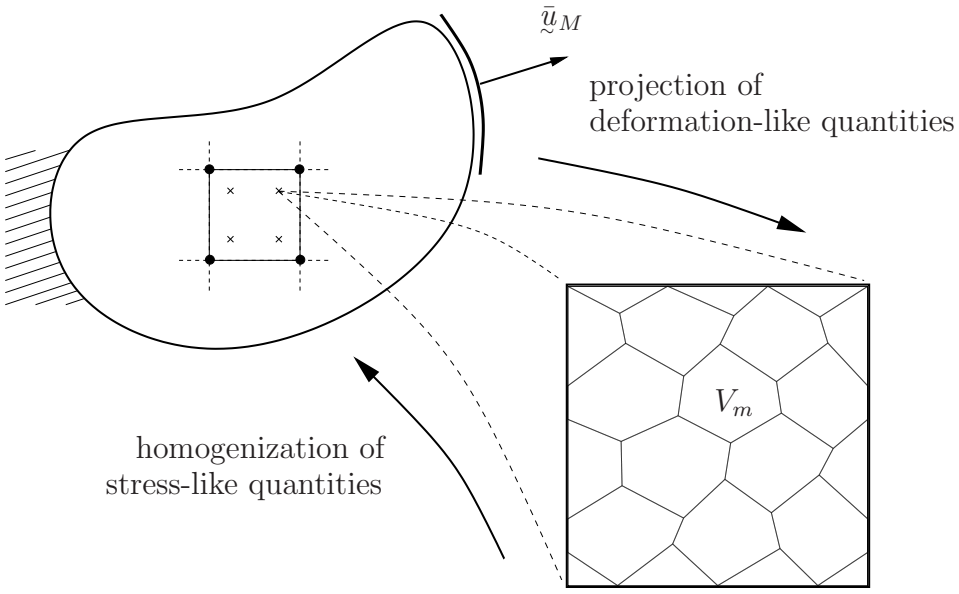

Figure 1.7: The FE^2-method: Solving a nested boundary value problem

ary value problems (BVP), refer to Feyel [33, 34, 35] or Kouznetsova [67]. Since the nested BVPs especially on the microscale are computationally expensive, improvements like, for example, consistent material tangents have been suggested by Miehe [72, 73] and Schröder [87] and, in addition, distributed computing of the microscopic BVPs has been performed [67].

There are first-order FE^2 schemes with standard continuum theories on both macro- and microlevel [73], and schemes of higher-order with extended continuum theories at least on the macrolevel [28, 36, 37, 38, 63, 62].

The microstructure itself can be either a Representative Volume Element (RVE) as proposed by Hill [52] or a Testing Volume Element (TVE) as introduced by Nemat-Nasser and Hori [75]. The RVE is chosen such that it represents statistically the micromechanical properties of the material. In general this leads to large RVEs and therefore to a high number of degrees of freedom, as demonstrated for hardened cement paste by Hain [46]. In contrast, the TVE is much smaller than the RVE. The TVE only provides the basic mechanical properties of the material, i.e. that it can be too stiff or too weak depending on its boundary conditions.

1.3 Scope and outline of this work

In the above mentioned work on numerical homogenization the underlying (microstructural) finite element discretizations were based on either dimensionally reduced elements and / or low-order continuum solid elements and thus might suffer from model errors, locking phenomena and low convergence rates. In order to overcome such problems, in this thesis spatial discretization strategies based on continuum higher-order finite element methods (p-FEM) are

suggested for two- and three-dimensional first- and higher-order multiscale methods[1]. Let us highlight the major advantages of this novel approach:

- Higher-order finite elements have been demonstrated to provide high convergence rates, i.e. they are computationally more efficient, and are robust against locking effects in linear and nonlinear problems of solid and structural mechanics [22, 23, 25, 26, 27, 51, 76, 91].

- In a continuum-based approach the numerical treatment of geometrical nonlinearities of thin-walled structures is straight-forward since no drilling degrees of freedom arising in classical beam, plate, and shell theories need to be considered. Another advantage of continuum-based modeling is that three-dimensional constitutive models can be applied directly without any additional assumptions like, for example, vanishing transverse normal stresses ($\sigma_{zz} = 0$).

- Thin- and thick-walled beam-like or shell-like structures can be accurately discretized with anisotropic continuum-based elements, where different polynomial degrees are chosen in thickness and in longitudinal respectively in plane direction.

We will demonstrate the p-version's efficiency by several numerical examples whereby the focus lies on open-cell materials: In two dimensions cross-like and honeycomb structures are concerned, and in three dimensions real-world sandwich materials with an open-cell core are investigated.

After having defined the scope of this work let us give a detailed *outline*:

- In chapter 2 a summary of classical continuum mechanics is given. The summary comprises kinematics, balance equations, variational formulation, and constitutive modeling for the hyperelastic case. Furthermore, the micromorphic continuum theory is briefly introduced, which will be the basis for the higher-order FE^2 scheme.

- Spatial discretization techniques for classical continua are discussed in chapter 3:

  - The p-version of the FEM for hyperelasticity is reviewed and improved further. The review includes the discretization of the variational formulation, shape functions, anisotropic elements for thin structures, and mapping techniques. In order to reduce the computational effort a *quasi-spatial* formulation has been developed and implemented. The gain in efficiency compared to the previous *material* formulation has been estimated and verified numerically.
  - The finite cell method (FCM) which is a fictitious domain method of higher-order is briefly discussed. In this method the burden of mesh generation is shifted to the numerical integration. Therefore, it is highly attractive for discretizing material specimens stemming from three-dimensional micro tomography (CT-scans).

[1]Note that the higher-order FE^2 methods enhanced by p-FEM within this thesis are based on joint works with JÄNICKE ET AL. [62, 63], where the micromorphic continuum theory has been applied.

- In chapter 4 multiscale methods are presented where the microscale is discretized by the p-version of the FEM. In two dimensions we propose a first-order FE^2 scheme designed for large deformations using distributed computing of the microstructures, and in addition a higher-order FE^2 scheme for small deformations is set up. In the higher-order FE^2 scheme special attention has been paid to the design of projection rules suited for the p-version. In three dimensions a homogenization approach of first-order suited for small deformations applying the FCM was developed. This approach allows for directly computing effective material parameters from micro CT-scans.

- In the numerical examples given in chapter 5 the special mechanical features of cellular materials are investigated:

  - The first-order scheme was mainly applied to detect deformation-induced anisotropy in artificially generated honeycomb microstructures. In addition, boundary conditions for such microstructures have been proposed and numerically verified.
  - Size effects were studied by the higher-order FE^2 scheme for cross- and foam-like microstructures. Furthermore, an application to a sandwich structure under bending is included. All of the computations have been verified by microscopic reference computations.
  - The three-dimensional homogenization approach was used for extracting effective material parameters of microstructured materials. Hereby, general guidelines for an efficient discretization of cellular materials (given in terms of CT-scans) and for a representative number of foam cells has been developed. Equipped with these guidelines open-cell Polyurethane foams have been homogenized and the results have been validated by experiments with the pure foam material and composites, namely sandwich plates.
  - The last part of the examples is dedicated to stability considerations including eigenvalue analysis at two- and three-dimensional foam-like structures under large strain compression.

- A summary of this work and future research possibilities can be found in chapter 6.

Chapter 2

Continuum mechanics

In this chapter we review some basics of continuum mechanics as far as they are of interest within this work. In section 2.1 classical continuum mechanics is considered, while in section 2.2 an extended continuum theory, the micromorphic continuum theory, is presented.

2.1 Classical continuum mechanics

In this section we deal with kinematics, stress state and balance equations, variational formulations and finally constitutive modeling with focus on hyperelasticity. The contents are strongly influenced by textbooks like [8, 49, 105], where the reader can find more details.

2.1.1 Kinematics

This section describes the motion of a deformable body and suitable strain measures.

2.1.1.1 Motion

The motion of a deformable body B is considered as depicted in Figure 2.1. The body can be viewed as an ensemble of continuously distributed *particles* or *material points*. These points are labeled by the coordinates $\underset{\sim}{X}$ of the reference configuration at time t_0 utilizing the CARTESIAN basis $\underset{\sim}{E}_I$. The current positions of these points are described by the coordinates $\underset{\sim}{x}$ of the current configuration at t with the CARTESIAN basis $\underset{\sim}{e}_i$. Note that in the following only $\underset{\sim}{E}_I$ will be used within figures.

Within this thesis quantities like, for example, tensors or operators referring to the reference configuration are denoted by capital letters or in some exceptions by an index 0, and small letters are used for quantities of the current configuration. The position of a particle at time t is given by the mapping

$$\underset{\sim}{x} = \underset{\sim}{\varphi}(\underset{\sim}{X}, t)\,. \tag{2.1}$$

One has to distinguish between two ways of describing the motion of a body:

- The EULERIAN way utilizes the *spatial* description. Here, the observer monitors at a distinct spatial position the movement of particles passing through this position.

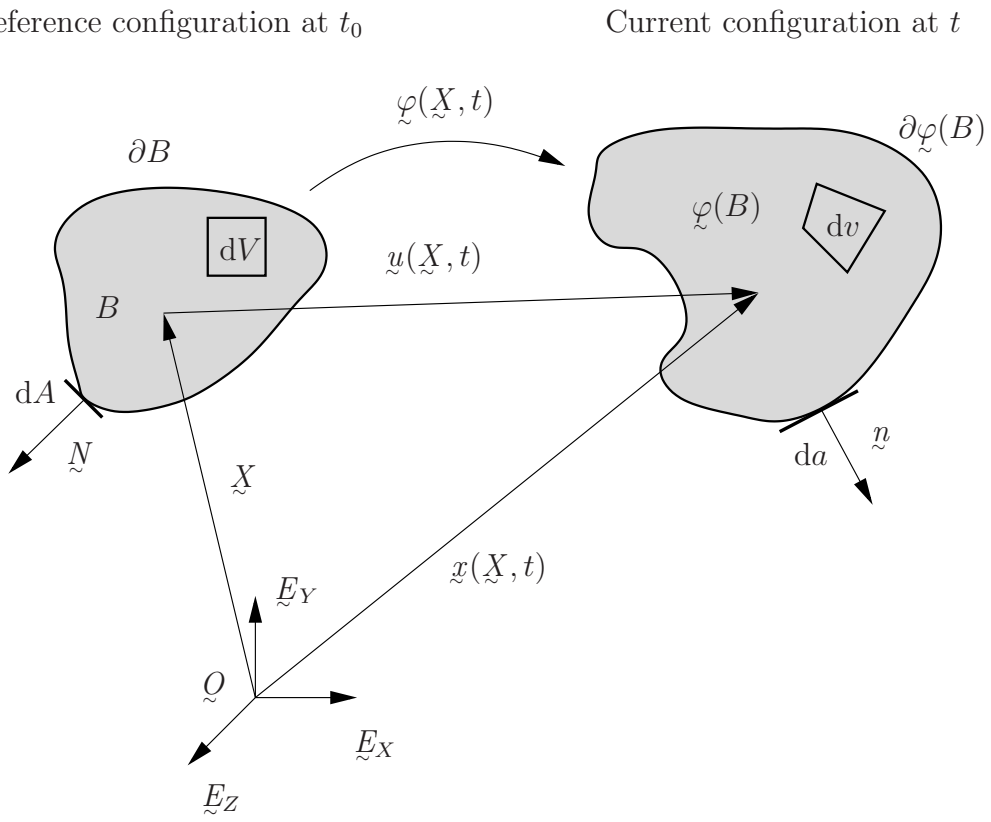

Figure 2.1: Motion of a deformable body [105]

- In the LAGRANGIAN approach the *material* description is used. The observer is connected to a distinct material point.

The EULERIAN approach is commonly applied in fluid mechanics. In solid and structural mechanics the LAGRANGIAN description is very popular. To describe the deformation of the body, the deformation gradient tensor $\underset{\sim}{\mathrm{F}}$ is introduced

$$\mathrm{d}\underset{\sim}{x} \;=\; \underset{\sim}{\mathrm{F}}\,\mathrm{d}\underset{\sim}{X}\,, \tag{2.2}$$

which associates infinitesimal line elements $\mathrm{d}\underset{\sim}{x}$ of the current configuration with line elements of the reference configuration $\mathrm{d}\underset{\sim}{X}$. $\underset{\sim}{\mathrm{F}}$ is commonly denoted as

$$\underset{\sim}{\mathrm{F}} \;=\; \mathrm{Grad}\,\underset{\sim}{\varphi}(\underset{\sim}{X},t) = F_{iI}\,\underset{\sim}{e}_i \otimes \underset{\sim}{E}_I = \frac{\partial x_i}{\partial X_I}\,\underset{\sim}{e}_i \otimes \underset{\sim}{E}_I = x_{i,I}\,\underset{\sim}{e}_i \otimes \underset{\sim}{E}_I \tag{2.3}$$

and classified as a two-point tensor with base vectors of both configurations. The uniqueness of the mapping (2.1) excludes any singularity of $\underset{\sim}{\mathrm{F}}$. Therefore, the determinant of $\underset{\sim}{\mathrm{F}}$ must fulfill

$$J \;=\; \det\underset{\sim}{\mathrm{F}} > 0\,. \tag{2.4}$$

The JACOBIAN J is utilized for the transformation of surface area elements between both configurations via NANSON's formula

$$\mathrm{d}\underset{\sim}{a} \;=\; \underset{\sim}{n}\,\mathrm{d}a = J\,\underset{\sim}{\mathrm{F}}^{-\mathrm{T}}\,\underset{\sim}{N}\,\mathrm{d}A = J\,\underset{\sim}{\mathrm{F}}^{-\mathrm{T}}\,\mathrm{d}\underset{\sim}{A} \tag{2.5}$$

where $\underset{\sim}{n}$ and $\underset{\sim}{N}$ are the outer normal vectors of the deformed and undeformed bodies, respectively, see Figure 2.1. Volume elements of both configurations are related by

$$\mathrm{d}v = J\,\mathrm{d}V\,. \tag{2.6}$$

The displacement vector $\underset{\sim}{u}(\underset{\sim}{X},t)$ is defined as

$$\underset{\sim}{u}(\underset{\sim}{X},t) = \underset{\sim}{x} - \underset{\sim}{X} = \underset{\sim}{\varphi}(\underset{\sim}{X},t) - \underset{\sim}{X}\,. \tag{2.7}$$

Inserting (2.7) into (2.3) yields

$$\underset{\sim}{\mathrm{F}} = \mathrm{Grad}\,(\underset{\sim}{X} + \underset{\sim}{u}(\underset{\sim}{X},t)) = \underset{\sim}{\mathrm{I}} + \mathrm{Grad}\,\underset{\sim}{u} = \underset{\sim}{\mathrm{I}} + \underset{\sim}{\mathrm{H}}\,, \tag{2.8}$$

with $\underset{\sim}{\mathrm{I}}$ denoting the second-order unit tensor. The following transformation applied to an arbitrary vector field $\underset{\sim}{W}(\underset{\sim}{X}) = \underset{\sim}{w}(\underset{\sim}{x})$

$$\mathrm{Grad}\,\underset{\sim}{W} = \mathrm{grad}\,\underset{\sim}{w}\,\underset{\sim}{\mathrm{F}} \qquad \Longleftrightarrow \qquad \mathrm{grad}\,\underset{\sim}{w} = \mathrm{Grad}\,\underset{\sim}{W}\,\underset{\sim}{\mathrm{F}}^{-1} \tag{2.9}$$

allows us to express the inverse of $\underset{\sim}{\mathrm{F}}$ in terms of $\mathrm{grad}\,\underset{\sim}{u}$

$$\underset{\sim}{\mathrm{F}}^{-1} = \underset{\sim}{\mathrm{I}} - \mathrm{grad}\,\underset{\sim}{u}\,. \tag{2.10}$$

2.1.1.2 Strain measures

In this section we introduce different strain measures which will be utilized in this thesis. The Green-Lagrange strain tensor is defined as

$$\underset{\sim}{\mathrm{E}} = \frac{1}{2}\,(\underset{\sim}{\mathrm{C}} - \underset{\sim}{\mathrm{I}})\,, \tag{2.11}$$

where

$$\underset{\sim}{\mathrm{C}} = \underset{\sim}{\mathrm{F}}^{\mathrm{T}}\,\underset{\sim}{\mathrm{F}} \tag{2.12}$$

is the right Cauchy-Green deformation tensor related to the reference configuration. In indical notation $\underset{\sim}{\mathrm{E}}$ can be written as

$$\underset{\sim}{\mathrm{E}} = E_{IJ}\,\underset{\sim}{E}_I \otimes \underset{\sim}{E}_J \quad \text{with} \quad E_{IJ} = \frac{1}{2}\,(F_{iI}F_{iJ} - \delta_{IJ})\,. \tag{2.13}$$

The Kronecker symbol is defined as

$$\delta_{ij} = \begin{cases} 1 & \text{if } i = j \\ 0 & \text{if } i \neq j \end{cases}\,. \tag{2.14}$$

Inserting (2.8) into (2.11) yields

$$\underset{\sim}{\mathrm{E}} = \frac{1}{2}\,(\underset{\sim}{\mathrm{H}} + \underset{\sim}{\mathrm{H}}^{\mathrm{T}} + \underset{\sim}{\mathrm{H}}^{\mathrm{T}}\,\underset{\sim}{\mathrm{H}})\,, \tag{2.15}$$

highlighting the nonlinearity of $\underset{\sim}{\mathrm{E}}$. When considering infinitesimal (small) deformations $\underset{\sim}{\mathrm{H}}^{\mathrm{T}}\,\underset{\sim}{\mathrm{H}}$ is neglected and we obtain the classical engineering strain tensor

$$\underset{\sim}{\varepsilon} = \frac{1}{2}\,(\underset{\sim}{\mathrm{H}} + \underset{\sim}{\mathrm{H}}^{\mathrm{T}}) = \frac{1}{2}\,(u_{I,J} + u_{J,I})\,\underset{\sim}{E}_I \otimes \underset{\sim}{E}_J\,. \tag{2.16}$$

A strain measure related to the current configuration is the EULER-ALMANSI strain tensor

$$\underset{\sim}{\mathrm{e}} = \frac{1}{2}\left(\underset{\sim}{\mathrm{I}} - \underset{\sim}{\mathrm{b}}^{-1}\right), \tag{2.17}$$

with

$$\underset{\sim}{\mathrm{b}} = \underset{\sim}{\mathrm{F}}\,\underset{\sim}{\mathrm{F}}^{\mathrm{T}} \tag{2.18}$$

denoting the left CAUCHY-GREEN deformation tensor. The relation between $\underset{\sim}{\mathrm{e}}$ and $\underset{\sim}{\mathrm{E}}$ is established by *push forward*

$$\underset{\sim}{\mathrm{e}} = \underset{\sim}{\mathrm{F}}^{-\mathrm{T}}\,\underset{\sim}{\mathrm{E}}\,\underset{\sim}{\mathrm{F}}^{-1} \tag{2.19}$$

and *pull back* operations

$$\underset{\sim}{\mathrm{E}} = \underset{\sim}{\mathrm{F}}^{\mathrm{T}}\,\underset{\sim}{\mathrm{e}}\,\underset{\sim}{\mathrm{F}}\,. \tag{2.20}$$

2.1.2 Stress state and balance equations

Imagine a deformable body in its current configuration where a force $\Delta\underset{\sim}{\hat{p}}$ acts on an area Δa normal to $\underset{\sim}{n}$ at a point $\underset{\sim}{x}$ as shown in Figure 2.2. The spatial traction vector is defined as

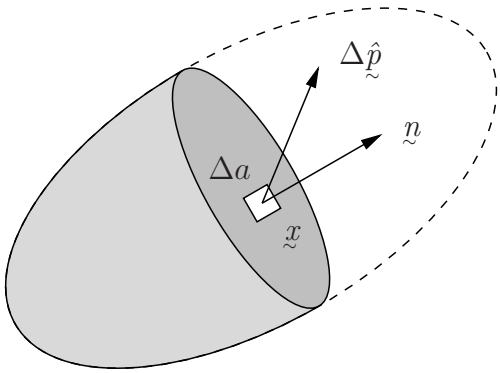

Figure 2.2: Stress state in the current configuration

$$\underset{\sim}{t} = \lim_{\Delta a \to 0} \frac{\Delta\underset{\sim}{\hat{p}}}{\Delta a}\,. \tag{2.21}$$

The CAUCHY theorem associates $\underset{\sim}{t}$ with $\underset{\sim}{n}$ via a linear relation

$$\underset{\sim}{t} = \underset{\sim}{\sigma}\,\underset{\sim}{n}\,, \tag{2.22}$$

where $\underset{\sim}{\sigma}$ is the CAUCHY stress tensor.

The local equilibrium of a deformable body is governed by balance equations. In a system where mass is conserved, the *balance of mass* must hold

$$\rho\,\mathrm{d}v = \rho_0\,\mathrm{d}V\,, \tag{2.23}$$

where ρ and ρ_0 are the current and initial densities, respectively. The *local balance of equilibrium* is formulated as

$$\operatorname{div} \underset{\sim}{\sigma} + \rho \underset{\sim}{f} \;=\; \underset{\sim}{0} \tag{2.24}$$

with $\rho \underset{\sim}{f}$ representing volume forces. The *balance of equilibrium of momentum* yields

$$\underset{\sim}{\sigma} \;=\; \underset{\sim}{\sigma}^{\mathrm{T}}, \tag{2.25}$$

resulting in the symmetry of the CAUCHY stress tensor. A continuum fulfilling (2.25) is called a classical or BOLTZMANN continuum[1].

Up to now stresses only refer to the current configuration. In general and more particular in the context of numerical homogenization (see chapter 4) it is desirable to have additional stress measures. Since a given state of stress does not change physically when referred to another configuration the following transformation applying equation (2.5) is valid

$$\int_a \underset{\sim}{\sigma}\, \underset{\sim}{n}\, \mathrm{d}a \;=\; \int_A \underset{\sim}{\sigma}\, J\, \underset{\sim}{\mathrm{F}}^{-\mathrm{T}}\, \underset{\sim}{N}\, \mathrm{d}A = \int_A \underset{\sim}{\mathrm{P}}\, \underset{\sim}{N}\, \mathrm{d}A \tag{2.26}$$

yielding the first PIOLA-KIRCHHOFF stress tensor

$$\underset{\sim}{\mathrm{P}} \;=\; J\, \underset{\sim}{\sigma}\, \underset{\sim}{\mathrm{F}}^{-\mathrm{T}} = P_{iI}\, \underset{\sim}{e}_i \otimes \underset{\sim}{E}_I \quad \text{with} \quad P_{iI} = J\, \sigma_{ij}\, (F_{Ij})^{-1}. \tag{2.27}$$

Note that $\underset{\sim}{\mathrm{P}}$ is a two-point tensor. The counterpart to the spatial traction vector (2.22) is the first PIOLA-KIRCHHOFF stress vector

$$\underset{\sim}{p} \;=\; \underset{\sim}{\mathrm{P}}\, \underset{\sim}{N}\,. \tag{2.28}$$

Finally, the balance of equilibrium with respect to the reference configuration can be reformulated as

$$\operatorname{Div} \underset{\sim}{\mathrm{P}} + \rho_0 \underset{\sim}{f} \;=\; \underset{\sim}{0}\,. \tag{2.29}$$

A stress measure only referring to the initial configuration is the second PIOLA-KIRCHHOFF stress tensor

$$\underset{\sim}{\mathrm{S}} \;=\; \underset{\sim}{\mathrm{F}}^{-1}\, \underset{\sim}{\mathrm{P}} = J\, \underset{\sim}{\mathrm{F}}^{-1}\, \underset{\sim}{\sigma}\, \underset{\sim}{\mathrm{F}}^{-\mathrm{T}}\,. \tag{2.30}$$

It represents a full *pull back* of $\underset{\sim}{\sigma}$. In Table 2.1 useful conversions between the different stress tensors are summarized.

2.1.3 Variational formulations

In the previous sections kinematical relations, stress measures and balance equations with respect to both reference and current configuration have been presented in terms of partial differential equations. A discussion of constitutive relations, which link stresses with strains, is postponed to section 2.1.4. In order to set up a boundary value problem (BVP), boundary conditions have to be considered:

[1] Extended continua will be addressed in section 2.2.2.

Table 2.1: Conversion between stress tensors [49]

		$\underset{\sim}{\mathrm{P}}$	$\underset{\sim}{\mathrm{S}}$	$\underset{\sim}{\sigma}$
First PIOLA stress tensor	$\underset{\sim}{\mathrm{P}}$		$\underset{\sim}{\mathrm{F}}\,\underset{\sim}{\mathrm{S}}$	$J\,\underset{\sim}{\sigma}\,\underset{\sim}{\mathrm{F}}^{-\mathrm{T}}$
Second PIOLA stress tensor	$\underset{\sim}{\mathrm{S}}$	$\underset{\sim}{\mathrm{F}}^{-1}\,\underset{\sim}{\mathrm{P}}$		$J\,\underset{\sim}{\mathrm{F}}^{-1}\,\underset{\sim}{\sigma}\,\underset{\sim}{\mathrm{F}}^{-\mathrm{T}}$
CAUCHY stress tensor	$\underset{\sim}{\sigma}$	$J^{-1}\,\underset{\sim}{\mathrm{P}}\,\underset{\sim}{\mathrm{F}}^{\mathrm{T}} = J^{-1}\,\underset{\sim}{\mathrm{F}}\,\underset{\sim}{\mathrm{P}}^{\mathrm{T}}$	$J^{-1}\,\underset{\sim}{\mathrm{F}}\,\underset{\sim}{\mathrm{S}}\,\underset{\sim}{\mathrm{F}}^{\mathrm{T}}$	

- Displacement or DIRICHLET boundary conditions

$$\underset{\sim}{u} \;=\; \underset{\sim}{\bar{u}} \tag{2.31}$$

  are prescribed either on ∂v_u or ∂V_u.

- Traction or NEUMANN boundary conditions either refer to ∂v_t

$$\underset{\sim}{t} \;=\; \underset{\sim}{\bar{t}} \tag{2.32}$$

  or to ∂V_t

$$\underset{\sim}{T} \;=\; \underset{\sim}{\bar{T}}\,. \tag{2.33}$$

Assuming that constitutive relations will be specified later, the BVP is complete in its *strong form*. Unfortunately, an analytical solution is in general only possible for simple BVPs, and approximation methods like the Finite Element Method, which will be dealt with in chapter 3, are commonly applied. Here, the governing partial differential equations have to be fulfilled only in a *weak* sense. The necessary variational formulations leading to a *weak form* will be derived in the following. The derivation for the initial configuration starts from the balance of equilibrium (2.29). According to the method of weighted residuals we multiply (2.29) by a test function $\underset{\sim}{y}$, which vanishes on ∂V_u and integrate over the computational domain V, leading to

$$G(\underset{\sim}{\varphi}, \underset{\sim}{y}) \;=\; \int_V \left(\mathrm{Div}\,\underset{\sim}{\mathrm{P}} + \rho_0\,\underset{\sim}{f}\right) \cdot \underset{\sim}{y}\,\mathrm{d}V = 0\,. \tag{2.34}$$

Integration by parts, application of the divergence theorem, and incorporation of traction boundary conditions gives

$$G(\underset{\sim}{\varphi}, \underset{\sim}{y}) \;=\; \int_V \underset{\sim}{\mathrm{P}} \cdot \mathrm{Grad}\,\underset{\sim}{y}\,\mathrm{d}V - \int_V \rho_0\,\underset{\sim}{f} \cdot \underset{\sim}{y}\,\mathrm{d}V - \int_{\partial V_t} \underset{\sim}{T} \cdot \underset{\sim}{y}\,\mathrm{d}A = 0\,. \tag{2.35}$$

Interpreting $\mathrm{Grad}\,\underset{\sim}{y}$ as the directional derivative[2] of the deformation gradient which corresponds to the first variation $\delta\underset{\sim}{\mathrm{F}}$ of $\underset{\sim}{\mathrm{F}}$ highlights the work conjugacy of $\underset{\sim}{\mathrm{P}}$ and $\delta\underset{\sim}{\mathrm{F}}$.

[2]Refer to section 3.1 for more details.

To further modify (2.35) two transformations can be performed: *Firstly*, using $\underset{\sim}{\mathrm{P}} \cdot \operatorname{Grad} \underset{\sim}{y} = \underset{\sim}{\mathrm{S}} \cdot \delta \underset{\sim}{\mathrm{E}}$, where

$$\delta \underset{\sim}{\mathrm{E}} = \frac{1}{2}(\underset{\sim}{\mathrm{F}}^{\mathrm{T}} \operatorname{Grad} \underset{\sim}{y} + \operatorname{Grad}^{\mathrm{T}} \underset{\sim}{y}\, \underset{\sim}{\mathrm{F}}) \,, \tag{2.36}$$

equation (2.35) is rewritten as

$$G(\underset{\sim}{\varphi}, \underset{\sim}{y}) = \int_V \underset{\sim}{\mathrm{S}} \cdot \delta \underset{\sim}{\mathrm{E}} \,\mathrm{d}V - \int_V \rho_0 \underset{\sim}{f} \cdot \underset{\sim}{y} \,\mathrm{d}V - \int_{\partial V_t} \underset{\sim}{T} \cdot \underset{\sim}{y} \,\mathrm{d}A = 0 \,. \tag{2.37}$$

Secondly, transforming (2.35) with the help of equations (2.6), (2.9), (2.23), and Table 2.1 to the current configuration yields

$$g(\underset{\sim}{\varphi}, \underset{\sim}{y}) = \int_v \underset{\sim}{\sigma} \cdot \operatorname{grad} \underset{\sim}{y} \,\mathrm{d}v - \int_v \rho \underset{\sim}{f} \cdot \underset{\sim}{y} \,\mathrm{d}v - \int_{\partial v_t} \underset{\sim}{t} \cdot \underset{\sim}{y} \,\mathrm{d}a = 0 \,. \tag{2.38}$$

The symmetry of $\underset{\sim}{\sigma}$ enables us to replace $\operatorname{grad} \underset{\sim}{y}$ by the symmetric expression

$$\nabla^{\mathrm{S}} \underset{\sim}{y} = \frac{1}{2} \left(\operatorname{grad} \underset{\sim}{y} + \operatorname{grad}^{\mathrm{T}} \underset{\sim}{y} \right) \,. \tag{2.39}$$

Inserting (2.39) into (2.38) finally results in

$$g(\underset{\sim}{\varphi}, \underset{\sim}{y}) = \int_v \underset{\sim}{\sigma} \cdot \nabla^{\mathrm{S}} \underset{\sim}{y} \,\mathrm{d}v - \int_v \rho \underset{\sim}{f} \cdot \underset{\sim}{y} \,\mathrm{d}v - \int_{\partial v_t} \underset{\sim}{t} \cdot \underset{\sim}{y} \,\mathrm{d}a = 0 \,. \tag{2.40}$$

2.1.4 Constitutive models

In section 2.1.2 the equilibrium equations have been established in terms of stresses without any knowledge about the material under consideration. Knowing that the stresses result from the deformation of the material, which itself can be described by strains, it is convenient to establish relationships between stresses and strains. These relationships are known as constitutive equations and depend on the type of material.

2.1.4.1 Hyperelastic materials

Throughout this thesis only (hyper-)elastic materials are considered. For these materials the work done by stresses is only dependent on the initial state at time t_0 and the current state at time t of deformation. This behavior is termed *path independent*. An important consequence of the path-independency is that a strain energy (density) function Ψ per unit volume exists. Assuming that Ψ depends on the initial configuration the second Piola-Kirchhoff stress tensor can be derived as [8]

$$\underset{\sim}{\mathrm{S}} = 2 \frac{\partial \Psi}{\partial \underset{\sim}{\mathrm{C}}} = \frac{\partial \Psi}{\partial \underset{\sim}{\mathrm{E}}} \,. \tag{2.41}$$

A push forward of (2.41) yields the Cauchy stress tensor. In the reference configuration the relationship between the stress state and the strain state is given by the symmetric fourth-order *material* or Lagrangian elasticity tensor

$$\overset{4}{\underset{\sim}{\mathrm{C}}} = \frac{\partial \underset{\sim}{\mathrm{S}}}{\partial \underset{\sim}{\mathrm{E}}} = 2 \frac{\partial \underset{\sim}{\mathrm{S}}}{\partial \underset{\sim}{\mathrm{C}}} = 4 \frac{\partial^2 \Psi}{\partial \underset{\sim}{\mathrm{C}} \, \partial \underset{\sim}{\mathrm{C}}} = C_{IJKL} \, \underset{\sim}{E}_I \otimes \underset{\sim}{E}_J \otimes \underset{\sim}{E}_K \otimes \underset{\sim}{E}_L \,. \tag{2.42}$$

Performing a push forward the *spatial* or EULERIAN elasticity tensor emerges as

$$\overset{4}{\underset{\sim}{\mathrm{c}}} = J^{-1} F_{iI} F_{jJ} F_{kK} F_{lL} C_{IJKL} \, \underset{\sim}{e}_i \otimes \underset{\sim}{e}_j \otimes \underset{\sim}{e}_k \otimes \underset{\sim}{e}_l \,. \tag{2.43}$$

Now, let us present two different hyperelastic materials: We start with the isotropic ST. VENANT-KIRCHHOFF material. The strain energy density function is given by

$$\Psi = \frac{1}{2} \Lambda \, (\mathrm{tr}(\underset{\sim}{\mathrm{E}}))^2 + \mu \, \underset{\sim}{\mathrm{E}} \cdot \underset{\sim}{\mathrm{E}} \tag{2.44}$$

with $\mathrm{tr}(\cdot)$ denoting the trace operator and Λ and μ are the material or LAMÉ constants[3]. The application of equations (2.41) and (2.42) leads to

$$\underset{\sim}{\mathrm{S}} = \Lambda \, \mathrm{tr}(\underset{\sim}{\mathrm{E}}) \, \underset{\sim}{\mathrm{I}} + 2 \, \mu \, \underset{\sim}{\mathrm{E}} \tag{2.45}$$

$$\overset{4}{\underset{\sim}{\mathrm{C}}} = 2 \, \mu \, \overset{4}{\underset{\sim}{\mathrm{I}}} + \Lambda \, \underset{\sim}{\mathrm{I}} \otimes \underset{\sim}{\mathrm{I}} \,, \tag{2.46}$$

with $\overset{4}{\underset{\sim}{\mathrm{I}}}$ as the fourth-order unit tensor. The elasticity tensor in equation (2.46) is identical to the one of the classical HOOKEAN material law of linear elasticity. In order to transform equations (2.44) and (2.45) to the linear case $\underset{\sim}{\mathrm{E}}$ has to be replaced by $\underset{\sim}{\varepsilon}$. The ST. VENANT-KIRCHHOFF material law is applicable when dealing with large rotations, but for large strains it is not useful. To be more illustrative, imagine a rod with initial length $L = 1$ which is subjected to tension and compression. In Figure 2.3 the reaction force is plotted against l. Two observations can be made for the compressive regime: At $l = \sqrt{3}/3$ the reaction force

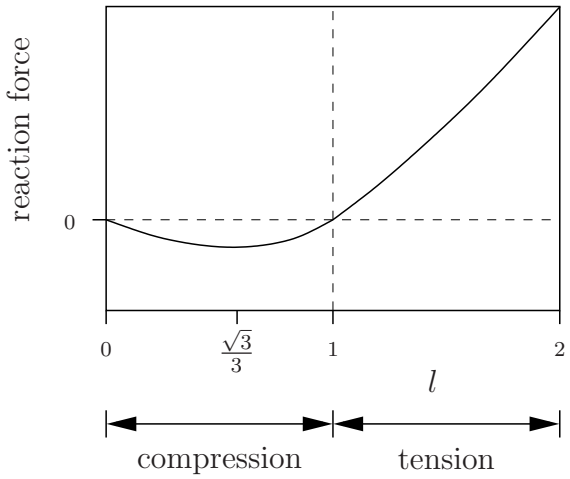

Figure 2.3: ST. VENANT-KIRCHHOFF's material law under large uniaxial strains

exhibits a minimum, i.e. there is a point of instability, and at $l = 0$ the reaction force vanishes which is, of course, unphysical. In order to circumvent these problems, an isotropic NEO-HOOKEAN material [8] is utilized within this thesis where the strain energy (density) function per unit volume is given by

$$\Psi = \frac{\mu}{2} \, (I_{\underset{\sim}{\mathrm{C}}} - 3) - \mu \ln(J) + \frac{\Lambda}{2} (\ln(J))^2 \tag{2.47}$$

[3]Note that these constants are related to YOUNG's modulus via $E = (3\,\Lambda + 2\,\mu)\mu/(\Lambda + \mu)$ and to POISSON's ratio via $\nu = \Lambda/(2\,(\Lambda + \mu))$.

with $I_{\underset{\sim}{C}} = \mathrm{tr}(\underset{\sim}{C})$. The corresponding second PIOLA-KIRCHHOFF stress tensor equals

$$\underset{\sim}{S} = \mu\,(\underset{\sim}{I} - \underset{\sim}{C}^{-1}) + \Lambda \ln(J)\,\underset{\sim}{C}^{-1}\,, \tag{2.48}$$

and the *material* elasticity tensor is

$$\overset{4}{\underset{\sim}{C}} = \Lambda\,\underset{\sim}{C}^{-1} \otimes \underset{\sim}{C}^{-1} + 2\,(\mu - \Lambda \ln(J))\,\overset{4}{\underset{\sim}{I}}^{C^{-1}}\,, \tag{2.49}$$

where

$$\overset{4}{\underset{\sim}{I}}^{C^{-1}} = I^{C^{-1}}_{IJKL}\,\underset{\sim}{E}_I \otimes \underset{\sim}{E}_J \otimes \underset{\sim}{E}_K \otimes \underset{\sim}{E}_L \quad \text{with} \quad I^{C^{-1}}_{IJKL} = (\underset{\sim}{C}^{-1})_{IK}\,(\underset{\sim}{C}^{-1})_{JL}\,. \tag{2.50}$$

The CAUCHY stress tensor emerges as

$$\underset{\sim}{\sigma} = \frac{\mu}{J}(\underset{\sim}{b} - \underset{\sim}{I}) + \frac{\Lambda}{J}\ln(J)\,\underset{\sim}{I}\,, \tag{2.51}$$

and the *spatial* elasticity tensor reads

$$\overset{4}{\underset{\sim}{C}} = \frac{\Lambda}{J}\,\underset{\sim}{I} \otimes \underset{\sim}{I} + \frac{2}{\Lambda}(\mu - \Lambda \ln(J))\,\overset{4}{\underset{\sim}{\iota}} \tag{2.52}$$

In equation (2.52) $\overset{4}{\underset{\sim}{\iota}}$ is the push forward of (2.50) with components

$$\iota_{ijkl} = F_{iI}\,F_{jJ}\,F_{kK}\,F_{lL}\,I^{C^{-1}}_{IJKL} = \delta_{ik}\,\delta_{jl}\,. \tag{2.53}$$

2.2 The micromorphic continuum theory

In this section a brief review of the micromorphic continuum theory is given. The contents are strongly influenced by [62] and the literature cited therein, where more details and further reading can be found. The section includes kinematics, deformation measures and balance equations. Finally some remarks concerning constitutive modeling are stated. Throughout this section, index M indicates macroscopic quantities, and m is used for microscopic quantities.

2.2.1 Kinematics and deformation measures

The deformable body B consists of a set of infinitesimal *material points*. In contrast to the classical continuum theory as described in section 2.1 these material points are deformable and capture a small but *finite space*. In order to resolve the contradiction between the infinitesimal character of a material point on the one hand and its finite dimension on the other hand we replace each deformable point by a geometrical point P and an attached triad of vectors $\Delta\underset{\sim}{X}$. These vectors represent the additional degrees of freedom stemming from the deformation of the material points. A micromorphic material point P can be described by the position vector $\underset{\sim}{X}_M$ of its volume centroid and the attached vector $\Delta\underset{\sim}{X}$, see the physical picture in Figure 2.4. In ERINGEN [30] the definition of micromorphic continuum of grade *one* is given as follows: *A material body B is called micromorphic continuum of grade* one*, if its motions are described by the mappings*

$$\underset{\sim}{x}_M = \hat{\underset{\sim}{\varphi}}_M(\underset{\sim}{X}_M, t) \qquad \textit{and} \qquad \Delta\,\underset{\sim}{x} = \Delta\,\hat{\underset{\sim}{\varphi}}(\underset{\sim}{X}_M, \Delta\underset{\sim}{X}, t)\,, \tag{2.54}$$

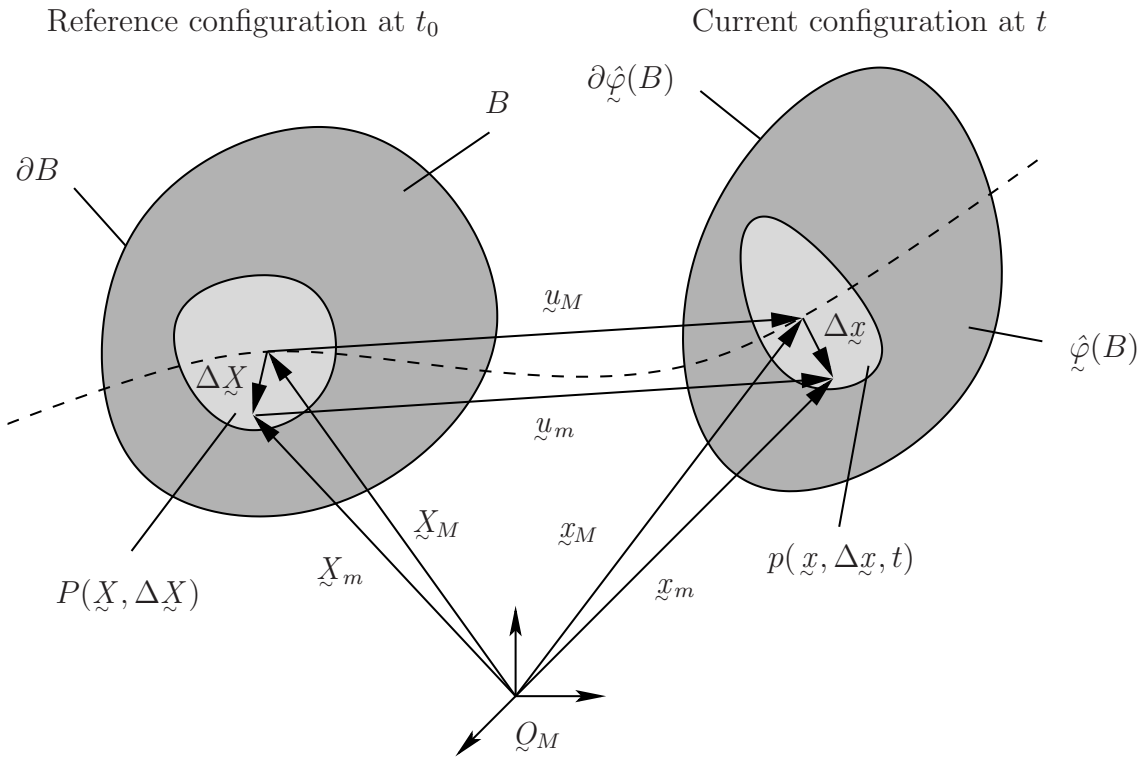

Figure 2.4: The physical picture of a micromorphic continuum

which possess continuous partial derivatives with respect to $\underset{\sim}{X}_M$ *and* t*, and if they are invertible uniquely*

$$\underset{\sim}{X}_M = \hat{\underset{\sim}{\varphi}}_M^{-1}(\underset{\sim}{x}_M, t) \qquad \textit{and} \qquad \Delta\underset{\sim}{X} = \Delta\,\hat{\underset{\sim}{\varphi}}^{-1}(\underset{\sim}{x}_M, \Delta\underset{\sim}{x}, t)\,. \tag{2.55}$$

The macroscopic deformation gradient is defined in the classical way (see equation (2.2)) as

$$\mathrm{d}\underset{\sim}{x}_M \;=\; \underset{\sim}{\mathrm{F}}_M\,\mathrm{d}\underset{\sim}{X}_M\,, \tag{2.56}$$

with

$$J_M \;=\; \det\underset{\sim}{\mathrm{F}}_M \tag{2.57}$$

denoting its determinant.

For the microdeformation within a micromorphic continuum of grade *one* we assume a linear mapping

$$\Delta\underset{\sim}{x} \;=\; \bar{\underset{\sim}{\chi}}_M\,\Delta\underset{\sim}{X}\,, \tag{2.58}$$

in which $\bar{\underset{\sim}{\chi}}_M$ denotes the *microdeformation* tensor. A polar decomposition of $\bar{\underset{\sim}{\chi}}_M$ reads

$$\bar{\underset{\sim}{\chi}}_M \;=\; \bar{\underset{\sim}{\mathrm{R}}}_M\,\bar{\underset{\sim}{\mathrm{U}}}_M\,, \tag{2.59}$$

where $\bar{\underset{\sim}{\mathrm{R}}}_M$ is called rotation tensor and $\bar{\underset{\sim}{\mathrm{U}}}_M$ denotes the stretch tensor. These tensors possess the following properties

$$\bar{\underset{\sim}{\mathrm{R}}}_M^{\mathrm{T}} = \bar{\underset{\sim}{\mathrm{R}}}_M^{(-1)}\,, \quad \det\bar{\underset{\sim}{\mathrm{R}}}_M = 1\,, \qquad \bar{\underset{\sim}{\mathrm{U}}}_M = \bar{\underset{\sim}{\mathrm{U}}}_M^{\mathrm{T}}\,. \tag{2.60}$$

Now, focusing on $\bar{\underset{\sim}{\chi}}_M$ we can distinguish different subcontinua:

- If $\bar{\underset{\sim}{U}}_M = \underset{\sim}{I}$ and $\bar{\underset{\sim}{\chi}}_M = \bar{\underset{\sim}{R}}_M$ only rigid body rotations of the material points can be represented. This subcontinuum is called *micropolar* or COSSERAT continuum, [15].
- Setting $\bar{\underset{\sim}{R}}_M = \underset{\sim}{I}$ and $\bar{\underset{\sim}{\chi}}_M = \bar{j}_M \underset{\sim}{I}$, where $\bar{j}_M$ is called microdilantancy, we obtain the *microdilatant* continuum.
- Allowing for symmetric microdeformations, i.e. $\bar{\underset{\sim}{R}}_M = \underset{\sim}{I}$ and $\bar{\underset{\sim}{\chi}}_M = \bar{\underset{\sim}{\chi}}^{\mathrm{T}}_M$, leads to the microstrain continuum.
- A combination of the *microdilatant* and *micropolar* continuum is called *microstretch* continuum where $\bar{\underset{\sim}{\chi}}_M = \bar{j}_M \bar{\underset{\sim}{R}}_M$.

A general review of different subcontinua has been given by FOREST [39].

The calculation of the square of the deformed arc length

$$(\mathrm{d}(\underset{\sim}{x}_m + \Delta\underset{\sim}{x}))^2 = \left(\underset{\sim}{F}_M \,\mathrm{d}\underset{\sim}{X}_M + \bar{\underset{\sim}{\chi}}_M \,\mathrm{d}\Delta\underset{\sim}{X} + \left(\overset{23}{\mathrm{Grad}^{\mathrm{T}}}\, \bar{\underset{\sim}{\chi}}_M \,\Delta\underset{\sim}{X}\right) \Delta\underset{\sim}{X}\right)^2 \tag{2.61}$$

motivates the introduction of a set of three independent deformation measures $\underset{\sim}{F}_M$, $\bar{\underset{\sim}{\chi}}_M$, and $\mathrm{Grad}\,\bar{\underset{\sim}{\chi}}_M$ which are two-point tensors and not objective in general. A form-invariant set of deformation measures is given by the *microdeformation* tensor

$$\bar{\underset{\sim}{F}}_M = \bar{\underset{\sim}{\chi}}^{(-1)}_M \underset{\sim}{F}_M \,, \tag{2.62}$$

the right CAUCHY-GREEN microdeformation tensor

$$\bar{\underset{\sim}{C}}_M = \bar{\underset{\sim}{\chi}}^{\mathrm{T}}_M \bar{\underset{\sim}{\chi}}_M \,, \tag{2.63}$$

and the *curvature* tensor

$$\overset{3}{\bar{\underset{\sim}{\Gamma}}}_M = \bar{\underset{\sim}{\chi}}^{(-1)}_M \,\mathrm{Grad}\, \bar{\underset{\sim}{\chi}}_M \,. \tag{2.64}$$

Note that (2.62) to (2.64) refer to the reference configuration.

2.2.2 Balance equations

In the current configuration the *balance of equilibrium* reads

$$\mathrm{div}\, \underset{\sim}{\sigma}_M + \rho \underset{\sim}{f}_M = \underset{\sim}{0} \tag{2.65}$$

compare with equation (2.24), and the *balance of equilibrium of momentum* is

$$\mathrm{div}\, \overset{3}{\underset{\sim}{q}}_M + \underset{\sim}{\sigma}_M - \underset{\sim}{h}_M + \rho \underset{\sim}{c}_M = \underset{\sim}{0} \tag{2.66}$$

with $\rho \underset{\sim}{c}_M$ as the volumic double forces which can be interpreted, for example, as an intrinsic angular momentum. In (2.66) *spatial* higher-order stress tensors appear, namely the *couple* stress tensor $\overset{3}{\underset{\sim}{q}}_M$ and the *hyper* stress tensor $\underset{\sim}{h}_M = \underset{\sim}{h}^{\mathrm{T}}_M$, which allow for $\underset{\sim}{\sigma}_M \neq \underset{\sim}{\sigma}^{\mathrm{T}}_M$ in general.

The transformation of (2.65) and (2.66) to the reference configuration yields

$$\operatorname{Div} \underset{\sim}{\mathrm{P}}_M + \rho_0 \underset{\sim}{f}_M \;=\; \underset{\sim}{0} \tag{2.67}$$

and

$$\operatorname{Div} \overset{3}{\underset{\sim}{\mathrm{Q}}}_M + (\underset{\sim}{\mathrm{P}}_M - \underset{\sim}{\mathrm{H}}_M)\underset{\sim}{\mathrm{F}}_M^{\mathrm{T}} + \rho_0 \underset{\sim}{\mathrm{c}}_M \;=\; \underset{\sim}{0}\,. \tag{2.68}$$

Here, the first PIOLA-KIRCHHOFF stress tensor

$$\underset{\sim}{\mathrm{P}}_M \;=\; J_M \underset{\sim}{\sigma}_M \underset{\sim}{\mathrm{F}}_M^{-\mathrm{T}} \tag{2.69}$$

the *material* version of the *hyper* stress tensor

$$\underset{\sim}{\mathrm{H}}_M \;=\; J_M \underset{\sim}{\mathrm{h}}_M \underset{\sim}{\mathrm{F}}_M^{-\mathrm{T}}\,, \tag{2.70}$$

and the *material* version of the *couple* stress tensor

$$\overset{3}{\underset{\sim}{\mathrm{Q}}}_M \;=\; J_M \overset{3}{\underset{\sim}{\mathrm{q}}}_M \underset{\sim}{\mathrm{F}}_M^{-\mathrm{T}} \tag{2.71}$$

have been introduced. Note that in analogy to $\underset{\sim}{\mathrm{P}}_M$, $\underset{\sim}{\mathrm{H}}_M$ and $\overset{3}{\underset{\sim}{\mathrm{Q}}}_M$ are two-point tensors.

2.2.3 Constitutive models

Constitutive models for extended continua can be found e.g. in [17, 18, 36, 37, 74]. As mentioned above, additional material parameters are required which are difficult to obtain from experiments [70]. Thus, (numerical) multiscale methods, which circumvent such difficulties, are justified.

Chapter 3

Spatial discretization

In this chapter we discretize the classical (nonlinear) continua as described in section 2.1. Note, however, that these concepts can be applied to extended continua as well, compare with [62, 78]. The discretization is based on the p-version of FEM on the one hand and its specialization the FCM on the other hand. The general derivation of the FEM is strongly guided by [8, 105], the p-version's part refers to [21, 90, 91], and the FCM is described in [24, 80]. The outline of this chapter is as follows: Starting from the linearization of the variational formulation the FEM including shape functions and iterative solution methods is presented, whereby special focus lies on an efficient formulation suited for the p-version. Afterwards, the FCM is briefly re-called.

3.1 Linearization of the variational formulation

Nonlinear problems in continuum mechanics are treated by linearization of the nonlinear set of equations and iteratively solving a series of linear systems of equations. In the context of the FEM the Newton-Raphson method which is based on a consistent linearization of the variational problem is very popular. In this section the linearized weak forms of section 2.1.3 are derived. It is convenient to perform the linearization of the weak form in the reference configuration and push it forward to the current configuration. The reason for this approach is that the reference volume element $\mathrm{d}V$ is constant during linearization. The linearized representation of the weak form is given by

$$\mathrm{L}\left[G\right]\Big|_{\underset{\sim}{\varphi}=\bar{\underset{\sim}{\varphi}}} = \underbrace{G(\bar{\underset{\sim}{\varphi}}, \underset{\sim}{v})}_{(2.37)_{\underset{\sim}{\varphi}=\bar{\underset{\sim}{\varphi}}}} + \mathrm{D}\, G(\bar{\underset{\sim}{\varphi}}, \underset{\sim}{v})\left[\Delta \underset{\sim}{u}\right] = 0\,, \tag{3.1}$$

where $\bar{\underset{\sim}{\varphi}}$ is a known state of deformation[1]. In (3.1) $G(\bar{\underset{\sim}{\varphi}}, \underset{\sim}{v})$ is the weak form evaluated at $\bar{\underset{\sim}{\varphi}}$. If we assume that both body forces and external forces are independent of the state of deformation, only the first part of (2.37) has to be considered for the directional derivative in

[1] Since we restrict ourselves to hyperelasticity in this thesis only the state of deformation is relevant.

the direction of $[\Delta \underset{\sim}{u}]$. Applying the product rule we obtain

$$\begin{aligned} \mathrm{D}\, G(\underset{\sim}{\bar{\varphi}}, \underset{\sim}{y})\,[\Delta \underset{\sim}{u}] &= \mathrm{D} \left(\int_V \underset{\sim}{S} \cdot \delta \underset{\sim}{E}\, \mathrm{d}V \right) [\Delta \underset{\sim}{u}] \\ &= \int_V (\mathrm{D}\, \underset{\sim}{S}\,[\Delta \underset{\sim}{u}] \cdot \delta \underset{\sim}{E} + \underset{\sim}{S} \cdot \mathrm{D}\, \delta \underset{\sim}{E}\,[\Delta \underset{\sim}{u}])\, \mathrm{d}V\,. \end{aligned} \tag{3.2}$$

The directional derivative of $\delta \underset{\sim}{E}$ as stated in equation (2.36) reads

$$\mathrm{D}\, \delta \underset{\sim}{E}\,[\Delta \underset{\sim}{u}] = \frac{1}{2} \left(\mathrm{Grad}^{\mathrm{T}}\, \Delta \underset{\sim}{u}\, \mathrm{Grad}\, \underset{\sim}{y} + \mathrm{Grad}^{\mathrm{T}}\, \underset{\sim}{y}\, \mathrm{Grad}\, \Delta \underset{\sim}{u} \right) \tag{3.3}$$

where

$$\mathrm{D}\, \underset{\sim}{F}\,[\Delta \underset{\sim}{u}] = \frac{\mathrm{d}}{\mathrm{d}\epsilon} (\underset{\sim}{I} + \mathrm{Grad}\,(\underset{\sim}{u} + \epsilon\, \Delta \underset{\sim}{u})) \Big|_{\epsilon=0} = \mathrm{Grad}\, \Delta \underset{\sim}{u} \tag{3.4}$$

was used. The directional derivative of the second Piola-Kirchhoff stress tensor is

$$\mathrm{D}\, \underset{\sim}{S}\,[\Delta \underset{\sim}{u}] = \overset{4}{\underset{\sim}{C}}\, \Delta \underset{\sim}{E} \tag{3.5}$$

with

$$\Delta \underset{\sim}{E} = \mathrm{D}\, \underset{\sim}{E}\,[\Delta \underset{\sim}{u}] = \frac{1}{2} (\underset{\sim}{F}^{\mathrm{T}}\, \mathrm{Grad}\, \Delta \underset{\sim}{u} + \mathrm{Grad}^{\mathrm{T}}\, \Delta \underset{\sim}{u}\, \underset{\sim}{F})\,, \tag{3.6}$$

and, assuming hyperelasticity, $\overset{4}{\underset{\sim}{C}}$ is defined by equation (2.42). Inserting (3.3) and (3.6) into (3.2) we finally arrive at

$$\mathrm{D}\, G(\underset{\sim}{\bar{\varphi}}, \underset{\sim}{y})\,[\Delta \underset{\sim}{u}] = \int_V \left(\mathrm{Grad}\, \Delta \underset{\sim}{u}\, \underset{\sim}{S} \cdot \mathrm{Grad}\, \underset{\sim}{y} + \delta \underset{\sim}{E} \cdot \overset{4}{\underset{\sim}{C}}\, \Delta \underset{\sim}{E} \right) \mathrm{d}V\,, \tag{3.7}$$

where the symmetry of $\underset{\sim}{S}$ was exploited. A push forward of (3.7) gives the directional derivative of the weak form with respect to the current configuration

$$\mathrm{D}\, g(\underset{\sim}{\bar{\varphi}}, \underset{\sim}{y})\ [\Delta \underset{\sim}{u}] = \int_v \left(\mathrm{grad}\, \Delta \underset{\sim}{u}\, \underset{\sim}{\sigma} \cdot \mathrm{grad}\, \underset{\sim}{y} + \nabla_x^{\mathrm{S}}\, \underset{\sim}{y} \cdot \overset{4}{\underset{\sim}{c}}\, \nabla_x^{\mathrm{S}}\, \Delta \underset{\sim}{u} \right) \mathrm{d}v\,. \tag{3.8}$$

The elasticity tensor $\overset{4}{\underset{\sim}{c}}$ can be computed by means of (2.43). With (2.40) evaluated at $\underset{\sim}{\bar{\varphi}}$ and (3.8) we obtain the linearized weak form of the current configuration

$$\mathrm{L}\,[g] \Big|_{\underset{\sim}{\varphi}=\underset{\sim}{\bar{\varphi}}} = \underbrace{g(\underset{\sim}{\bar{\varphi}}, \underset{\sim}{y})}_{(2.40)_{\underset{\sim}{\varphi}=\underset{\sim}{\bar{\varphi}}}} + \mathrm{D}\, g(\underset{\sim}{\bar{\varphi}}, \underset{\sim}{y})\,[\Delta \underset{\sim}{u}] = 0\,. \tag{3.9}$$

3.2 The Finite Element Method

In this section we closely follow WRIGGERS [105] and BONET and WOOD [8] when discretizing the weak forms and their linearizations by the FEM. The goal is to arrive at a series of systems of linear equations which can be solved iteratively by the NEWTON-RAPHSON method. As stated in section 2.1.1.1 there are basically two approaches: The *spatial* one related to the current configuration, and the *material* one related to the reference configuration, which lead, of course, to the same results. It is well-known that a *spatial* formulation is more efficient than a *material* formulation [7, 8, 48, 105]. Especially in the context of numerical homogenization involving large deformations a *spatial* formulation would help to lower the high computational effort on the microscale. Referring to section 1.3 we apply the *p*-version of the FEM to the microscopic scale which is known to be very efficient. The *p*-version utilizes larger elements than the classical *h*-version and commonly applies a mapping concept with mapping functions defined in the reference configuration, see section 3.4.5. Thus, we developed and implemented a *quasi-spatial* formulation where the undeformed geometry is discretized but differentiation and integration operations are performed with respect to the *spatial* configuration. In the following the weak forms in both configurations will be discretized in order to illustrate the differences between the above mentioned formulations whereby a special focus lies on the *spatial* formulation in order to highlight its importance. Note that a BUBNOV-GALERKIN approach is used, where for both the field variables $\underset{\sim}{u}$ and the test functions $\underset{\sim}{v}$ the same Ansatz is made.

3.2.1 Basic concepts

Let us recall the main idea of the FEM: The original domain V with boundary ∂V is approximated by Ω and $\partial\Omega$. The approximation, called discretization, is provided by subdividing Ω into n_e finite elements Ω_e

$$V \approx \Omega = \bigcup_{e=1}^{n_e} \Omega_e \tag{3.10}$$

where $\bigcup$ denotes the assembly operator. The primary field variables are approximated within one element by

$$\boldsymbol{u}_{\mathrm{EX}} \approx \boldsymbol{u}_{\mathrm{FE}} = \boldsymbol{N}\,\boldsymbol{u}\,, \tag{3.11}$$

where $\boldsymbol{N}$ is the matrix of shape functions. To be more specific, we define

$$\begin{aligned}
\boldsymbol{u}_{\mathrm{FE}}^{\mathrm{T}} &= \begin{bmatrix} u_x & u_y & u_z \end{bmatrix}, \\
\boldsymbol{N} &= \begin{bmatrix} N_1(\boldsymbol{\xi}) & 0 & 0 & N_2(\boldsymbol{\xi}) & 0 & \dots & 0 \\ 0 & N_1(\boldsymbol{\xi}) & 0 & 0 & N_2(\boldsymbol{\xi}) & \dots & 0 \\ 0 & 0 & N_1(\boldsymbol{\xi}) & 0 & 0 & \dots & N_n(\boldsymbol{\xi}) \end{bmatrix}, \\
\boldsymbol{u}^{\mathrm{T}} &= \begin{bmatrix} u_{x_1} & u_{y_1} & u_{z_1} & u_{x_2} & u_{y_2} & u_{z_2} & \cdots & u_{x_n} & u_{y_n} & u_{z_n} \end{bmatrix},
\end{aligned} \tag{3.12}$$

where $N_i(\boldsymbol{\xi})$ are the n shape functions[2] defined in the element's local $\boldsymbol{\xi}$-coordinate system, compare with the simplified two-dimensional representation of Figure 3.1. The column vector $\boldsymbol{u}$ contains the coefficients related to the shape functions of the finite element approximation. The linearized weak forms contain derivatives with respect to global coordinates. Since the

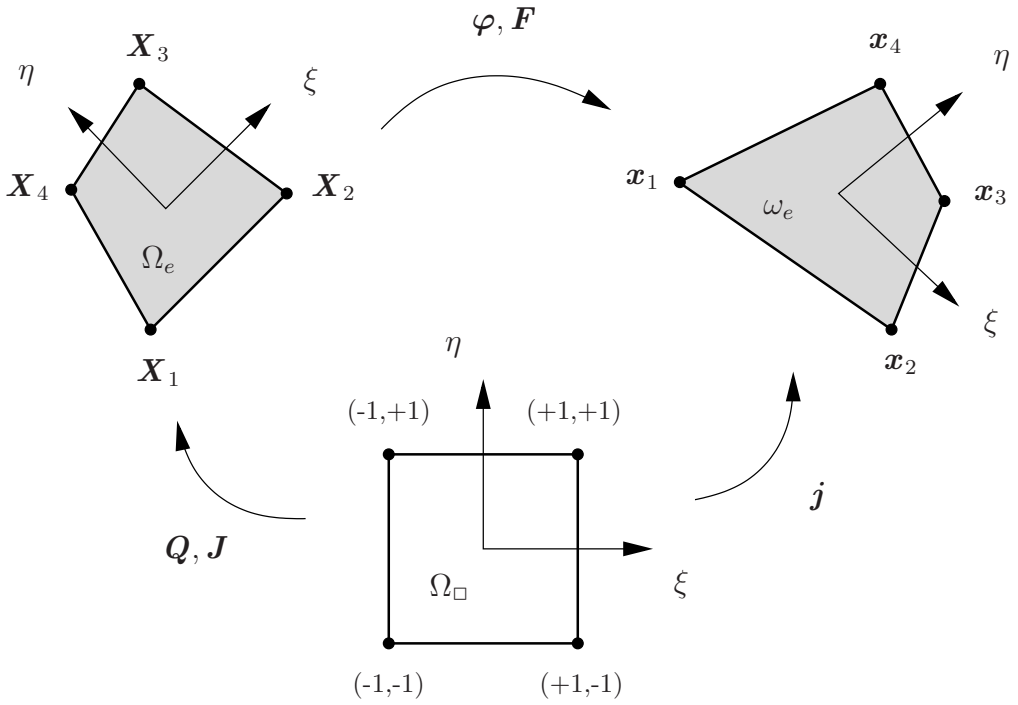

Figure 3.1: Mapping of the deformation of a finite element Ω_e [105]

shape functions are defined in the element's local coordinate system the following transformations stemming from the chain rule are performed

$$\nabla_X N_J = \boldsymbol{J}^{-1} \nabla_\xi N_J \,, \tag{3.13}$$

$$\nabla_x N_j = \boldsymbol{j}^{-1} \nabla_\xi N_j \,, \tag{3.14}$$

where

$$\boldsymbol{J} = \begin{bmatrix} X_{1,\xi} & X_{2,\xi} & X_{3,\xi} \\ X_{1,\eta} & X_{2,\eta} & X_{3,\eta} \\ X_{1,\zeta} & X_{2,\zeta} & X_{3,\zeta} \end{bmatrix}, \quad \boldsymbol{j} = \begin{bmatrix} x_{1,\xi} & x_{2,\xi} & x_{3,\xi} \\ x_{1,\eta} & x_{2,\eta} & x_{3,\eta} \\ x_{1,\zeta} & x_{2,\zeta} & x_{3,\zeta} \end{bmatrix} \tag{3.15}$$

are called JACOBIAN matrices. Here, a bijective mapping based on local element coordinates $\boldsymbol{\xi}$ is used

$$\boldsymbol{X} = \boldsymbol{Q}(\boldsymbol{\xi}) \quad \Longleftrightarrow \quad \boldsymbol{\xi} = \boldsymbol{Q}^{-1}(\boldsymbol{X}) \,, \tag{3.16}$$

where the mapping function $\boldsymbol{Q}$ can be quite general, refer to section 3.4.5 for more details on mapping functions. The global coordinates $\boldsymbol{x}$ (in the current configuration) and hence $\boldsymbol{j}$

[2] More details on these functions will be presented in section 3.4.

needed for the *spatial* derivatives are not known initially. However, this is not a problem for a *quasi-spatial* formulation: Referring to Figure 3.1 and again following the chain rule we can deduce that

$$\boldsymbol{j} = \boldsymbol{J}\,\boldsymbol{F}^{\mathrm{T}}\,, \tag{3.17}$$

where the deformation gradient $\boldsymbol{F}$ can be determined directly via equation (2.8), here in matrix notation and discrete quantities

$$\boldsymbol{F} \;=\; \boldsymbol{I} + \mathrm{Grad}\,\boldsymbol{u} = \boldsymbol{I} + \sum_{J=1}^{n} \boldsymbol{u}_J \otimes \nabla_X N_J\,. \tag{3.18}$$

Note that in a pure *spatial* formulation the situation is vice versa. Here, $\boldsymbol{j}$ is available, but for $\boldsymbol{F}$ more computational effort is required, since the derivatives with respect to reference configuration as given in (3.13) cannot be computed directly. In order to resolve this circumstance, one would have to evaluate equation (2.10) and then invert the resulting quantity. Hence, the term *quasi* will be skipped.

3.2.2 Integration

The weak forms involve integration over the computational domain. Since in the Finite Element Method the domain is subdivided into a number of elements, the integration is to be carried out within each element individually. It is common to perform the integration within the standard element's domain $\Omega_\square$

$$\begin{aligned}
\int_{\Omega_e} (\cdot)\mathrm{d}\Omega_e \;&=\; \int_{\Omega_\square} (\cdot)\det\boldsymbol{J}\,\mathrm{d}\Omega_\square = \int_{\boldsymbol{\xi}} (\cdot)\det\boldsymbol{J}\,\mathrm{d}\boldsymbol{\xi}\,, \\
\int_{\omega_e} (\cdot)\mathrm{d}\omega_e \;&=\; \int_{\Omega_\square} (\cdot)\det\boldsymbol{j}\,\mathrm{d}\Omega_\square = \int_{\boldsymbol{\xi}} (\cdot)\det\boldsymbol{j}\,\mathrm{d}\boldsymbol{\xi}\,.
\end{aligned} \tag{3.19}$$

Since in general the integration cannot be performed analytically a Gaussian quadrature is applied, which reads in a one-dimensional setting as follows

$$\int_{-1}^{1} (\cdot)\,\mathrm{d}\xi \;\approx\; \sum_{i}^{n} (\cdot)|_{\xi_i}\, w_{\xi_i}\,. \tag{3.20}$$

In (3.20) ξ_i denote the quadrature points at which the integrand $(\cdot)$ has to be evaluated and w_{ξ_i} are the corresponding weights [90]. Applying n quadrature points allows to integrate a polynomial of degree $p = 2n - 1$ exactly. However, one has to bear in mind that, due to the mapping, the integrand is usually not a polynomial. Therefore, the quadrature is not exact, even if the number of integration points will be increased. The one-dimensional quadrature can be extended in a straightforward manner to two-dimensional integrals

$$\int_{-1}^{1}\int_{-1}^{1} (\cdot)\det\mathfrak{J}\,\mathrm{d}\xi\,\mathrm{d}\eta \;\approx\; \sum_{j}^{n_j}\sum_{i}^{n_i} (\cdot)|_{(\xi_i,\eta_j)}\det\mathfrak{J}|_{(\xi_i,\eta_j)}\; w_{\xi_i}\; w_{\eta_j}\,, \tag{3.21}$$

and to three-dimensional integrals

$$\int_{-1}^{1}\int_{-1}^{1}\int_{-1}^{1}(\cdot)\det\mathfrak{J}\,\mathrm{d}\xi\,\mathrm{d}\eta\,\mathrm{d}\zeta \;\approx\; \sum_{k}^{n_k}\sum_{j}^{n_j}\sum_{i}^{n_i}(\cdot)|_{(\xi_i,\eta_j,\zeta_k)}\det\mathfrak{J}|_{(\xi_i,\eta_j,\zeta_k)}\;w_{\xi_i}\;w_{\eta_j}\;w_{\zeta_k}\,, \tag{3.22}$$

where $\mathfrak{J}$ represents either $\boldsymbol{J}$ or $\boldsymbol{j}$.

3.2.3 Discretization of the weak forms

Now, let us discretize the weak form in the current configuration, see (2.40). In view of a computer implementation it is common to apply the VOIGT notation. With

$$\begin{aligned}\underset{\sim}{\sigma} \;&\Longleftrightarrow\; \boldsymbol{\sigma}^{\mathrm{T}} = \left[\begin{array}{cccccc}\sigma_{xx} & \sigma_{yy} & \sigma_{zz} & \sigma_{xy} & \sigma_{yz} & \sigma_{xz}\end{array}\right], \\ \nabla^{\mathrm{S}}_x \underset{\sim}{v} \;&\Longleftrightarrow\; (\nabla^{\mathrm{S}}_x \boldsymbol{v})^{\mathrm{T}} = \left[\begin{array}{cccccc} v_{x,x} & v_{y,y} & v_{z,z} & (v_{x,y}+v_{y,x}) & (v_{y,z}+v_{z,y}) & (v_{x,z}+v_{z,x})\end{array}\right]\end{aligned} \tag{3.23}$$

we rewrite the first term of (2.40)

$$\begin{aligned}\int_v \underset{\sim}{\sigma}\cdot\nabla^{\mathrm{S}}_x \underset{\sim}{v}\,\mathrm{d}v \;&=\; \bigcup_{e=1}^{n_e}\int_{\omega_e}(\nabla^{\mathrm{S}}_x\boldsymbol{v})^{\mathrm{T}}\,\boldsymbol{\sigma}\,\mathrm{d}\omega_e \\ &=\; \bigcup_{e=1}^{n_e}\sum_{i=1}^{n}\boldsymbol{v}_i^{\mathrm{T}}\int_{\omega_e}\boldsymbol{b}_i^{\mathrm{T}}\,\boldsymbol{\sigma}\,\mathrm{d}\omega_e \\ &=\; \bigcup_{e=1}^{n_e}\sum_{i=1}^{n}\boldsymbol{v}_i^{\mathrm{T}}\int_{\Omega_\square}\boldsymbol{b}_i^{\mathrm{T}}\,\boldsymbol{\sigma}\,\det\boldsymbol{j}\,\mathrm{d}\Omega_\square = \bigcup_{e=1}^{n_e}\sum_{i=1}^{n}\boldsymbol{v}_i^{\mathrm{T}}\boldsymbol{r}_i(\boldsymbol{u}) = \mathbf{v}^{\mathrm{T}}\mathbf{r}(\mathbf{u})\,,\end{aligned} \tag{3.24}$$

where

$$\boldsymbol{b}_j^{\mathrm{T}} \;=\; \left[\begin{array}{cccccc} N_{j,x} & 0 & 0 & N_{j,y} & 0 & N_{j,z} \\ 0 & N_{j,y} & 0 & N_{j,x} & N_{j,z} & 0 \\ 0 & 0 & N_{j,z} & 0 & N_{j,y} & N_{j,x}\end{array}\right] \tag{3.25}$$

is the *spatial* strain-displacement matrix which exhibits a sparse structure as in the linear case, and $\boldsymbol{r}_i$ is the element's vector of internal forces[3]. The counterpart to (3.24) can be derived in an analogous way leading to

$$\int_V \underset{\sim}{\mathrm{S}}\cdot\delta\underset{\sim}{\mathrm{E}}\,\mathrm{d}V \;=\; \bigcup_{e=1}^{n_e}\sum_{I=1}^{n}\boldsymbol{v}_I^{\mathrm{T}}\int_{\Omega_\square}\boldsymbol{B}_I^{\mathrm{T}}\,\boldsymbol{S}\,\det\boldsymbol{J}\,\mathrm{d}\Omega_\square = \bigcup_{e=1}^{n_e}\sum_{I=1}^{n}\boldsymbol{v}_I^{\mathrm{T}}\boldsymbol{R}_I(\boldsymbol{u}) = \mathbf{v}^{\mathrm{T}}\mathbf{R}(\mathbf{u})\,. \tag{3.26}$$

[3]In the context of numerical homogenization this vector is useful for computing nodal (reaction) forces at boundaries with DIRICHLET boundary conditions, refer to [50].

Note that the strain-displacement matrix with respect to the reference configuration is fully populated

$$\boldsymbol{B}_J = \begin{bmatrix} F_{11}\,N_{J,X} & F_{21}\,N_{J,X} & F_{31}\,N_{J,X} \\ F_{12}\,N_{J,Y} & F_{22}\,N_{J,Y} & F_{32}\,N_{J,Y} \\ F_{13}\,N_{J,Z} & F_{23}\,N_{J,Z} & F_{33}\,N_{J,Z} \\ F_{11}\,N_{J,Y} + F_{12}\,N_{J,X} & F_{21}\,N_{J,Y} + F_{22}\,N_{J,X} & F_{31}\,N_{J,Y} + F_{32}\,N_{J,X} \\ F_{12}\,N_{J,Z} + F_{13}\,N_{J,Y} & F_{22}\,N_{J,Z} + F_{23}\,N_{J,Y} & F_{32}\,N_{J,Z} + F_{33}\,N_{J,Y} \\ F_{13}\,N_{J,X} + F_{11}\,N_{J,Z} & F_{23}\,N_{J,X} + F_{21}\,N_{J,Z} & F_{33}\,N_{J,X} + F_{31}\,N_{J,Z} \end{bmatrix} . \tag{3.27}$$

For the remaining terms in (2.40) and (2.37) we obtain

$$\begin{aligned} \int_v \rho \underset{\sim}{f} \cdot \underset{\sim}{v}\,\mathrm{d}v + \int_{\partial v_t} \underset{\sim}{t} \cdot \underset{\sim}{v}\,\mathrm{d}a &= \bigcup_{e=1}^{n_e} \sum_{i=1}^{n} \boldsymbol{v}_i^{\mathrm{T}} \int_{\omega_e} \rho \boldsymbol{f}\, N_i\,\mathrm{d}\omega_e \\ &+ \bigcup_{r=1}^{n_r} \sum_{i=1}^{n} \boldsymbol{v}_i^{\mathrm{T}} \int_{\partial\omega_{t_e}} N_i\,\boldsymbol{t}\,\mathrm{d}\partial\omega_{t_e} \\ &= \bigcup_{e=1}^{n_e} \sum_{i=1}^{n} \boldsymbol{v}_i^{\mathrm{T}}\,\boldsymbol{p}_i + \bigcup_{r=1}^{n_r} \sum_{i=1}^{n} \boldsymbol{v}_i^{\mathrm{T}}\,\boldsymbol{p}_i^t = \mathbf{v}^{\mathrm{T}}\mathbf{p}\,, \end{aligned} \tag{3.28}$$

respectively

$$\begin{aligned} \int_V \rho_0 \underset{\sim}{f} \cdot \underset{\sim}{v}\,\mathrm{d}V + \int_{\partial V_t} \underset{\sim}{T} \cdot \underset{\sim}{v}\,\mathrm{d}A &= \bigcup_{e=1}^{n_e} \sum_{I=1}^{n} \boldsymbol{v}_I^{\mathrm{T}} \int_{\Omega_e} \rho_0 \boldsymbol{f}\, N_I\,\mathrm{d}\Omega_e \\ &+ \bigcup_{r=1}^{n_r} \sum_{I=1}^{n} \boldsymbol{v}_I^{\mathrm{T}} \int_{\partial\Omega_{t_e}} N_I\,\boldsymbol{T}\,\mathrm{d}\partial\Omega_{t_e} \\ &= \bigcup_{e=1}^{n_e} \sum_{I=1}^{n} \boldsymbol{v}_I^{\mathrm{T}}\,\boldsymbol{P}_I + \bigcup_{r=1}^{n_r} \sum_{I=1}^{n} \boldsymbol{v}_I^{\mathrm{T}}\,\boldsymbol{P}_I^t = \mathbf{v}^{\mathrm{T}}\mathbf{P}\,, \end{aligned} \tag{3.29}$$

where n_r is number of element edges / faces corresponding to the NEUMANN boundary.

With (3.24) and (3.28) (and (3.26) and (3.29), respectively) the discrete versions of the weak forms are

$$\mathbf{v}^{\mathrm{T}}\,(\mathbf{r}(\mathbf{u}) - \mathbf{p}) = 0\,, \tag{3.30}$$

$$\mathbf{v}^{\mathrm{T}}\,(\mathbf{R}(\mathbf{u}) - \mathbf{P}) = 0\,. \tag{3.31}$$

Due to the arbitrariness of the test function $\mathbf{v}$ we arrive at systems of nonlinear equations

$$\mathbf{g}(\mathbf{u}) = \mathbf{r}(\mathbf{u}) - \mathbf{p} = \mathbf{0}\,, \tag{3.32}$$

$$\mathbf{G}(\mathbf{u}) = \mathbf{R}(\mathbf{u}) - \mathbf{P} = \mathbf{0}\,. \tag{3.33}$$

3.2.4 Discretization of the linearized weak forms

In this section the linearized weak forms (3.9) and (3.1) respectively will be discretized. Herein, only the directional derivatives $\mathrm{D}\, g(\underset{\sim}{\bar{\varphi}}, \underset{\sim}{y})\ [\Delta \underset{\sim}{y}]$ and $\mathrm{D}\, G(\underset{\sim}{\bar{\varphi}}, \underset{\sim}{y})\ [\Delta \underset{\sim}{y}]$ respectively need to be considered, since $G(\underset{\sim}{\bar{\varphi}}, \underset{\sim}{y})$ and $g(\underset{\sim}{\bar{\varphi}}, \underset{\sim}{y})$ respectively have already been treated above. With the discretization of the spatial gradients

$$\begin{aligned} \operatorname{grad} \Delta \boldsymbol{u} &= \sum_{k=1}^{n} \Delta \boldsymbol{u}_k \otimes \nabla_x N_k \,, \\ \operatorname{grad} \boldsymbol{v} &= \sum_{i=1}^{n} \boldsymbol{v}_i \otimes \nabla_x N_i \,, \end{aligned} \tag{3.34}$$

the first term of (3.8) becomes

$$\int_v \operatorname{grad} \Delta \underset{\sim}{y}\, \underset{\sim}{\sigma} \cdot \operatorname{grad} \underset{\sim}{y}\, \mathrm{d}v = \bigcup_{e=1}^{n_e} \sum_{i=1}^{n} \sum_{k=1}^{n} \boldsymbol{v}_i^{\mathrm{T}} \int_{\omega_e} \boldsymbol{g}_i^{\mathrm{T}}\, \hat{\boldsymbol{\sigma}}\, \boldsymbol{g}_k \, \mathrm{d}\omega_e \, \Delta \boldsymbol{u}_k \,, \tag{3.35}$$

where

$$\boldsymbol{g}_j^{\mathrm{T}} = \begin{bmatrix} N_{j,x} & N_{j,y} & N_{j,z} & 0 & 0 & 0 & 0 & 0 & 0 \\ 0 & 0 & 0 & N_{j,x} & N_{j,y} & N_{j,z} & 0 & 0 & 0 \\ 0 & 0 & 0 & 0 & 0 & 0 & N_{j,x} & N_{j,y} & N_{j,z} \end{bmatrix} . \tag{3.36}$$

Note that (3.35) is commonly referred to as the *geometric* part of the stiffness matrix. In (3.35) the CAUCHY stresses are arranged such that

$$\hat{\boldsymbol{\sigma}} = \begin{bmatrix} \check{\boldsymbol{\sigma}} & & \\ & \check{\boldsymbol{\sigma}} & \\ & & \check{\boldsymbol{\sigma}} \end{bmatrix} \quad \text{with} \quad \check{\boldsymbol{\sigma}} = \begin{bmatrix} \sigma_{xx} & \sigma_{xy} & \sigma_{xz} \\ & \sigma_{yy} & \sigma_{yz} \\ \text{sym} & & \sigma_{zz} \end{bmatrix} . \tag{3.37}$$

For the second term of (3.8) the discretization gives

$$\int_v \nabla_x^{\mathrm{S}} \underset{\sim}{y}\ \cdot \overset{4}{\underset{\sim}{\mathrm{c}}} \nabla_x^{\mathrm{S}} \Delta \underset{\sim}{y}\, \mathrm{d}v = \bigcup_{e=1}^{n_e} \sum_{i=1}^{n} \sum_{k=1}^{n} \boldsymbol{v}_i^{\mathrm{T}} \int_{\omega_e} \boldsymbol{b}_i^{\mathrm{T}}\, \boldsymbol{d}\, \boldsymbol{b}_k \, \mathrm{d}\omega_e \, \Delta \boldsymbol{u}_k \,, \tag{3.38}$$

where $\boldsymbol{d}$ is the matrix form[4] of $\overset{4}{\underset{\sim}{\mathrm{c}}}$, and $\boldsymbol{b}_j$ is given by equation (3.25). Now, the advantage of a *spatial* formulation compared to a *material* one is obvious: Due to the sparsity of $\boldsymbol{b}_j$ multiplications in the matrix-matrix products $\boldsymbol{b}_i^{\mathrm{T}}\, \boldsymbol{d}\, \boldsymbol{b}_k$ can be avoided reducing the overall computational effort. Combining (3.35) and (3.38) yields

$$\int_v \left(\operatorname{grad} \Delta \underset{\sim}{y}\, \underset{\sim}{\sigma} \cdot \operatorname{grad} \underset{\sim}{y} + \nabla_x^{\mathrm{S}} \underset{\sim}{y}\ \cdot \overset{4}{\underset{\sim}{\mathrm{c}}} \nabla_x^{\mathrm{S}} \Delta \underset{\sim}{y} \right) \mathrm{d}v = \bigcup_{e=1}^{n_e} \sum_{i=1}^{n} \sum_{k=1}^{n} \boldsymbol{v}_i^{\mathrm{T}}\, \boldsymbol{k}_{T_{ik}}\, \Delta \boldsymbol{u}_k \tag{3.39}$$

[4] How to cast a (fourth-order) tensor into matrix form is outlined in [48].

with the spatial element tangent (or stiffness) matrix of dimension 3×3 in 3D

$$\boldsymbol{k}_{T_{ik}} = \int_{\omega_e} \left(\boldsymbol{g}_i^{\mathrm{T}} \, \hat{\boldsymbol{\sigma}} \, \boldsymbol{g}_k + \boldsymbol{b}_i^{\mathrm{T}} \, \boldsymbol{d} \, \boldsymbol{b}_k \right) \mathrm{d}\omega_e \tag{3.40}$$

related to the unknowns i and k. The application of the assembly operator $\bigcup$ gives

$$\bigcup_{e=1}^{n_e} \sum_{i=1}^{n} \sum_{k=1}^{n} \boldsymbol{v}_i^{\mathrm{T}} \, \boldsymbol{k}_{T_{ik}} \, \Delta \boldsymbol{u}_k = \mathbf{v}^{\mathrm{T}} \, \mathbf{k}_T \, \Delta \mathbf{u} \tag{3.41}$$

where $\mathbf{k}_T$ is the global tangent (or stiffness) matrix. The way to discretize the directional derivative with respect to the reference configuration (3.7) is similar. The resulting tangent element matrix of dimension 3×3 in 3D is

$$\boldsymbol{K}_{T_{IK}} = \int_{\Omega_e} \left(\boldsymbol{G}_I^{\mathrm{T}} \, \hat{\boldsymbol{S}} \, \boldsymbol{G}_K + \boldsymbol{B}_I^{\mathrm{T}} \, \boldsymbol{D} \, \boldsymbol{B}_K \right) \mathrm{d}\Omega_e \,, \tag{3.42}$$

where all derivatives are to be computed with respect to the reference configuration. In (3.42) $\boldsymbol{G}_I^{\mathrm{T}} \, \hat{\boldsymbol{S}} \, \boldsymbol{G}_K$ has the same structure as its *spatial* counterpart and hence the computational effort is similar. But for $\boldsymbol{B}_I^{\mathrm{T}} \, \boldsymbol{D} \, \boldsymbol{B}_K$ this is not the case. The reason is that the *material* strain-displacement matrix $\boldsymbol{B}$, see (3.27), is fully populated and does not allow for efficient multiplications. Note that in section 3.5 a comparison between a *spatial* formulation and a *material* formulation is carried out.

Now, let us summarize equations (3.24), (3.28), and (3.41) in order to obtain the discrete linearized weak form of the current configuration

$$\mathbf{v}^{\mathrm{T}} \left(\mathbf{k}_T \, \Delta \mathbf{u} + \mathbf{r}(\mathbf{u}) - \mathbf{p} \right) = 0 \,. \tag{3.43}$$

Again, due to the arbitrariness of the test function we arrive at

$$\mathbf{k}_T \, \Delta \mathbf{u} + \underbrace{\mathbf{r}(\mathbf{u}) - \mathbf{p}}_{\mathbf{g}(\mathbf{u})} = \mathbf{k}_T \, \Delta \mathbf{u} + \mathbf{g}(\mathbf{u}) = \mathbf{0} \,. \tag{3.44}$$

The counterpart to (3.44) is

$$\mathbf{K}_T \, \Delta \mathbf{u} + \underbrace{\mathbf{R}(\mathbf{u}) - \mathbf{P}}_{\mathbf{G}(\mathbf{u})} = \mathbf{K}_T \, \Delta \mathbf{u} + \mathbf{G}(\mathbf{u}) = \mathbf{0} \,. \tag{3.45}$$

3.2.5 Relative error in the energy norm

In this section we introduce the *relative error in the energy norm* $\|\mathbf{e}\|_{E(\Omega)}$ which is a useful measure for the quality of a discretization. We define

$$\|\mathbf{e}\|_{E(\Omega)} = \sqrt{\frac{|\mathcal{U}_{\mathrm{Ref}} - \mathcal{U}_{\mathrm{FE}}|}{\mathcal{U}_{\mathrm{Ref}}}} \,, \tag{3.46}$$

where $\mathcal{U}_{\mathrm{Ref}}$ is the reference strain energy, and $\mathcal{U}_{\mathrm{FE}}$ corresponds to the FE-approximation. The strain energy itself is obtained by integrating a general strain energy (density) function Ψ, as introduced in section 2.1.4, in the reference configuration for all elements

$$\mathcal{U} = \sum_{e=1}^{n_e} \int_{\Omega_e} \Psi_e \, \mathrm{d}\Omega_e \,. \tag{3.47}$$

In the case of a linear relationship between strains and stresses we can further specify (3.47) for St. Venant-Kirchhoff's material law as

$$\mathcal{U}_{\mathrm{SV}} = \frac{1}{2} \sum_{e=1}^{n_e} \int_{\Omega_e} \boldsymbol{S}_e^{\mathrm{T}} \, \boldsymbol{E}_e \, \mathrm{d}\Omega_e \,, \tag{3.48}$$

and consequently for Hooke's law

$$\mathcal{U}_{\mathrm{H}} = \frac{1}{2} \sum_{e=1}^{n_e} \int_{\Omega_e} \boldsymbol{\sigma}_e^{\mathrm{T}} \, \boldsymbol{\varepsilon}_e \, \mathrm{d}\Omega_e \,. \tag{3.49}$$

3.3 Solution of the linearized system of equations

The nonlinear algebraic equation system (refer to equations (3.32) and (3.33) respectively) stemming from the FE-discretization is rewritten

$$\mathbf{g}(\mathbf{u}, \lambda) = \mathbf{r}(\mathbf{u}) - \lambda \, \mathbf{p} = \mathbf{0} \,, \tag{3.50}$$

$$\mathbf{G}(\mathbf{u}, \lambda) = \mathbf{R}(\mathbf{u}) - \lambda \, \mathbf{P} = \mathbf{0} \,, \tag{3.51}$$

where λ scales the applied loads. For simplicity, the notation of the *spatial* version will be used in the following.

Thanks to the linearization (3.44), the solution of the nonlinear system (3.50) can be reduced to solving a series of linear systems. Within this series we continuously evaluate a modified version of (3.44), namely

$$\mathbf{g}(\mathbf{u}_k, \lambda_k) + \mathbf{k}_T(\mathbf{u}_k) \, \Delta\mathbf{u} = \mathbf{0} \,, \tag{3.52}$$

at a known state $\mathbf{u}_k$ and for a specific load level λ_k. The Newton-Raphson scheme is summarized in Algorithm A-1.

With a view to numerical homogenization the so called *discrete* Newton-Raphson algorithm is of interest. Here, an analytical derivation of the tangent matrix is circumvented. Instead, a forward difference scheme is applied where

$$\mathbf{k}_m \approx \frac{1}{\Delta_h} \left[\mathbf{g}(\mathbf{u}_k + \Delta_h \cdot \mathbf{e}_m, \lambda_k) - \mathbf{g}(\mathbf{u}_k, \lambda_k) \right] \,, \tag{3.53}$$

is obtained for the m-th column of the tangent matrix. In (3.53) Δ_h is the step size and $\mathbf{e}_m$ is a vector which has one non-zero entry (=1) at position m and is zero elsewhere. For the case of N unknowns the tangent matrix is assembled as

$$\mathbf{k}_T = \left[\begin{array}{cccc} \mathbf{k}_1 & \mathbf{k}_2 & \cdots & \mathbf{k}_N \end{array} \right] . \tag{3.54}$$

Algorithm A-1 NEWTON-RAPHSON algorithm

set $k = 1$, $\mathbf{u}_1^0 = \mathbf{0}$
define load steps $\lambda_1, \ldots, \lambda_n$
repeat
  set $i = 0$
  repeat
    compute $\mathbf{g}_k^i = \mathbf{g}(\mathbf{u}_k^i, \lambda_k)$ and $\mathbf{k}_{T_k}^i = \mathbf{k}_T(\mathbf{u}_k^i)$
    solve the linear system of equations $\mathbf{g}_k^i + \mathbf{k}_{T_k}^i \, \Delta\mathbf{u}_k^{i+1} = \mathbf{0}$
    compute $\mathbf{u}_k^{i+1} = \mathbf{u}_k^i + \Delta\mathbf{u}_k^{i+1}$
    set $i = i + 1$
  until $\|\mathbf{u}_k^i\| < tolerance$
  set $\mathbf{u}_{k+1}^0 = \mathbf{u}_k^i$, $k = k + 1$
until $\lambda_k = \lambda_n$

Provided a proper choice of Δ_h this scheme can give useful results, see [105] and the literature cited therein. Unfortunately, due to the large number of evaluations of $\mathbf{g}$ the computational effort is high.

3.4 Shape functions

As indicated above, there are basically two versions of the FEM, which control the error of the discretization differently: The h-version that applies mesh-refinement and the p-version that keeps the mesh fixed and raises the polynomial degree of the Ansatz function. A combination of both methods is called hp-version. In Figure 3.2 the relative error in the energy norm (as defined in (3.46)) is plotted for different refinement strategies using a double-logarithmic scale. The h- and p-versions show algebraic rates of convergence for a problem with singularities,

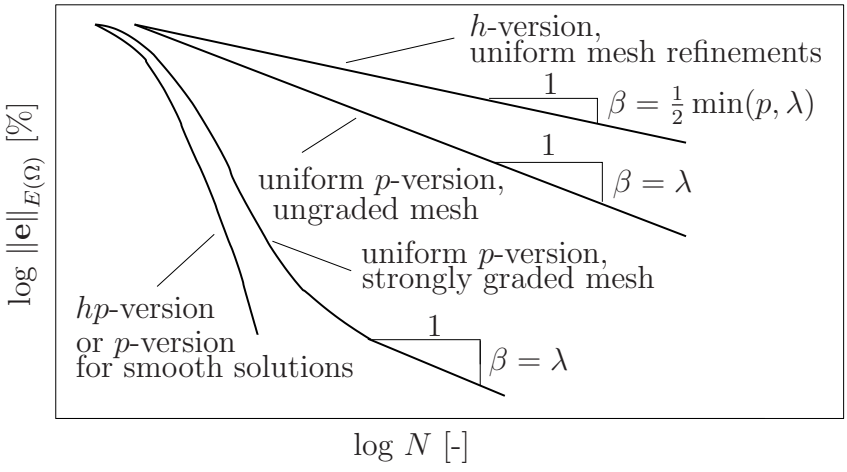

Figure 3.2: Relative error in the energy norm for h-, p- and hp-version FEM for a two-dimensional linear elastic problem with singularities

where the p-version has twice the convergence rate of the h-version. The hp-version shows

exponential convergence. If there are no singularities, the p-version converges exponentially, too.

3.4.1 Introductory example

Before going into detail with the p-version's shape functions, we demonstrate with a numerical example some advantages of the p-version like, for example, robustness against locking effects even for high element aspect ratios. In this example, a small ring is deformed by two opposite forces, see Figure 3.3. Here, not only shear locking but also other phenomena like membrane or trapezoidal locking may occur [66]. In Figure 3.4 the mechanical model is illustrated. Due

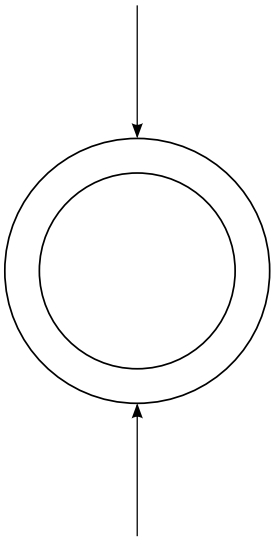

Figure 3.3: Pinched ring - setup

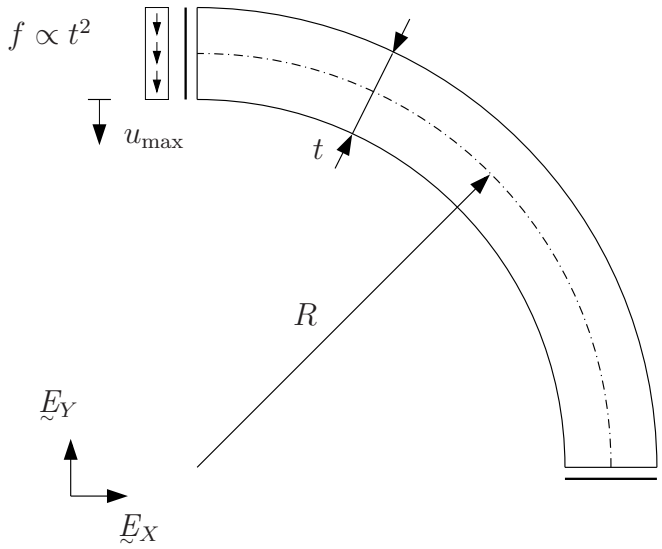

Figure 3.4: Pinched ring - mechanical model

to double symmetry only a quarter of the whole ring has to be considered, and symmetry boundary conditions are applied. The discretization is depicted for the lowest and highest aspect ratio R/t in Figures 3.5 and 3.6. Since there are singularities at the edge where the load is applied, a strongly graded mesh is utilized. An analytical solution of the maximum

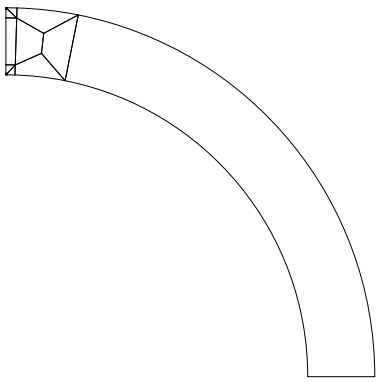

Figure 3.5: Pinched ring - mesh for $R/t = 5$

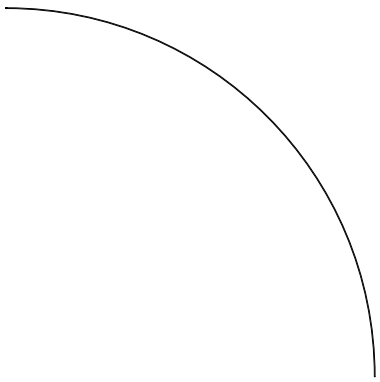

Figure 3.6: Pinched ring - mesh for $R/t = 500$

deflection $u_{\max}$, which is based on the classical beam theory, can be found in [45] and reads

$$u_{\max} = \frac{F\,R^3}{8\,E\,I}\left(\pi - \frac{8}{\pi}\right) ,$$

where $F = \int_t f \,\mathrm{d}t$. In the following, R is constant and YOUNG's modulus E is chosen such that $u_{\max} = 1$ if no locking is present. Now, let us investigate the maximum deflection $u_{\max}$ depending on the slenderness R/t. In Figure 3.7 the results are shown for polynomial degrees p from one to eight in a double-logarithmic style. Obviously, locking is encountered with

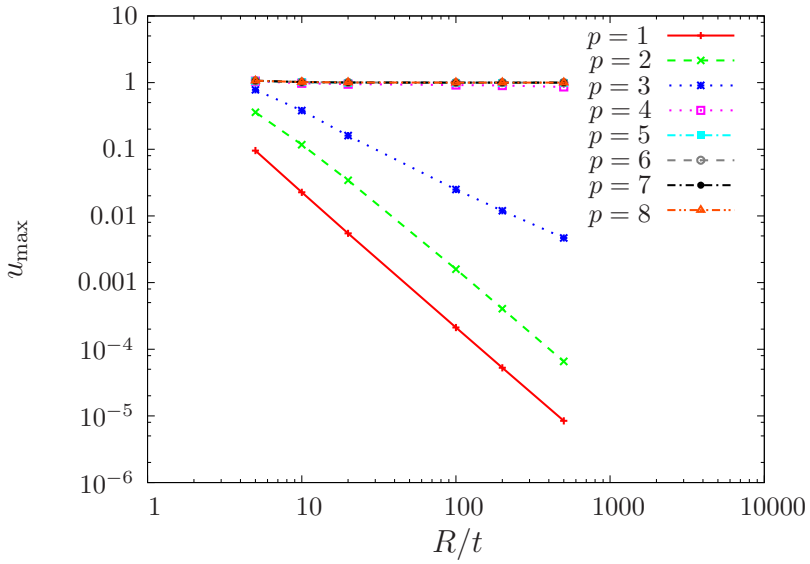

Figure 3.7: Pinched ring - locking effects

polynomial degrees from one to four. In the case of $p = 4$ locking is not that pronounced, and from $p = 5$ on locking no longer plays a role. In Figure 3.8 the relative error in the energy norm is plotted against the number of degrees of freedom N in a double-logarithmic style. We observe a high rate of convergence for the different aspect ratios. With the exception of $R/t = 500$, where conditioning problems are present, the error can be reduced significantly below 1% due to the p-extension. In order to further improve the results an hp-version has to be applied. In the following sections we illuminate the p-version's shape functions.

3.4.2 Higher-order shape functions for 1D

For higher-order finite elements that are used in the p-version either LAGRANGIAN or hierarchic shape functions can be used. Both of them lead, of course, to the same results, but hierarchic shape functions have some advantages, for example a better condition number of the resulting stiffness matrices and a hierarchic structure. These advantages will be addressed below.

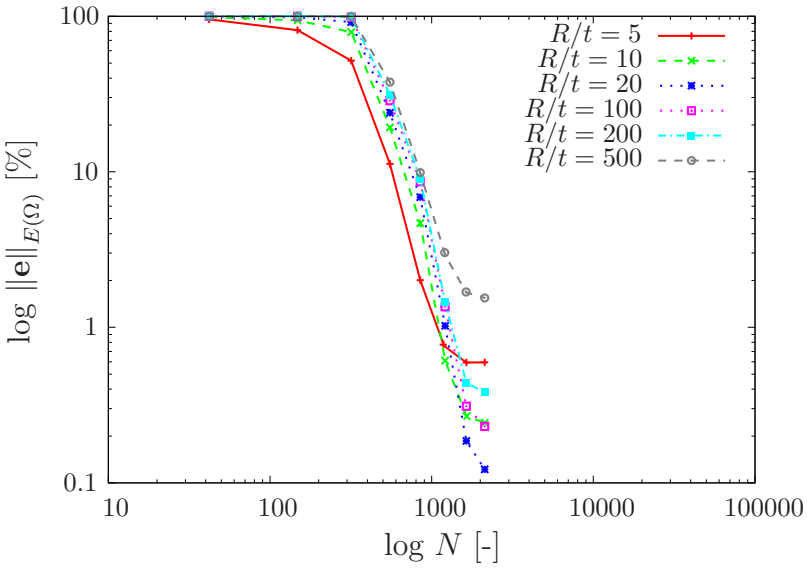

Figure 3.8: Pinched ring - relative error in the energy norm

3.4.2.1 LAGRANGIAN shape functions

LAGRANGIAN polynomials are given by the formula

$$N_i^{(p)}(\xi) = \prod_{j=1,\, j\neq i}^{p+1} \frac{\xi - \xi_j}{\xi_i - \xi_j}, \tag{3.55}$$

where p is the polynomial degree and ξ_i and ξ_j are the coordinates of the nodes. The sum of all LAGRANGE polynomials for a given polynomial degree p equals 1, i.e. they form a *partition of unity*.

LAGRANGIAN elements of order p have $p+1$ nodes; all of the nodes are equally spaced. For each polynomial degree the complete set of shape functions changes. The LAGRANGIAN shape functions for polynomial order one, two, and three are

for $p = 1$:

$$\begin{aligned} N_1^{(1)}(\xi) &= 1/2(1-\xi) \\ N_2^{(1)}(\xi) &= 1/2(1+\xi) \end{aligned} \tag{3.56}$$

for $p = 2$:

$$\begin{aligned} N_1^{(2)}(\xi) &= 1/2\,\xi\,(\xi-1) \\ N_2^{(2)}(\xi) &= (1+\xi)\,(1-\xi) \\ N_3^{(2)}(\xi) &= 1/2\,(\xi+1)\,\xi \end{aligned} \tag{3.57}$$

for $p = 3$:

$$\begin{aligned} N_1^{(3)}(\xi) &= -1/16\ (3\,\xi + 1)\,(3\,\xi - 1)\,(\xi - 1) \\ N_2^{(3)}(\xi) &= 9/16\ (\xi + 1)\,(3\,\xi - 1)\,(\xi - 1) \\ N_3^{(3)}(\xi) &= -9/16\ (\xi + 1)\,(3\,\xi + 1)\,(\xi - 1) \\ N_4^{(3)}(\xi) &= 1/16\ (\xi + 1)\,(3\,\xi + 1)\,(3\,\xi - 1) \end{aligned} \tag{3.58}$$

Figure 3.9 shows the LAGRANGIAN shape functions up to $p = 3$.

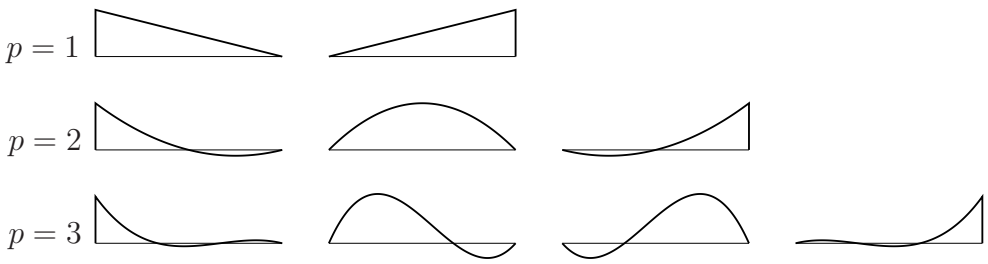

Figure 3.9: LAGRANGIAN shape functions for p= 1, 2, 3

3.4.2.2 Hierarchic shape functions

Hierarchic shape functions are given by

$$\begin{aligned} N_1(\xi) &= 1/2(1 - \xi) \\ N_2(\xi) &= 1/2(1 + \xi) \\ N_i(\xi) &= \phi_{i-1}(\xi), \quad i = 3, 4, ..., p + 1 \end{aligned} \tag{3.59}$$

with

$$\phi_j(\xi) = \sqrt{\frac{2j-1}{2}} \int_{-1}^{\xi} L_{j-1}(x)\,\mathrm{d}x = \frac{1}{\sqrt{4j-2}}(L_j(\xi) - L_{j-2}(\xi))\,, \quad j = 2, 3, ...$$

where $L_j(\xi)$ are the LEGENDRE polynomials. The LEGENDRE polynomials can be determined by applying the RODRIGUEZ formula

$$L_n(x) = \frac{1}{2^n\,n!}\frac{\mathrm{d}^n}{\mathrm{d}\,x^n}\,(x^2 - 1)^n\,, \quad x \in (-1, 1), \quad n = 0, 1, 2, ...\ . \tag{3.60}$$

The hierarchic shape functions for $p = 1, 2, 3, ..., 8$ are given by

$$\begin{aligned}
N_1(\xi) &= 1/2(1-\xi) \\
N_2(\xi) &= 1/2(1+\xi) \\
N_3(\xi) &= 1/4\sqrt{6}\left(\xi^2-1\right) \\
N_4(\xi) &= 1/4\sqrt{10}\left(\xi^2-1\right)\xi \\
N_5(\xi) &= 1/16\sqrt{14}\left(5\,\xi^4-6\,\xi^2+1\right) \\
N_6(\xi) &= 3/16\sqrt{2}\xi\ \left(7\,\xi^4-10\,\xi^2+3\right) \\
N_7(\xi) &= 1/32\sqrt{22}\left(21\,\xi^6-35\,\xi^4+15\,\xi^2-1\right) \\
N_8(\xi) &= 1/32\sqrt{26}\xi\ \left(33\,\xi^6-63\,\xi^4+35\,\xi^2-5\right) \\
N_9(\xi) &= 1/256\sqrt{30}\left(-140\,\xi^2-924\,\xi^6+630\,\xi^4+5+429\,\xi^8\right)\ .
\end{aligned} \tag{3.61}$$

Hierarchic elements have no internal nodes. Only the linear shape functions are nodal shape functions. The remaining shape functions correspond to internal modes or bubble modes. A new shape function is added for each polynomial degree. The other shape functions remain the same as before which allows for an elegant implementation. Note that for hierarchic shape functions the *partition of unity* is not fulfilled. Figure 3.10 shows the hierarchic shape functions up to $p = 3$. The orthogonality property of LEGENDRE polynomials implies

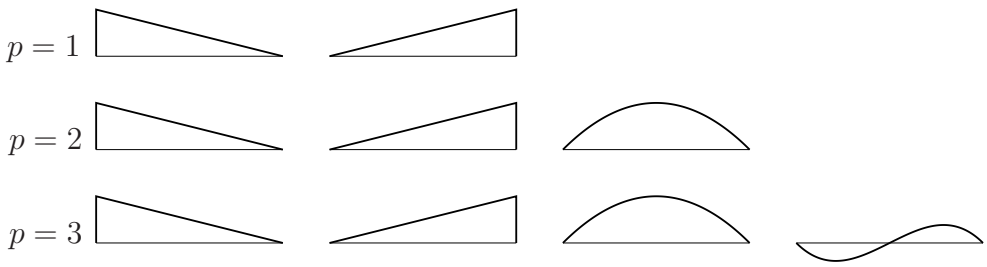

Figure 3.10: Hierarchic shape functions for p=1, 2, 3

$$\int_{-1}^{1} \frac{\mathrm{d}\,N_i}{\mathrm{d}\xi}\,\frac{\mathrm{d}\,N_j}{\mathrm{d}\xi}\,\mathrm{d}\xi \;=\; \delta_{ij}, \quad i \geq 3 \text{ and } j \geq 1 \quad \text{or} \quad i \geq 1 \text{ and } j \geq 3\,, \tag{3.62}$$

which results in a better conditioning of the corresponding stiffness matrices.

3.4.3 Hierarchic shape functions for quadrilaterals

In two dimensions, a quadrilateral element formulation applying the Ansatz functions introduced by SZABÓ and BABUŠKA [90] is used. Here, two different types of Ansatz spaces are taken into consideration: the *trunk space* $\mathcal{S}_{\mathrm{ts}}^{p_\xi,p_\eta}(\Omega_\square^{\mathrm{q}})$ and the larger *tensor product space* $\mathcal{S}_{\mathrm{ps}}^{p_\xi,p_\eta}(\Omega_\square^{\mathrm{q}})$.

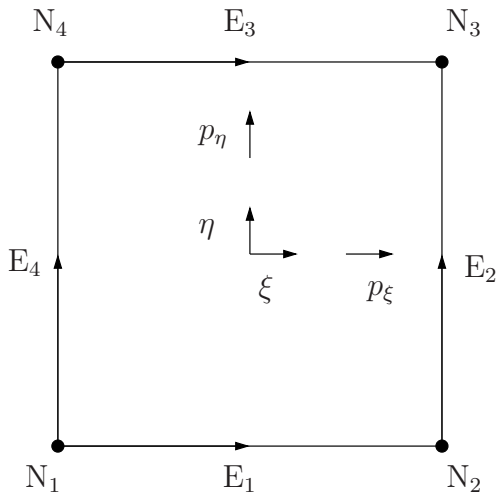

$$\Omega_{\square}^{\mathrm{q}} = [(-1,1) \times (-1,1)]$$

Figure 3.11: Standard quadrilateral element: definition of nodes, edges and polynomial degree

In Figure 3.11 the standard quadrilateral finite element is depicted which allows for different polynomial degrees in the element's local directions. We obtain the shape functions by tensor products of one-dimensional shape functions as provided by equation (3.59). The shape functions can be divided into three groups, compare with Figure 3.12:

1. **Nodal modes:** These modes

$$N_{1,1}^{\mathrm{N}_i}(\xi,\eta) \;=\; \frac{1}{4}\,(1+\xi_i\,\xi)(1+\eta_i\,\eta)\,, \quad i=1,...,4 \tag{3.63}$$

   are the standard bilinear shape functions with (ξ_i, η_i) denoting the local coordinates of the ith node.

2. **Edge modes:** They are defined separately for each individual edge and by construction vanish at all the other edges. The corresponding modes for edge E_1 read:

$$N_{i,1}^{\mathrm{E}_1}(\xi,\eta) \;=\; \frac{1}{2}\,(1-\eta)\phi_i(\xi) \tag{3.64}$$

3. **Internal modes:** The internal modes

$$N_{i,j}^{\mathrm{int}}(\xi,\eta) \;=\; \phi_i(\xi)\phi_j(\eta) \tag{3.65}$$

   are nonzero only in the interior of the quadrilateral element.

The indices i, j of the shape functions denote the polynomial degrees in the local directions ξ, η. The matrix of shape functions $\boldsymbol{N}$ as given in equation (3.12) can now be specified as

$$\boldsymbol{N} \;=\; \left[\, \boldsymbol{N}^{\mathrm{N}} \quad \boldsymbol{N}^{\mathrm{E}} \quad \boldsymbol{N}^{\mathrm{int}} \,\right], \tag{3.66}$$

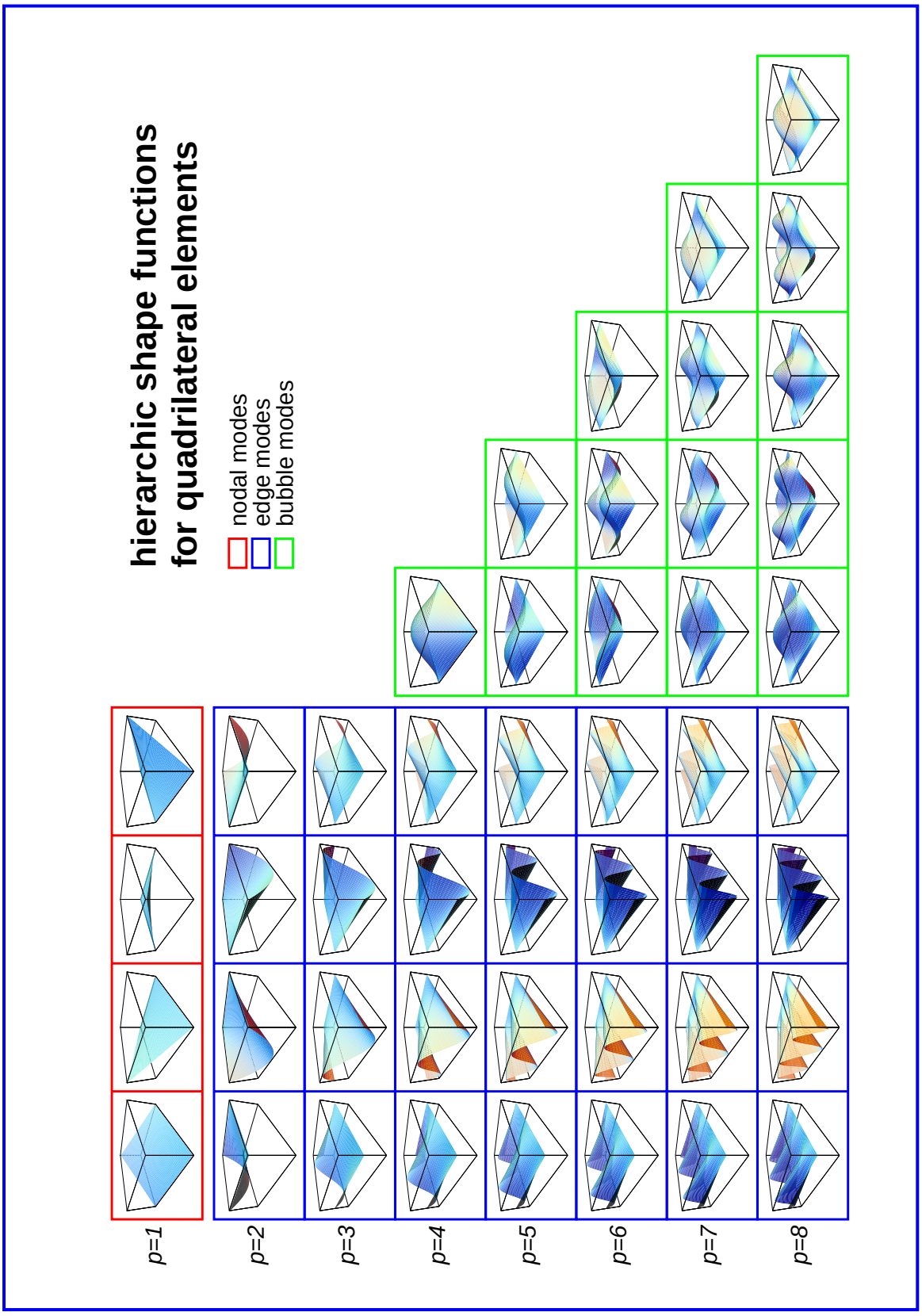

Figure 3.12: Hierarchic shape functions for quadrilaterals assuming the *trunk space* [82]

where

$$\boldsymbol{N}^{\mathrm{N}} = \begin{bmatrix} N_{1,1}^{\mathrm{N}_1} & & \ldots & N_{1,1}^{\mathrm{N}_4} & \\ & N_{1,1}^{\mathrm{N}_1} & \ldots & & N_{1,1}^{\mathrm{N}_4} \end{bmatrix} \tag{3.67}$$

represents the nodal modes, and

$$\boldsymbol{N}^{\mathrm{E}} = \begin{bmatrix} \boldsymbol{N}^{\mathrm{E}_1} & \ldots & \boldsymbol{N}^{\mathrm{E}_4} \end{bmatrix} \tag{3.68}$$

collects for each edge the edge modes separately. For edge E_1, for example, we have

$$\boldsymbol{N}^{\mathrm{E}_1} = \begin{bmatrix} N_{2,1}^{\mathrm{E}_1} & & \ldots & N_{p_\xi,1}^{\mathrm{E}_4} & \\ & N_{2,1}^{\mathrm{E}_1} & \ldots & & N_{p_\xi,1}^{\mathrm{E}_4} \end{bmatrix}. \tag{3.69}$$

Finally, $\boldsymbol{N}^{\mathrm{int}}$ includes the internal modes

$$\boldsymbol{N}^{\mathrm{int}} = \begin{bmatrix} N_{2,2}^{\mathrm{int}} & & \ldots & N_{p_\xi,p_\eta}^{\mathrm{int}} & \\ & N_{2,2}^{\mathrm{int}} & \ldots & & N_{p_\xi,p_\eta}^{\mathrm{int}} \end{bmatrix}. \tag{3.70}$$

Note that zero entries have been skipped in equations (3.67)-(3.70). Let us consider two-dimensional thin-walled structures, for example the pinched ring presented in section 3.4.1[5] or cell walls of foam-like materials. Here, the thickness direction has to be treated differently in order to obtain an efficient discretization. As indicated above, this is accounted for by using anisotropic Ansatz functions for the two-dimensional displacement field. Therefore, the polynomial degree q in the thickness direction is chosen differently from the polynomial degree p in the longitudinal direction, see Figure 3.13, whereby $p \geq q$.

3.4.4 Hierarchic shape functions for hexahedrals

In three dimensions, the p-version's implementation is based on a hexahedral element formulation as shown in Figure 3.14 [21, 22], again using the Ansatz functions introduced by Szabó and Babuška [90], whereby three different types of Ansatz spaces are considered: the *trunk space* $\mathcal{S}_{\mathrm{ts}}^{p_\xi,p_\eta,p_\zeta}(\Omega_\square^{\mathrm{h}})$, the *tensor product space* $\mathcal{S}_{\mathrm{ps}}^{p_\xi,p_\eta,p_\zeta}(\Omega_\square^{\mathrm{h}})$ and the *anisotropic tensor product space* $\mathcal{S}^{p,p,q}(\Omega_\square^{\mathrm{h}})$. The three-dimensional shape functions are classified into four groups:

1. **Nodal modes:** These modes

$$N_{1,1,1}^{\mathrm{N}_i}(\xi,\eta,\zeta) = \frac{1}{8}(1+\xi_i\,\xi)(1+\eta_i\,\eta)(1+\zeta_i\zeta), \quad i=1,...,8 \tag{3.71}$$

   are the standard trilinear shape functions where (ξ_i,η_i,ζ_i) are the local coordinates of the ith node.

[5] Note that only isotropic elements have been applied in this example. Using anisotropic elements would lower the overall number of degrees of freedom.

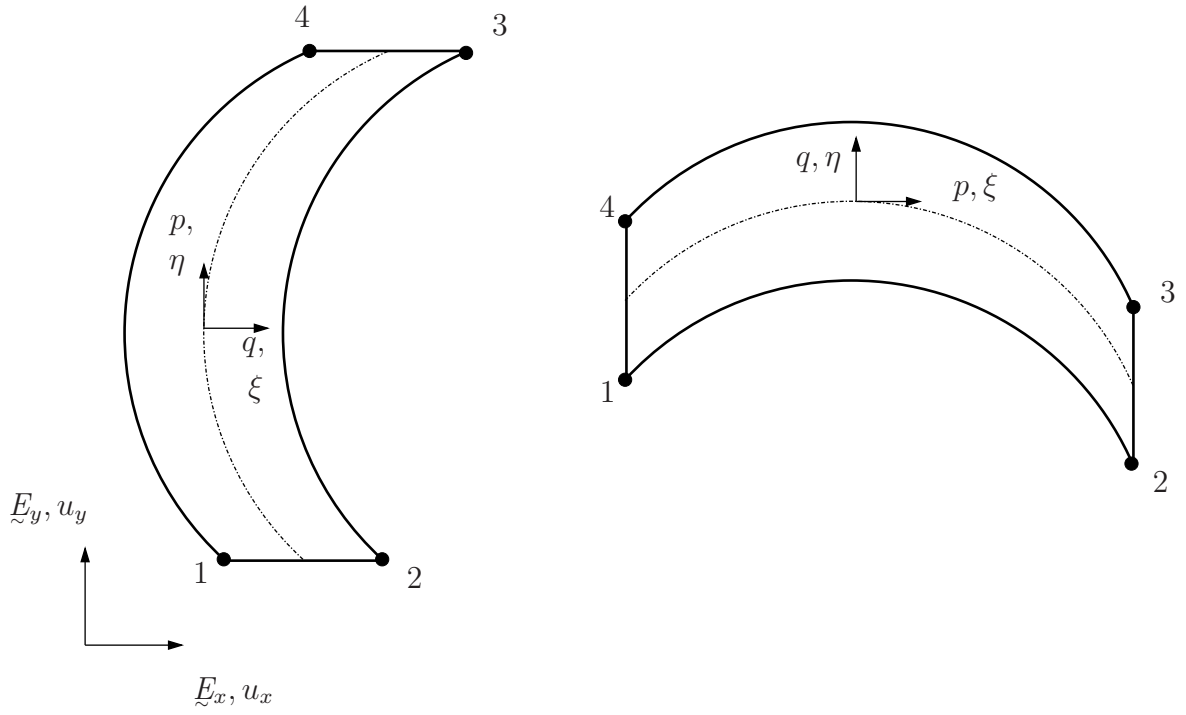

Figure 3.13: Beam-like element with different local orientations and polynomial degrees

2. **Edge modes:** They are defined separately for each individual edge. If we consider, for example, edge E_1 (see Figure 3.14), the corresponding edge modes read:

$$N^{\mathrm{E}_1}_{i,1,1}(\xi,\eta,\zeta) \;=\; \frac{1}{4}(1-\eta)(1-\zeta)\phi_i(\xi) \tag{3.72}$$

3. **Face modes:** These modes are defined separately for each individual face. If we consider, for example, face F_1, the corresponding face modes read:

$$N^{\mathrm{F}_1}_{i,j,1}(\xi,\eta,\zeta) \;=\; \frac{1}{2}(1-\zeta)\phi_i(\xi)\phi_j(\eta) \tag{3.73}$$

4. **Internal modes:** The internal modes

$$N^{\mathrm{int}}_{i,j,k}(\xi,\eta,\zeta) \;=\; \phi_i(\xi)\phi_j(\eta)\phi_k(\zeta) \tag{3.74}$$

   are purely internal and nonzero only within the hexahedral element.

The indices i, j, k of the shape functions again denote the polynomial degrees in the local directions ξ, η, ζ. Having defined the complete set of shape functions for the three-dimensional hexahedral element, the matrix of shape functions can be set up

$$\boldsymbol{N} \;=\; \left[\, \boldsymbol{N}^{\mathrm{N}} \quad \boldsymbol{N}^{\mathrm{E}} \quad \boldsymbol{N}^{\mathrm{F}} \quad \boldsymbol{N}^{\mathrm{I}} \,\right], \tag{3.75}$$

where the superscripts N, E, F, I indicate nodal, edge, face and internal modes respectively. At the end of this section let us illustrate how to discretize thin-walled structures by an example,

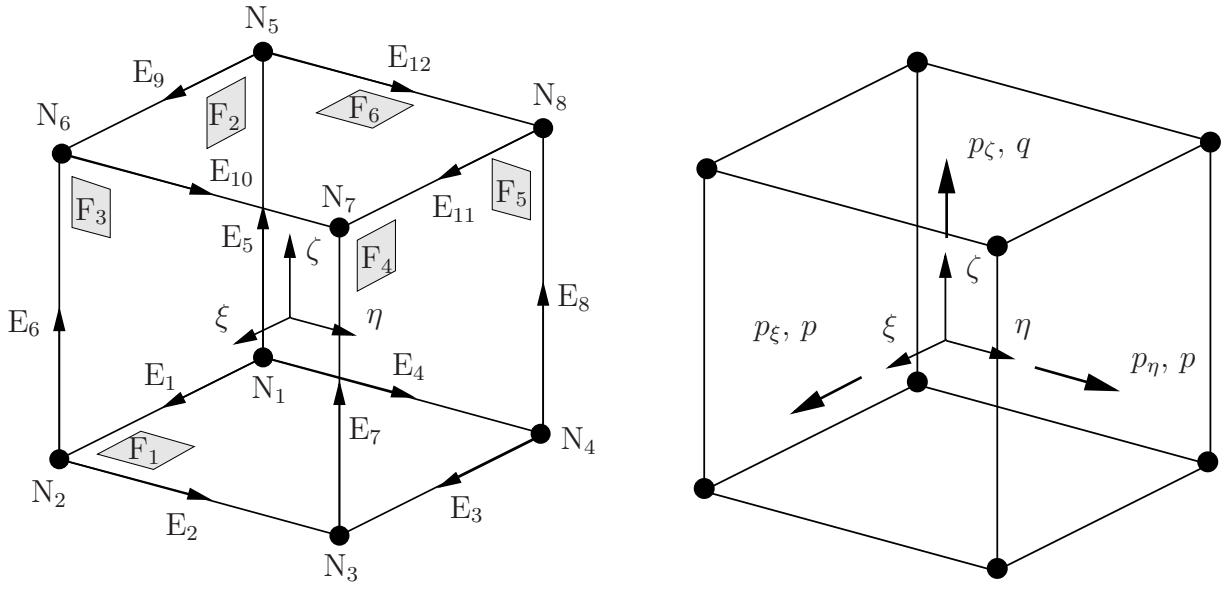

$\Omega_{\square}^{\mathrm{h}} = [(-1,1) \times (-1,1) \times (-1,1)]$ $\mathcal{S}_{\mathrm{ts}}^{p_\xi,p_\eta,p_\zeta}(\Omega_{\square}^{\mathrm{h}}), \mathcal{S}_{\mathrm{ps}}^{p_\xi,p_\eta,p_\zeta}(\Omega_{\square}^{\mathrm{h}}), \mathcal{S}^{p,p,q}(\Omega_{\square}^{\mathrm{h}})$

Figure 3.14: Standard hexahedral element $\Omega_{\square}^{\mathrm{h}}$: definition of nodes, edges, faces and polynomial degree [21]

see Figure 3.15. Here, all hexahedral elements are oriented such that their local ζ-direction corresponds to the thickness direction of the plate. Thus, it is easy to apply anisotropic Ansatz spaces like, for example, the *anisotropic tensor product space* $\mathcal{S}^{p,p,q}(\Omega_{\square}^{\mathrm{h}})$.

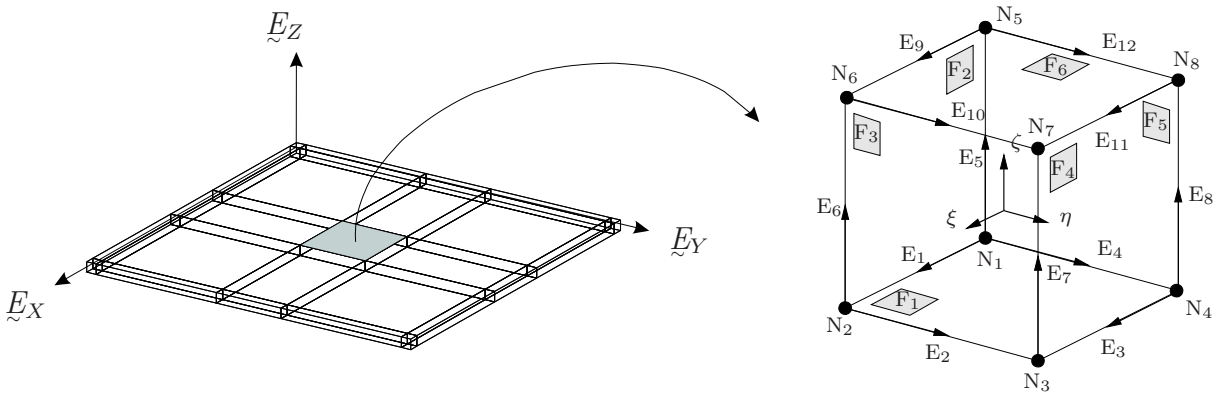

Figure 3.15: Modeling plate-like structures with hexahedral elements [21]

3.4.5 Mapping functions

As stated above, in the p-version the mesh is left unchanged, and convergence is obtained by local or global increase in the polynomial degree. Therefore, it is very important to accurately

model the geometry of the structure with the fixed number of elements in use. This calls for a method which is able to describe complex geometries using a few elements only. To this end, the *blending function method* proposed by Gordon and Hall [44] is applied.

Before describing this method, it is useful to classify the different mapping concepts:

- **the isoparametric concept**
  This concept implies that the shape functions describing the variation of the unknowns are the same as those applied for the definition of geometry.
- **the superparametric concept**
  The shape functions used for the description of the geometry are more complex than those for the unknown function.
- **the subparametric concept**
  Here, the description of the unknown function is more general than that of the geometry.

It is important to distinguish between the different mapping concepts because the accuracy of a finite element solution is not only given by the approximation of the unknowns but also depends on the description of geometry.

Let us now illustrate the *blending function method* in two dimensions[6] by considering a quadrilateral element where edge E_2 is assumed to be part of a curved boundary (see Figure 3.16). The geometry of edge E_2 is defined by a parametric function $\boldsymbol{E}_2 = [E_{2X}(\eta), E_{2Y}(\eta)]^{\mathrm{T}}$. The

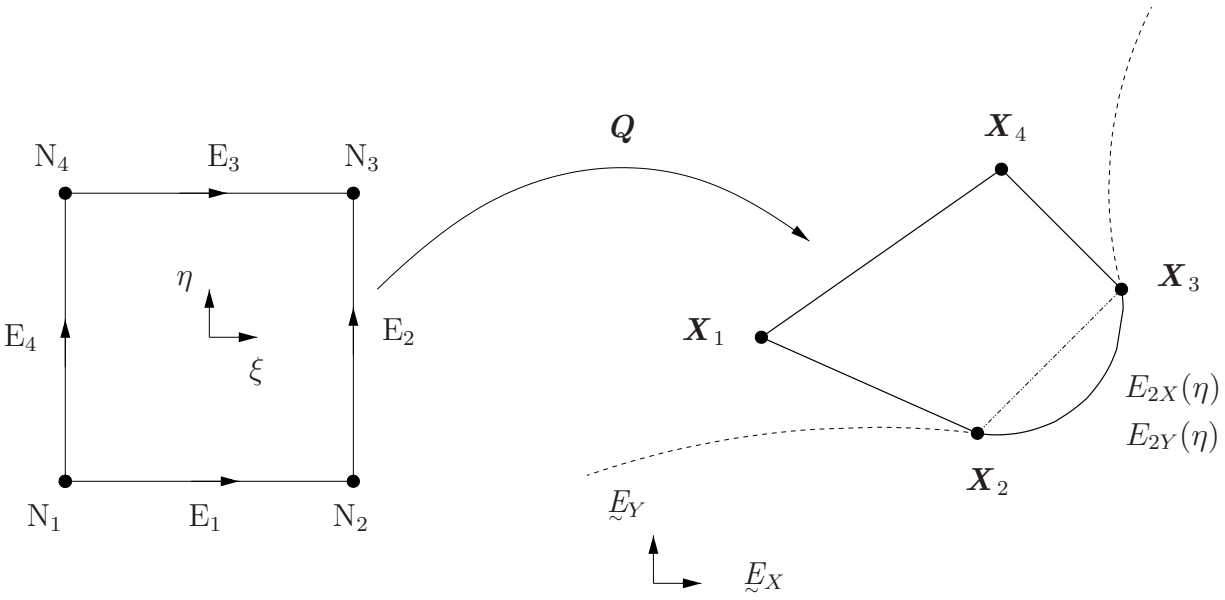

Figure 3.16: Blending function method for quadrilateral elements [21]

transformation of the local coordinates into the global coordinates as stated in equation (3.16)

[6]For the three-dimensional case refer to [11, 22, 91].

can be formulated by the two functions

$$X = Q_X(\xi,\eta) = \sum_{i=1}^{4} N_{1,1}^{\mathrm{N}_i}(\xi,\eta)\, X_i + \left(E_{2X}(\eta) - \left(\frac{1-\eta}{2}\, X_2 + \frac{1+\eta}{2}\, X_3 \right) \right) \frac{1+\xi}{2}$$

$$Y = Q_Y(\xi,\eta) = \sum_{i=1}^{4} N_{1,1}^{\mathrm{N}_i}(\xi,\eta)\, Y_i + \left(E_{2Y}(\eta) - \left(\frac{1-\eta}{2}\, Y_2 + \frac{1+\eta}{2}\, Y_3 \right) \right) \frac{1+\xi}{2}\,,$$

where the first term corresponds to the standard bilinear mapping, which is familiar from the isoparametric concept for quadrilateral elements with $p = 1$. The second term takes the curved edge E_2 into account. Therefore, the bilinear mapping is augmented by the blended difference between the curve $\boldsymbol{E}_2 = [E_{2X}(\eta), E_{2Y}(\eta)]^{\mathrm{T}}$ and the straight line connecting the nodes N_2 and N_3. The blending term $(1+\xi)/2$ ensures that the opposite edge E_4 – where $(1+\xi)/2 = 0$ – is not affected by the curvilinear description of edge E_2.

If a quadrilateral is to be considered where all the edges are curved, the *blending function method* can be expanded such that the mapping reads:

$$\begin{aligned} X = Q_X(\xi,\eta) &= \frac{1}{2}(1-\eta)E_{1X}(\xi) + \frac{1}{2}(1+\xi)E_{2X}(\eta) + \frac{1}{2}(1+\eta)E_{3X}(\xi) + \frac{1}{2}(1-\xi)E_{4X}(\eta) - \\ &\quad - \sum_{i=1}^{4} N_{1,1}^{\mathrm{N}_i}(\xi,\eta)\, X_i \\ Y = Q_Y(\xi,\eta) &= \frac{1}{2}(1-\eta)E_{1Y}(\xi) + \frac{1}{2}(1+\xi)E_{2Y}(\eta) + \frac{1}{2}(1+\eta)E_{3Y}(\xi) + \frac{1}{2}(1-\xi)E_{4Y}(\eta) - \\ &\quad - \sum_{i=1}^{4} N_{1,1}^{\mathrm{N}_i}(\xi,\eta)\, Y_i \end{aligned} \tag{3.76}$$

where:

$$\begin{aligned} &E_{iX}(\xi), \quad E_{iY}(\xi), \quad \text{for} \quad i = 1,3 \\ &E_{iX}(\eta), \quad E_{iY}(\eta), \quad \text{for} \quad i = 2,4 \end{aligned} \tag{3.77}$$

are parametric functions describing the geometry of the edges $\mathrm{E}_i, i = 1,\ldots,4$. The *blending function method*, therefore, allows for a large variety of element shapes which are defined by the nodal coordinates $\boldsymbol{X}_i = [X_i, Y_i]^{\mathrm{T}}$, $i = 1,\ldots,4$ and the parametric functions (3.77) describing the geometry of the edges.

3.5 Comparison between a *spatial* and a *material* finite element formulation

This section is subdivided into two parts: Firstly, we will give an estimation of the speedup of a *spatial* formulation as compared to a *material* formulation, where we assume three-dimensional hyperelastic behavior based on the Neo-Hookean material law, see equation (2.47). In the second part, we will verify our estimation within a numerical hyperelastic compression test.

3.5.1 Estimation of the computational effort

In this section the effort for computing the tangential stiffness matrices $\boldsymbol{k}_T$, equation (3.40), and $\boldsymbol{K}_T$, equation (3.42), respectively will be estimated in terms of floating point multiplications and depending on the polynomial degree p.

The number of degrees of freedom N for the *tensor product space* of a LAMÉ-problem is

$$N(p) = d\,(p+1)^d\,, \tag{3.78}$$

and the number of integration points I of a GAUSSIAN quadrature equals

$$I(p) = (p+1)^d\,. \tag{3.79}$$

As indicated above, the *spatial* formulation mainly influences the second part of the tangential stiffness matrix, $\boldsymbol{k}_T$, namely $\boldsymbol{b}^{\mathrm{T}}\,\boldsymbol{d}\,\boldsymbol{b}$. Firstly, we will focus on the *spatial* formulation: $\boldsymbol{b}$ given in equation (3.25) is sparse or, more precisely, half of the entries are zero. The matrix representation of the spatial NEO-HOOKEAN elasticity tensor $\overset{4}{\underset{\sim}{\mathrm{c}}}$, refer to (2.52), with the abbreviations $\Lambda' = \Lambda/J$ and $\mu' = (\mu - \Lambda \ln J)/J$,

$$\boldsymbol{d} \;=\; \begin{bmatrix} \Lambda'+2\mu' & \Lambda' & \Lambda' & 0 & 0 & 0 \\ & \Lambda'+2\mu' & \Lambda' & 0 & 0 & 0 \\ & & \Lambda'+2\mu' & 0 & 0 & 0 \\ & & & \mu' & 0 & 0 \\ & & & & \mu' & 0 \\ \text{sym} & & & & & \mu' \end{bmatrix} \tag{3.80}$$

has only 12 non-zero entries. In order to investigate the number of multiplications the product $\boldsymbol{b}^{\mathrm{T}}\,\boldsymbol{d}\,\boldsymbol{b}$ can be split into two parts. For $\boldsymbol{x} = \boldsymbol{b}^{\mathrm{T}}\,\boldsymbol{d}$ we have

$$n_x(p) = 2\,d \cdot N(p) \cdot I(p)\,, \tag{3.81}$$

multiplications, and for $\boldsymbol{y} = \boldsymbol{x}\,\boldsymbol{b}$ we have

$$n_y(p) = d \cdot N(p) \cdot \frac{(N(p)+1)}{2} \cdot I(p) \tag{3.82}$$

multiplications whereby symmetry was accounted for. The total number of multiplications is

$$n_{b^{\mathrm{T}}db}(p) \;=\; n_x(p) + n_y(p)\,. \tag{3.83}$$

Secondly, the *material* formulation will be considered: Here, both $\boldsymbol{B}$ and $\boldsymbol{D}$ are fully *populated*[7]. For $\boldsymbol{X} = \boldsymbol{B}^{\mathrm{T}}\,\boldsymbol{D}$ we have

$$n_X(p) = 2\,d \cdot 2\,d \cdot N(p) \cdot I(p)\,, \tag{3.84}$$

[7]For $\boldsymbol{D}$ compare with the corresponding tensor quantity as stated in equation (2.49).

and for $\boldsymbol{Y} = \boldsymbol{X}\,\boldsymbol{B}$

$$n_Y(p) = 2\,d \cdot N(p) \cdot \frac{(N(p)+1)}{2} \cdot I(p)\,, \tag{3.85}$$

resulting in

$$n_{B^{\mathrm{T}}DB}(p) = n_X(p) + n_Y(p) \tag{3.86}$$

multiplications.

The estimated reduction of floating point multiplications thanks to $\boldsymbol{b}^{\mathrm{T}}\,\boldsymbol{d}\,\boldsymbol{b}$ can be measured by

$$E^{\mathrm{theo}}_{b^{\mathrm{T}}db} = 100 \cdot \frac{(n_{B^{\mathrm{T}}DB} - n_{b^{\mathrm{T}}db})}{n_{B^{\mathrm{T}}DB}}\,. \tag{3.87}$$

As stated above, the effort for the product $\boldsymbol{g}^{\mathrm{T}}\,\hat{\boldsymbol{\sigma}}\,\boldsymbol{g}$ and $\boldsymbol{G}^{\mathrm{T}}\,\hat{\boldsymbol{S}}\,\boldsymbol{G}$ is similar and thus the number of multiplications, avoiding zero entries and exploiting symmetry, is

$$n_{g^{\mathrm{T}}\hat{\sigma}\,g}(p) \;=\; n_{G^{\mathrm{T}}\hat{S}\,G}(p) = d \cdot N(p) \cdot I(p) + d \cdot N(p) \cdot \frac{(\frac{N(p)}{d}+1)}{2} \cdot I(p)\,. \tag{3.88}$$

A comprehensive survey has to take into account the effort for providing the matrices $\boldsymbol{b}$, $\boldsymbol{g}$ and $\boldsymbol{B}$, $\boldsymbol{G}$, respectively. This effort will be investigated separately for both formulations. For the *material* formulation the evaluation of shape functions and the filling of $\boldsymbol{b}$ requires

$$n_b(p) = d \cdot N(p) \cdot p^2 \cdot I(p)\,, \tag{3.89}$$

and for $\boldsymbol{B}$

$$n_B(p) = 2\,d \cdot N(p) \cdot p^2 \cdot I(p)\,. \tag{3.90}$$

We observe that the *spatial* formulation only requires half of the effort, when comparing (3.89) with (3.90). For $\boldsymbol{g}$ and $\boldsymbol{G}$ respectively, the only thing that has to be taken into account is the filling of the corresponding matrices, because the corresponding shape functions have already been computed. Knowing that $\boldsymbol{g}$ and $\boldsymbol{G}$ have the same structure we can define

$$n_g(p) \;=\; n_G(p) = d \cdot N(p) \cdot I(p)\,. \tag{3.91}$$

The overall number of multiplications for the computation of the tangential stiffness matrices is

$$n_{k_T}(p) \;=\; n_{b^{\mathrm{T}}db}(p) + n_b(p) + n_{g^{\mathrm{T}}\hat{\sigma}g}(p) + n_g(p)\,, \tag{3.92}$$

$$n_{K_T}(p) \;=\; n_{B^{\mathrm{T}}DB}(p) + n_B(p) + n_{G^{\mathrm{T}}\hat{S}G}(p) + n_G(p)\,, \tag{3.93}$$

and the estimated overall reduction of floating point multiplications is defined analogously to (3.87) as

$$E^{\mathrm{theo}}_{k_T} = 100 \cdot \frac{(n_{K_T} - n_{k_T})}{n_{K_T}}\,. \tag{3.94}$$

3.5.2 Numerical example

In order to verify the estimation for the *tensor product space*, an inhomogeneous three-dimensional hyperelastic compression test as shown in Figure 3.17 is performed [81].

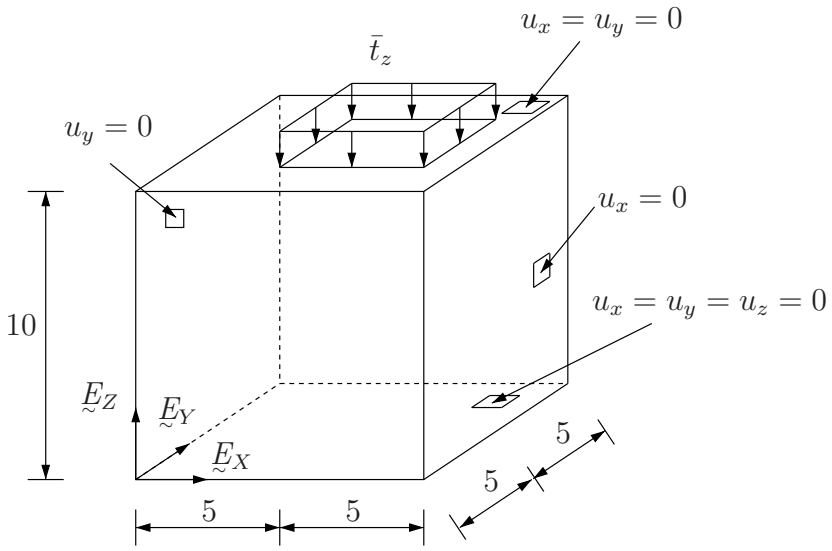

Figure 3.17: Inhomogeneous compression test: geometry and boundary conditions

The material parameters in (2.47) are $\mu = 80.194$ MPa and $\Lambda = 400889$ MPa. The face load is applied incrementally until it reaches a magnitude of $\bar{t}_z = 100$ MPa. We discretize the ge-

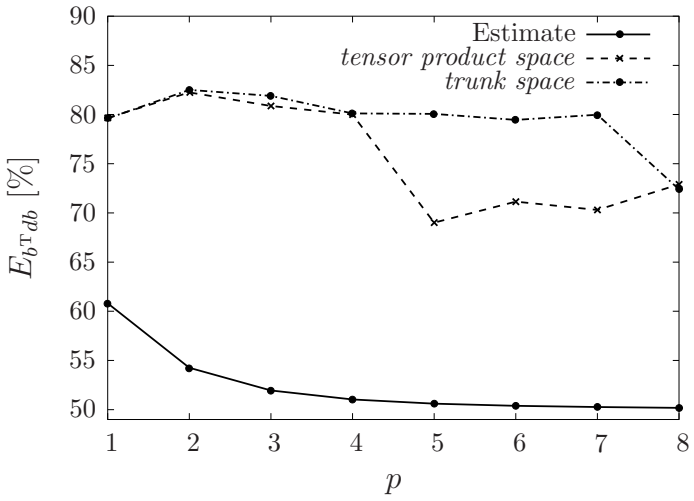

Figure 3.18: Relative reduction in multiplications due to $\boldsymbol{b}^{\mathrm{T}}\,\boldsymbol{d}\,\boldsymbol{b}$: Estimation for the *tensor product space* and numerical experiment

ometry depicted in Figure 3.17 by 108 isotropic hexahedral elements and apply both the *trunk space* and the *tensor product space*. In Figure 3.18 the estimated and the measured relative

reduction $E_{b^{\mathrm{T}}db}$ thanks to the application of $\boldsymbol{b}^{\mathrm{T}}\,\boldsymbol{d}\,\boldsymbol{b}$ instead of $\boldsymbol{B}^{\mathrm{T}}\,\boldsymbol{D}\,\boldsymbol{B}$ is plotted against the polynomial degrees $p = 1, \ldots, 8$. Note that the comparison of the numerical experiment with the estimation is based on the reduction in computation time, assuming a linear relationship between the number of multiplications and the computation time. The estimation $E^{\mathrm{theo}}_{b^{\mathrm{T}}db}$ tends to 50%, which simply stems from the fact that only half of the entries in the *spatial* matrices are non-zero whereas the *material* matrices are fully populated. The measured value shows a higher reduction for both Ansatz spaces. This discrepancy can be explained by the fact that the estimation does not account for the hardware. The loss of efficiency for the *tensor product space* from $p = 5$ and from $p = 8$ for the *trunk space* on stems from the very large size of the matrices, which no longer fit into the cache of the utilized computer (AMD Opteron 2.4 GHz, 4GB RAM, Cache 1MB, Linux) anymore. Figure 3.19 depicts the overall reduction E_{k_T}, taking into account all steps in generating the tangential stiffness matrix. Compared to

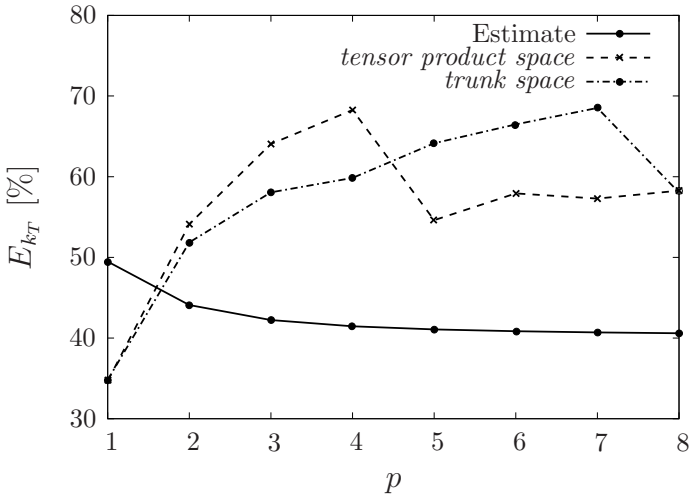

Figure 3.19: Reduction due to the *spatial* formulation: Estimation for the *tensor product space* and numerical experiment

Figure 3.18 where only $\boldsymbol{b}^{\mathrm{T}}\,\boldsymbol{d}\,\boldsymbol{b}$ was considered, a lower threshold is obtained for $E^{\mathrm{theo}}_{k_T}$. This originates from that computational part which is not influenced by the spatial formulation, namely the multiplications in $\boldsymbol{g}^{\mathrm{T}}\,\hat{\boldsymbol{\sigma}}\,\boldsymbol{g}$ and $\boldsymbol{G}^{\mathrm{T}}\,\hat{\boldsymbol{S}}\,\boldsymbol{G}$ and the computations of shape functions. Fortunately, both the estimation and the numerical experiment indicate that this part is small and therefore its influence on the element stiffness matrix is low.

3.6 The Finite Cell Method

This section explains the basic concepts of the Finite Cell Method (FCM) as far as they are essential within the context of numerical homogenization. The presentation closely follows the work of [24, 80], where the reader can find more information.

3.6.1 Basic concepts

The FCM can be interpreted as a combination of a fictitious or embedding domain approach with high-order Finite Element Methods. It therefore combines the fast, simple generation of meshes with high convergence rates. The main idea is to embed the original or physical domain Ω into a geometrically larger domain Ω_{em} of a simpler shape. This is shown in Figure 3.20 where DIRICHLET and NEUMANN boundary conditions are indicated for completeness, but will not be discussed further. For the discretization of the embedded domain an indicator

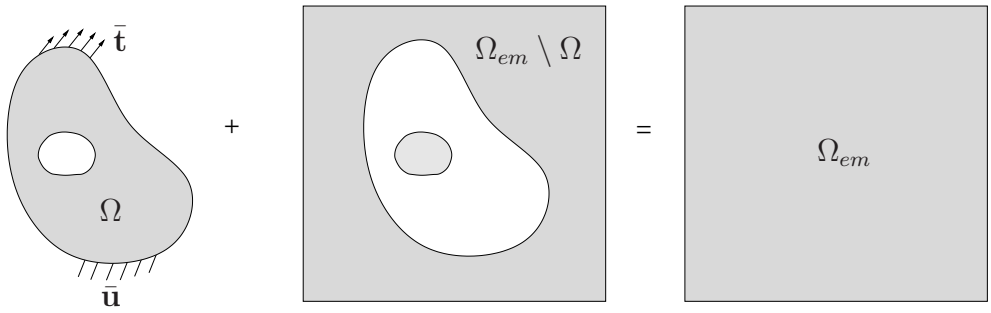

Figure 3.20: The domain Ω is embedded in Ω_{em}

function

$$\alpha(\mathbf{X}) \;=\; \begin{cases} 1.0 & \forall\, \mathbf{X} \in \Omega \\ 0.0 & \forall\, \mathbf{X} \in \Omega_{em} \setminus \Omega \end{cases} \tag{3.95}$$

is introduced. This indicator function allows for a mesh which is independent of the original domain, i.e. the elements of the embedding domain do not necessarily fulfill the usual geometric properties of elements for the original domain Ω, as they may be intersected by $\partial\Omega$. To distinguish them from classical elements they will be called *finite cells*. It is simpler and more advantageous to initially assume cells to be rectangular hexahedrals (cuboids) resulting in a constant JACOBIAN matrix, see Equation (3.15), of the cell-wise mapping. Figure 3.21 illustrates the situation for a two-dimensional setting, where cells lying completely outside the physical domain (i.e. $\alpha = 0.0$) have been omitted. The union of all n_c cells forms the embedding domain

$$\Omega_{em} \;=\; \bigcup_{c=1}^{n_c} \Omega_c \,, \tag{3.96}$$

where Ω_c is the domain represented by a cell. For the computation of a cell's stiffness matrices, the indicator function $\alpha(\boldsymbol{X})$ is again crucial. We simply insert α into (3.40) and (3.42)

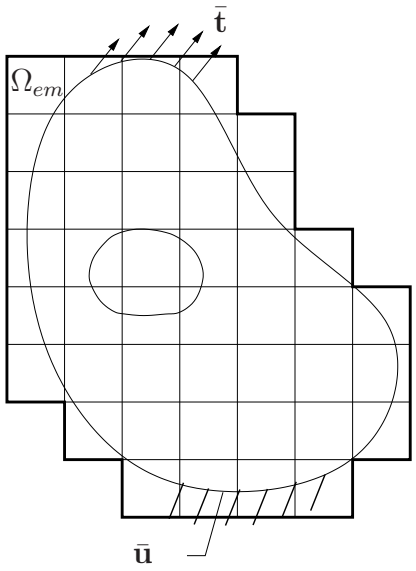

Figure 3.21: The embedding domain Ω_{em} is discretized using rectangular cells

respectively and obtain

$$\boldsymbol{K}_{c_{IK}} = \int_{\Omega_c} \left(\boldsymbol{B}_{c_I}^{\mathrm{T}} \, \alpha(\boldsymbol{X}) \, \boldsymbol{D} \, \boldsymbol{B}_{c_K} \right) \mathrm{d}\Omega_c \,. \tag{3.97}$$

In a practical implementation (3.97) is integrated by a GAUSSIAN quadrature, see section 3.2.2. Here, two cases have to be taken into account:

- For cells which are completely filled with homogeneous material, the numerical integration is exact due to the constant JACOBIAN matrix.
- For cells which are cut by $\partial\Omega$ a composed integration is necessary due to the discontinuous integrand. To this end, a cell is subdivided into n_{sc} block-shaped sub-cells, equipped with an rst-coordinate system, see Figure 3.22.

Note that with a proper integration scheme and depending on the type of problem, the FCM can yield an exponential rate of convergence, if a p-extension is performed.

3.6.2 Grid generation for the FCM

The main advantage of the FCM and embedding or fictitious domain methods in general is their extremely fast and simple grid generation. Since the CARTESIAN grids applied in the analysis do not need to be aligned to curved boundaries, the meshing process is straightforward. A structured mesh with a resolution of $n_x \times n_y \times n_z$ cells in the x, y and z-direction is created and cells which are completely outside the domain Ω are disregarded. It is therefore evident that FCM is especially well suited to problems where the original definition of the computational domain is based on voxel models, like those obtained from a CT-scan, for example from an open-cell foam as shown in section 4.3.2. When using standard Finite Element Methods, major difficulties arise in the creation of the geometrical model required for the process of

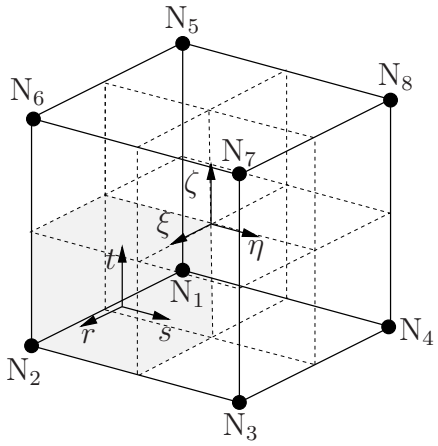

Figure 3.22: Composed integration of hexahedral elements based on sub-cells [24]

mesh generation. Our approach, which is based on the Finite Cell Method, has the important advantage that the voxel model obtained from a CT-scan can be used as an immediate basis for the computation, without the necessity of segmentation.

Chapter 4

Numerical homogenization

In this chapter we will cover both two- and three-dimensional multiscale analysis. In two dimensions, first- and higher-order homogenization methods will be presented, whereby in the first-order analysis large deformations are included. The higher-order homogenization methods are restricted to small strains. Here, non-homogeneous DIRICHLET boundary conditions suited for p-FEM play an important role and are discussed in detail. In three dimensions a first-order scheme designed for small deformations will be developed whereby the focus lies on the extraction of effective material properties from real-world cellular materials via CT-scans and FCM. Note that the notation of section 2.2 is adopted, i.e. M indicates macroscopic quantities, and m is used for microscopic quantities.

4.1 Introduction

In section 1.2 the FE^2 method was introduced. It allows for the coupling of different scales, i.e. quantities are transferred from the macro- to the microlevel and vice versa. There are FE^2 methods of first- and higher-order. In first-order FE^2 scheme the macroscale is assumed to be much larger than the microscale and no microstructural length information like for example, the cell's height, has to be transported. Therefore, classical continua are sufficient on both scales. Size effects are excluded within such schemes but deformation-induced anisotropy under large deformations can be modeled [88].

Higher-order FE^2 methods are based on extended continua at least on the macroscale and offer the possibility of transporting microstructural length information. They have been successfully applied to investigating boundary layer dependent size effects within cellular materials [28, 36, 37, 38, 63, 67].

Now, let us go into more detail and illuminate how the coupling of scales is performed: At each macroscopic integration point a microstructure is attached, and the (constant) macroscopic deformation-like quantities are projected onto the microstructure's boundary leading to a DIRICHLET BVP_m. After solving the BVP_m, homogenized stress-like quantities are transferred back to the macroscale. The resulting nested BVP is sketched for the two-dimensional case in Figure 4.1.

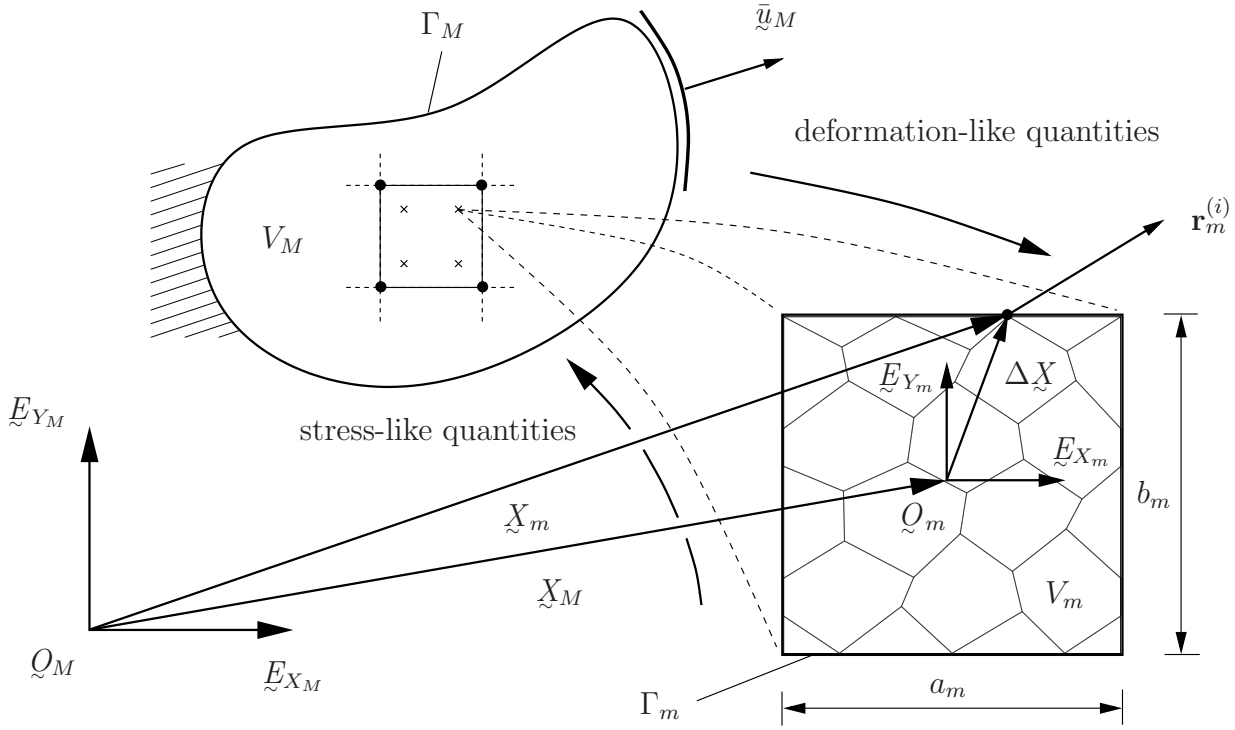

Figure 4.1: Nested boundary value problem in the reference configuration

4.2 Two-dimensional multiscale analysis

Note that this section is strongly guided by [62] and the literature cited therein where more information and especially microstructural interpretations can be found.

4.2.1 FE^2 method of first-order

In this section we summarize the FE^2 method of first-order including large deformations, compare with Feyel and Chaboche [35] and Kouznetsova [67]. The summary includes projection and homogenization rules and some ideas for an efficient implementation.

4.2.1.1 Projection

Referring to Figure 4.1, the attached microstructure assuming unit thickness $t_m = 1$ is a rectangle with dimensions a_m and b_m and volume $V_m = t_m \cdot a_m \cdot b_m$. The center of the microstructure is located at position $\underset{\sim}{X}_M$, and $\Delta\underset{\sim}{X}$ is called the branch vector. Now, let us investigate the relation between the microscopic and the macroscopic displacement field. We have to minimize the difference between both fields

$$\mathcal{F}(\underset{\sim}{u}_M) \;=\; \langle(\underset{\sim}{u}_m - \underset{\sim}{u}_M)^2\rangle \rightarrow \min\,, \tag{4.1}$$

where the volume average is based on an averaging theorem as stated in [67] and [75]

$$\langle\cdot\rangle \;=\; \frac{1}{V_m}\int_{V_m}(\cdot)\,\mathrm{d}V_m\,. \tag{4.2}$$

The minimization of (4.1) is carried out by evaluating

$$\frac{\partial \mathcal{F}}{\partial \underset{\sim}{u}_M} = \underset{\sim}{0} \tag{4.3}$$

and results in

$$\langle \underset{\sim}{u}_m - \underset{\sim}{u}_M \rangle = \underset{\sim}{0} \,. \tag{4.4}$$

With $\Delta \underset{\sim}{u} = \underset{\sim}{u}_m - \underset{\sim}{u}_M$ we can rewrite (4.4) yielding

$$\langle \Delta \underset{\sim}{u} \rangle = \langle \underset{\sim}{u}_m - \underset{\sim}{u}_M \rangle = \underset{\sim}{0} \,, \tag{4.5}$$

which means that beside a rigid body motion due to $\underset{\sim}{u}_M$ the average of the microscopic displacement field vanishes. Furthermore, one may define

$$\operatorname{Grad} \underset{\sim}{u}_M = \langle \operatorname{Grad} \underset{\sim}{u}_m \rangle \,, \tag{4.6}$$

compare with [67]. In order to establish a projection rule we assume the microscopic displacement field to be a polynomial of degree one

$$\Delta \bar{\underset{\sim}{u}} = \underset{\sim}{A}_M(\underset{\sim}{X}_M, t) + \underset{\sim}{B}_M(\underset{\sim}{X}_M, t) \Delta \underset{\sim}{X} + \underset{\sim}{v} \,, \tag{4.7}$$

where $\bar{(\cdot)}$ emphasizes the fact that the projection rule will lead to a DIRICHLET boundary value problem. In (4.7) $\underset{\sim}{v}$ represents possible periodic fluctuations of the microscopic displacement field. These fluctuations are associated with *periodic boundary conditions* and can be regarded as a relaxation of the DIRICHLET boundary value problem. Note that in this thesis alternative concepts are proposed and applied respectively and thus we assume $\underset{\sim}{v} = \underset{\sim}{0}$ [1]. The coefficient tensors $\underset{\sim}{A}_M$ and $\underset{\sim}{B}_M$ only depend on $\underset{\sim}{X}_M$ and t, and therefore are constant on V_m. In order to express the coefficient tensors in terms of macroscopic quantities we insert (4.7) into (4.5) and (4.6) and solve the resulting system of equations. We then obtain

$$\begin{aligned} \underset{\sim}{A}_M &= \underset{\sim}{0} \\ \underset{\sim}{B}_M &= \operatorname{Grad} \underset{\sim}{u}_M \,, \end{aligned}$$

where $\underset{\sim}{A}_M = \underset{\sim}{0}$ means that rigid body modes are excluded. Finally, the projection rule emerges as

$$\Delta \bar{\underset{\sim}{u}} = \operatorname{Grad} \underset{\sim}{u}_M \, \Delta \underset{\sim}{X} \,. \tag{4.8}$$

4.2.1.2 Homogenization

In order to derive a homogenization rule we have to evaluate the HILL-MANDEL condition which demands the equivalence of the strain energy rate in the macroscopic material point and the volume average of the microscopic strain energy rate of the attached microstructure [52, 53]. In the reference configuration the HILL-MANDEL condition reads

$$\langle \underset{\sim}{P}_m \cdot (\operatorname{Grad} \Delta \bar{\underset{\sim}{u}})' \rangle = \underset{\sim}{P}_M \cdot (\operatorname{Grad} \underset{\sim}{u}_M)' \tag{4.9}$$

[1] In [67] the reader can find more information on *periodic boundary conditions*.

where

$$(\cdot)' = \frac{\mathrm{d}(\cdot)}{\mathrm{d}t} = \frac{\partial(\cdot)}{\partial t} + \operatorname{grad}(\cdot)\,\underset{\sim}{x}' \tag{4.10}$$

is the material time derivative.

Firstly, we rewrite the left-hand side of (4.9) by inserting the balance of moment (2.29) (neglecting volume forces) and applying the divergence theorem

$$\begin{aligned}
\langle \underset{\sim}{\mathrm{P}}_m \cdot (\operatorname{Grad} \Delta\bar{\underset{\sim}{u}})' \rangle &= \frac{1}{V_m} \int_{V_m} \underset{\sim}{\mathrm{P}}_m \cdot (\operatorname{Grad} \Delta\bar{\underset{\sim}{u}})' \,\mathrm{d}V_m \\
&= \frac{1}{V_m} \int_{V_m} \left(\operatorname{Div} (\underset{\sim}{\mathrm{P}}_m^{\mathrm{T}} (\Delta\bar{\underset{\sim}{u}})') - (\Delta\bar{\underset{\sim}{u}})' \cdot \underbrace{\operatorname{Div} \underset{\sim}{\mathrm{P}}_m}_{=\rho_0 \underset{\sim}{f} = \underset{\sim}{0}} \right) \mathrm{d}V_m \\
&= \frac{1}{V_m} \int_{V_m} \operatorname{Div} (\underset{\sim}{\mathrm{P}}_m^{\mathrm{T}} (\Delta\bar{\underset{\sim}{u}})') \,\mathrm{d}V_m \\
&= \frac{1}{V_m} \int_{\Gamma_m} \underset{\sim}{p}_m \cdot (\Delta\bar{\underset{\sim}{u}})' \,\mathrm{d}\Gamma_m \,,
\end{aligned} \tag{4.11}$$

whereby

$$\operatorname{Div}(\underset{\sim}{\mathrm{A}}^{\mathrm{T}}\, \underset{\sim}{b}) = \underset{\sim}{\mathrm{A}} \cdot \operatorname{Grad} \underset{\sim}{b} + \underset{\sim}{b} \cdot \operatorname{Div} \underset{\sim}{\mathrm{A}}$$

has been applied. Note that in (4.11) $\underset{\sim}{p}_m = \underset{\sim}{\mathrm{P}}_m\, \underset{\sim}{N}_m$ is the first Piola-Kirchhoff stress vector as stated in equation (2.28).

Secondly, the time derivative of (4.8)

$$(\Delta\bar{\underset{\sim}{u}})' = (\operatorname{Grad} \underset{\sim}{u}_M\, \Delta\underset{\sim}{X})' = (\operatorname{Grad} \underset{\sim}{u}_M)'\, \Delta\underset{\sim}{X} \tag{4.12}$$

is inserted into (4.11)

$$\begin{aligned}
\langle \underset{\sim}{\mathrm{P}}_m \cdot (\operatorname{Grad} \Delta\bar{\underset{\sim}{u}})' \rangle &= \frac{1}{V_m} \int_{\Gamma_m} (\underset{\sim}{p}_m \cdot (\operatorname{Grad} \underset{\sim}{u}_M)'\, \Delta\underset{\sim}{X}) \,\mathrm{d}\Gamma_m \\
&= \frac{1}{V_m} \int_{\Gamma_m} (\underset{\sim}{p}_m \otimes \Delta\underset{\sim}{X}) \,\mathrm{d}\Gamma_m \cdot (\operatorname{Grad} \underset{\sim}{u}_M)' \\
&= \langle \underset{\sim}{\mathrm{P}}_m \rangle \cdot (\operatorname{Grad} \underset{\sim}{u}_M)' = \underset{\sim}{\mathrm{P}}_M \cdot (\operatorname{Grad} \underset{\sim}{u}_M)'
\end{aligned} \tag{4.13}$$

allowing the identification of the homogenization rule. The integration of (4.13) can be simplified when using discrete quantities at the nodes, see Figure 4.1, of the microscopic finite element discretization

$$\langle \mathbf{P}_m \rangle = \frac{1}{V_m} \sum_{i=1}^{n} \mathbf{r}_m^{(i)} \otimes \Delta\mathbf{X}^{(i)} \,. \tag{4.14}$$

To this end the sum of the dyadic product of the nodal forces $\mathbf{r}_m^{(i)}$, compare with equation (3.24) and the branch vector for all boundary nodes ($i = 1, \ldots, n$) is evaluated. In order to obtain the CAUCHY stresses from (4.14) we perform a push forward (compare with Table 2.1)

$$\boldsymbol{\sigma}_M = \frac{1}{J_M} \langle \mathbf{P}_m \rangle \, \mathbf{F}_M^{\mathrm{T}} \,. \tag{4.15}$$

4.2.1.3 Implementation aspects

We want to give some remarks regarding practical implementation. Due to the *MMM-principle* we have k independent microscopic BVP$_m$s and hence the FE^2 approach is perfectly parallelizable. This is illustrated in Figure 4.2. Within the nonlinear BVP$_M$ the Master program

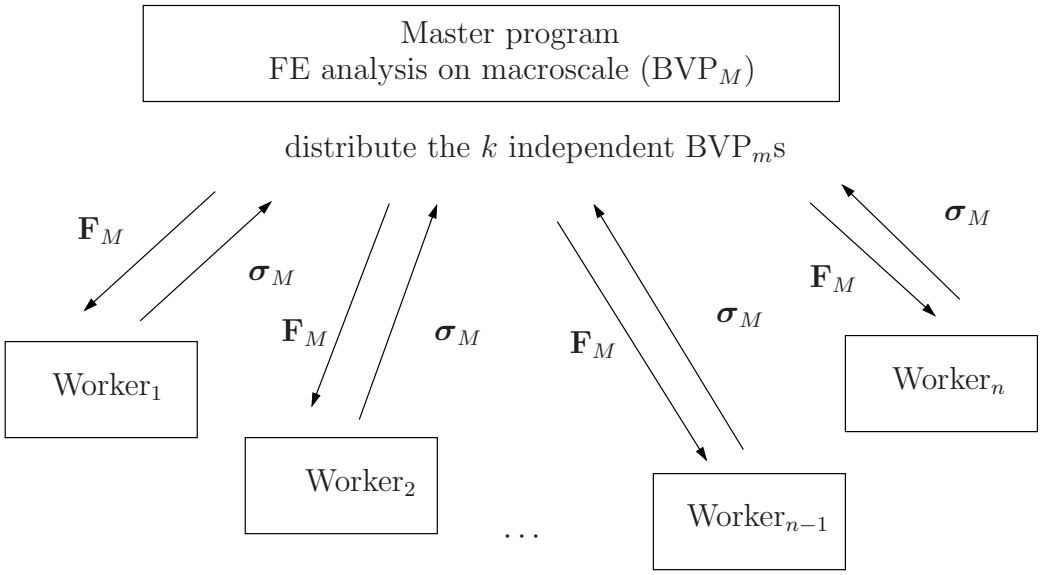

Figure 4.2: Distributed computing of microscopic BVP$_m$s

distributes in each step of the iterative solution procedure the k independent BVP$_m$s to the Workers, obtains the homogenized stresses $\boldsymbol{\sigma}_M$ and solves the macroscopic equation system. The Master program is based on a *discrete* NEWTON-RAPHSON algorithm (i.e. applying a numerical tangent) as mentioned at the end of section 3.3. Note that this algorithm is sufficient for our purpose since we are only dealing with geometric nonlinearities, for including material nonlinearities like viscosity or damage suitable algorithms are described in works of MIEHE, e.g. [72]. On the microlevel (i.e. the Workers) a hyperelastic high-order finite element formulation as described in chapter 3 is applied. The different BVP$_m$s are solved by a NEWTON-RAPHSON scheme on a *Linux* cluster.

4.2.2 FE^2 method of higher-order

As stated above, boundary layer dependent size effects are present in cellular materials. In order to account for these effects higher-order FE^2 methods are required, compare with section 1.2. The higher-order projection and homogenization scheme applied within this thesis has

already been derived for micromorphic continua in [62]. It is briefly reviewed and then adapted to the *p*-version. For the adaption an efficient treatment of non-homogeneous DIRICHLET boundary conditions, which arise within the microscopic BVP$_m$s, has been developed and implemented.

4.2.2.1 Projection

Similar to section 4.2.1.1 we have to introduce a functional

$$\mathcal{F}(\underset{\sim}{u}_M, \bar{\underset{\sim}{\chi}}_M) = \langle \Big\{ \underset{\sim}{u}_m - \Big(\underset{\sim}{u}_M + (\bar{\underset{\sim}{\chi}}_M - \underset{\sim}{\mathrm{I}})\, \Delta\underset{\sim}{X} \Big) \Big\}^2 \rangle \to \min , \tag{4.16}$$

where the macroscopic displacement field $\underset{\sim}{u}_M + (\bar{\underset{\sim}{\chi}}_M - \underset{\sim}{\mathrm{I}})\, \Delta\underset{\sim}{X}$ refers to the micromorphic theory of grade *one*. Minimization of (4.16)

$$\mathrm{d}\,\mathcal{F} = \underbrace{\frac{\partial \mathcal{F}}{\partial \underset{\sim}{u}_M}}_{=\underset{\sim}{0}} \cdot \mathrm{d}\underset{\sim}{u}_M + \underbrace{\frac{\partial \mathcal{F}}{\partial \bar{\underset{\sim}{\chi}}_M}}_{=\underset{\sim}{0}} \cdot \mathrm{d}\bar{\underset{\sim}{\chi}}_M = 0 \tag{4.17}$$

yields

$$\frac{\partial \mathcal{F}}{\partial \underset{\sim}{u}_M} = 0 : \qquad \langle \Delta\underset{\sim}{u} \rangle = \underset{\sim}{0} , \tag{4.18}$$

$$\frac{\partial \mathcal{F}}{\partial \bar{\underset{\sim}{\chi}}_M} = 0 : \qquad \bar{\underset{\sim}{\chi}}_M - \underset{\sim}{\mathrm{I}} = \langle \Delta\underset{\sim}{u} \otimes \Delta\underset{\sim}{X} \rangle\, \underset{\sim}{\mathrm{G}}_m^{-1} . \tag{4.19}$$

Note that (4.18) corresponds to (4.5) of the first-order case. In (4.19)

$$\underset{\sim}{\mathrm{G}}_m = \langle \Delta\underset{\sim}{X} \otimes \Delta\underset{\sim}{X} \rangle \tag{4.20}$$

is the geometry tensor depending on the microstructure's shape. Particularizing to the rectangular case, see Figure 4.1, the components of $\underset{\sim}{\mathrm{G}}_m$ are

$$[\underset{\sim}{\mathrm{G}}_m] = \frac{1}{12} \begin{bmatrix} a_m^2 & 0 \\ 0 & b_m^2 \end{bmatrix} . \tag{4.21}$$

For the microscopic displacement field we assume

$$\begin{aligned} \Delta\bar{\underset{\sim}{u}} = {} & \underset{\sim}{A}_M(\underset{\sim}{X}_M, t) + \underset{\sim}{\mathrm{B}}_M(\underset{\sim}{X}_M, t)\Delta\underset{\sim}{X} + \frac{1}{2}\, \overset{3}{\underset{\sim}{\mathrm{C}}}_M(\underset{\sim}{X}_M, t)(\Delta\underset{\sim}{X} \otimes \Delta\underset{\sim}{X}) \\ & + \frac{1}{6}\, \overset{4}{\underset{\sim}{\mathrm{D}}}_M(\underset{\sim}{X}_M, t)(\Delta\underset{\sim}{X} \otimes \Delta\underset{\sim}{X} \otimes \Delta\underset{\sim}{X}) , \end{aligned} \tag{4.22}$$

which is polynomial of degree three. Note that due to the extended kinematics and deformation quantities a polynomial of degree three is required. Similar to section 4.2.1.1, the coefficient tensors can be expressed in terms of macroscopic quantities

$$\underset{\sim}{A}_M = -\frac{1}{2}\, \mathrm{Grad}\, \bar{\underset{\sim}{\chi}}_M\, \underset{\sim}{\mathrm{G}}_m \tag{4.23}$$

$$\underset{\sim}{\mathrm{B}}_M = \frac{1}{2} \Big(5\, (\bar{\underset{\sim}{\chi}}_M - \underset{\sim}{\mathrm{I}}) - 3\, \mathrm{Grad}\, \underset{\sim}{u}_M \Big) \tag{4.24}$$

$$\overset{3}{\underset{\sim}{\mathrm{C}}}_M = \mathrm{Grad}\, \bar{\underset{\sim}{\chi}}_M \tag{4.25}$$

$$\overset{4}{\underset{\sim}{\mathrm{D}}}_M = 5 \Big((\bar{\underset{\sim}{\chi}}_M - \underset{\sim}{\mathrm{I}}) - \mathrm{Grad}\, \underset{\sim}{u}_M \Big)\, \overset{4}{\underset{\sim}{\mathrm{I}}}\, \underset{\sim}{\mathrm{G}}_m^{-1} . \tag{4.26}$$

Again, rigid body modes are excluded, and we set $\underset{\sim}{A}_M = \underset{\sim}{0}$. Inserting equations (4.24) to (4.26) into (4.22) gives the complete projection rule

$$\begin{aligned}\Delta\bar{\underset{\sim}{u}} &= \frac{1}{2}\left((5(\bar{\underset{\sim}{\chi}}_M - \underset{\sim}{\mathrm{I}}) - 3\,\mathrm{Grad}\,\underset{\sim}{u}_M)\,\Delta\underset{\sim}{X} + \mathrm{Grad}\,\bar{\underset{\sim}{\chi}}_M(\Delta\underset{\sim}{X}\otimes\Delta\underset{\sim}{X})\right) \\ &\quad -\frac{5}{6}\left(\left\{(\bar{\underset{\sim}{\chi}}_M - \underset{\sim}{\mathrm{I}}) - \mathrm{Grad}\,\underset{\sim}{u}_M\right\}\overset{4}{\underset{\sim}{\mathrm{I}}}\,\underset{\sim}{\mathrm{G}}_m^{-1}\right)(\Delta\underset{\sim}{X}\otimes\Delta\underset{\sim}{X}\otimes\Delta\underset{\sim}{X})\,.\end{aligned} \tag{4.27}$$

The consistency of the extended projection rule (4.27) with the one of the first-order projection rule, see (4.8), is shown in [62]. Let us briefly illustrate the idea: Firstly, we set the extended quantities in (4.27) to zero. Then the remaining higher-order projection rule and the first-order rule (4.8) are evaluated at the boundaries and, as expected, lead to the same results.

In component form (4.27) reads

$$\begin{aligned}\Delta\bar{u}_x &= \frac{1}{2}\left((5\,(\bar{\chi}_{xx_M} - 1) - 3\,u_{x,X_M})\Delta X + 5\,(\bar{\chi}_{xy_M} - 3\,u_{x,Y_M})\Delta Y\right. \\ &\quad + \bar{\chi}_{xx,X_M}\,(\Delta X)^2 + 2\,\bar{\chi}_{xy,X_M}\,\Delta X\,\Delta Y + \bar{\chi}_{xy,Y_M}\,(\Delta Y)^2\big) \\ &\quad -\left(\frac{10}{a_m\cdot a_m}\,(\bar{\chi}_{xx_M} - 1 - u_{x,X_M})(\Delta X)^3 + \frac{10}{b_m\cdot b_m}\,(\bar{\chi}_{xy_M} - u_{x,Y_M})(\Delta Y)^3\right)\end{aligned} \tag{4.28}$$

and

$$\begin{aligned}\Delta\bar{u}_y &= \frac{1}{2}\left((5\,(\bar{\chi}_{yx_M} - 1) - 3\,u_{y,X_M})\Delta X + 5\,(\bar{\chi}_{yy_M} - 3\,u_{y,Y_M})\Delta Y\right. \\ &\quad + \bar{\chi}_{yx,X_M}\,(\Delta X)^2 + 2\,\bar{\chi}_{yx,Y_M}\,\Delta X\,\Delta Y + \bar{\chi}_{yy,Y_M}\,(\Delta Y)^2\big) \\ &\quad -\left(\frac{10}{a_m\cdot a_m}\,(\bar{\chi}_{yx_M} - u_{y,X_M})(\Delta X)^3 + \frac{10}{b_m\cdot b_m}\,(\bar{\chi}_{yy_M} - 1 - u_{y,Y_M})(\Delta Y)^3\right)\,.\end{aligned} \tag{4.29}$$

In Figure 4.6 and 4.7 a deformation mode, where all strain-like quantities except for u_{y,X_M} are zero, is shown. For additional modes and further discussions please refer to [62, 64].

4.2.2.2 Dirichlet boundary conditions for p-FEM

The projection of the extended deformation modes defines a nonhomogeneous BVP_m in the reference configuration with a prescribed polynomial displacement field $\Delta\bar{\underset{\sim}{u}}(\Delta\underset{\sim}{X})$ up to order three as presented in section 4.2.2.1. In the p-version elements are larger than in the classical h-version. Therefore, we face two problems with our p-elements: The linear nodal modes which interpolate the nodal values are not sufficient for an accurate representation of $\Delta\bar{\underset{\sim}{u}}(\Delta\underset{\sim}{X})$ and the hierarchic edge modes are non-interpolatory and can therefore not be directly applied to impose the Dirichlet boundary conditions defined at the edge of a two-dimensional p-finite element. In order to resolve this problem, in a first step we interpolate $\bar{\underset{\sim}{u}}(\Delta\underset{\sim}{X})$ by means of Lagrangian nodal shape functions applying the non-equidistant collocation points proposed by Babuška and Chen [14], compare with table A.1. In a second step we perform a projection of the interpolatory polynomial into the set of hierarchic shape functions utilized by the p-finite elements.

In the following we will show the details of this approach: For the ease of notation we consider just one component of the prescribed CARTESIAN displacement vector[2], denoted by $\Delta\bar{u}$. Since computational efficiency plays an important role in the FE^2-method, we take advantage of the fact that the edges of the p-elements, which are applied to discretize the microstructure, are parallel to the CARTESIAN coordinate system. To be more specific, let us consider the situation as depicted in Figure 4.3. A straight boundary edge of a p-element is parallel to

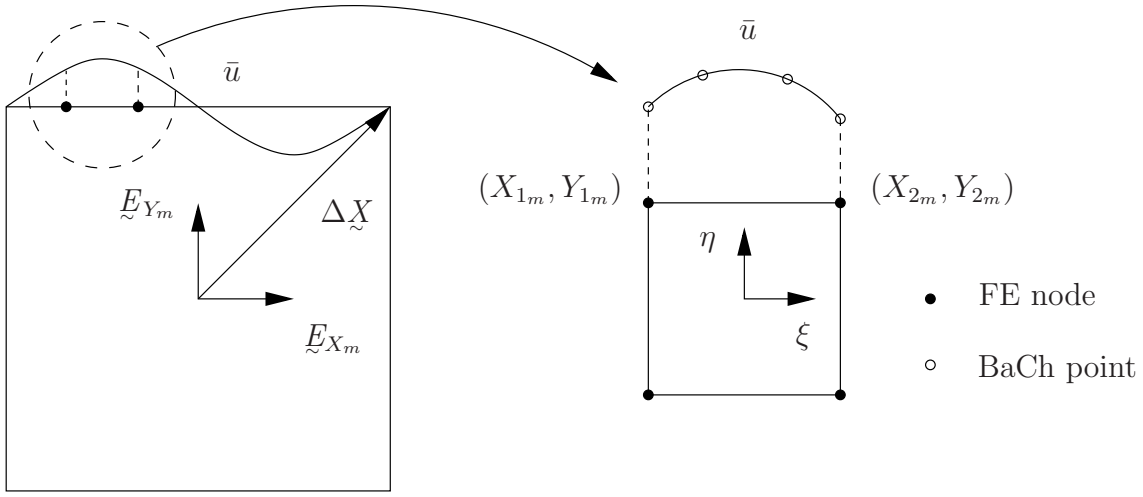

Figure 4.3: Discretized microstructure with one-dimensional prescribed displacement function $\Delta\bar{u}$ of degree $p = 3$

either $\underset{\sim}{E}_{X_m}$ or $\underset{\sim}{E}_{Y_m}$ and bounded by two nodes (X_{1_m}, Y_{1_m}) and (X_{2_m}, Y_{2_m}). Depending on the orientation of the element, the corresponding local coordinate of the element's edge is either ξ or η. Considering the element depicted in Figure 4.3, we have $Y_{1_m} = Y_{2_m}$ and the mapping function of the corresponding edge simplifies to

$$Y_m = Y_m \quad \rightarrow \quad X_m(\xi) = N_1(\xi)\, X_{m_1} + N_2(\xi)\, X_{m_2}$$

and we obtain a constant JACOBIAN

$$J \;=\; \frac{\mathrm{d}X_m}{\mathrm{d}\xi} = \frac{X_{m_2} - X_{m_1}}{2}\,. \tag{4.30}$$

The interpolation of $\bar{u}$ (where Δ has been omitted for the sake of simplicity) with $n^L = p^L + 1$ LAGRANGIAN polynomials of degree p^L reads

$$\bar{u}^L \;=\; \sum_{j=1}^{n^L} N_j^{(p^L)}(\xi)\, \bar{u}_j^L = \boldsymbol{N}^{(p^L)}\, \bar{\boldsymbol{u}}^L \quad \text{with} \quad \bar{u}_j^L = \bar{u}(\Delta\underset{\sim}{X}(\xi^{\mathrm{BaCh}})) \tag{4.31}$$

where ξ^{BaCh} denote the aforementioned collocation points. In order to obtain the corresponding representation in terms of the hierarchic shape functions N_i, a least-squares fit of the

[2]This is not a general restriction and is only made for simplifying the discussion. In the practical implementation $\Delta\underset{\sim}{\bar{u}}$ has the spatial dimension $d = 2$.

derivatives of the prescribed displacement functions is performed

$$\begin{aligned}
\mathcal{F} &= \frac{1}{2}\int_{X_{m_1}}^{X_{m_2}} \left(\frac{\mathrm{d}\bar{u}^N}{\mathrm{d}X} - \frac{\mathrm{d}\bar{u}^L}{\mathrm{d}X}\right)^2 \mathrm{d}X \qquad (4.32)\\
&= \frac{1}{2}\int_{-1}^{1} \left(\sum_{i=1}^{n^N} \frac{\mathrm{d}N_i}{\mathrm{d}\xi} J^{-1}\,\bar{u}_i^N - \sum_{j=1}^{n^L} \frac{\mathrm{d}N_j^{(p^L)}}{\mathrm{d}\xi} J^{-1}\,\bar{u}_j^L\right)^2 J\,\mathrm{d}\xi\\
&= \frac{1}{2}\int_{-1}^{1} \left(\sum_{i=1}^{n^N} \frac{\mathrm{d}N_i}{\mathrm{d}\xi} \bar{u}_i^N - \sum_{j=1}^{n^L} \frac{\mathrm{d}N_j^{(p^L)}}{\mathrm{d}\xi} \bar{u}_j^L\right)^2 \mathrm{d}\xi\, J^{-1} \;\to\; \min.
\end{aligned}$$

Note that $n^N = p^N + 1$ is the number of the hierarchic shape functions up to a polynomial degree of p^N, where $p^N \geq p^L$. Minimization of (4.32) yields a linear equation system

$$\begin{aligned}
\frac{\partial \mathcal{F}}{\partial \bar{u}_k^N} &= \int_{-1}^{1} \left(\frac{\mathrm{d}N_k}{\mathrm{d}\xi}\left(\sum_{i=1}^{n^N} \frac{\mathrm{d}N_i}{\mathrm{d}\xi}\bar{u}_i^N - \sum_{j=1}^{n^L} \frac{\mathrm{d}N_j^{(p^L)}}{\mathrm{d}\xi}\bar{u}_j^L\right)\right) \mathrm{d}\xi\, J^{-1} = 0 \qquad (4.33)\\
&\overset{k=1,\ldots,n^N}{\to} \int_{-1}^{1} \left(\left(\frac{\mathrm{d}\boldsymbol{N}}{\mathrm{d}\xi}\right)^{\mathrm{T}} \frac{\mathrm{d}\boldsymbol{N}}{\mathrm{d}\xi}\,\bar{\boldsymbol{u}}^N - \left(\frac{\mathrm{d}\boldsymbol{N}}{\mathrm{d}\xi}\right)^{\mathrm{T}} \frac{\mathrm{d}\boldsymbol{N}^{(p^L)}}{\mathrm{d}\xi}\,\bar{\boldsymbol{u}}^L\right) \mathrm{d}\xi\, J^{-1}\\
&= (\boldsymbol{K}\,\bar{\boldsymbol{u}}^N - \boldsymbol{A}\,\bar{\boldsymbol{u}}^L)\, J^{-1} = \boldsymbol{0}
\end{aligned}$$

with

$$\boldsymbol{K} = \begin{bmatrix}
\frac{1}{2} & -\frac{1}{2} & 0 & 0 & \ldots & 0\\
 & \frac{1}{2} & 0 & 0 & \ldots & 0\\
 & & 1 & 0 & \ldots & 0\\
 & & & 1 & \ldots & 0\\
 & & & & \ddots & \\
\text{sym} & & & & & 1
\end{bmatrix} \qquad \boldsymbol{A} = \begin{bmatrix}
\frac{1}{2} & -\frac{1}{2} & 0 & 0 & \ldots & 0\\
-\frac{1}{2} & \frac{1}{2} & 0 & 0 & \ldots & 0\\
A_{31} & A_{32} & A_{33} & A_{34} & \ldots & A_{3n^L}\\
A_{41} & A_{42} & A_{43} & A_{44} & \ldots & A_{4n^L}\\
 & & & & \ddots & \\
A_{n^N1} & A_{n^N2} & A_{n^N3} & A_{n^N4} & \ldots & A_{n^Nn^L}
\end{bmatrix}.$$

Now, the advantage of taking the derivatives of the displacement functions is obvious: Except for the first two rows / columns, $\boldsymbol{K}$ is only populated on the main diagonal, compare with equation (3.62). In addition, due to the fact that the nodal values can be determined directly, i.e. $\bar{u}_1^N = \bar{u}_1^L$ and $\bar{u}_2^N = \bar{u}_2^L$, only a matrix-vector multiplication $\boldsymbol{A}\,\bar{\boldsymbol{u}}^L$ has to be computed and no system of equations has to be solved.

4.2.2.2.1 Numerical example

Here, a macroscopic state of deformation

$$\underset{\sim}{\mathrm{F}}_M = \begin{bmatrix} 0+1 & 1.0 \\ 0 & 0+1 \end{bmatrix} \underset{\sim}{e}_{i_M} \otimes \underset{\sim}{E}_{I_M}$$

i.e. with $u_{x,Y_M} = 1.0$ is considered. Inserting this state into (4.28) results in a superposition of linear and cubic modes. These modes are then projected onto two quadratic homogeneous microstructures of identical size $(1 \times 1)\,mm$ but with different discretizations: Discretization 1 uses only one p-element while discretization 2 is based on 400 p-elements, see Figures 4.4 and 4.5 respectively. In both cases the *tensor product space* is applied. Furthermore, we assume linear elastic, isotropic behavior with YOUNG's modulus $E = 210\,GPa$ and POISSON's ratio $\nu = 0.3$. For a polynomial degree of $p = p^N = p^L = 3$, each discretization exactly represents

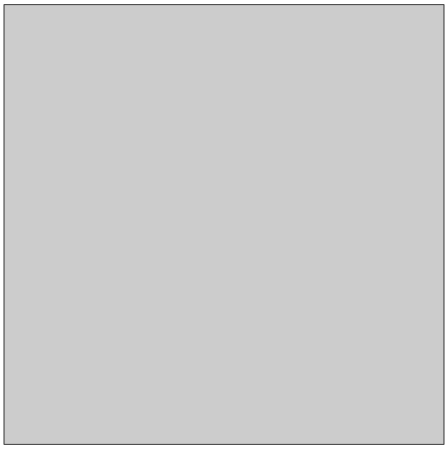

Figure 4.4: Discretization 1 using one p-element

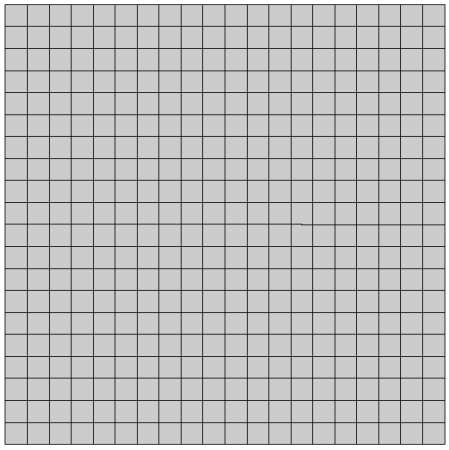

Figure 4.5: Discretization 2 using 400 p-elements

the boundary's deformation pattern, see Figures 4.6 and 4.7. However, the differences in the contourplots of the shear stresses[3] σ_{xy}, for which the same color scheme ($\sigma_{xy} \in (-55, 484)\,GPa$) has been used, indicate that a polynomial degree $p = 3$ for discretization 1 is too low, and a p-extension is suggested. In Figure 4.8 the relative error in the energy norm, compare with Equation (3.49), of discretization 1 is plotted against the number of degrees of freedom N in a double-logarithmic style. The reference value has been obtained by a p-extension with discretization 2. Due to singularities at the corners we only obtain an algebraic rate of convergence. Nevertheless, from $p = 5$ on, $\|\mathbf{e}\|_{E(\Omega)}$ is significantly below 1 %.

[3]The shear stresses were exemplarily chosen, i.e. all other strains/stresses differ, too.

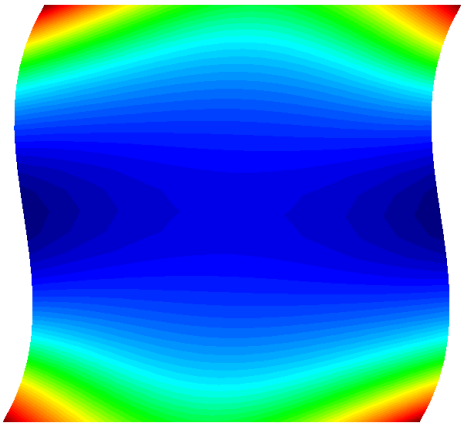

Figure 4.6: Discretization 1: deformation due to $u_{x,Y_M} = 1.0$, contour plot of σ_{xy} for $p = 3$; scaling factor 0.1

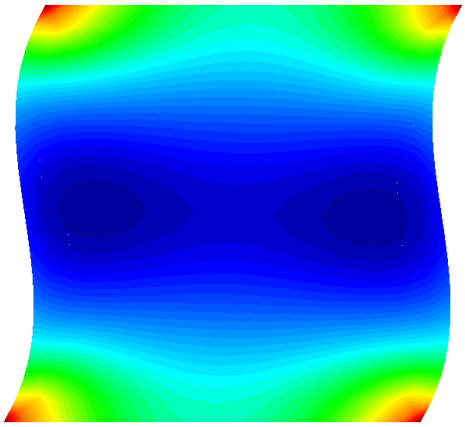

Figure 4.7: Discretization 2: deformation due to $u_{x,Y_M} = 1.0$, contour plot of σ_{xy} for $p = 3$; scaling factor 0.1

4.2.2.3 Homogenization

The departure point for the derivation of appropriate homogenization rules is the extended Hill-Mandel condition particularized to the reference configuration

$$\begin{aligned}\langle \underset{\sim}{\mathrm{P}}_m \cdot (\mathrm{Grad}\,\Delta\underset{\sim}{y})' \rangle &= \bar{\underset{\sim}{\mathrm{P}}}_M \cdot \left(\frac{5}{2}(\bar{\underset{\sim}{\chi}}_M)' - \frac{3}{2}(\underset{\sim}{\mathrm{F}}_M)' \right) + \bar{\underset{\sim}{\mathrm{H}}}_M \cdot \left((\bar{\underset{\sim}{\chi}}_M)' - (\underset{\sim}{\mathrm{F}}_M)' \right) \\ &\quad + \overset{3}{\underset{\sim}{\mathrm{Q}}}_M \cdot (\mathrm{Grad}\,\bar{\underset{\sim}{\chi}}_M)' \,,\end{aligned} \tag{4.34}$$

where

$$\bar{\underset{\sim}{\mathrm{P}}}_M = \underset{\sim}{\mathrm{P}}_M + \hat{\underset{\sim}{\mathrm{H}}}_M \,, \tag{4.35}$$

$$\bar{\underset{\sim}{\mathrm{H}}}_M = -\frac{5}{2}\underset{\sim}{\mathrm{P}}_M - \frac{3}{2}\hat{\underset{\sim}{\mathrm{H}}}_M \,, \tag{4.36}$$

$$\hat{\underset{\sim}{\mathrm{H}}}_M = (\underset{\sim}{\mathrm{H}}_M - \underset{\sim}{\mathrm{P}}_M)\,\bar{\underset{\sim}{\mathrm{F}}}_M^{(\mathrm{T})} \,, \tag{4.37}$$

$$\overset{3}{\bar{\underset{\sim}{\mathrm{Q}}}}_M = \overset{3}{\underset{\sim}{\mathrm{Q}}}_M \hat{\cdot} (\bar{\underset{\sim}{\chi}}_M^{(-\mathrm{T})}, \underset{\sim}{\mathrm{I}}) \,. \tag{4.38}$$

Note that the operator $\hat{\cdot}$ in (4.38) is defined as

$$\overset{3}{\underset{\sim}{\mathrm{C}}} \hat{\cdot} (\underset{\sim}{\mathrm{A}}, \underset{\sim}{\mathrm{B}}) = C_{KLM}\, A_{LN}\, B_{MO}\, \underset{\sim}{E}_K \otimes \underset{\sim}{E}_N \otimes \underset{\sim}{E}_O \,. \tag{4.39}$$

Transforming the left hand side of (4.34) as shown in (4.11) and again inserting the time derivative of the microscopic displacement field (4.22)

$$\begin{aligned}(\Delta\bar{\underset{\sim}{u}})' &= (\underset{\sim}{\mathrm{B}}_M(\underset{\sim}{X}_M, t))'\Delta\underset{\sim}{X} + \frac{1}{2}\,(\overset{3}{\underset{\sim}{\mathrm{C}}}_M(\underset{\sim}{X}_M, t))'(\Delta\underset{\sim}{X} \otimes \Delta\underset{\sim}{X}) \\ &\quad + \frac{1}{6}\,(\overset{4}{\underset{\sim}{\mathrm{D}}}_M(\underset{\sim}{X}_M, t))'(\Delta\underset{\sim}{X} \otimes \Delta\underset{\sim}{X} \otimes \Delta\underset{\sim}{X})\end{aligned} \tag{4.40}$$

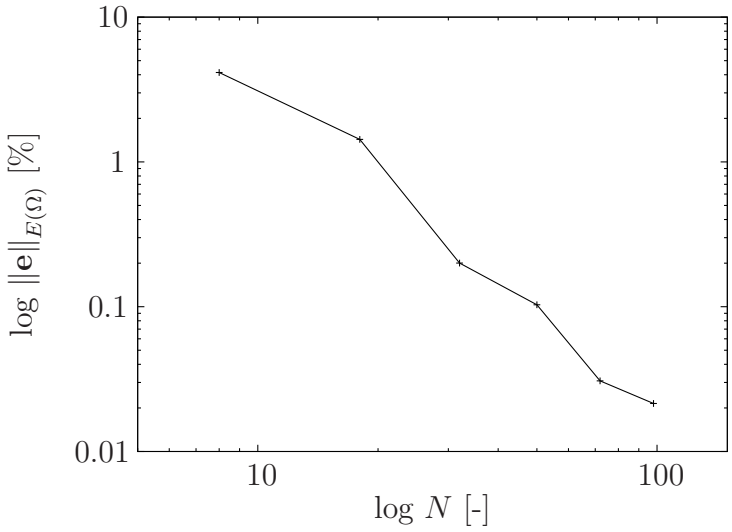

Figure 4.8: Discretization 1: p-extension with $p = 3, \ldots, 8$

gives

$$\begin{aligned}\langle \underset{\sim}{\mathrm{P}}_m \cdot (\mathrm{Grad}\, \Delta\, \underset{\sim}{y})' \rangle &= \frac{1}{V_m} \int_{\Gamma_m} (\underset{\sim}{p}_m \otimes \Delta \underset{\sim}{X})\, \mathrm{d}\Gamma_m \cdot (\underset{\sim}{\mathrm{B}}_M(\underset{\sim}{X}_M, t))' \\ &\quad + \frac{1}{2\, V_m} \int_{\Gamma_m} (\underset{\sim}{p}_m \otimes \Delta \underset{\sim}{X} \otimes \Delta \underset{\sim}{X})\, \mathrm{d}\Gamma_m \cdot (\overset{3}{\underset{\sim}{\mathrm{C}}}_M(\underset{\sim}{X}_M, t))' \\ &\quad + \frac{1}{6\, V_m} \int_{\Gamma_m} (\underset{\sim}{p}_m \otimes \Delta \underset{\sim}{X} \otimes \Delta \underset{\sim}{X} \otimes \Delta \underset{\sim}{X})\, \mathrm{d}\Gamma_m \cdot (\overset{4}{\underset{\sim}{\mathrm{D}}}_M(\underset{\sim}{X}_M, t))' \,. \end{aligned} \tag{4.41}$$

We can identify in (4.41)

$$\bar{\underset{\sim}{\mathrm{P}}}_M = \frac{1}{V_m} \int_{\Gamma_m} (\underset{\sim}{p}_m \otimes \Delta \underset{\sim}{X})\, \mathrm{d}\Gamma_m \,, \tag{4.42}$$

$$\overset{3}{\bar{\underset{\sim}{\mathrm{Q}}}}_M = \frac{1}{2\, V_m} \int_{\Gamma_m} (\underset{\sim}{p}_m \otimes \Delta \underset{\sim}{X} \otimes \Delta \underset{\sim}{X})\, \mathrm{d}\Gamma_m \,, \tag{4.43}$$

$$\overset{4}{\bar{\underset{\sim}{\mathrm{H}}}}_M = \frac{1}{6\, V_m} \int_{\Gamma_m} (\underset{\sim}{p}_m \otimes \Delta \underset{\sim}{X} \otimes \Delta \underset{\sim}{X} \otimes \Delta \underset{\sim}{X})\, \mathrm{d}\Gamma_m \,. \tag{4.44}$$

Note that for a rectangular microstructure the fourth-order hyper stress tensor can be reduced to the second-order one via

$$\bar{\underset{\sim}{\mathrm{H}}}_M = -5\, \overset{4}{\bar{\underset{\sim}{\mathrm{H}}}}_M (\overset{4}{\underset{\sim}{\mathrm{I}}}\, \underset{\sim}{\mathrm{G}}_m^{-1}) \,. \tag{4.45}$$

For a practical implementation equations (4.42) to (4.44) have to be brought into a discrete (i.e. nodal based) form as demonstrated for the first-order FE^2 scheme, refer to equation (4.14).

4.3 Three-dimensional homogenization

This section is structured as follows: After a short introduction to the three-dimensional FE^2 method of first-order with restriction to small strains we focus on a homogenization approach to determine effective material parameters of real microstructured materials. This approach was proposed by Hain [46]. Its basic idea is to transform CT-scans of micro structured materials into RVEs[4]. The effective material parameters can be extracted from the RVEs. In contrast to [46], which followed an h-FEM discretization strategy for the RVEs, we apply here the FCM, as introduced in section 3.6.

4.3.1 Projection and homogenization

Here, the projection and homogenization rules for the three-dimensional case assuming infinitesimal strains are summarized, refer also to Figure 4.9. A formal derivation is skipped since it has been presented in section 4.2. The projection rule

$$\Delta \bar{\underset{\sim}{u}} \;=\; \underset{\approx}{\varepsilon}_M \, \Delta \underset{\sim}{X} \,, \tag{4.46}$$

has the same structure as (4.8). The only difference lies in the strain-like quantity, namely $\operatorname{Grad} \underset{\sim}{u}_M$ is replaced by $\underset{\approx}{\varepsilon}_M$. For the homogenization we replace in (4.14) $\mathbf{P}_m$ by $\boldsymbol{\sigma}_m$ yielding

$$\langle \boldsymbol{\sigma}_m \rangle \;=\; \frac{1}{V_m} \sum_{i=1}^{n} \mathbf{r}_m^{(i)} \otimes \Delta \mathbf{X}^{(i)} \tag{4.47}$$

where n is the number of boundary nodes. For the extraction of effective material parameters

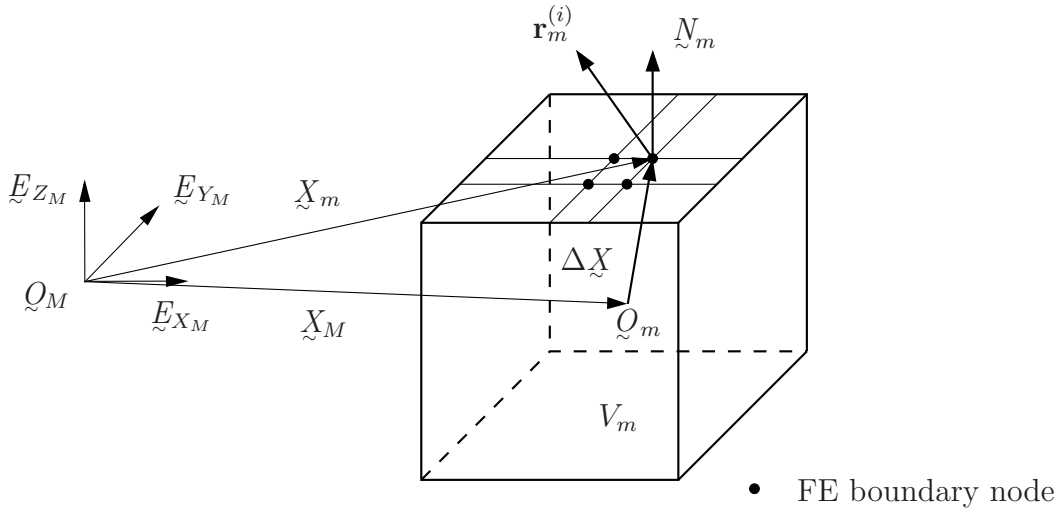

Figure 4.9: Three-dimensional microstructure with boundary nodes

the average engineering strain tensor is of importance. We define

$$\langle \underset{\approx}{\varepsilon}_m \rangle \;=\; \frac{1}{2} \left(\langle \operatorname{Grad} \underset{\sim}{u}_m \rangle + \langle \operatorname{Grad} \underset{\sim}{u}_m \rangle^{\mathrm{T}} \right) . \tag{4.48}$$

[4]Note that RVE stands for Representative Volume Element and was introduced in section 1.2.

where the average displacement gradient reads

$$\langle \mathrm{Grad}\, \underset{\sim}{u}_m \rangle \;=\; \frac{1}{V_m} \int\limits_{V_m} (\,\mathrm{Grad}\, \underset{\sim}{u}_m)\, \mathrm{d}V_m \,. \tag{4.49}$$

Next, the volume integral is transformed to a surface integral resulting in

$$\langle \mathrm{Grad}\, \underset{\sim}{u}_m \rangle \;=\; \frac{1}{V_m} \int\limits_{\Gamma_m} (\,\underset{\sim}{u}_m \otimes \underset{\sim}{N}_m)\, \mathrm{d}\Gamma_m \tag{4.50}$$

with $\underset{\sim}{N}_m$ as the outer unit normal vector, compare with Figure 4.9.

Now, rewriting (4.48) we obtain

$$\langle\, \underset{\approx}{\varepsilon}_m \rangle \;=\; \frac{1}{2\,V_m} \int\limits_{\Gamma_m} (\,\underset{\sim}{u}_m \otimes \underset{\sim}{N}_m + \underset{\sim}{N}_m \otimes \underset{\sim}{u}_m)\, \mathrm{d}\Gamma_m \,. \tag{4.51}$$

Finally, we arrive at the discrete form of (4.51)

$$\langle \boldsymbol{\varepsilon}_m \rangle \;=\; \frac{1}{2\,V_m} \sum_{i=1}^{n} \Big((\mathbf{u}_m^{(i)} \otimes \mathbf{N}_m^{(i)} + \mathbf{N}_m^{(i)} \otimes \mathbf{u}_m^{(i)})\, A_m^{(i)} \Big) \tag{4.52}$$

whereby $A_m^{(i)}$ is the area associated with node (i). For an equidistant FCM grid with element size h the resulting surface mesh is depicted in Figure 4.10. One only has to distinguish

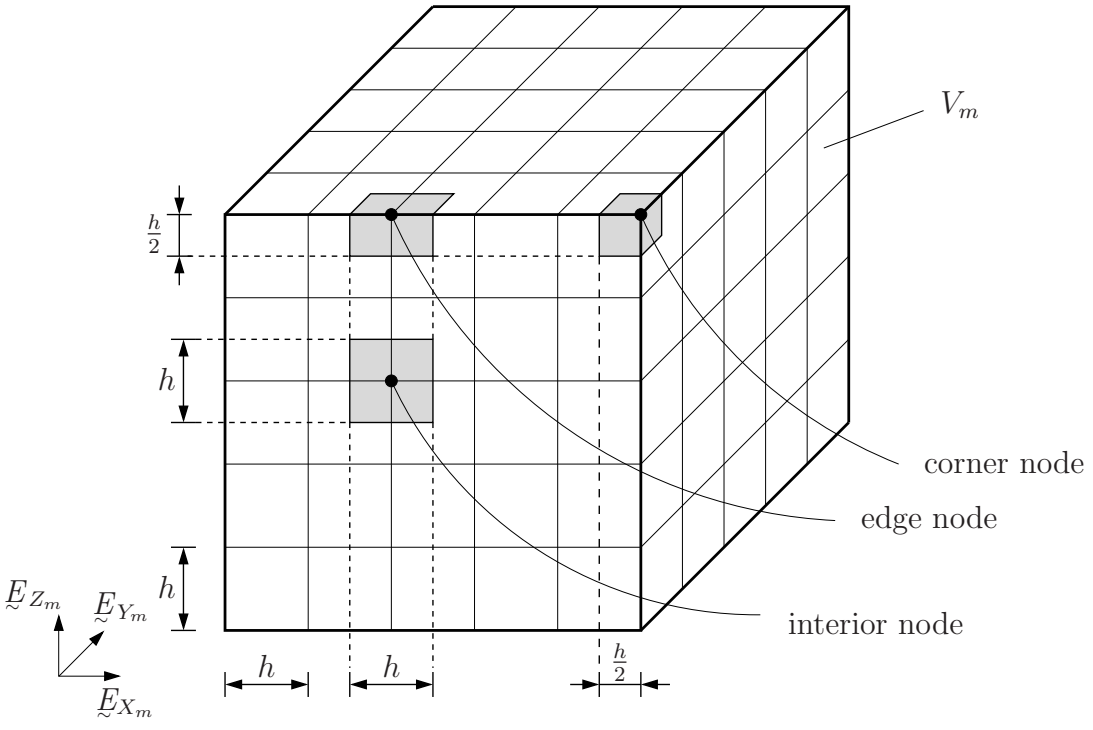

Figure 4.10: Equidistant surface mesh with gray-shaded areas $A_m^{(i)}$

between areas associated with corner, edge and interior nodes. However, at edge and corner nodes there are two and three possibilities, respectively, of how to define a normal vector. In order to circumvent this problem, these nodes are treated two and three times, respectively, in (4.52), whereby only the area associated with the corresponding normal vector is used.

4.3.2 Effective material parameters

The departing point for computing the effective material parameters is, as mentioned above, a micro CT-scan with domain Ω_{CT} from which we extract a subdomain Ω_{sub}. Now, one could directly apply linear DIRICHLET boundary conditions as given in (4.46) to Ω_{sub}. However, when dealing with heterogeneous materials, boundary layer effects may become dominant, thus throwing doubt on the the resulting stresses and forces. In order to resolve this problem, one could apply *periodic boundary conditions* as mentioned in section 4.2.1.1 or, as performed in this thesis, one embeds the subdomain into a window Ω_{win} with thickness t_{win} and averaged stiffness which is - of course - initially unknown and thus has to be determined iteratively. This approach is known as the window or self-consistency method, refer to [46, 107] and the literature cited therein. In Figure 4.11 the procedure is sketched for the two-dimensional case, in three dimensions it works analogously. We are now in a position to set up the FCM-model:

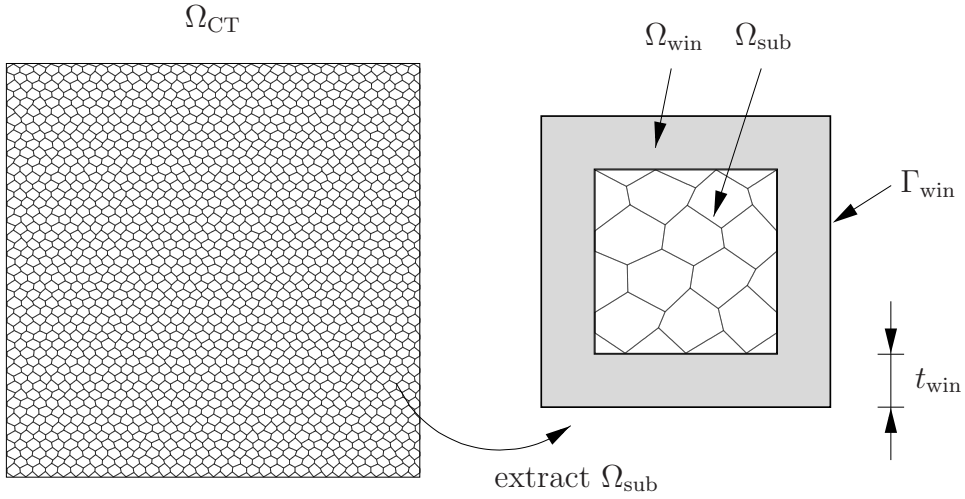

Figure 4.11: Two-dimensional illustration of the window method

For Ω_{sub} the FCM is used, and for Ω_{win} a classical p-version is sufficient, since no voids or inclusions are present there. Since in general the microstructure is represented by discrete voxel data and the derivation of a geometric model would be encountered with high effort, the current FCM-version mainly uses a voxel-based piecewise description of the geometry. Note that the microstructure's elastic properties within Ω_{sub} correspond to its bulk value, and - as mentioned above - the parameters of the window are the microstructure's effective parameters which are unknown initially and therefore have to be determined iteratively. Within this iterative process the effective parameters of the RVE, i.e. the entries of the material matrix $\mathbf{C}^{\mathrm{eff}}$, are computed by numerical differentiation, compare with the discrete version of the NEWTON-RAPHSON method as described in section 3.3. To this end we choose an arbitrary macroscopic state of strain $\underset{\sim}{\varepsilon}$ and disturb it component-wise by $\Delta\varepsilon \neq 0$ leading to seven load

cases[5]. Using VOIGT notation allows for column-wise storing of the load cases

$$\tilde{\boldsymbol{\varepsilon}} \;=\; \left[\; \tilde{\boldsymbol{\varepsilon}}_1 \;\; \ldots \;\; \tilde{\boldsymbol{\varepsilon}}_7 \;\right]. \tag{4.53}$$

We project (4.53) via (4.46) onto the window's boundary Γ_{win}, solve the BVP, and using (4.47) and (4.52) obtain stresses

$$\langle\tilde{\boldsymbol{\sigma}}\rangle \;=\; \left[\; \langle\tilde{\boldsymbol{\sigma}}_1\rangle \;\; \ldots \;\; \langle\tilde{\boldsymbol{\sigma}}_7\rangle \;\right] \tag{4.54}$$

and strains

$$\langle\tilde{\boldsymbol{\varepsilon}}\rangle \;=\; \left[\; \langle\tilde{\boldsymbol{\varepsilon}}_1\rangle \;\; \ldots \;\; \langle\tilde{\boldsymbol{\varepsilon}}_7\rangle \;\right]. \tag{4.55}$$

for the subdomain Ω_{sub}, respectively. Finally, the components of $\mathbf{C}^{\text{eff}}$ can be computed by

$$\mathrm{C}_{ij}^{\text{eff}} \;\approx\; \begin{cases} \dfrac{(\langle\tilde{\sigma}_1^i\rangle - \langle\tilde{\sigma}_{j+1}^i\rangle)}{\|\langle\tilde{\boldsymbol{\varepsilon}}_1\rangle - \langle\tilde{\boldsymbol{\varepsilon}}_{j+1}\rangle\|_{\mathrm{L}_2}} & \text{if } j <= 3 \\[2ex] \dfrac{1}{2}\dfrac{(\langle\tilde{\sigma}_1^i\rangle - \langle\tilde{\sigma}_{j+1}^i\rangle)}{\|\langle\tilde{\boldsymbol{\varepsilon}}_1\rangle - \langle\tilde{\boldsymbol{\varepsilon}}_{j+1}\rangle\|_{\mathrm{L}_2}} & \text{if } j > 3 \end{cases}, \tag{4.56}$$

where superscripts index the individual vector-components of the $(\tilde{\cdot})$-quantities and the factor $1/2$ is due to VOIGT notation. Note that $\mathbf{C}^{\text{eff}}$ is written down explicitly in equation (A.1). In order to determine a proper window size this procedure is carried out for different values of t_{win}. In Algorithm A-2 we summarize the whole procedure. Note that for each t_{win} the computation of the effective properties is repeated until the FROBENIUS norm of the difference of two consecutively computed effective material matrices falls within a prescribed tolerance.

Some remarks to Algorithm A-2:

- Since the material parameters of the subdomain Ω_{sub} are constant, the stiffness matrices $\boldsymbol{K}_e^{\text{sub}}$ need to be computed only once.
- For setting up DIRICHLET boundary conditions the penalty method is used, see [32].
- The solution to $\mathbf{K}\,\tilde{\mathbf{u}} = \mathbf{F}(\Delta\tilde{\bar{\mathbf{u}}})$ is computed efficiently by the *Parallel Sparse Direct Solver PARDISO* which allows for multiple right-hand sides [85, 86].

[5]Note that indices m and M will be skipped within this section in order to avoid overloading the notation.

Algorithm A-2 Determination of $\mathbf{C}^{\text{eff}}$

read in CT data Ω_{CT}
extract a subdomain Ω_{sub} from Ω_{CT}
discretize Ω_{sub} by the FCM
for all e_{sub} **do**
  compute $\boldsymbol{K}_e^{\text{sub}}$
end for
set $\mathbf{C}^{\text{eff}} = \mathbf{I}$
for $c = 1, \ldots, 7$ **do**
  $\tilde{\boldsymbol{\varepsilon}}_c = \mathbf{I}$
  if $c > 1$ **then**
    $\tilde{\varepsilon}_c^{c-1} - = \Delta\varepsilon$
  end if
end for
for all t_{win} **do**
  embed Ω_{sub} into the window with n^{win} boundary nodes
  repeat
    set $\mathbf{C}^{\text{old}} = \mathbf{C}^{\text{eff}}$
    set $\boldsymbol{C}_e^{\text{win}} = \mathbf{C}^{\text{eff}}$
    for all e_{win} **do**
      compute $\boldsymbol{K}_e^{\text{win}} = \int\limits_{\Omega_e} \boldsymbol{B}_e^{\text{T win}}\, \boldsymbol{C}_e^{\text{win}}\, \boldsymbol{B}_e^{\text{win}}\, \mathrm{d}\Omega_e$
    end for
    assemble global stiffness matrix $\mathbf{K}$ out of $\boldsymbol{K}_e^{\text{sub}}$ and $\boldsymbol{K}_e^{\text{win}}$
    for $i = 1, \ldots, n^{\text{win}}$ **do**
      for $c = 1, \ldots, 7$ **do**
        $\Delta\tilde{\mathbf{u}}_c^{(i)} = \tilde{\boldsymbol{\varepsilon}}_c\, \Delta\mathbf{X}^{(i)}$
      end for
    end for
    set up DIRICHLET problem and solve $\mathbf{K}\,\tilde{\mathbf{u}} = \mathbf{F}(\Delta\tilde{\tilde{\mathbf{u}}})$ simultaneously
    for $i = 1, \ldots, n^{\text{sub}}$ **do**
      for $c = 1, \ldots, 7$ **do**
        $\langle\tilde{\boldsymbol{\sigma}}_c\rangle + = \left(\tilde{\mathbf{r}}_c^{(i)} \otimes \Delta\mathbf{X}^{(i)}\right) / V_{\text{sub}}$
        $\langle\tilde{\boldsymbol{\varepsilon}}_c\rangle + = \left((\tilde{\mathbf{u}}_c^{(i)} \otimes \mathbf{N}^{(i)} + \mathbf{N}^{(i)} \otimes \tilde{\mathbf{u}}_c^{(i)}) A_{\text{sub}}^{(i)}\right) / V_{\text{sub}}$
      end for
    end for
    for $i = 1, \ldots, 6$ **do**
      for $c = 1, \ldots, 6$ **do**
        $\mathrm{C}_{ic}^{\text{eff}} = \left(\langle\tilde{\sigma}_1^i\rangle - \langle\tilde{\sigma}_{c+1}^i\rangle\right) / \left\|\langle\tilde{\boldsymbol{\varepsilon}}_1\rangle - \langle\tilde{\boldsymbol{\varepsilon}}_{c+1}\rangle\right\|_{\text{L}_2}$
        if $c > 3$ **then**
          $\mathrm{C}_{ic}^{\text{eff}} / = 2$
        end if
      end for
    end for
  until $\left(\left\|\mathbf{C}^{\text{eff}} - \mathbf{C}^{\text{old}}\right\|_{\text{Frob}} / \left\|\mathbf{C}^{\text{old}}\right\|_{\text{Frob}}\right) <$ tolerance
end for

Chapter 5

Numerical investigations

In this chapter we present our numerical examples. We hereby apply all of the homogenization schemes which were developed in chapter 4: In two dimensions the focus lies on deformation-induced anisotropy under large displacements and size effects. In three dimensions we will homogenize solid-like and foam-like materials and apply the resulting effective material parameters to verification and validation examples with special focus on sandwich structures. In addition, a microscopic approach will be performed for stability investigations of cellular materials.

5.1 Two-dimensional numerical homogenization

5.1.1 First-order FE^2 with large deformations

In this section the FE^2 approach of first-order including large deformations as described in section 4.2.1 will be investigated numerically for cellular materials [88]. Before going into detail, we briefly review some important publications concerning nonlinear analysis of cellular materials: Zhu et al. [108] subjected tetrakaidecahedral cells to high strain compression, and the numerical results were validated experimentally. Similar investigations can be found in the works of e.g. Laroussi et al. [71] or Wang and Cuitiño [100]. Note that Wang and Cuitiño included the analysis of deformation-induced anisotropy and anisotropy depending on the initial cell orientation. Two-dimensional computations with honeycomb structures under large deformations including plasticity can be found in Triantafyllidis and Schraad [97]. Ohno et al. [77] presented a homogenization framework allowing the study of microscopic bifurcation under compression. A method to determine an appropriate number of unit cells in an RVE was described by Saiki et al. [84]. Different load cases (tension, compression, and shear) were studied within a homogenization concept proposed by Hohe and Becker [55]. Deformation-induced anisotropy was detected here, too.

After this brief review let us give an outline of our analysis: We start with a TVE[1] where the accuracy of a corresponding discretization with p-FEM by means of a hierarchical p-refinement will be investigated. Then the proposed FE^2 framework of first-order in combination with the TVE is applied to three specific examples: A uniaxial tension test, a simple shear test

[1]Note that TVE stands for Testing Volume Element and was introduced in section 1.2.

and a bending test. Here, the focus lies on finding suitable boundary conditions for the TVE, the TVE's size, and measuring the deformation-induced anisotropy qualitatively and quantitatively.

5.1.1.1 TVE, discretization and boundary conditions

The TVE corresponds to a section of a fully resolved foam-like structure and its size should be large enough to provide basic deformation mechanisms. In Figure 5.1 an undisturbed TVE of size $< 1 >$ is depicted. $\text{TVE}_{<1>}$ consists of hexagons, whereby one hexagon is generated out of six beams. Note, that the hexagons have quadratic shapes, i.e. their beams do not have the same length. For a more realistic modeling of foam-like materials we introduce random

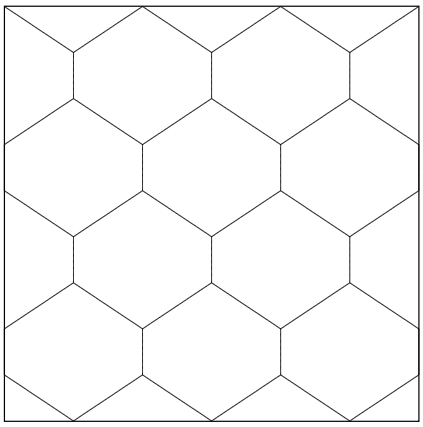

Figure 5.1: Undisturbed TVE of size $< 1 >$

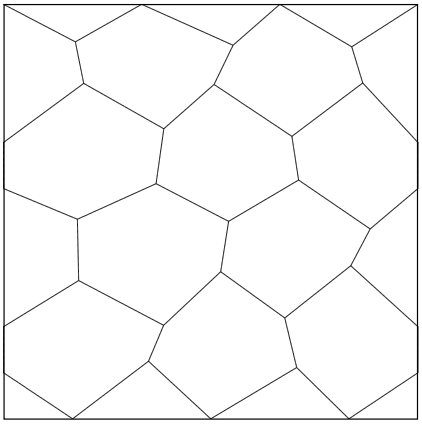

Figure 5.2: TVE of size $< 1 >$ with random disturbances [88]

disturbances to the geometry of the TVE. To achieve this, the original coordinates of the TVE are randomly disturbed, see Figure 5.2. These random disturbances can be regarded as imperfections, which govern microstructural buckling patterns, i.e. the secondary path is entered directly and therefore a possible bifurcation problem is circumvented. A detailed description of microstructural buckling phenomena including bifurcation analysis is given e.g. in [55, 77, 84, 106]. In order to study the influence of the TVE's size we introduce two additional TVEs of increasing size (where apart from disturbances, the geometric properties correspond to $\text{TVE}_{<1>}$), as shown in Figures 5.3 and 5.4. A fully resolved foam-like structure as shown in Figure 5.5 will be used for creating reference solutions. In a further step, we consider the discretization of the TVE. Figure 5.6 depicts $\text{TVE}_{<1>}$ being discretized with quadrilateral elements of high-order. By means of α_m the TVE's original $\underset{\sim}{E}_{X_m}, \underset{\sim}{E}_{Y_m}$-coordinate system can be rotated into the $\bar{\underset{\sim}{E}}_{X_m}, \bar{\underset{\sim}{E}}_{Y_m}$-coordinate system. The TVEs of size $< 2 >$ and $< 4 >$ are discretized analogously. Since the p-version of the FEM allows the use of continuum elements with high aspect ratio, the TVE is meshed by two-dimensional beam-like elements (Figure 5.6, B), that are connected by trapezoidal elements (Figure 5.6, A). Two different types of boundary conditions are defined: A hard support uses the element's edge for setting the displacement and therefore corresponds to prescribing both translational and rotational degrees of freedom as in classical beam theory (Figure 5.6, C); a soft support uses only one single node and therefore corresponds to a pin support (Figure 5.6, D). For the beam-like elements an anisotropic Ansatz in the local element directions (refer to section 3.4.3) is chosen,

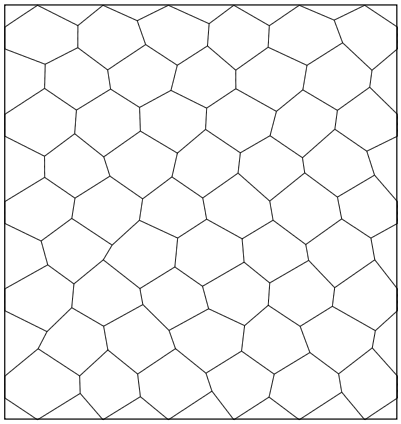

Figure 5.3: TVE of size $< 2 >$ with random disturbances [88]

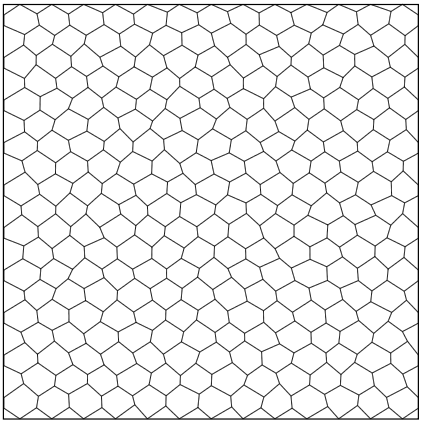

Figure 5.4: TVE of size $< 4 >$ with random disturbances [88]

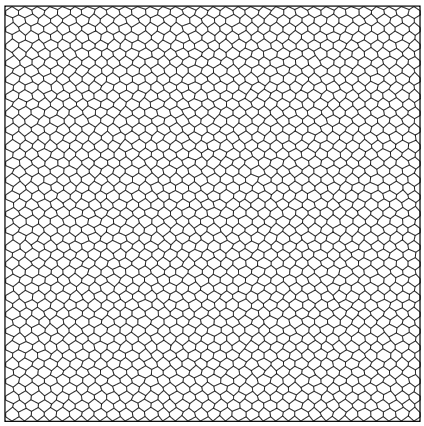

Figure 5.5: Fully resolved foam-like structure with random disturbances [88]

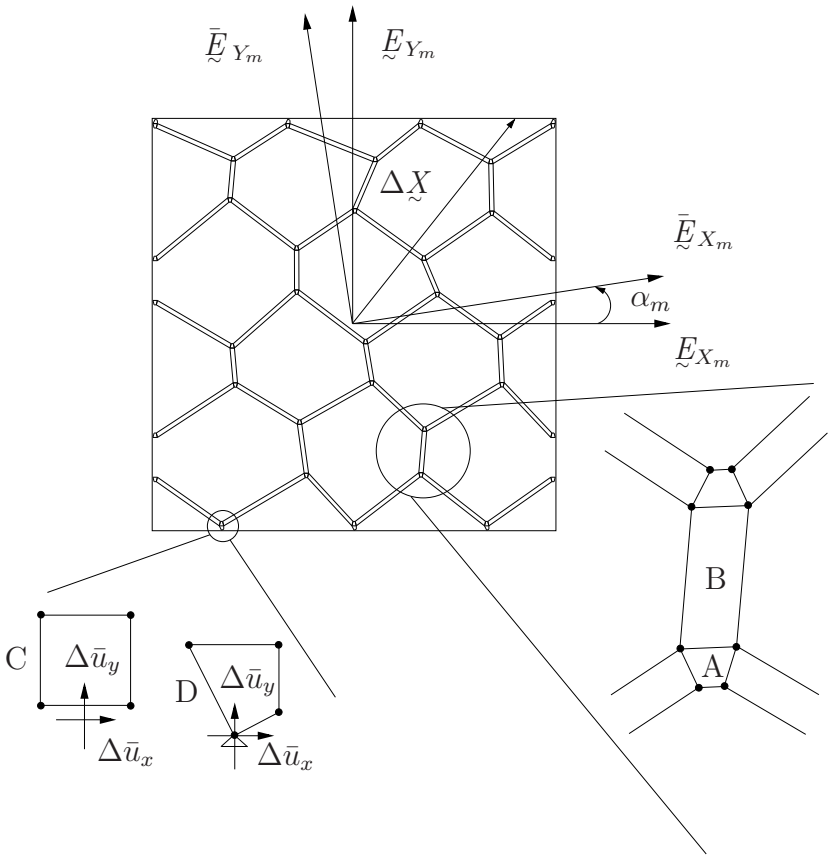

Figure 5.6: Discretized $\text{TVE}_{<1>}$ with random disturbances [88]

for the other elements the Ansatz is isotropic, i.e. $p = q$. The accuracy of a p-refinement based on the *tensor product space* should then be investigated. In [92] it is demonstrated that a polynomial degree of $q = 3$ in thickness direction is sufficient and yields a good accuracy. For the isotropic elements, we set $p = q = 3$ in both local directions of the element. The question of how to choose the polynomial degree p in the longitudinal direction of the beam-like elements is still open. To answer this question, we apply an arbitrary state of deformation to $\text{TVE}_{<1>}$ assuming soft support via (4.8), where

$$\underset{\sim}{\text{F}}_M = \begin{bmatrix} 0.1+1 & -0.13 \\ 0.16 & -0.15+1 \end{bmatrix} \underset{\sim}{e}_{i_M} \otimes \underset{\sim}{E}_{I_M}$$

is fully populated and unsymmetrical, leading to a nonlinear BVP_m. The deformation is applied in 10 load steps, assuming hyperelastic material behavior, see (2.47). We choose $\mu_m = 80.8$ GPa and $\Lambda_m = 121.1$ GPa, which corresponds to a compressible material, i.e. POISSON's ratio $\nu = 0.3$. The polynomial degree $p = 3, \ldots, 10$ is gradually increased. In Figure 5.7 the strain energy (3.47) is plotted against the number of degrees freedom N. It can be observed that $p = 5$ yields a good accuracy. For conservative results we set $p = 6$ for the subsequent numerical examples.

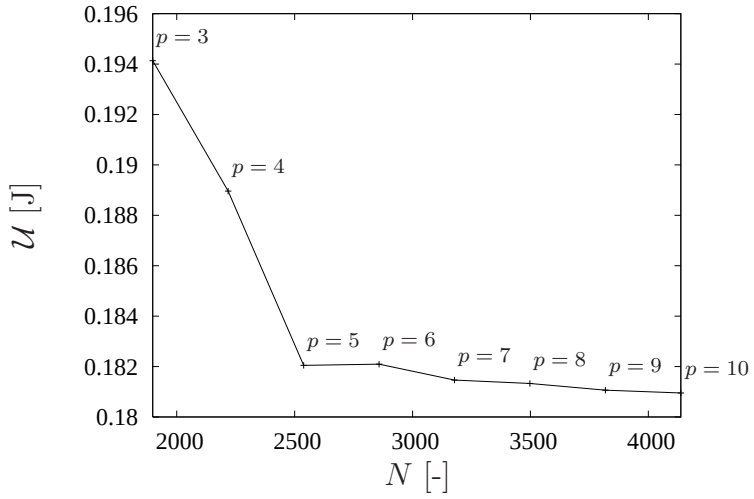

Figure 5.7: Strain energy at the final load step plotted against the number of degrees of freedom [88]

5.1.1.2 Numerical examples

The numerical examples presented in this section are obtained by applying the proposed FE^2 framework. On the **macroscale** we use bi-quadratic eight-noded LAGRANGIAN finite elements, each with 4 GAUSSIAN points. Note that the underintegration does not lead to any numerical problems. This is due to the fact that the zero energy modes, which might occur, are non-communicable; also refer to [66]. The load on the macroscale is applied incrementally. At each GAUSSIAN point of the macroscale a microstructure (TVE) is attached. For each macroscopic integration point the corresponding microstructure is randomly disturbed (as depicted in Figure 5.2), yielding a statistical distribution of the disturbances which leads to small inhomogeneities in macroscopic stresses and strains even when dealing with homogeneous macroscopic boundary conditions. Again, the material parameters in (2.47) are set to $\mu_m = 80.8$ GPa and $\Lambda_m = 121.1$ GPa.

5.1.1.2.1 Uniaxial tension test

We start with a macroscopic uniaxial tension test as shown in Figure 5.8. To this end, the displacement $\overline{u}$ is split into a top and a bottom displacement, on the left boundary symmetry conditions are applied, and the right boundary is free. The macroscopic mesh consists of 10×10 bi-quadratic finite elements. The width of the mesh is $B = 2\,mm$ and the height is $H = 2\,mm$. A series of FE^2 computations for a varying size of the TVE is performed and the results are compared to a reference solution. In the FE^2 computations α_m is set to 0° for all microstructures. The reference solution is obtained by using the fully resolved microstructure (microscopic computation), applying 2D continuum p-elements with $p = 6$ and $q = 3$ resulting in 367680 degrees of freedom, refer to Figure 5.5. Note that nearly no difference between soft and hard support conditions for the reference solutions was observed for moderate engineering strains ($\leq 10\,\%$). This fact can be explained by ST. VENANT's principle: The boundary layers are very small compared to the whole structure and therefore do not influence the overall mechanical behavior. As DIRICHLET boundary conditions for the TVE we chose hard

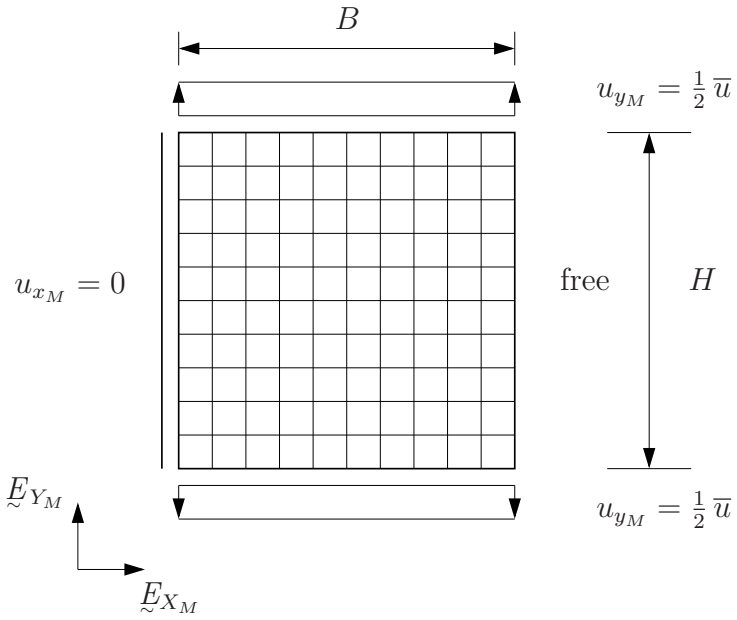

Figure 5.8: Uniaxial tension test [88]

support conditions. In a first step, the influence of the size of the microstructure (TVE) is investigated in the **small strain regime** for both types of boundary conditions. In Figure 5.9 the results for the hard support conditions are compared. To do so, the resulting force $F_y = \int_a \sigma_{yy}\,\mathrm{d}a$ is plotted against the engineering strain ε_{yy}. From this it can be observed that the FE^2 computation with hard support yields a very stiff behavior even for $\mathrm{TVE}_{<4>}$. The reason for this stiffening effect lies in the accumulation of strong boundary layer effects within each TVE. Note that in this case a smaller TVE yields a stiffer mechanical behavior, see [19]. For soft support conditions a much better agreement with the reference solution for an increasing size of the microstructure can be observed, see Figure 5.10. In fact, for $\mathrm{TVE}_{<4>}$ nearly no difference with the microscopic computation is observed.

Next, we investigate the influence of **large strains**. In Figure 5.11 the macroscopic load-engineering-strain curve (F_y vs. ε_{yy}) is depicted. From this it is evident that in the case of a hard support, the stiffness is dramatically overestimated, as expected (FE^2 $\mathrm{TVE}_{<1>}$ and hard support). Considering a soft support, the FE^2 computation agrees well with the curve of a reference solution, until a strain of $\varepsilon_{yy} \approx 10\,\%$ is reached. For higher strains the difference between both curves becomes more pronounced (FE^2 with $\mathrm{TVE}_{<1>}$ and soft support). If the size of the microstructure (TVE) is increased, a better agreement with the reference solution is obtained (FE^2 with $\mathrm{TVE}_{<2>}$ and soft support). This curve ends at a strain $\varepsilon_{yy} \approx 27.5\,\%$ due to highly distorted elements.

To investigate the effect of anisotropy, the TVE is rotated by an angle of $\alpha_m = 90°$. Again, a reference solution is obtained based on a fully resolved structure, where the geometry and material parameters are chosen to be the same. The resulting curves are depicted in Figure 5.12. Again, it is observed that the FE^2 computation with hard support differs significantly

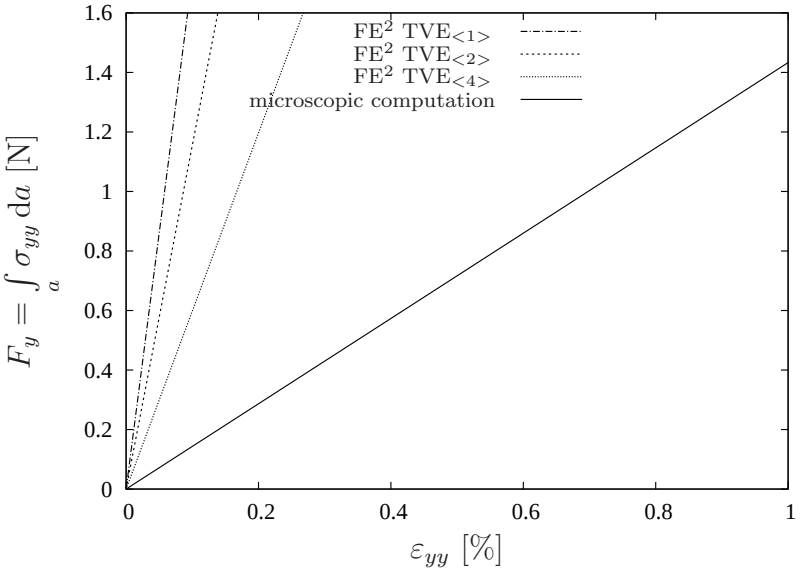

Figure 5.9: Tension test: Influence of the microstructure's size applying hard support, $\alpha_m = 0°$ [88]

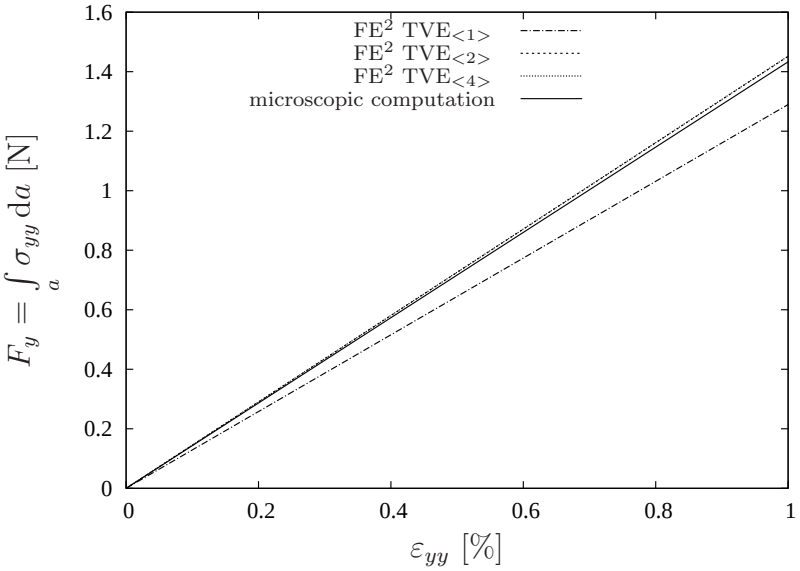

Figure 5.10: Tension test: Influence of the microstructure's size applying soft support, $\alpha_m = 0°$ [88]

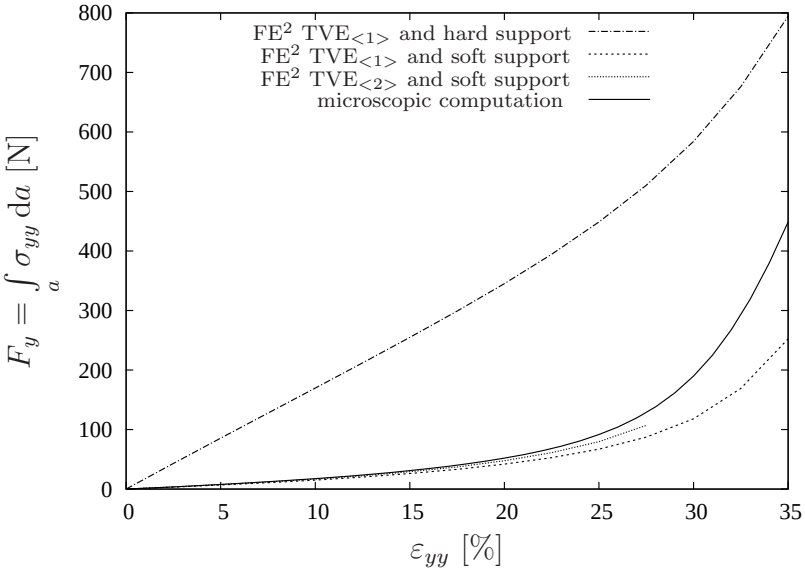

Figure 5.11: Tension test: Load-engineering-strain curve for orientation $\alpha_m = 0°$ [88]

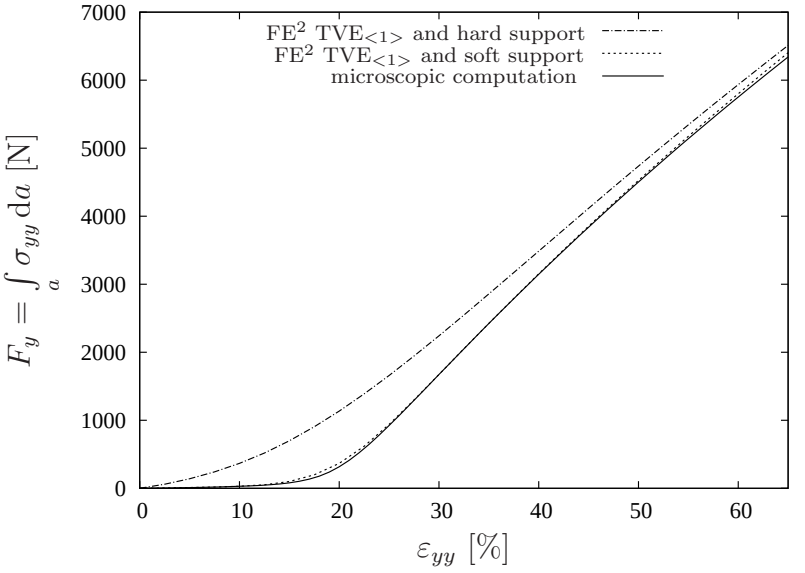

Figure 5.12: Tension test: Load-engineering-strain curve for orientation $\alpha_m = 90°$ [88]

from the reference solution (microscopic approach), especially for small values of ε_{yy}. However, the soft support boundary conditions yield a very good agreement with the reference solution (microscopic computation). Therefore, we apply in the following only **soft support** conditions. These soft support conditions can be regarded as fluctuations relaxing the DIRICHLET boundary conditions.

In Figure 5.13, the transversal contraction $\frac{\Delta B}{\Delta H}$ is plotted against the engineering strain. In both cases a high transversal contraction is obtained. For $\alpha_m = 90°$ one observes even a maximum. The result is not surprising, since in general foam-like structures exhibit high transversal contractions in tension.

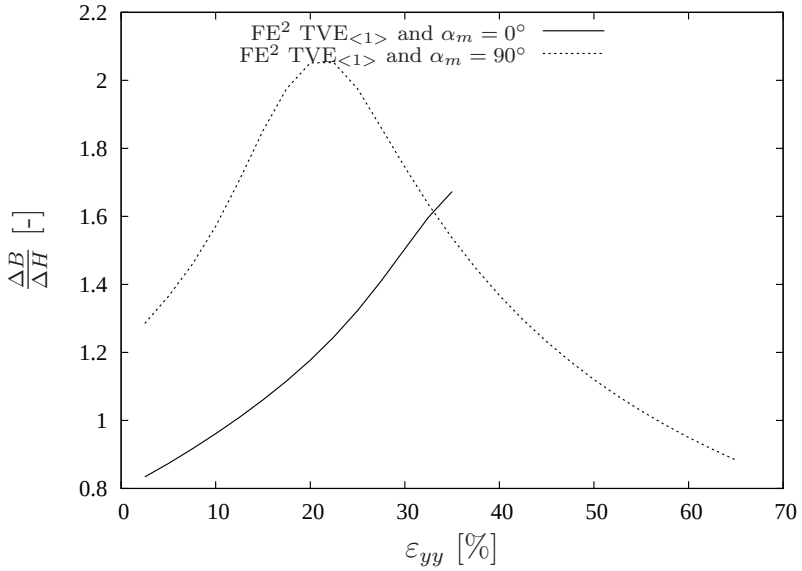

Figure 5.13: Tension test: Transversal contraction for orientations $\alpha_m = 0°$ and $\alpha_m = 90°$ [88]

5.1.1.2.2 Simple shear test

In the simple shear test as depicted in Figure 5.14 we apply periodic boundary conditions to the left and to the right boundary. One benefit of the periodic boundary conditions is, of course, the reduction in the number of elements; here only 1×10 elements are used. Note that this shear test could also be performed with one single TVE. This would be more efficient, but the small inhomogeneities in macroscopic stresses and strains due to statistical disturbances varying between the TVEs would be excluded. The height of the specimen is set to $H = 2\,mm$. In Figure 5.15 the macroscopic load-shearing-angle curve (F_{xy} vs. $\tan(\gamma) = \frac{\overline{u}}{H}$) and the deformed TVEs at the midpoint $\underset{\sim}{M}_M$ (refer to Figure 5.14) for two different orientations of the TVE are shown. A nonlinear curve is observed until $\tan(\gamma) \approx 0.3$, which then transforms into a straight line. The pictures of the deformed TVEs indicate that there is a deformation-induced anisotropy, i.e. the gradual change of the load carrying behavior from bending to tension; compare with [55, 100]. For a more quantitative investigation of this deformation-induced anisotropy, the principal angle for the CAUCHY stress tensor $\underset{\sim}{\sigma}$ and the EULER-ALMANSI

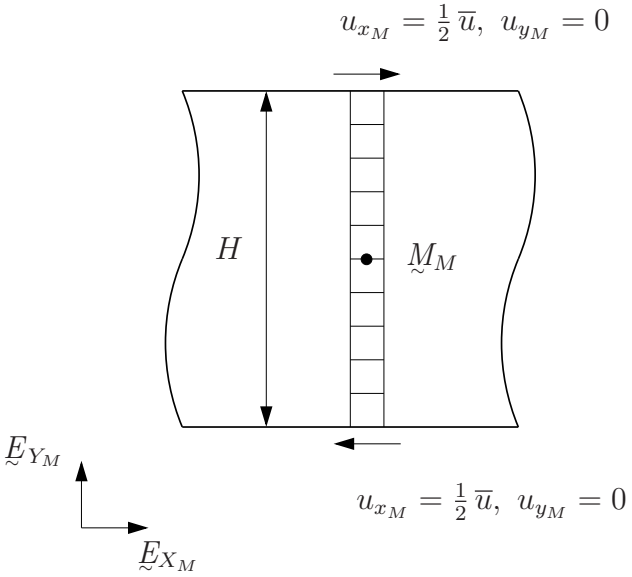

Figure 5.14: Simple shear test with periodic boundary conditions [88]

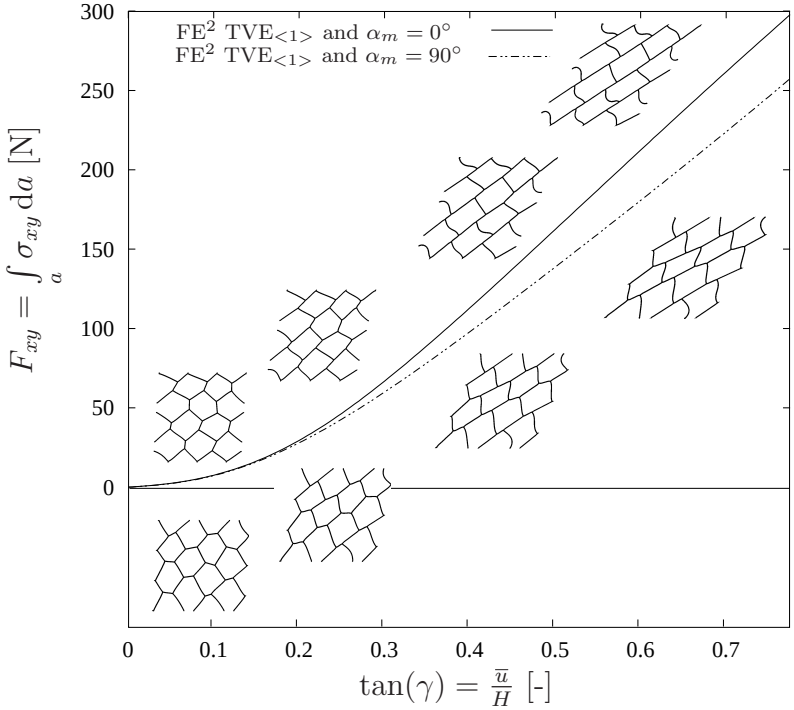

Figure 5.15: Shear test: Load-shearing-angle curve for orientations $\alpha_m = 0°$ and $\alpha_m = 90°$; for both orientations the deformed TVEs at the midpoint $\underset{\sim}{M}_M$ (refer to Figure 5.14) are plotted [88]

strain tensor $\underset{\sim}{e}$

$$\begin{aligned} \varphi_{\underset{\sim}{\sigma}} &= \frac{1}{2}\operatorname{atan}\left(\frac{2\,\sigma_{xy}}{\sigma_{xx}-\sigma_{yy}}\right) \\ \varphi_{\underset{\sim}{e}} &= \frac{1}{2}\operatorname{atan}\left(\frac{2\,e_{xy}}{e_{xx}-e_{yy}}\right) \end{aligned} \tag{5.1}$$

are introduced respectively. We define the ratio between $\varphi_{\underset{\sim}{\sigma}}$ and $\varphi_{\underset{\sim}{e}}$ as

$$\mathcal{R} = \frac{\varphi_{\underset{\sim}{\sigma}}}{\varphi_{\underset{\sim}{e}}}. \tag{5.2}$$

Note that for an isotropic material law $\mathcal{R} = 1$. In Figure 5.16 the ratio-shearing-angle curves ($\mathcal{R}$ vs. $\tan(\gamma) = \frac{\overline{u}}{H}$) are plotted for the midpoint $\underset{\sim}{M}_M$ of the structure. A curve obtained by using the isotropic macroscopic material law as stated in (2.47) is included, too. In contrast

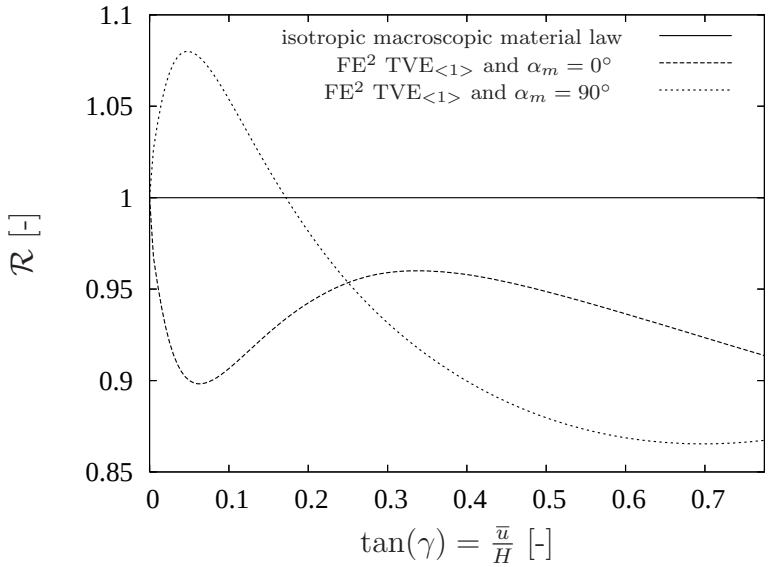

Figure 5.16: Shear test: Ratio-shearing-angle curve for orientations $\alpha_m = 0°$ and $\alpha_m = 90°$ [88]

to the computation based on this isotropic macroscopic material law, the ratios of the FE^2 computations are not constant, which is an indicator of anisotropic material behavior.

Next, we consider the influence of the orientation α_m of the TVEs on the resulting stress, compare with [100]. We apply the same state of deformation (i.e. shearing)

$$\underset{\sim}{F}_M = \begin{bmatrix} 1+0.0 & 0.1 \\ 0.0 & 1+0.0 \end{bmatrix} \underset{\sim}{e}_{i_M} \otimes \underset{\sim}{E}_{I_M}$$

to TVE$_{<1>}$, TVE$_{<2>}$, and TVE$_{<4>}$ for each α_m, which is subdivided into five load steps. In Figures 5.17 to 5.25 the components of the homogenized CAUCHY stresses are plotted using

the same scale for all TVEs. They show obvious anisotropic behavior, i.e. they depend on α_m, and their shape depends on the TVE size. Note that there is no significant influence of the disturbances on the anisotropy, i.e. the disturbances are too small to regularize the mechanical behavior. Comparing the maximum stress values for the three TVEs, one realizes that they decrease with increasing TVE size. This decrease is directly associated with the application of displacement boundary conditions: If the TVE size is increased, the stresses will converge to a limit, i.e. the TVE is representative for the material under consideration and can therefore be termed RVE [52, 67]. Note however that our TVEs are too small to be representative, since no convergence in stresses is obtained, yet. Another interesting point is, that, although we are dealing with a shear test, the normal stresses σ_{xx_M} and σ_{yy_M} are dominant. This observation is directly connected to the inherent properties of the microstructure (TVE). In Figures 5.26, 5.27, and 5.28 the principal angle computed from the CAUCHY stress tensor is plotted. Again, an anisotropic behavior depending on α_m can be observed.

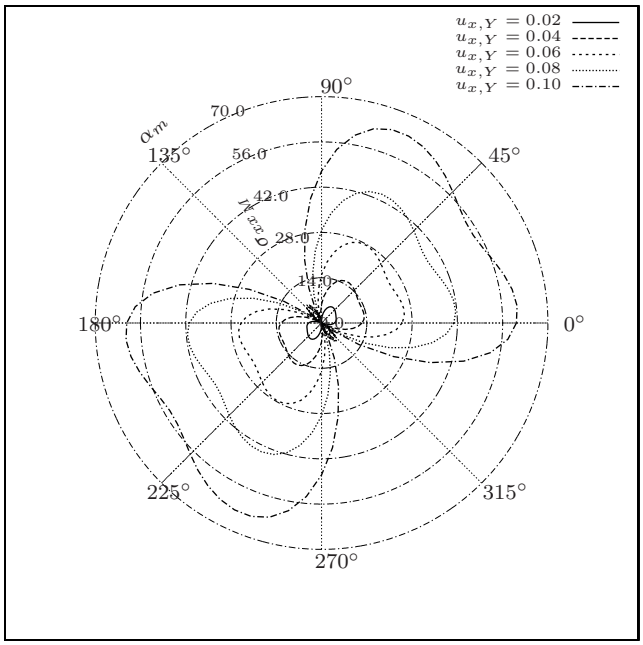

Figure 5.17: Stresses σ_{xx_M} for $\text{TVE}_{<1>}$ orientations $\alpha_m = 0°, \ldots, 360°$ and $u_{x,Y} = 0.02, \ldots, 0.1$ [88]

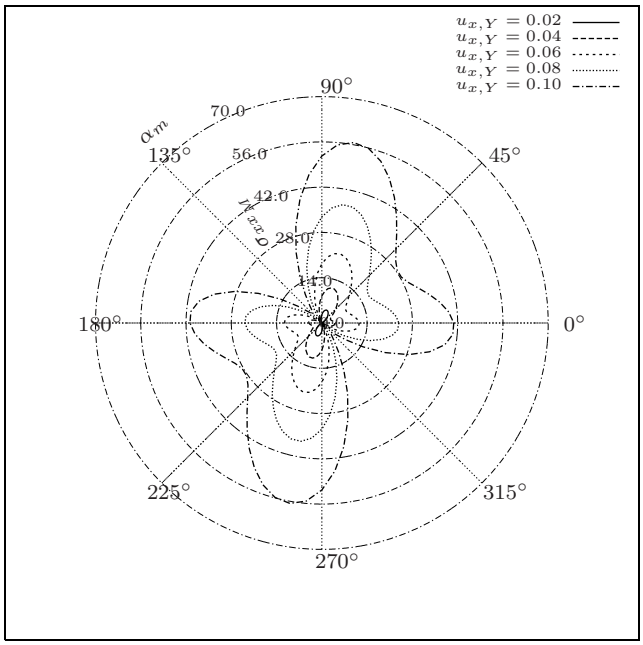

Figure 5.18: Stresses σ_{xx_M} for $\text{TVE}_{<2>}$ orientations $\alpha_m = 0°, \ldots, 360°$ and $u_{x,Y} = 0.02, \ldots, 0.1$ [88]

5.1.1.2.3 Bending test

In the macroscopic bending test a beam-like structure is symmetrically loaded by a prescribed displacement. Due to symmetry only half of the system has to be modeled, see Figure 5.29. The macroscopic mesh consists of 20×5 elements. The length is $L = 8\,mm$ and the height is $H = 2\,mm$. Therefore, the aspect ratio L/H of the beam equals 4. This example is referred to as inhomogeneous, since bending is in general a combination of shear, tension and compression. The macroscopic load-displacement curves (F_{xy} vs. $\overline{u}$) for two different TVE orientations $\alpha_m = 0°$ and $\alpha_m = 90°$ are shown in Figure 5.30. From this it is evident that the

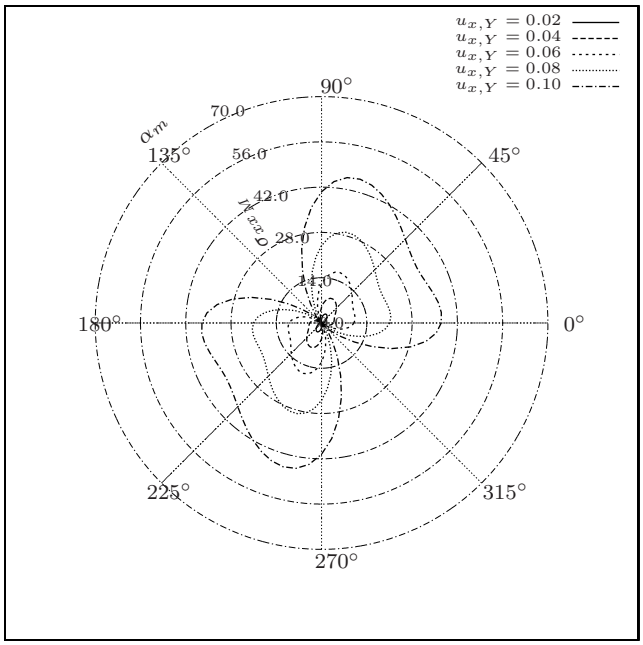

Figure 5.19: Stresses σ_{xx_M} for $\text{TVE}_{<4>}$ orientations $\alpha_m = 0°, \ldots, 360°$ and $u_{x,Y} = 0.02, \ldots, 0.1$ [88]

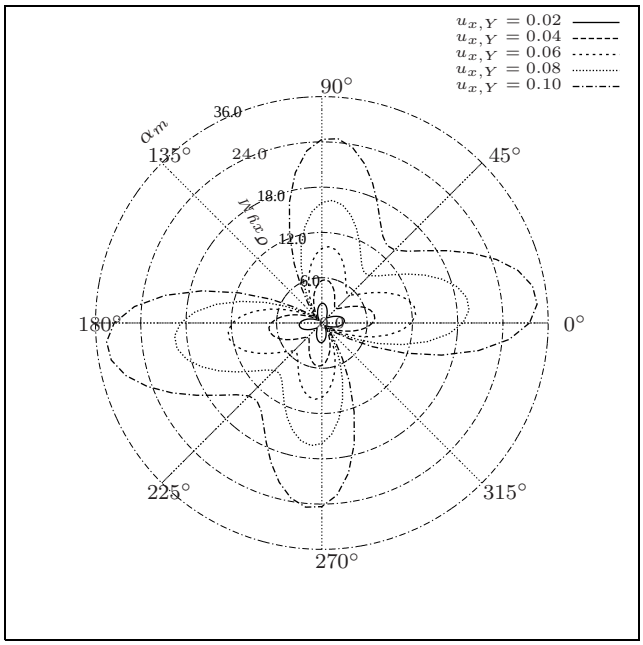

Figure 5.20: Stresses σ_{xy_M} for $\text{TVE}_{<1>}$ orientations $\alpha_m = 0°, \ldots, 360°$ and $u_{x,Y} = 0.02, \ldots, 0.1$ [88]

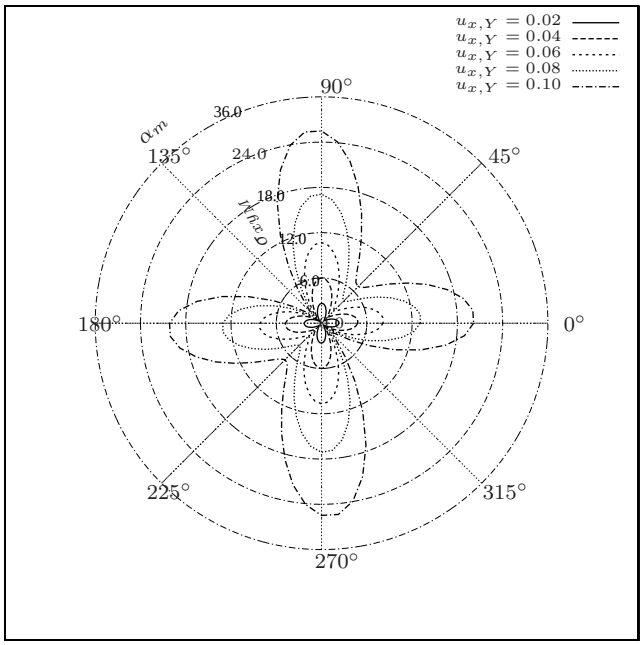

Figure 5.21: Stresses σ_{xy_M} for $\text{TVE}_{<2>}$ orientations $\alpha_m = 0°, \ldots, 360°$ and $u_{x,Y} = 0.02, \ldots, 0.1$ [88]

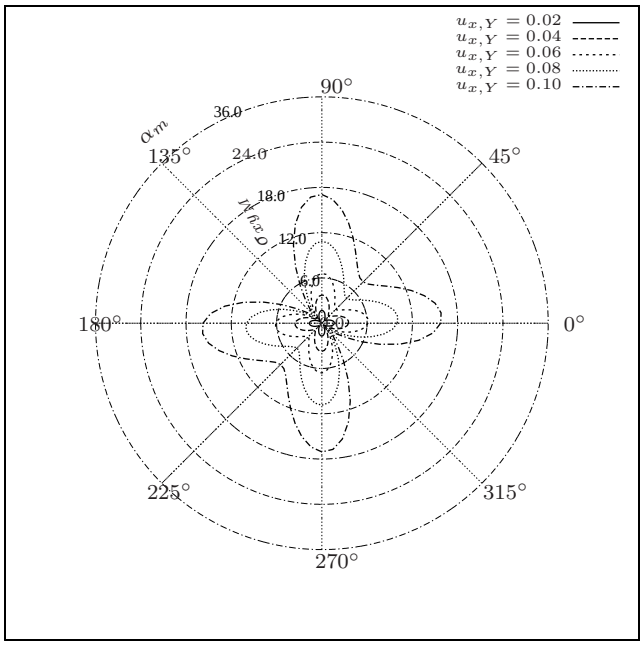

Figure 5.22: Stresses σ_{xy_M} for $\text{TVE}_{<4>}$ orientations $\alpha_m = 0°, \ldots, 360°$ and $u_{x,Y} = 0.02, \ldots, 0.1$ [88]

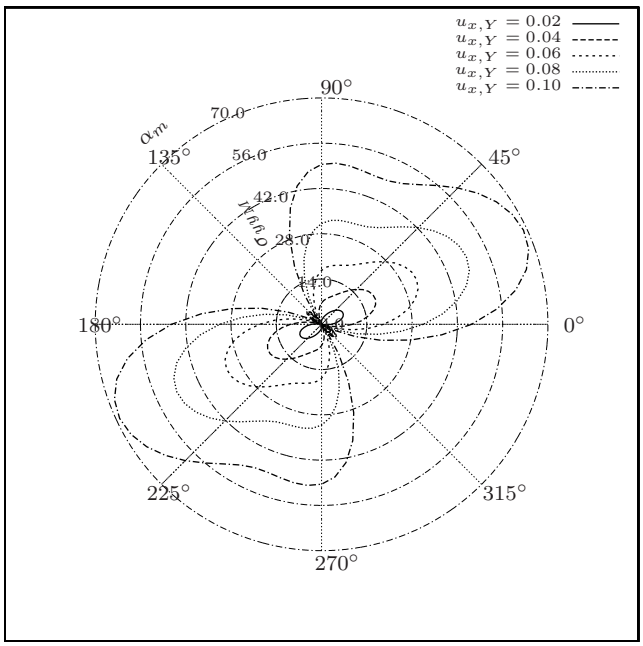

Figure 5.23: Stresses σ_{yy_M} for $\text{TVE}_{<1>}$ orientations $\alpha_m = 0°, \ldots, 360°$ and $u_{x,Y} = 0.02, \ldots, 0.1$ [88]

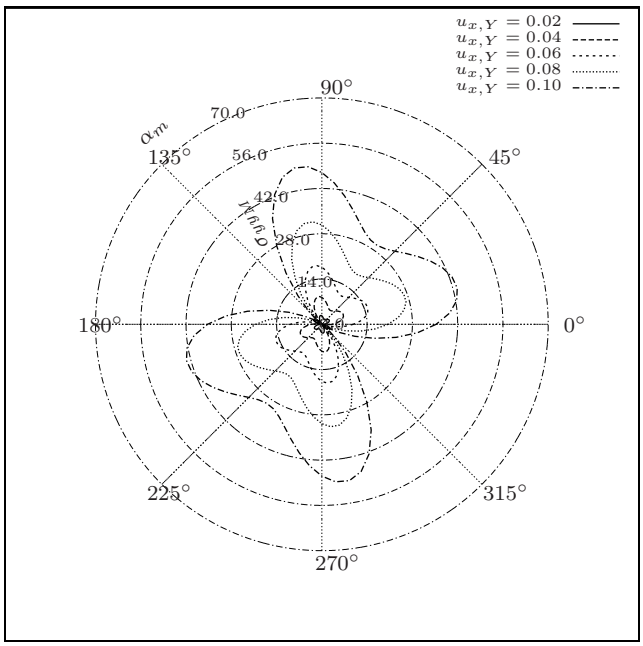

Figure 5.24: Stresses σ_{yy_M} for $\text{TVE}_{<2>}$ orientations $\alpha_m = 0°, \ldots, 360°$ and $u_{x,Y} = 0.02, \ldots, 0.1$ [88]

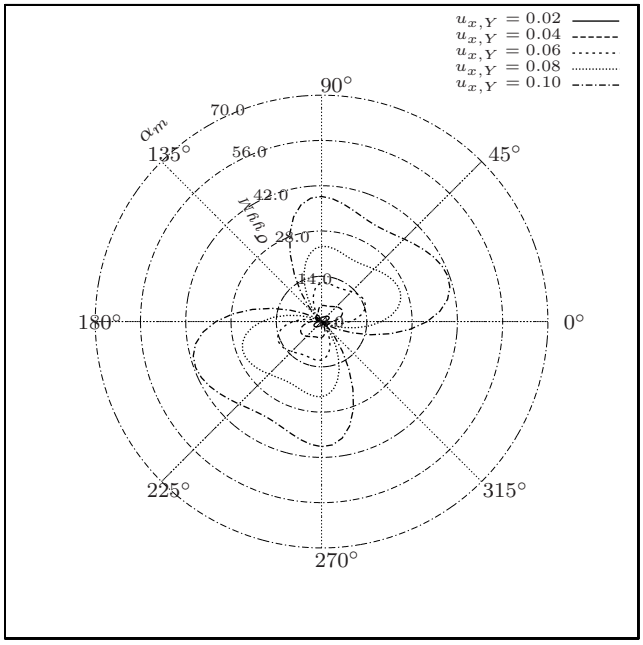

Figure 5.25: Stresses σ_{yy_M} for $\text{TVE}_{<4>}$ orientations $\alpha_m = 0°, \ldots, 360°$ and $u_{x,Y} = 0.02, \ldots, 0.1$ [88]

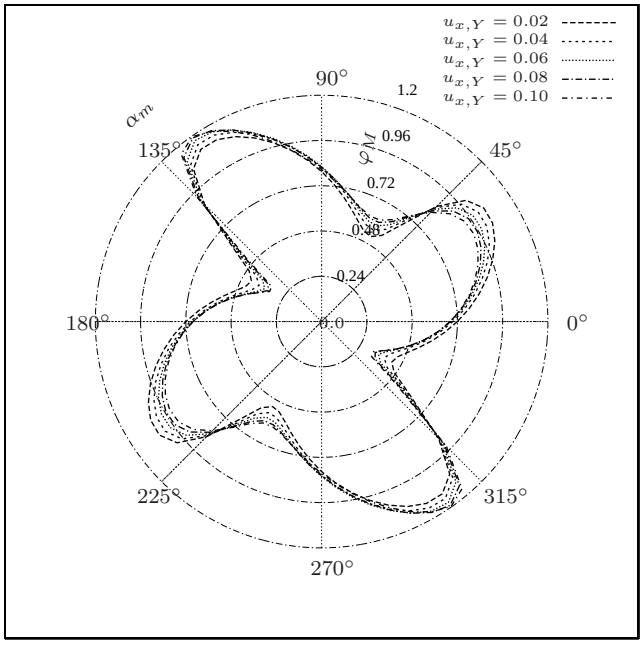

Figure 5.26: Principal angle φ_M for $\text{TVE}_{<1>}$ orientations $\alpha_m = 0°, \ldots, 360°$ and $u_{x,Y} = 0.02, \ldots, 0.1$ [88]

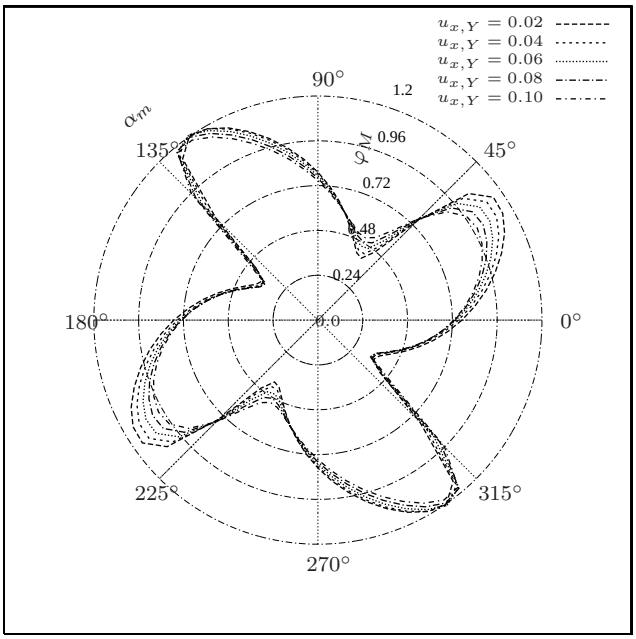

Figure 5.27: Principal angle φ_M for TVE$_{<2>}$ orientations $\alpha_m = 0°, \ldots, 360°$ and $u_{x,Y} = 0.02, \ldots, 0.1$ [88]

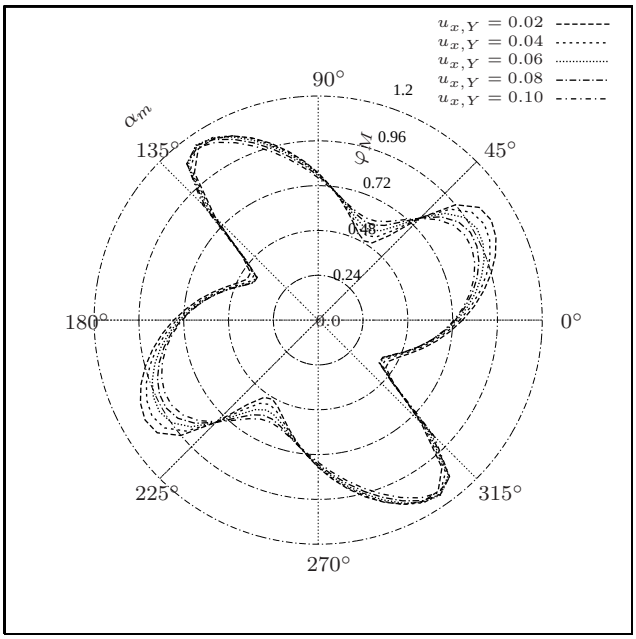

Figure 5.28: Principal angle φ_M for TVE$_{<4>}$ orientations $\alpha_m = 0°, \ldots, 360°$ and $u_{x,Y} = 0.02, \ldots, 0.1$ [88]

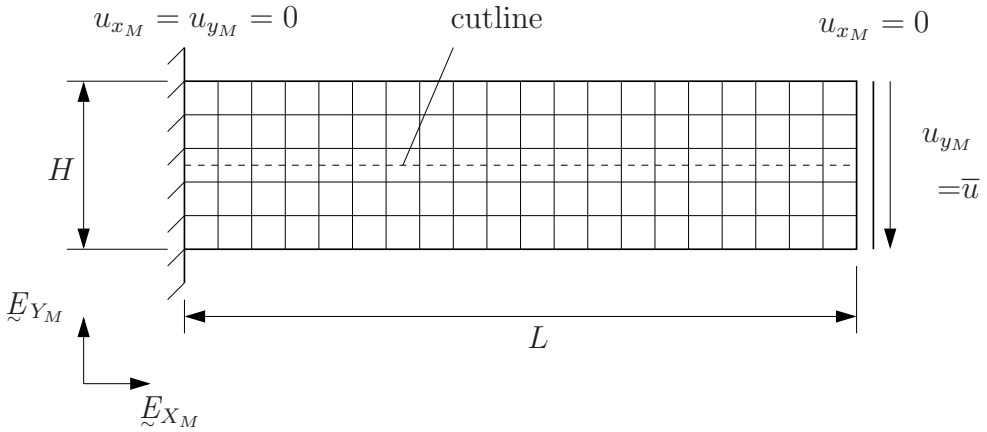

Figure 5.29: Bending test [88]

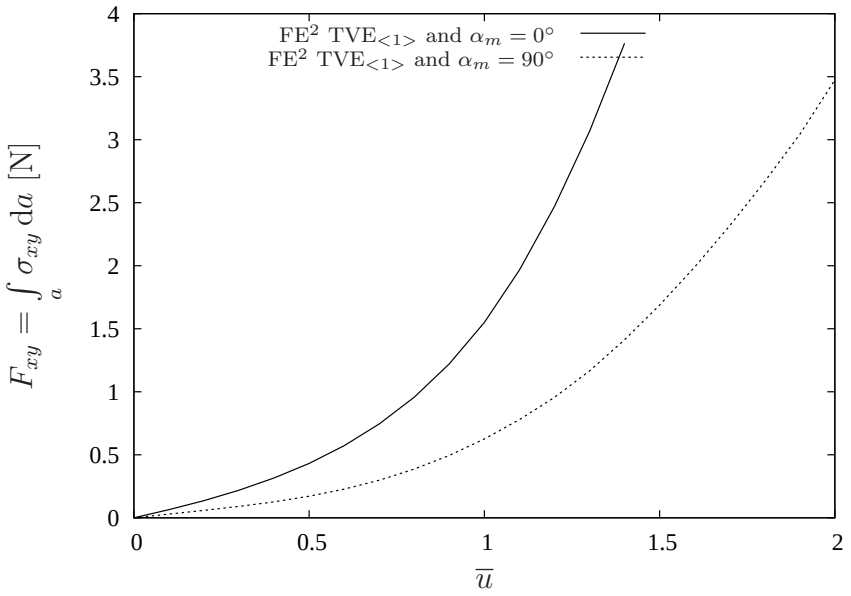

Figure 5.30: Bending test: Load-displacement curve for TVE orientations $\alpha_m = 0°$ and $\alpha_m = 90°$ [88]

load-displacement curves obey nonlinear behavior. Let us focus on the displacement u_{y_M} at the midline of the macrostructure which is evaluated at the cutline indicated in Figure 5.29. Figure 5.31 shows u_{y_M} for $\overline{u} = 1.0$ over the beam's length for the two different orientations of the TVE and additionally for a computation based on an isotropic macroscopic material law. Whereas the rotation of the TVE by 90° is almost without effect, a very small difference between the results of the FE^2 approach and the isotropic macroscopic material law can be observed.

5.1.1.3 Computational effort

Finally, let us give an impression of the computational effort: The FE^2-computation in the large strain tension test with TVE$_{<2>}$, refer to Figure 5.11, took around two days[2] on a *Linux* cluster. On this cluster the BVP$_M$ is solved by an AMD Athlon 2500+ CPU and the BVP$_m$s are distributed to 10 Worker nodes based on Intel 2.4 GHz CPUs, compare with the implementation scheme as described in section 4.2.1.3. In contrast, the corresponding microscopic reference solution was computed within 2 hours using one single AMD Opteron with 2.4 GHz.

Therefore, from a computational point of view the FE^2-method is not attractive, and one may wonder why and where to apply such a demanding method in practice, or, in other words: *Is it possible to increase its efficiency and are there any cases where this method is of advantage?* Before answering this question please recall that our investigations have been performed within the scope of basic research: The FE^2-approach has been combined with p-FEM for the first

[2]Note that a similar computation time was measured for the bending test. Only the shear test could be computed within hours thanks to the application of periodic boundary conditions leading to a lower number of macroscopic integration points.

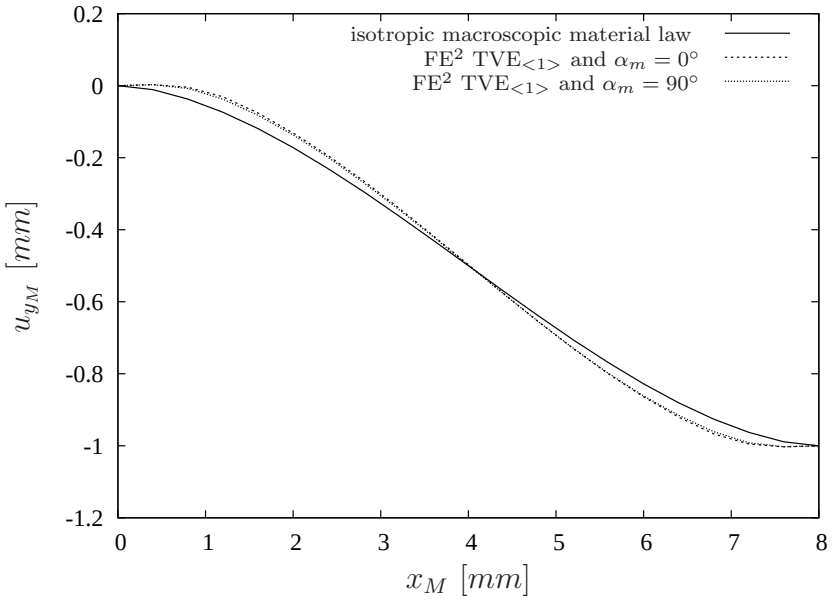

Figure 5.31: Bending test: Midline displacement u_{y_M} for $\overline{u} = 1.0$ [88]

time and applied to two-dimensional cellular materials, whereby proposals for polynomial degrees and boundary conditions have been derived. Coming back to the question one can state that FE^2-methods would be much more efficient if the nested BVP is avoided. This is, however, only possible if the material's answer on the microscopic level is assumed to be linear. In this case effective material properties can be extracted via numerical homogenization procedures first and then applied to arbitrary complex macroscopic structures where a pure microscopic approach would fail due to problems in mesh generation and non-manageable systems of equations even in 2D.

5.1.2 Higher-order FE^2 with small deformations

In this section, we want to apply the higher-order homogenization procedure introduced in section 4.2.2 to two different kinds of periodic grid structures which small statistical disturbances of the geometry. In particular, we focus on squared and honeycomb grid structures, refer to [64]. Linear-elastic material behavior in a regime of small strains is considered using HOOKE's law (YOUNG's modulus $E = 70$ GPa, POISSON's ratio $\nu = 0.3$). Due to this assumption a tabulated solution for the microstructures can be computed before hand and thus the nested BVP is circumvented.

Throughout the numerical examples, the struts connecting the grid nodes on the microscale exhibit a length $l_m = 1.5\,mm$ as well as a thickness of $t_m = 0.1\,mm$, i.e. the aspect ratio is 1/15. The struts are discretized by quadrilateral continuum elements accounting for anisotropic higher-order Ansatz functions, refer to section 3.4.3. Besides the unit-cell calculation, this micro discretization is also applied to generate reference solutions with full microscopic resolution. On the macroscale, rectangular finite elements are used with full quartic 16-noded LAGRANGIAN Ansatz functions for the displacement field as well as for the microdeformations.

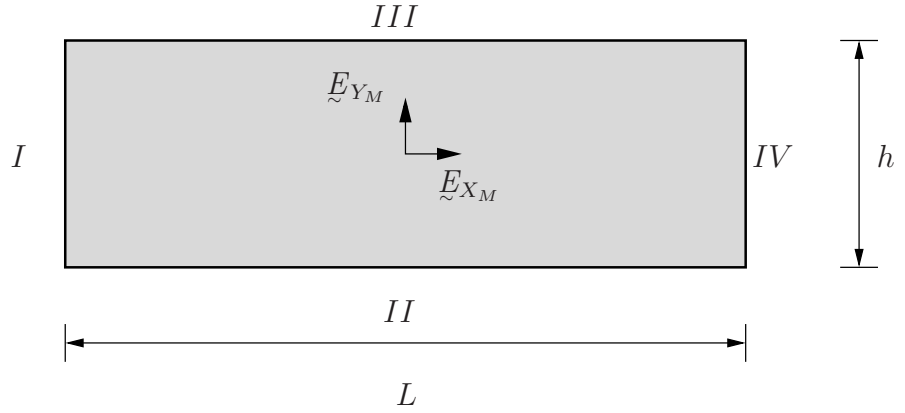

Figure 5.32: Schematic sketch of the macroscopic experimental setup, assignment of the boundaries and the sample dimensions [64].

At first, a slightly disturbed squared grid structure under shear deformation will be examined. Afterwards, the investigations will be extended to honeycomb structures under shear deformations. Additionally, a three-point bending test of a sandwich panel will be discussed.

5.1.2.1 Squared grid structure

5.1.2.1.1 Microtopology

Let us start our considerations with the microtopology of the squared grid structure. As has been mentioned before, we assume the microstructure to be slightly disturbed. To this end the positions of the different grid nodes may vary within a circle of radius $r = 2/3 \cdot \delta \cdot l_m$ around their exact position in a perfectly periodic structure, where δ is a disturbance parameter to be varied throughout the following studies. An exemplary disturbed unit cell as well as a representative sample for a reference experiment are depicted in Figures 5.33 a) and b) for ($\delta = 0.2$). In order to capture the statistics of unit cell disturbance within the proposed FE^2

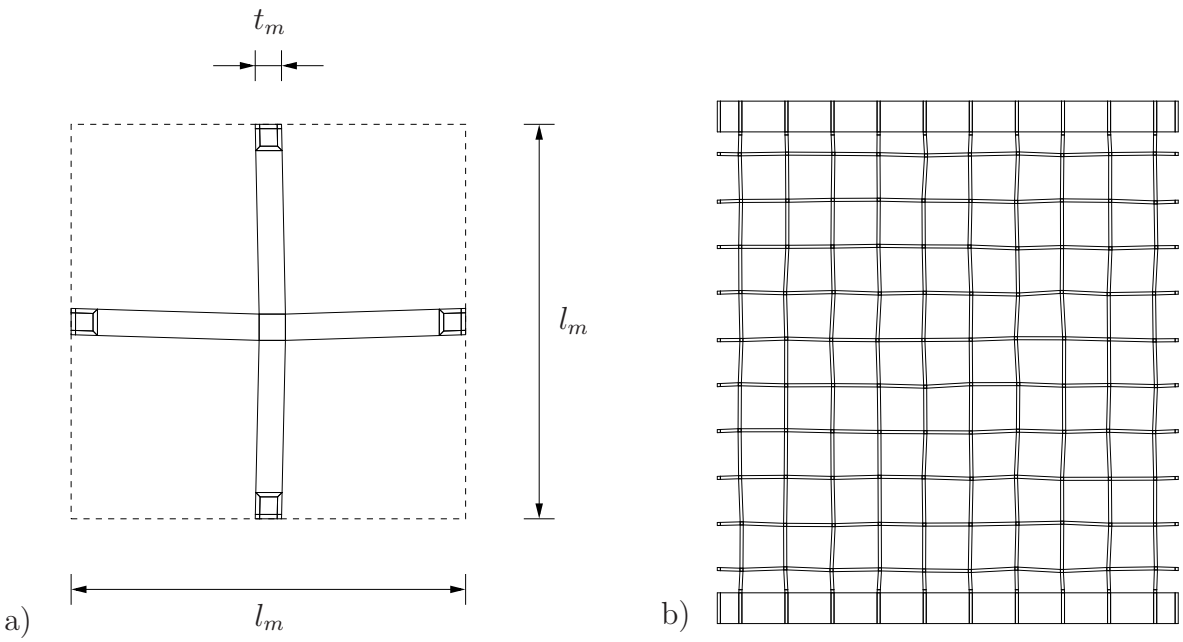

Figure 5.33: a) Disturbed unit cell and b) disturbed sample of the square grid structure ($\delta = 0.2$) [64]

scheme, the overall micromorphic material parameters have been computed evaluating 100 statistically disturbed unit cells. In comparison, the reference computations have also been averaged over 50 statistically disturbed states.

5.1.2.1.2 Shear test

For the shear test in the $\underset{\sim}{E}_{X_M}$ direction, the samples are assumed to be of infinite length $L \to \infty$, see Figure 5.32. Boundaries II and III are subjected to clamping conditions, i.e. no rotations of the beam-like connecting struts can appear. Expressed in terms of the microdeformation tensor of the micromorphic model, the clamping boundary condition reads $\underset{\sim}{\bar{\chi}}_M^{II} = \underset{\sim}{\bar{\chi}}_M^{III} = \underset{\sim}{\mathrm{I}}$. The overall shear stiffness for the squared grid structure has been investigated for increasing overall sample sizes h. As is well-known from the literature, e.g. [19, 94] and various others, this leads to the observation of a boundary layer effect due to clamping conditions which leads to stiffening. The boundary layer is only controlled by the distance to the boundary and, consequently, has the same thickness for small as well as for large samples, refer to Figure 5.34, where n denotes the number of unit cells in the $\underset{\sim}{E}_{Y_M}$ direction and therewith the overall height of the sample $h = n \cdot l_m$.

Besides the decreasing influence of the boundary layer with increasing sample size, one also may notice that the skew-symmetric part of the microdeformation tensor $\underset{\sim}{\bar{\chi}}_M$ is dominant and up to two orders of magnitude more pronounced than the symmetric part. This leads to the conclusion that the micropolar continuum model, by definition assuming an orthogonal microdeformation, should also be able to describe the overall material behavior of a squared grid structure. Indeed, micropolar media accounting for orthotropic material symmetries have been identified in the literature by analytical homogenization of squared grids composed of Bernoulli beam elements, [1, 5, 101].

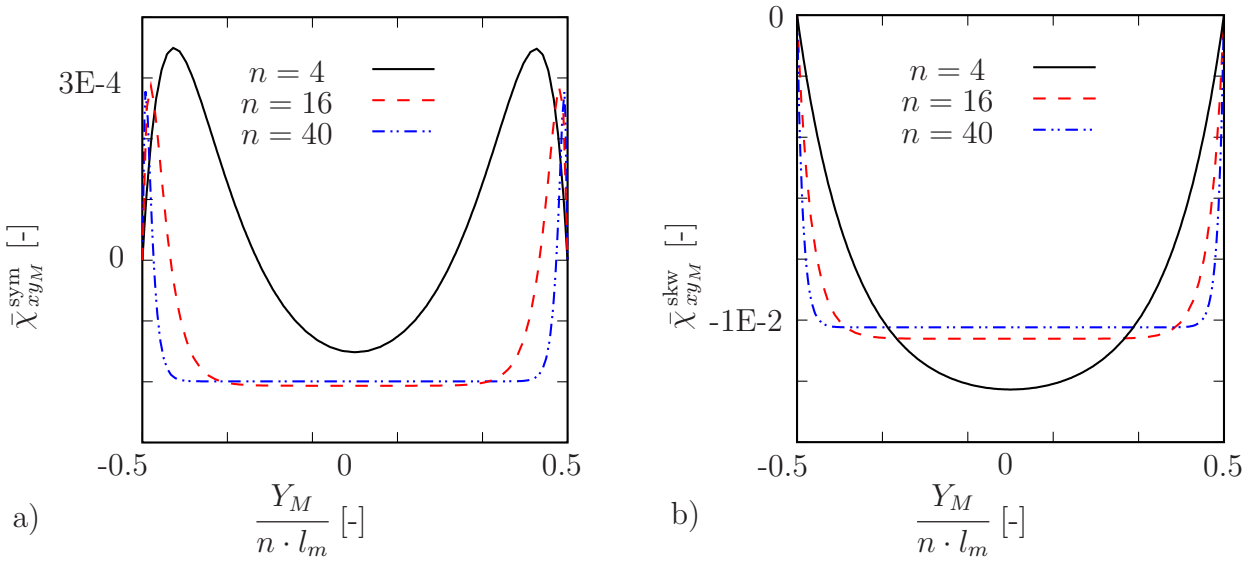

Figure 5.34: Shear test of a squared grid structure. Development of the microshear deformations over the normalized sample height within the FE^2 calculations of the shear test for several sample sizes, a) symmetric, b) skew-symmetric part [64]

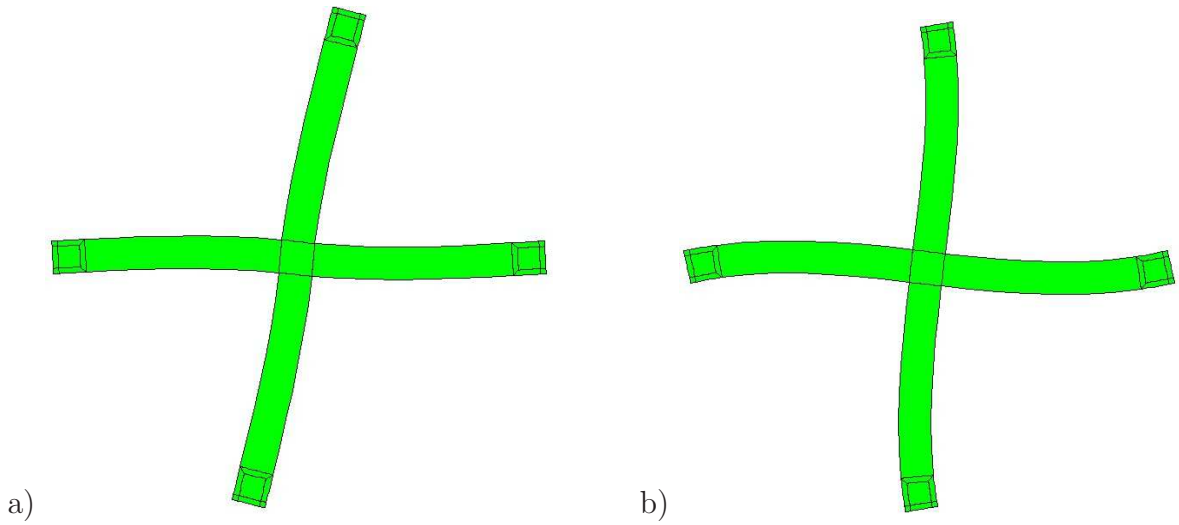

Figure 5.35: Deformed unit cell during shear test, a) center of the sample and b) at the top boundary of the sample. The deformation in a) is fully periodic. Note that this periodicity is achieved without application of any periodic fluctuation field but is only controlled by the cubic loading condition [64].

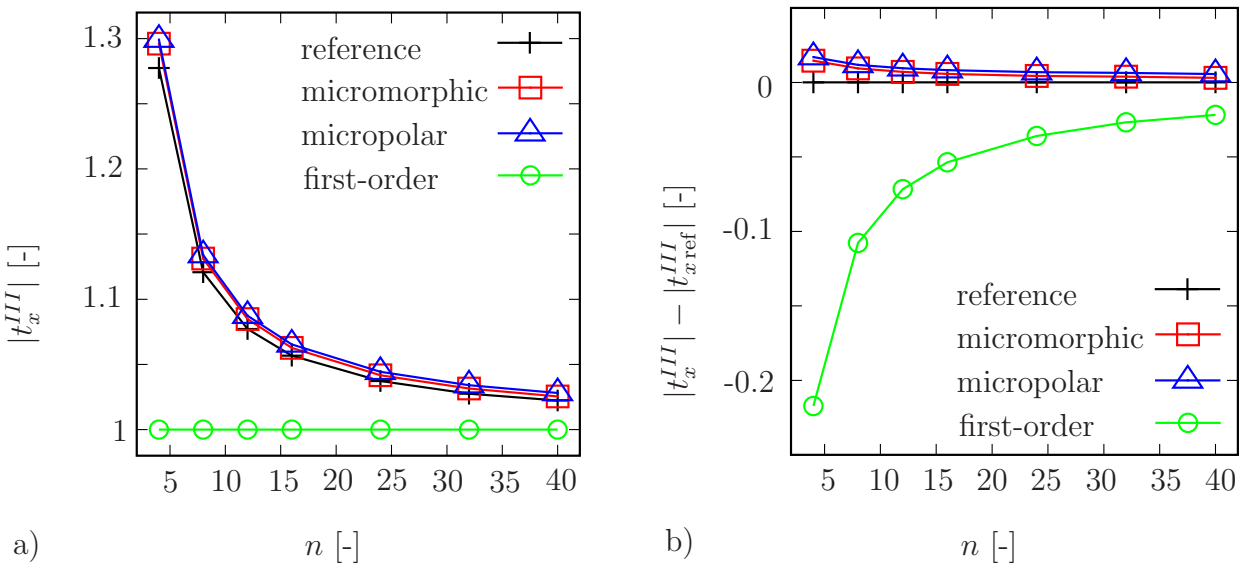

Figure 5.36: Shear test of a squared grid structure ($\delta = 0.3$). a) Normalized traction at surface III. b) Error of the FE^2 calculations relative to the reference solution [64].

In Figure 5.35, two representative deformation states of an undisturbed unit cell as predicted by the numerical homogenization approach are depicted for the shear test a) in the center of the sample and b) close to boundary III, respectively. It is remarkable that the introduced loading condition enriches the deformation modes in such a way that cubic periodicity is represented. Even in the situation Figure 5.35 a) far away from any clamped boundary the interplay between the shear components of the macroscopic displacement gradient on the one hand and the macroscopic microdeformation tensor on the other exhibits a deformation state which totally differs from that of first-order FE^2 linear loading conditions, compare with Figures 5.37 and 5.38. By contrast, the unit cell deformation predicted close to the boundary

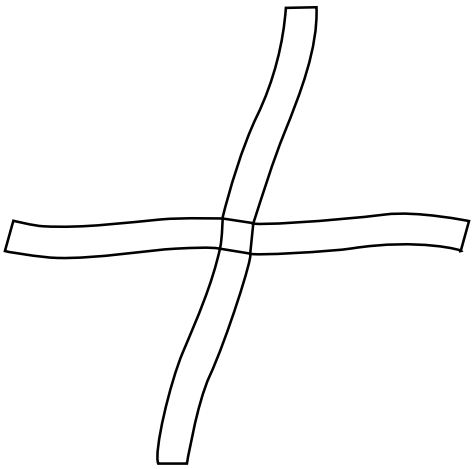

Figure 5.37: State of deformation due to first-order FE^2

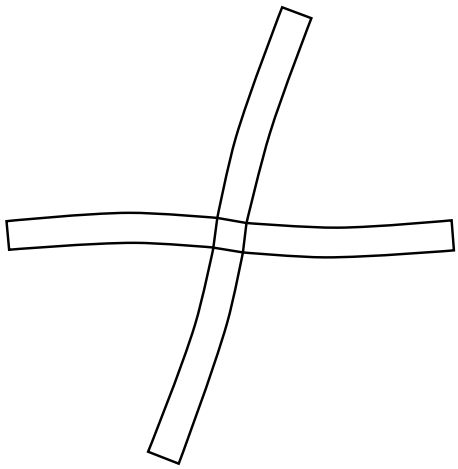

Figure 5.38: State of deformation due to higher-order FE^2

is dominated by bending of the struts similar to that which would be expected in reference

computations.

In order to verify the homogenization model in a quantitative manner, the shear moduli expressed in terms of normalized[3] shear boundary tractions are depicted for different sample sizes n in Figure 5.36. With regard to the reference computation, we observe the stiffening effect due to the boundary layer accounting for up to 27 % ($n = 4$). For increasing sample sizes, the stiffening effect decreases and vanishes for infinite sample heights. Whilst the first-order FE^2 approach is not able to describe bending effects and stiff boundary layers at all, the micromorphic as well as the micropolar homogenized model predict the reference computations with high accuracy even for the smallest sample ($n = 4$). Hence, the micropolar model seems to suffice for the overall modeling of squared grid structures.

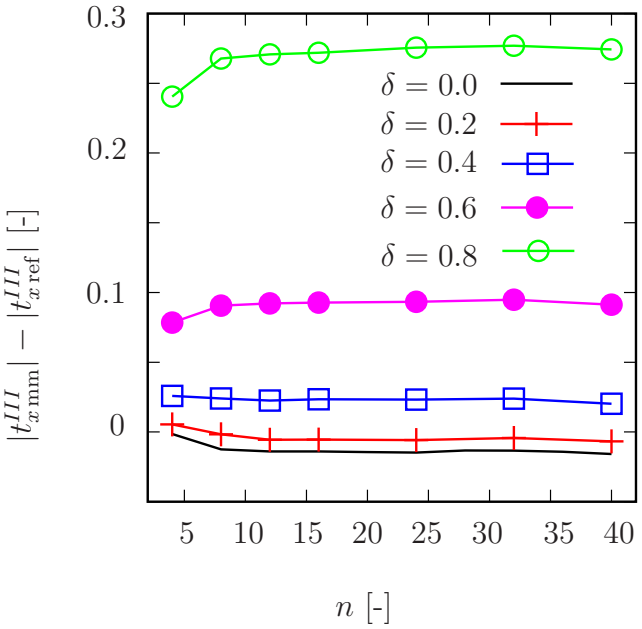

Figure 5.39: Shear test of a single-cross microstructure. Error of the micromorphic FE^2 calculations relative to the reference solution for different disturbance numbers δ [64].

Finally, we would like to discuss the influence of the disturbance. For that reason, the same evaluation as before was carried out with an increasing disturbance measure $0 \leq \delta \leq 0.8$, see Figure 5.39. We have found the quality of the homogenized model to strongly depend on the periodic regularity of the unit cell which is of course violated by the disturbance. For $\delta > 0.4$, this type of polynomial loading condition loses its geometrical relevance and fails.

[3]Note that the normalization is based on the first-order results, i.e. $|t^{III}_x| = t^{III}_x / t^{III}_{x\,\mathrm{first-order}}$.

5.1.2.2 Honeycomb grid structure

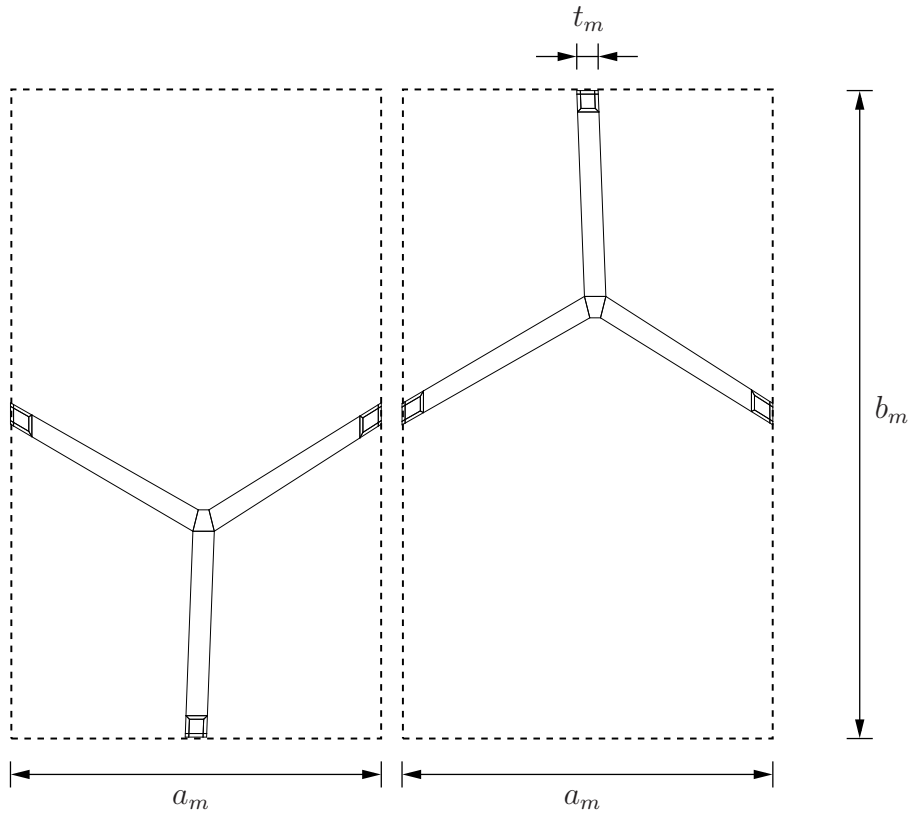

Figure 5.40: Disturbed unit cell of the honeycomb grid structure (δ=0.2). The unit cell is split into two microvolumes with the edge length $a_m = \sqrt{3} \cdot l_m/2$ and $b_m = 3 \cdot l_m/2$, where l_m is the length of the connecting struts in the undisturbed state [64].

5.1.2.2.1 Microtopology

In the sequel, we will discuss the higher-order homogenization scheme applied to honeycomb grid structures. Again, the ideal positions of the grid nodes have been statistically disturbed within a radius $r = 2/3 \cdot \delta \cdot l_m$ around their regular position. For the microscale modeling within the extended FE^2 scheme, two different orientations of grid nodes, resulting in the formulation of two different unit cells, can be found in Figure 5.40. The overall stress response of the microstructure can then be calculated as the average of the two different orientations.

5.1.2.2.2 Shear test

Let us consider first the shear test in the $\underset{\sim}{E}_{X_M}$ direction with $L \to \infty$, compare with Figure 5.32, where $h = 3/2 \cdot n \cdot l_m$. At boundary II and III, clamping conditions are prescribed, i.e. $\bar{\underset{\sim}{\chi}}{}^{II}_M = \bar{\underset{\sim}{\chi}}{}^{III}_M = \underset{\sim}{\mathrm{I}}$ in terms of the overall micromorphic model. In Figure 5.41, the shear components of the microdeformation tensor predicted by the homogenization approach are plotted over the sample height for different values n. Similar to the squared grid structure, we observe a pronounced size effect, dependent on the stiff boundary layer. But when comparing the results for $\bar{\chi}_{xy_M}$ and $\bar{\chi}_{yx_M}$, we do not observe any symmetry or skew-symmetry of the microdeformation tensor $\bar{\underset{\sim}{\chi}}_M$, either within the boundary layer or within the regions not

influenced by the clamping boundary conditions.

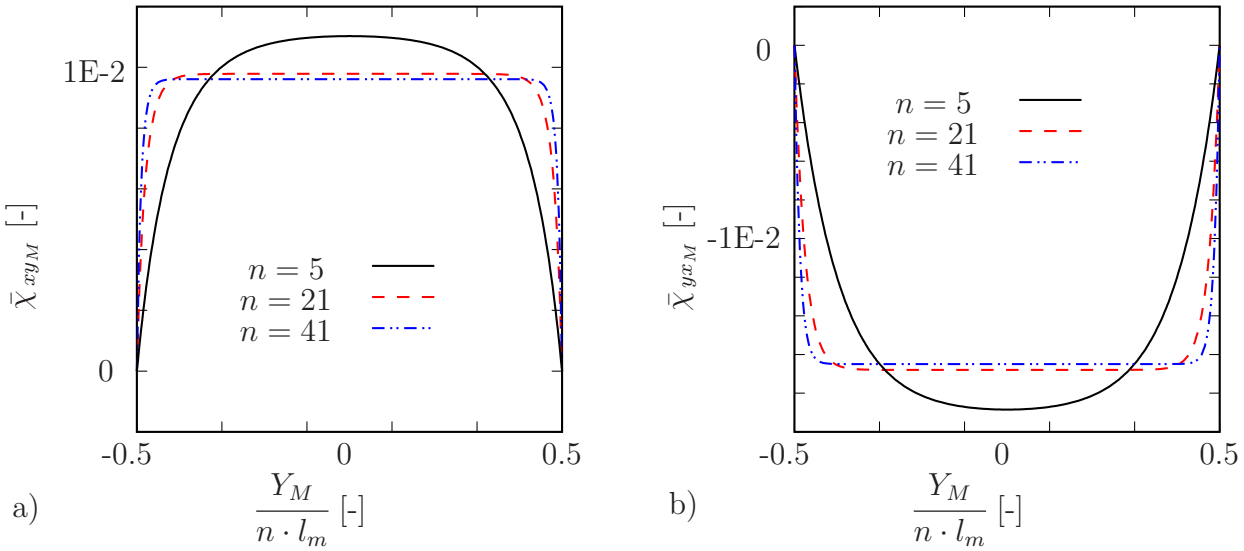

Figure 5.41: Shear test of a honeycomb microstructure. Development of the microshear deformations over the normalized sample height within the FE^2 calculations of the shear test for several sample sizes, a) $\bar{\chi}_{xy_M}$, b) $\bar{\chi}_{yx_M}$ [64].

Thus, for the proposed homogenization methodology with the introduced polynomial loading condition, the micropolar continuum model is not able to describe the micromechanical deformation processes of honeycomb structures in an adequate way. This result agrees with results found in the literature, e.g. [83, 95], where the authors were unable to identify micropolar material parameters for honeycomb structures in an unique way.

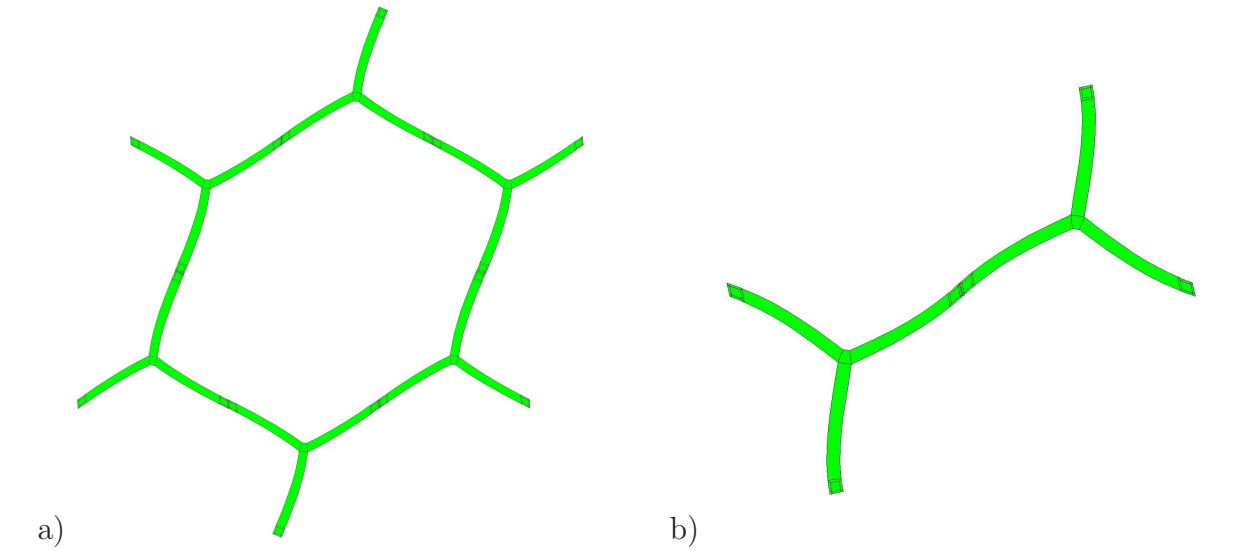

Figure 5.42: Deformed set of unit cells observed a) in the center b) on the top boundary of the sample. The unit cell in Figure a) is artificially continued due to the periodicity of the observed deformation states. Again, no further periodic fluctuations but the cubic projection polynomial have been taken into account [64].

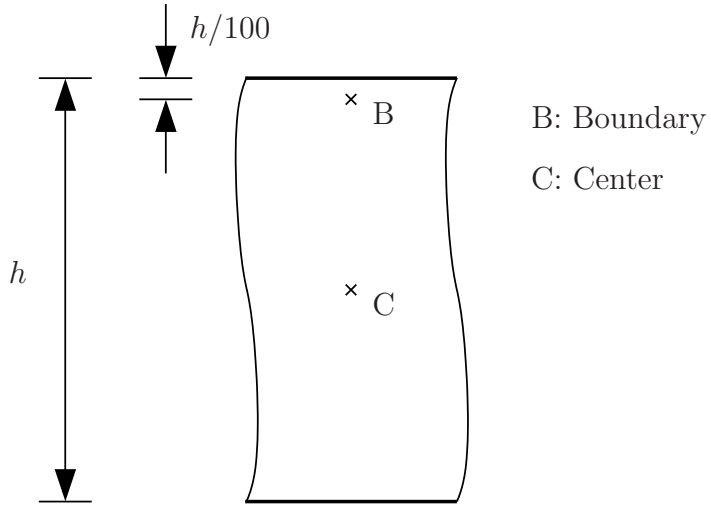

Figure 5.43: Positions of the deformed microstructures of Figure 5.42 in the sample

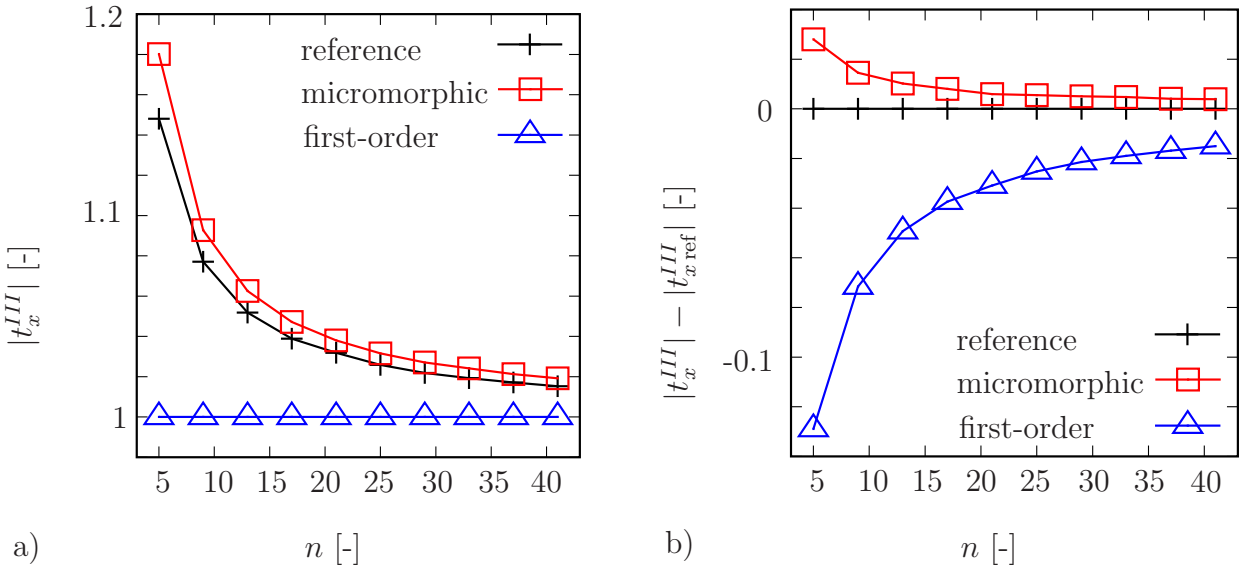

Figure 5.44: Shear test of a honeycomb microstructure ($\delta = 0.2$). a) Normalized traction at surface III. b) Error of the FE^2 calculations relative to the reference solution [64].

The deformation states predicted by the homogenized model are projected onto the unit cells and the resulting deformation patterns are visualized in Figures 5.42 a) and b) for the situation in the center of the sample and close to the boundary, respectively, see Figure 5.43 for the corresponding positions. In order to demonstrate the periodic character of the cubic deformation modes, the unit cell has been periodically continued for the former case. Note that, again, no fluctuations in addition to the polynomial loading conditions are taken into account.

Finally, let us quantitatively compare the effective shear modulus predicted by the homogenized model in comparison to the reference calculation. In Figure 5.44, the normalized surface traction is plotted versus the number of unit cells in vertical direction ($\delta = 0.2$). For $n = 5$ we observe a stiffening effect of about 1.15 compared to the (nearly) clamping free state at $n = 40$. Whereas the first-order FE^2 model accounting for linear loading conditions is only able to predict the (nearly) clamping-free state, the micromorphic homogenized model leads to reasonable results even for small sample sizes.

Due to the kinematical misfit of the micropolar overall continuum model, the homogenized model overestimates the stress responses which are not depicted here.

5.1.2.2.3 Bending test of a sandwich panel

In the following, we will extend the complexity of the macroscopic boundary value problem towards bending-dominated loading. The overall size of the sample is chosen to be $L = 16 \cdot \sqrt{3} \cdot l_m$ and $h = 3/2 \cdot n \cdot l_m$. In Figure 5.45 a fully resolved microstructure for reference computations is shown for $n = 9$.

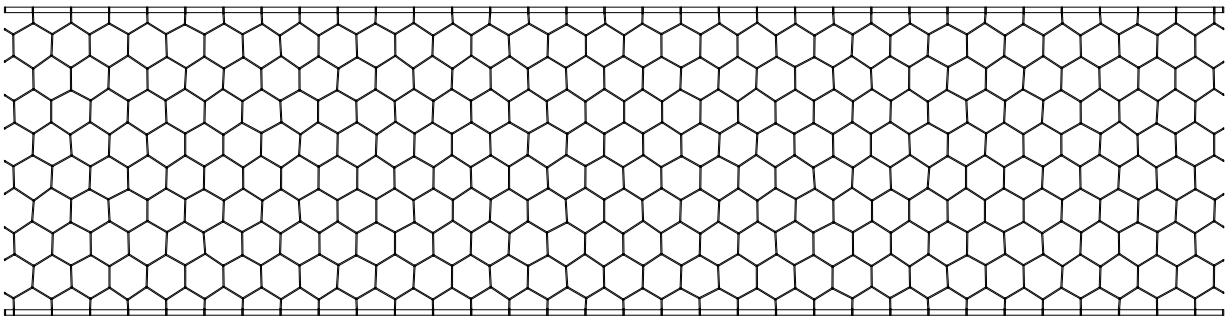

Figure 5.45: Sandwich structure: Microscopic resolution for $n = 9$ with $\delta = 0.2$

The left and the right boundaries I and IV are clamped. The top and the bottom boundaries II and III are glued to thin surface sheets ($E = 70\,\mathrm{GPa}$, $\nu = 0.3$) of thickness $t_m = 0.5\,mm$ such that clamping can also be assumed between the surface sheets and the cellular core. For the bending process, the right boundary IV undergoes the vertical displacement $u_{y_M} = -0.01\,mm$.

The components of the microdeformation tensor as predicted by the homogenized model are depicted in Figure 5.46. At first, one may observe that there are boundary layers active at

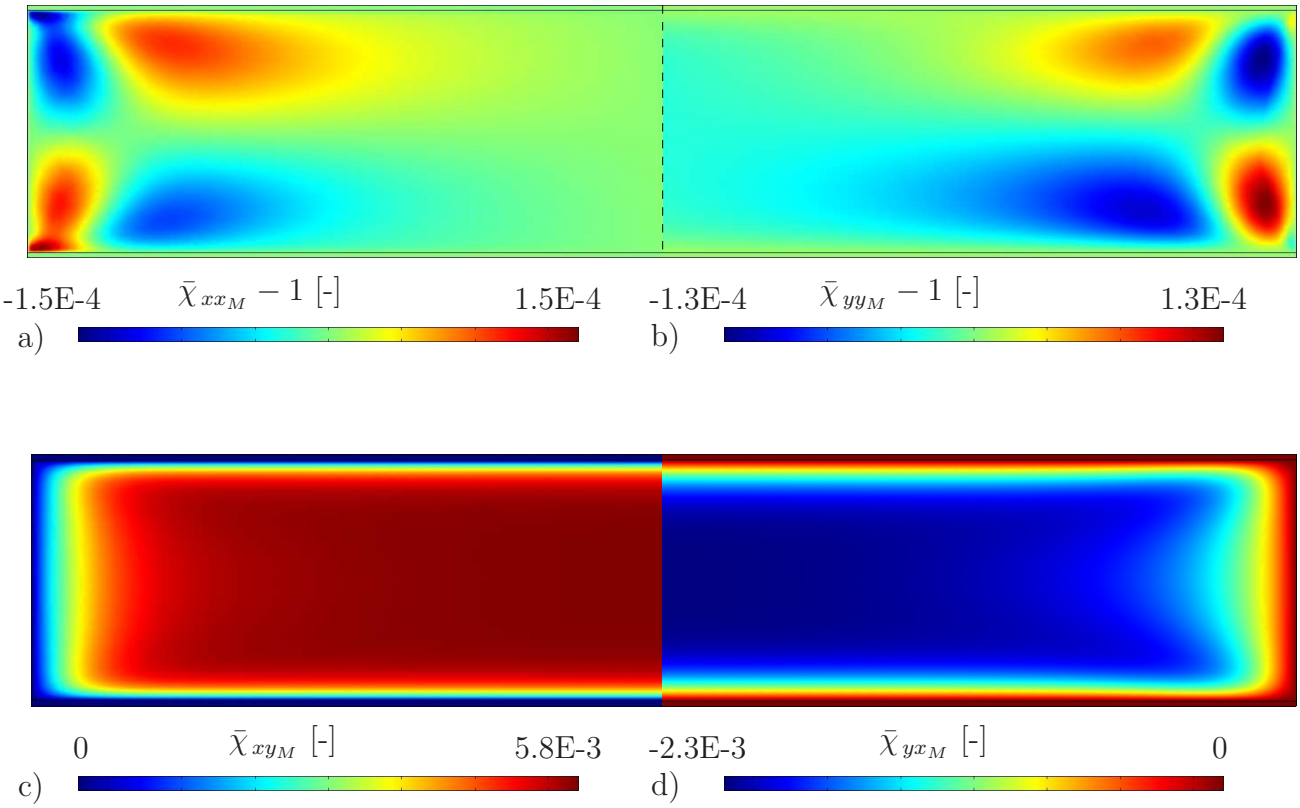

Figure 5.46: The four components of the microdeformation tensor $\bar{\underset{\sim}{\chi}}_M$ observed in the sandwich bending test for $n = 9$. Note that for visualization purposes the height has been scaled by $1.\bar{6}$ [64].

the clamped boundaries as well as at the glued surface sheets, compare with Figures 5.46 c) and d) for the microshear deformations. Again, the microshear deformations do not exhibit any symmetry or skew-symmetry. However, additional microstretch deformations can be observed, see Figures 5.46 a) and b), i.e. the micromechanical deformation behavior is much more complex than can be described by the micropolar continuum model within the proposed homogenization framework.

Finally, Figure 5.47 shows a quantitative comparison between the reference calculation and the homogenized model. As long as the structure is not chosen too small ($n > 4$ in the $\underset{\sim}{E}_{Y_M}$ direction), the stiffening effect due to the boundary layers by clamping are predicted in a highly accurate manner whereas the classical first-order approach is not sensitive to these effects by definition.

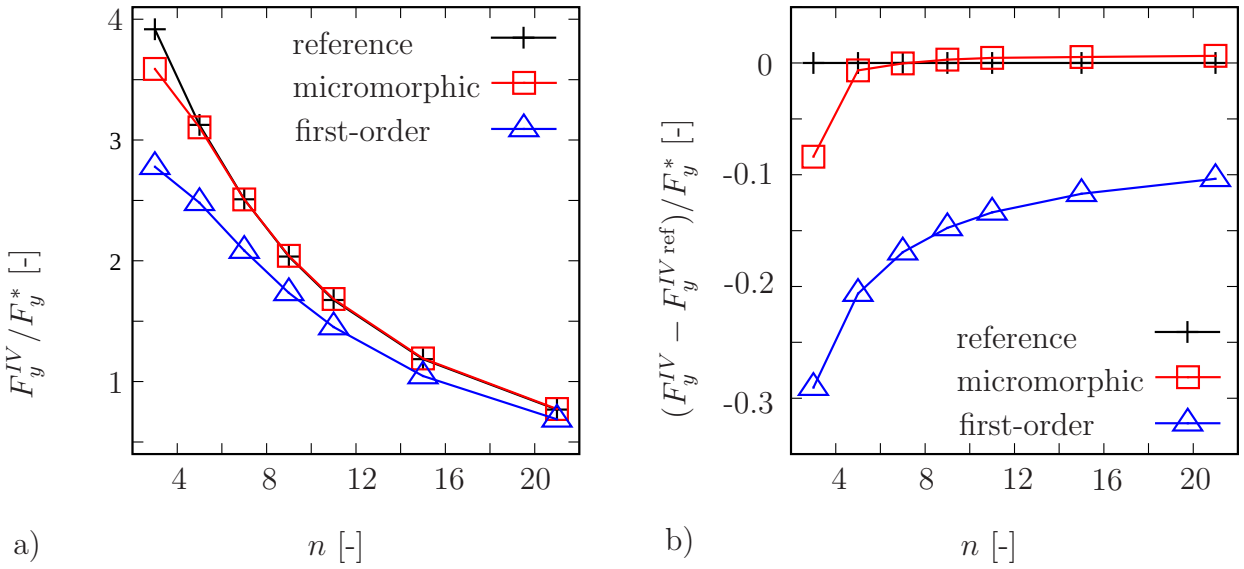

Figure 5.47: Bending test of the sandwich structure ($\delta = 0.2$). a) Reaction force in $\underset{\sim}{E}_{Y_M}$-direction on surface IV normalized with respect to a compact sample of the same mass as the compound. b) Error of the FE^2 calculations with respect to the reference solution [64].

5.1.2.3 Some remarks

In the numerical examples, the soundness of the proposed cubic loading conditions has been investigated for slightly disturbed periodic grid structures. In the shear test, it has been found that for squared grid structures the micromorphic as well as the micropolar homogenized model lead to reasonable results as long as the disturbances are not too large. In particular, stiffening effects due to boundary layers have been predicted in a very accurate manner. However, we have observed an increasing error in the homogenized model when increasing the disturbance parameter.

In an analogous way, the homogenized model has been applied to a disturbed honeycomb structure. Whereas the micropolar restriction has been found not to be the ideal choice due to the missing skew-symmetry of the microdeformation tensor, only the full micromorphic substitute

medium has been studied. For small disturbances, the homogenized model has produced reasonable results for the shear test as well as for the additional bending test of a sandwich panel.

Altogether, it has been demonstrated that the introduced homogenization approach is able to describe the micromechanical deformation mechanisms of the investigated grid structures in terms of overall extended deformation quantities and the related overall stresses. However, the proposed homogenization scheme has not been found to be very robust against statistical disturbances. Thus, a certain regularity of the microstructure is required and the periodicity should not be disturbed too much. One-to-one applicability to really stochastic cellular structures, e.g. found by VORONOI tessellation, can not be expected. This can be explained by the special choice of the cubic loading conditions accounting for a symmetry point at the center of each boundary of the unit cell. For slender structures, the cubic part of the loading condition describes a rotation of this symmetry point. Of course, this rotation is sound for the investigated unit cells, where connecting struts have been cut just in these boundary midpoints. For arbitrary cellular unit cells, this geometrical interpretation of the cubic parts as rotations loses its meaning because the connecting struts are then cut at arbitrary positions of the boundary of the unit cell which are in general not identical to the midpoints of these boundaries.

5.2 Three-dimensional numerical homogenization - effective material parameters

In this section the method for extracting effective material parameters, refer to section 4.3, is verified by numerical studies. Afterwards a short introduction to sandwich structures is given. Since in this thesis sandwich materials with cellular cores are dealt with, guidelines for extracting effective material parameters of such cores, i.e. of foams, will be developed. The numerical results are compared to experimental data and finally a complex sandwich structure is considered.

5.2.1 Verification of the proposed method

In order to verify the method as developed in section 4.3 we numerically investigate heterogeneous solid-like materials. Heterogeneous materials consist of at least two different materials like, for example, a matrix material with pores (no material) or inclusions. In this case one defines the volume fraction as

$$\varphi_V = \frac{V_{\text{pores/inclusions}}}{V_{\text{total}}} \cdot 100 \quad [\%] \,. \tag{5.3}$$

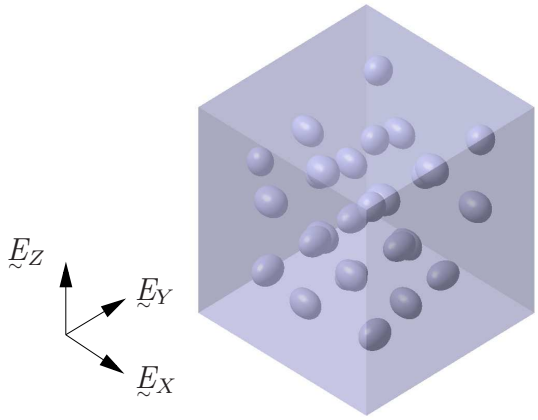

Figure 5.48: Material with randomly distributed pores

5.2.1.1 Geometry and BVPs

The materials are represented utilizing an *implicit* description of the geometry [24]. The overall dimensions are l^3, where $l = 10\,mm$. The first material consists of a matrix with randomly distributed ellipsoids with $\varphi_V = 3\,\%$, see Figure 5.48.

The second one can be regarded as a unidirectional fiber reinforced composite where the fibers are parallel to $\underset{\sim}{E}_X$ with $\varphi_V = 18\,\%$, compare with Figure 5.49.

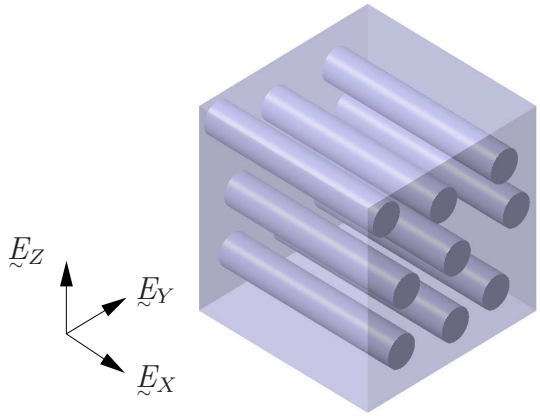

Figure 5.49: Unidirectional fiber reinforced composite

In both cases, the linear elastic material parameters of the matrix are YOUNG's modulus $E_{\text{matrix}} = 5000\,\text{MPa}$ and POISSON's ratio $\nu_{\text{matrix}} = 0.3$. For the ellipsoids, two cases are considered:

- pores (no material), i.e. $E_{\text{pores}} = 0.0\,\text{MPa}$ and $\nu_{\text{pores}} = 0.0$.
- stiffer material, i.e. $E_{\text{inc}} = 10 \cdot E_{\text{matrix}} = 50\,\text{GPa}$ and $\nu_{\text{inc}} = 0.3$.

For the fibers we choose $E_{\text{fiber}} = E_{\text{inc}}$ and $\nu_{\text{fiber}} = \nu_{\text{inc}}$.

In Figure 5.50 the surfaces of the materials are labeled by indices which will be used for the definition of boundary conditions.

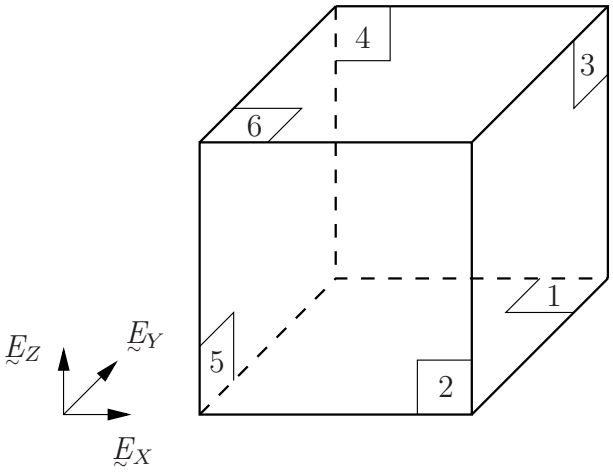

Figure 5.50: Surface indices for materials of Figures 5.48 and 5.49

We investigate two load cases, namely *uniaxial compression* and *general three-dimensional loading*, as summarized in Table 5.1.

Table 5.1: Load cases, boundary conditions, and loads of the macroscopic BVPs

		Surface					
Load case	Volume load	1	2	3	4	5	6
1: *Uniaxial compression*	no	$\bar{u}_z = 0$	free	free	$\bar{u}_y = 0$	$\bar{u}_x = 0$	$\bar{t}_z = -100$
2: *General loading*	$\bar{f}_x = 300$ $\bar{f}_y = 200$ $\bar{f}_z = 100$	$\bar{u}_z = 0$	free	free	$\bar{u}_y = 0$	$\bar{u}_x = 0$	free

The BVPs are solved

- with effective materials properties. To this end $\mathbf{C}^{\text{eff}}$s are extracted by Algorithm A-2 in combination with the FCM first and then applied to a macroscopic computation using classical p-FEM.
- directly
  - by the FCM and
  - by classical h-FEM using the commercial FE-Solver *Marc*[4].

5.2.1.2 Effective material parameters

We start with the extraction of effective material parameters: The domain Ω_{sub}, see Figure 4.11, is resolved by a grid of c^3 cells, whereby $c = 8$ corresponds to the coarse grid and $c = 16$ corresponds to the fine one. For the window's thickness we choose $t_{\text{win}} = \{\, 0.1, 1, 2, 3 \,\}$. The polynomial degree of all elements and cells varies from $p = 1, \ldots, 8$ for the coarse grid and from $p = 1, \ldots, 6$ for the fine grid. In all of the computations the *trunk space* is applied. For an accurate integration the number of Gaussian points in one direction is set to 20 for all cases and the finite cells are subdivided automatically into subcells, until the error in the volume is below 0.1 %, refer to Figure 3.22. The tolerance of Algorithm A-2 is set to 10^{-4} resulting in 2 to 6 iteration steps per window thickness.

Before we discuss the effective material matrices $\mathbf{C}^{\text{pores}}$, $\mathbf{C}^{\text{inc}}$, and $\mathbf{C}^{\text{fiber}}$ let us perform some preliminary studies first[5]. In these studies we investigate the influence of the window's thickness and of the polynomial degree by investigating $\mathrm{C}_{ii}^{\text{pores}}$, $i = 1, \ldots, 3$, and $c = 8$.

[4] *Marc* is a trademark of MSC Software Corporation, 2 MacArthur Place, Santa Ana, California 92707, US.
[5] Note that in order to ease the notation, the superscript 'eff' has been skipped.

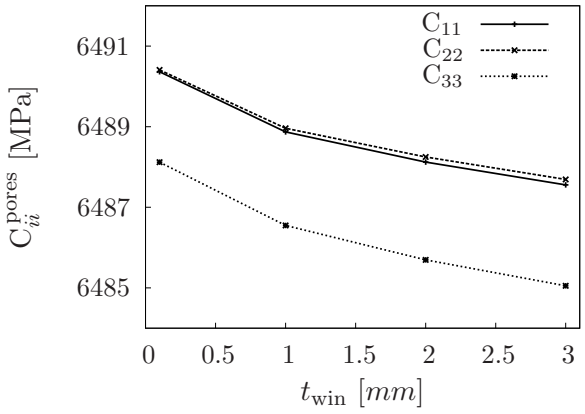

Figure 5.51: C_{ii}^{pores} vs. t_{win} for $c = 8$ and $p = 1$

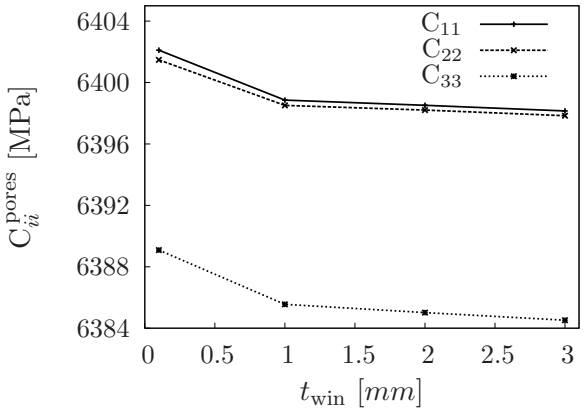

Figure 5.52: C_{ii}^{pores} vs. t_{win} for $c = 8$ and $p = 3$

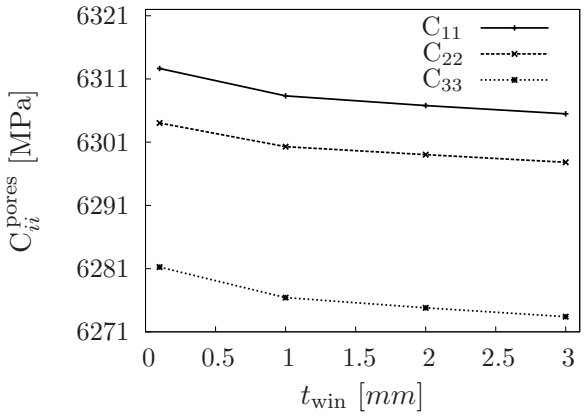

Figure 5.53: C_{ii}^{pores} vs. t_{win} for $c = 8$ and $p = 6$

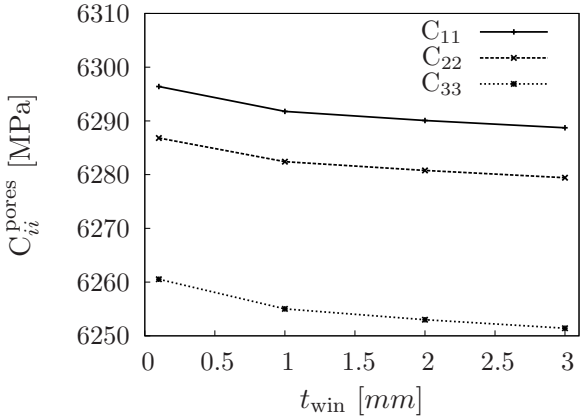

Figure 5.54: C_{ii}^{pores} vs. t_{win} for $c = 8$ and $p = 8$

In Figures 5.51 to 5.54 C_{ii}^{pores} for $c = 8$ is plotted against the window's thickness for different polynomial degrees. We realize that the window's influence is small especially when going to higher polynomial degrees, and from $t_{\text{win}} = 2\,mm$ there is nearly no change in C_{ii}^{pores}. Note that all other combinations of materials and resolutions indicated this fact, too. Thus, we choose $t_{\text{win}} = 2\,mm = l/5$ in what follows.

Next, C_{ii}^{pores}, C_{ii}^{inc}, and C_{ii}^{fiber} are plotted against the number of degrees of freedom N, refer to Figures 5.55 till 5.60. Comparing the C_{ii} obtained by the two grid resolutions and taking into account the number of degrees of freedom one can state that there is not that much difference at least for the higher polynomial degrees.

In order to give an impression about the speed of convergence in the effective values we exemplarily[6] consider $\mathbf{C}^{\text{fiber}}$ with $c = 8$ and $p = 8$. Here, we plot in single-logarithmic style

[6]Note that one observes similar behavior in the other examples, too.

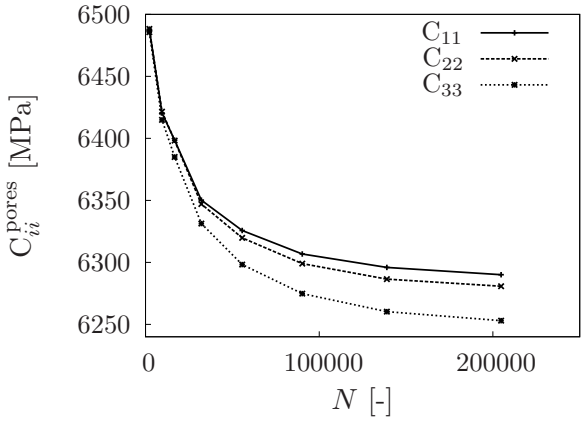

Figure 5.55: C_{ii}^{pores} vs. N for $c = 8$ and $t_{win} = 2\,mm$

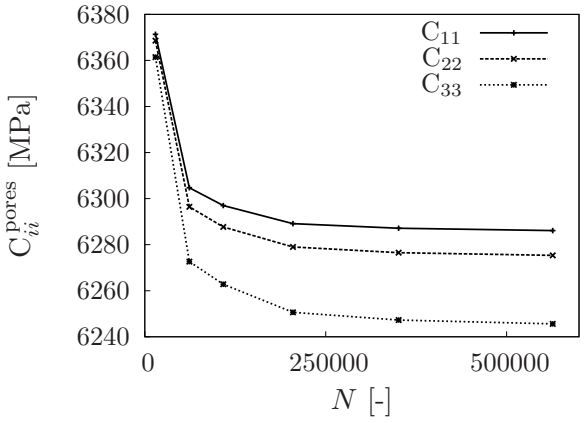

Figure 5.56: C_{ii}^{pores} vs. N for $c = 16$ and $t_{win} = 2\,mm$

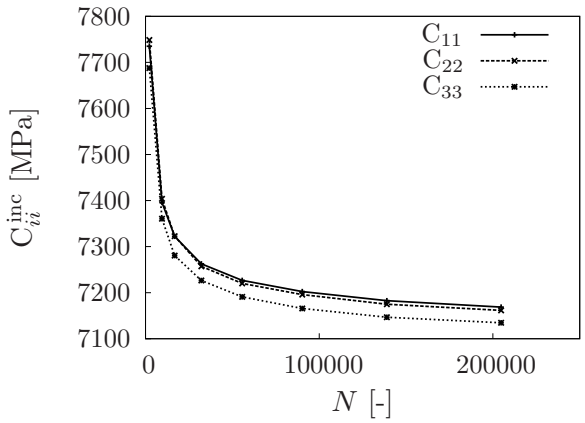

Figure 5.57: C_{ii}^{inc} vs. N for $c = 8$ and $t_{win} = 2\,mm$

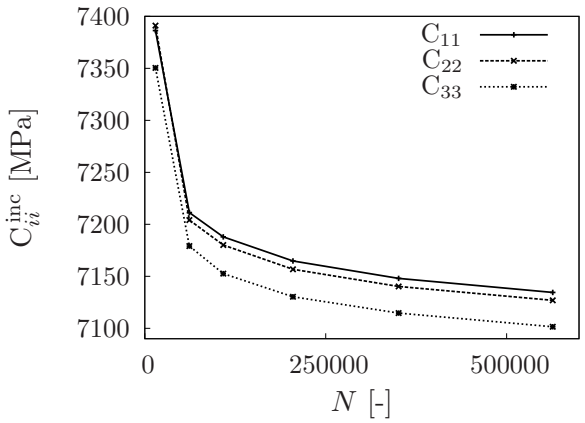

Figure 5.58: C_{ii}^{inc} vs. N for $c = 16$ and $t_{win} = 2\,mm$

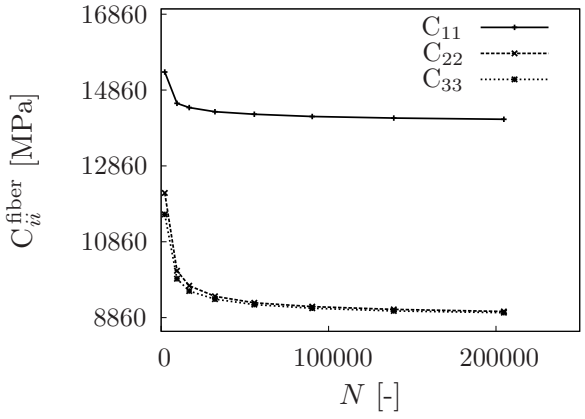

Figure 5.59: C_{ii}^{fiber} vs. N for $c = 8$ and $t_{win} = 2\,mm$

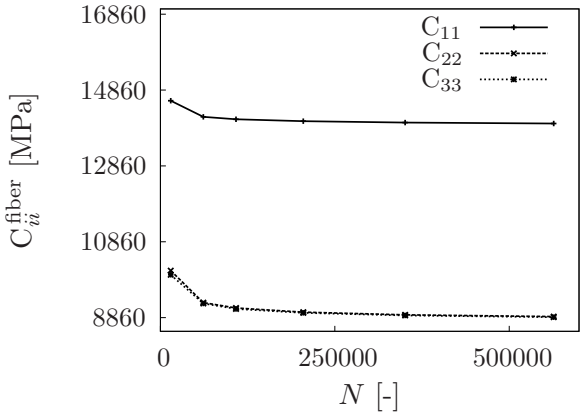

Figure 5.60: C_{ii}^{fiber} vs. N for $c = 16$ and $t_{win} = 2\,mm$

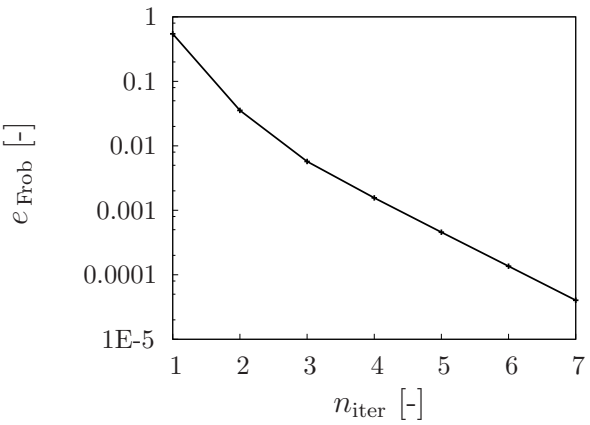

Figure 5.61: e_{Frob} vs. n_{iter}, again $c = 8$, $p = 8$ and $t_{\text{win}} = 2\,mm$

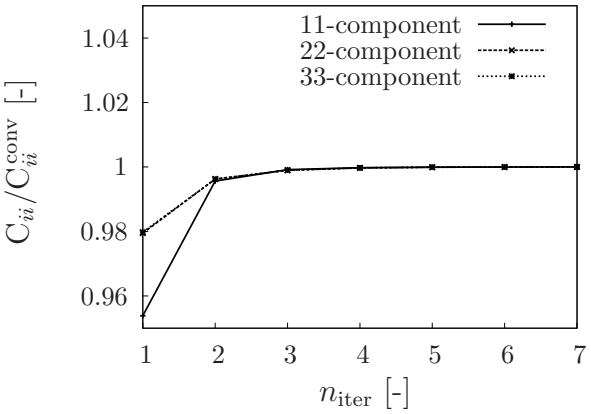

Figure 5.62: Normalized entries of C_{ii}^{inc} vs. n_{iter}, again $c = 8$, $p = 8$ and $t_{\text{win}} = 2\,mm$

the error in the FROBENIUS norm

$$e_{\text{Frob}} = \frac{\left\|\mathbf{C}^{\text{new}} - \mathbf{C}^{\text{old}}\right\|_{\text{Frob}}}{\left\|\mathbf{C}^{\text{old}}\right\|_{\text{Frob}}}$$

against the number of iterations n_{iter}, see Figure 5.61. In addition we investigate the convergence of the coefficients C_{ii}^{fiber} normalized by their corresponding converged values, where $i = 1, \ldots, 3$, refer to Figure 5.62. In both cases a fast convergence of the corresponding quantities can be observed. However, the FROBENIUS-norm is more restrictive and thus its application as a break-off criterion for our homogenization algorithm is justified.

Finally, we discuss the effective elasticity matrices. To this end we focus on the matrices related to the best approximation[7], i.e. with $p = 6$ and the fine grid ($c = 16$), which read

$$\mathbf{C}^{\text{pores}} = \begin{bmatrix} 6.28613 \cdot 10^3 & 2.63488 \cdot 10^3 & 2.62909 \cdot 10^3 & -1.19652 \cdot 10^0 & -2.76569 \cdot 10^{-1} & -3.06974 \cdot 10^0 \\ & 6.27533 \cdot 10^3 & 2.62677 \cdot 10^3 & -1.44268 \cdot 10^0 & -1.80284 \cdot 10^0 & -1.35254 \cdot 10^0 \\ & & 6.24562 \cdot 10^3 & -4.55691 \cdot 10^{-1} & -2.24396 \cdot 10^0 & -2.88244 \cdot 10^0 \\ & & & 1.81582 \cdot 10^3 & -5.18662 \cdot 10^{-1} & 3.32434 \cdot 10^{-1} \\ & & & & 1.80987 \cdot 10^3 & -2.13020 \cdot 10^{-1} \\ & \text{sym} & & & & 1.81167 \cdot 10^3 \end{bmatrix},$$

$$\mathbf{C}^{\text{inc}} = \begin{bmatrix} 7.13213 \cdot 10^3 & 3.01345 \cdot 10^3 & 3.01263 \cdot 10^3 & -4.78127 \cdot 10^{-1} & 8.26561 \cdot 10^{-1} & -7.21965 \cdot 10^{-1} \\ & 7.12445 \cdot 10^3 & 3.01197 \cdot 10^3 & -1.02383 \cdot 10^0 & -1.08522 \cdot 10^0 & 1.78403 \cdot 10^{-1} \\ & & 7.09903 \cdot 10^3 & 7.30914 \cdot 10^{-2} & -6.33184 \cdot 10^{-1} & -6.49574 \cdot 10^{-1} \\ & & & 2.04494 \cdot 10^3 & -4.46000 \cdot 10^{-2} & 5.82035 \cdot 10^{-1} \\ & & & & 2.03983 \cdot 10^3 & -6.79149 \cdot 10^{-3} \\ & \text{sym} & & & & 2.04140 \cdot 10^3 \end{bmatrix},$$

[7]Note that the other matrices have the same structure but differ in the absolute values.

and

$$\mathbf{C}^{\text{fiber}} = \begin{bmatrix} 1.39782 \cdot 10^4 & 3.79747 \cdot 10^3 & 3.79499 \cdot 10^3 & 0 & -4.53954 \cdot 10^0 & 0 \\ & 8.88768 \cdot 10^3 & 3.64284 \cdot 10^3 & 0 & -9.61436 \cdot 10^{-1} & 0 \\ & & 8.87197 \cdot 10^3 & 0 & -1.94896 \cdot 10^1 & 0 \\ & & & 2.72241 \cdot 10^3 & 0 & -3.88516 \cdot 10^0 \\ & & & & 2.52220 \cdot 10^3 & 0 \\ & \text{sym} & & & & 2.71572 \cdot 10^3 \end{bmatrix}.$$

We realize that all of the matrices indicate anisotropic material behavior. However, this behavior is small for the porous and the inclusion material when comparing the absolute values like, for example, C_{13}^{pores} with C_{15}^{pores} or C_{13}^{inc} with C_{14}^{inc}. In $\mathbf{C}^{\text{fiber}}$ the 11-direction is more pronounced which is, of course, due to fiber reinforcement.

5.2.1.3 Solution of the BVPs and comparison

After having determined all effective material matrices in the previous section we can solve the macroscopic BVPs defined in Table 5.1. Let us recall the different solution techniques and give more details:

- In the case of effective material parameters, the underlying p-FEM mesh consists of $(2 \times 2 \times 2) = 8$ equal standard hexahedral elements using the *trunk* space which leads to a very low number of degrees of freedom. Since effective material matrices as computed in the previous section are applied, this discretization is sufficiently accurate.

- For the pure FCM approach, the cell grids, the number of GAUSSIAN points, and the parameters for controlling the subcells correspond to the ones of section 5.2.1.2, and again the *trunk* space is applied.

- In the h-version approach we use ten-noded fully integrated tetrahedral elements and 15-noded fully integrated pentahedrals; to be more specific we have 27582 to 222719 tetrahedrals for the porous material, 35235 to 311464 tetrahedrals in the case of inclusions, and 5824 to 90916 pentahedrals in the fiber example. In Figures 5.63 to 5.66 the coarsest and the finest mesh are shown. Note that the meshes for the porous domain are not displayed since they are similar to the ones with the inclusions.

For comparing the quality of the different approaches the strain energy, refer to Equation (3.49), is plotted against the number of degrees of freedom N in Figures 5.67 to 5.72.

For the porous material there is a very good agreement of the strain energy between the different solution approaches especially for load case 1, see Figures 5.67 and 5.68. Notice that for the computation with effective material parameters, the strain energy is nearly constant during the p-extension. The reason for this is twofold: On the one hand $\mathbf{C}^{\text{pores}}$ is constant in all integration points and on the hand the material's anisotropy is not that pronounced, both of which lead to a quasi-homogeneous solution.

In load case 2 there is a very small but systematic deviation of the solution with effective parameters from the other ones, because the pore's influence on the overall volume load can

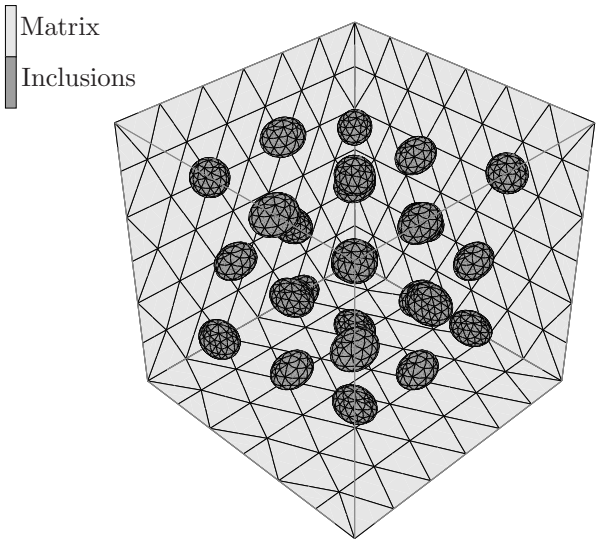

Figure 5.63: h-version: Coarsest mesh for the material with inclusions

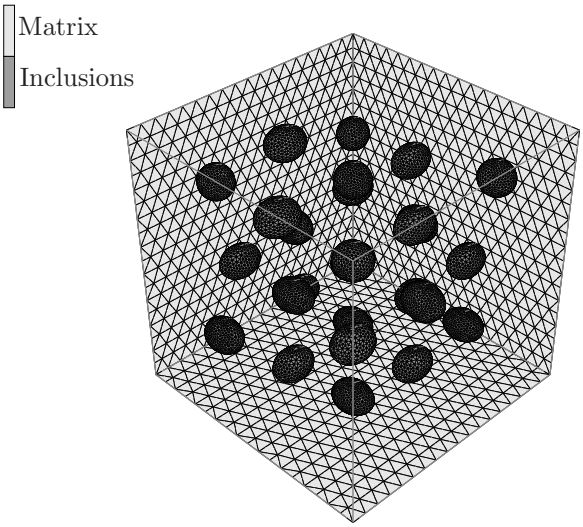

Figure 5.64: h-version: Finest mesh for the material with inclusions

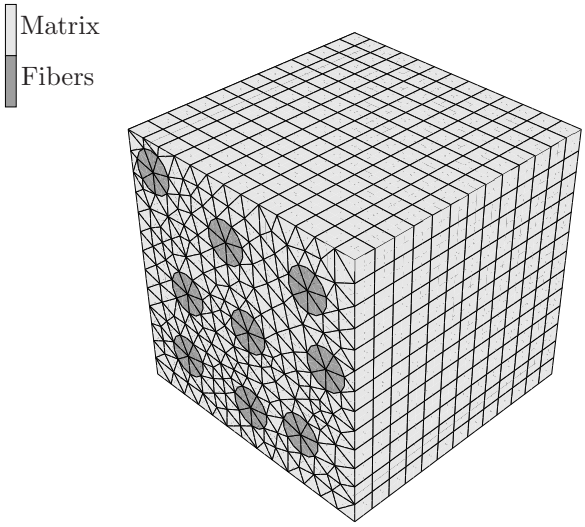

Figure 5.65: h-version: Coarsest mesh for the fiber reinforced material

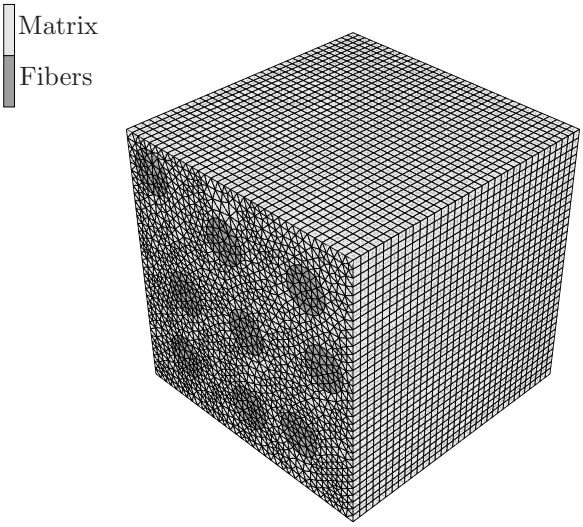

Figure 5.66: h-version: Finest mesh for the fiber reinforced material

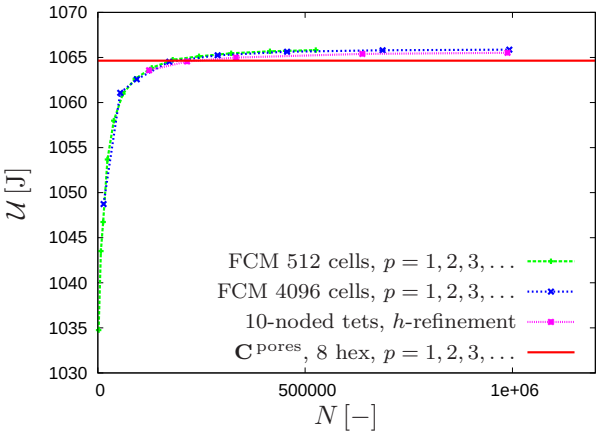

Figure 5.67: Load case 1: Strain energy for the porous material

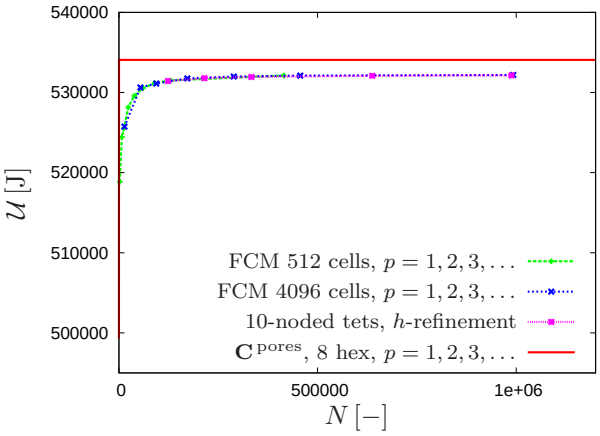

Figure 5.68: Load case 2: Strain energy for the porous material

only be approximated. To this end the volume loads in the effective computation are reduced by the pore's volume fraction, i.e. it is multiplied by 0.97.

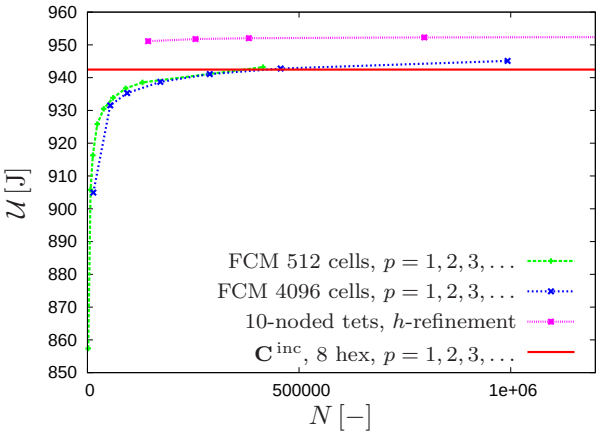

Figure 5.69: Load case 1: Strain energy in case of inclusions

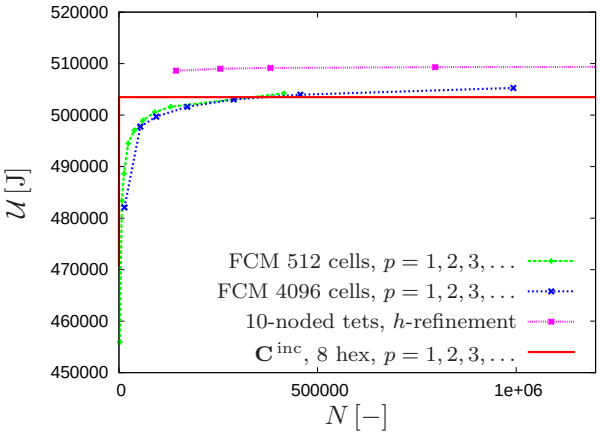

Figure 5.70: Load case 2: Strain energy in case of inclusions

In the example considering inclusions the pure FCM and the effective approach lead to similar results but seem to deviate slightly from the h-version, refer to Figures 5.69 and 5.70. This deviation stems from the fact that the material interfaces which lead to kinks in the displacement field are not resolved by the (CARTESIAN) FCM-grid. Of course, one could adjust the cells such that they match with the interfaces. If this were done the main advantage of the FCM, namely fast and simple grid generation, would be lost. However, when looking at the absolute values one can state that the deviation is negligible, i.e. it is about 1.3 % for load case 2.

There are some differences between the three approaches in the fiber example, compare with Figures 5.71 and 5.72. If we take the h-version solution as a reference the maximum error is about 2.7 %. This error occurs for load case 2 when computing with effective material param-

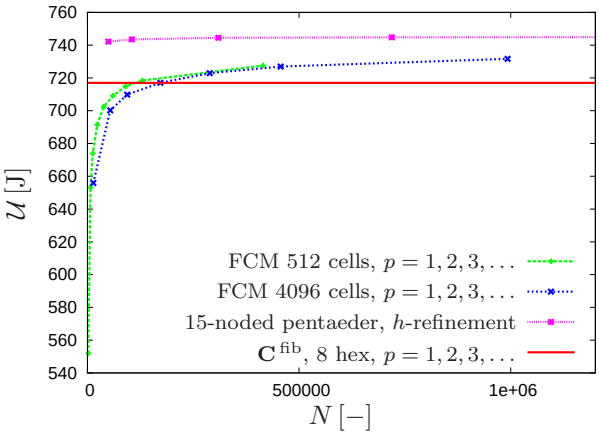

Figure 5.71: Load case 1: Strain energy in case of fiber reinforcement

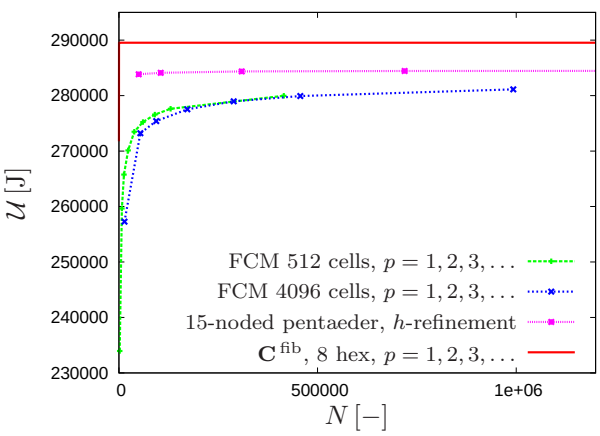

Figure 5.72: Load case 2: Strain energy in case of fiber reinforcement

eters.

In summary we can state that both the pure FCM and the effective computations lead to accurate results. Due to the fact that for a general volume load the exact positions of pores, inclusions or fibers are of higher importance, load case 2 is more demanding for the effective material parameter's solution which only approximates the geometry in an average sense.

5.2.2 Sandwich materials

In this section we start with an introduction to sandwich materials. Since we want to focus on sandwich structures with foamed cores we develop *general guidelines* for extracting effective parameters via CT-scans and numerical homogenization of any foamed materials. With these guidelines we compute effective parameters of polymeric foams, which are validated by mechanical experiments. Hereby, a sandwich plate with a foamed core is included.

5.2.2.1 Introduction

Following Altenbach [2] sandwich materials can be regarded as a special case of general laminates. Commonly, they consist of two thin faceplates of thickness t_{face} which enclose a core of thickness t_{core}, refer to Figure 5.73. The faceplates carry the major part of the normal stresses due to bending action, refer to Figure 5.74. Therefore, they are made of very stiff materials like, for example, metal sheets or fiber-reinforced laminates, which offer high tensile strength. In contrast, the core serves as a distance piece for the faceplates and it directly influences the bending stiffness, which is proportional to the third power of the thickness. It has to be designed for shear resistance, because the maximum shear stresses are expected there, see Figure 5.75.

Commonly, the core is fabricated of lightweight materials like, for example, foam- or honeycomb-like structures.

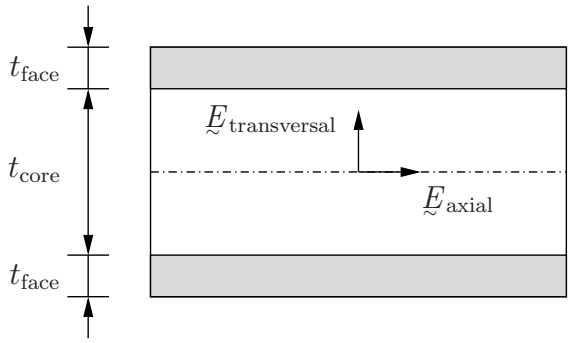

Figure 5.73: Three-layer sandwich plate with faceplates and core

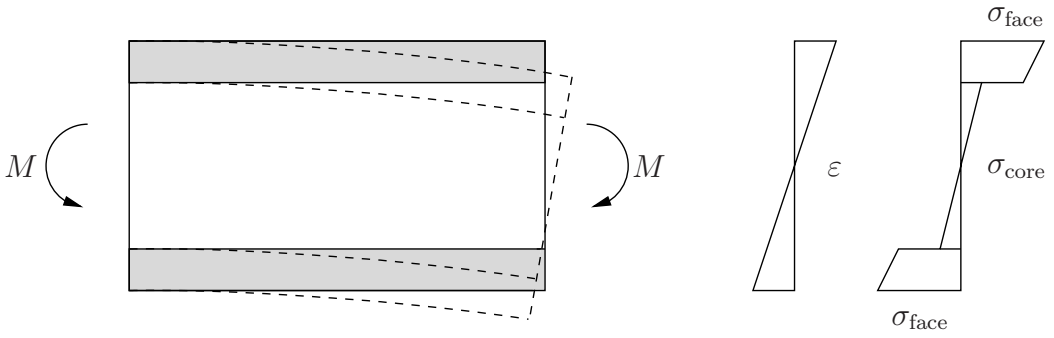

Figure 5.74: Three-layer sandwich plate under pure bending: displacement field, strains, stresses [103]

In the following different approaches for modeling of laminates and sandwich materials are discussed:

- **Equivalent single layer models (*ESL*):** These models are based on assumptions with respect to kinematics and stress distribution in thickness direction, whereby the originally three-dimensional structure is reduced to a two-dimensional one. The *classical laminate* theory (*CLT*) is based on KIRCHHOFF's assumptions of plates or shells and thus is restricted to thin laminates. The *first-order shear theory* (*FSDT*) applies MINDLIN's theory and is suited for thicker laminates, too. Beyond that there are *shear theories of higher-order* which are able to represent warping. All shear theories share the assumption that both the displacements and strains in thickness direction to be continuous. However, this assumption is not true at the layer interfaces if the stiffness of the layers strongly differs, which is the case for sandwich materials, compare with Figure 5.75 or with [79] for further explanations.

- ***Layer-wise theories*:** Here, a laminar structure is assumed in which each layer is equipped with an independent displacement field [96]. These displacement fields are coupled in a suitable way allowing for a more realistic description of the displacements in thickness direction since zig-zag distributions can be represented. The main disadvantage is that the overall number of degrees of freedom depends on the number of layers. *Zig-zag theories*, which are a sub-group of the layer-wise theories, enhance the displacement

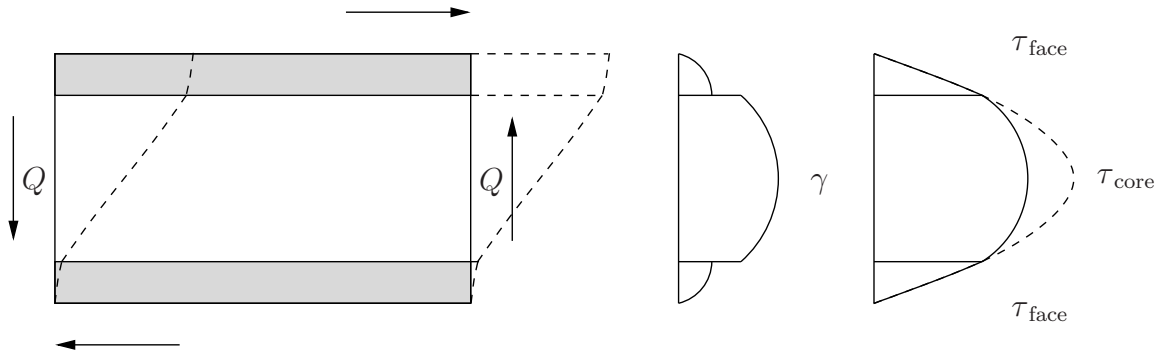

Figure 5.75: Three-layer sandwich plate under transverse shear load Q: displacement field, strains, stresses [103]

field of classical theories by piecewise zig-zag functions in order to be able to capture kinks in the displacement field independently of the number of layers. Examples for *layer-wise* and *zig-zag theories* can be found for beams in [57, 96], for plates in [16] and for three-dimensional approaches in [68, 79].

- **Homogenization strategies:** The previous approaches assume the individual layers to be homogeneous in general. In addition, analytical homogenization strategies have been developed in particular for non-homogeneous sandwich cores, refer to [54, 56, 58, 98]. For example these cores consist of honeycomb structures which are orthotropic in the thickness direction.

As mentioned earlier, in this thesis homogenization strategies allowing for a determination of effective material parameters of foamed cores will be developed and discussed.

5.2.2.2 Effective material parameters of foamed cores

The goal of this section is to extract effective material parameters of foamed materials, and in particular of Polyurethane (PU) foams. These parameters will then be applied amongst others to sandwich structures, compare with Figure 5.76.

First of all, it is worth highlighting some works related to effective material properties of foams: Huber and Gibson described the material behavior of foams by idealized three-dimensional unit cells and validated their results by experiments [59]. Later, Gong et al. published detailed geometric information about PU foams and established models based on Kelvin cells, [42, 43]. Their approach was improved by Jang et al. who used 3D CT-scans of polymeric and Aluminum foams as a basis for FE-models, [61]. These models are based on different types of cells, including also the Kelvin cells. A similar investigation has been performed for polymethacrylimide (PMI) foams by Wang et al., who utilized Kelvin cells [99]. The above-mentioned approaches have the drawback that the foam's real geometry is only approximated. In order to overcome these problems, Wismans et al. converted three-dimensional micro CT-scans of polymeric foams into FE-models in order to study elastic and hyperelastic properties [104]. However, their approach was restricted to two dimensions, neglecting the importance of the three-dimensional situation. In contrast to [104], we discretize the real three-dimensional

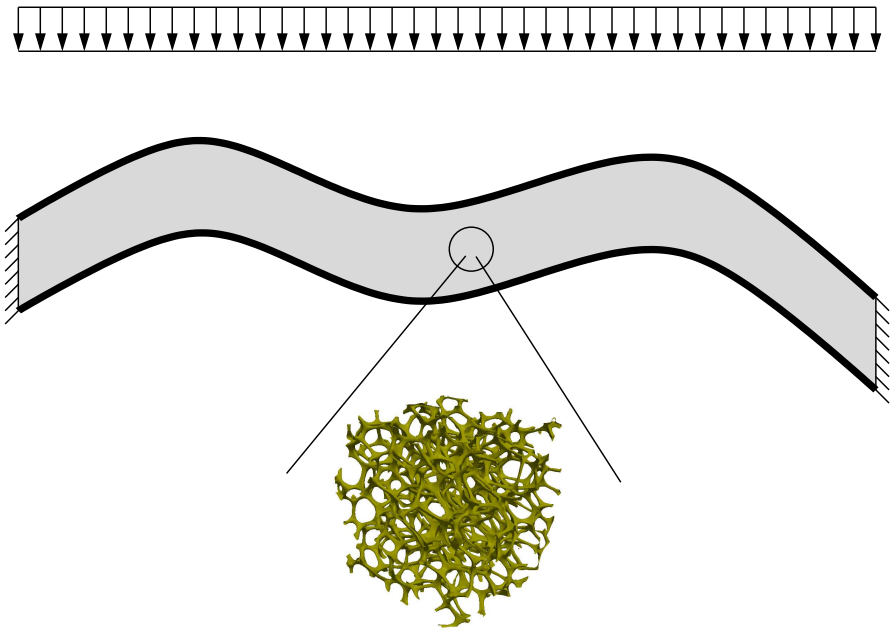

Figure 5.76: General sandwich structure with core made of PU foam

geometry which allows three-dimensional linear elastic effective material properties to be fully extracted.

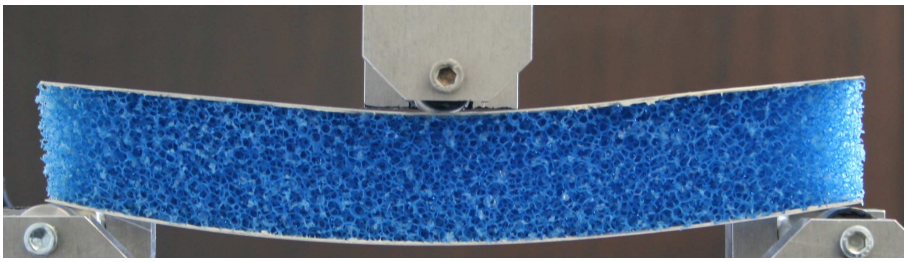

Figure 5.77: Bending test with a sandwich plate

This section is divided into three parts: The first paragraph includes a preliminary study with a foam's CT-scan in order to derive a suitable discretization strategy and to give an idea about a representative subdomain whereby a brief comparison to the literature is given. In the second part effective material parameters of PU foams are extracted for different ppi-values, i.e. **p**ores **p**er **i**nch, while in the last part the numerical results are validated.

5.2.2.2.1 Preliminary study

In our preliminary study we want to find a suitable discretization and a representative subdomain. To this end we investigate an equidistant CT-scan of an open-cell Aluminum foam with 10 ppi and $\varphi_V \approx 9\,\%$. The scan consists of $733 \times 729 \times 704$ voxel whereby each voxel has the volume $V = 60.331 \times 60.331 \times 60.331\,\mu m^3$ which provides a proper resolution of the individual

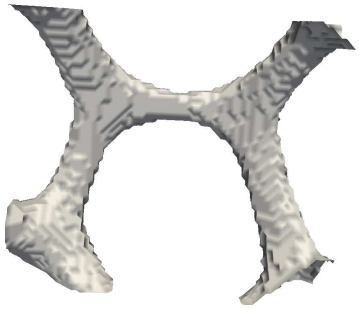

Figure 5.78: Proper resolution of the individual cell walls by the CT-scan

cell walls, compare with Figure 5.78. Since we want to keep this preliminary study as general as possible all measures will be given in terms of voxel. This is not a problem as long as a proper resolution of cell walls is ensured. As mechanical parameters for the cell walls within a linear elastic analysis we assume YOUNG's modulus $E = 70$ GPa and POISSON's ratio $\nu = 0.3$.

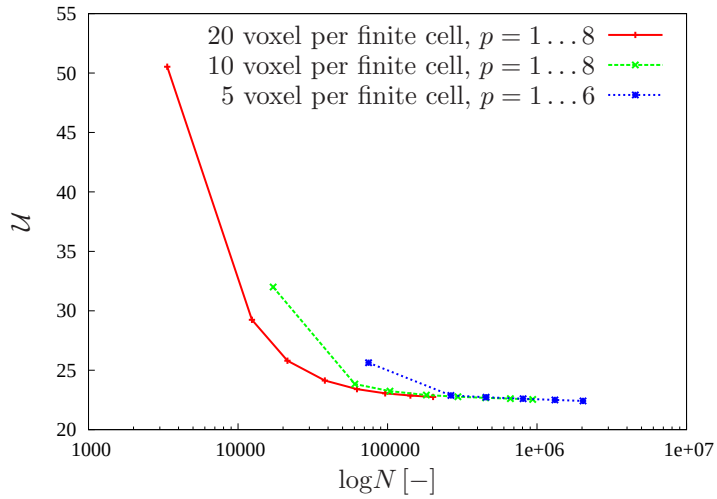

Figure 5.79: Strain energy $\mathcal{U}$ vs. number of degrees of freedom N for different FCM resolutions

We start with the discretization and cut out a subdomain of $n_x \times n_y \times n_z = 200 \times 200 \times 200 = l^3 = 200^3$ voxel at voxel position $(x, y, z) = (100, 100, 100)$ in positive coordinate directions. Note that approximately 18 foam cells are included in this subdomain. We formulate for this subdomain a BVP where the bottom is fully clamped and the top is loaded by $\bar{u}_z = -1.0$ voxel. A p-extension with three different finite cell resolutions is performed: 10^3, 20^3, and 40^3 finite cells, i.e. 20, 10, and 5 voxel per finite cell. In the adaptive numerical integration of the finite cells the number of GAUSSIAN points in one direction is 20. Based on numerical studies it turns out that a tolerance of 0.1 % for the integration error of the finite cells leads to accurate results. In Figure 5.79 the resulting strain energy $\mathcal{U}$ is plotted against the number of degrees of freedom N. If we relate the accuracy in the strain energy to the number of degrees of freedom the 10 voxel per finite cell resolution for $p \geq 5$ seems to be appropriate. To be

more specific, this resolution with $p = 5$ results in $N = 295335$, and the corresponding strain energy $\mathcal{U} \approx 26.31$ is only 1.3 % different to the finest resolution in which we have 5 voxel per finite cell and $p = 6$. Thus, we choose 10 voxel per finite cell and $p = 5$ in the following.

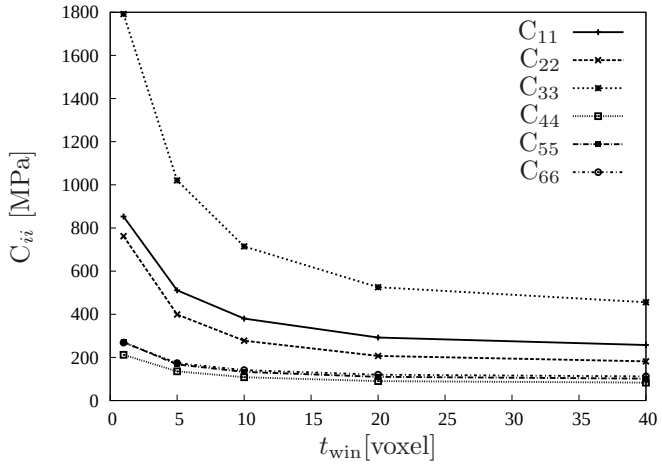

Figure 5.80: C_{ii} vs. t_{win} for the subdomain with $200 \times 200 \times 200$ voxel starting at position (100,100,100)

Next, we embed the subdomain into windows with a thickness of $t_{\text{win}} = \{\, 1, 5, 10, 20, 40 \,\}$. The window's influence on C_{ii} where $i = 1, \ldots, 6$ is depicted in Figure 5.80. In sections 5.1.1.2.1 and 5.1.2 it was demonstrated that cellular materials exhibit size dependent boundary layer effects under various load conditions (shear, tension, bending). Note that in general shear experiments exhibit a very high size dependency. In view of a two-scale approach such effects lead to an overestimation of the mechanical properties even when utilizing large subdomains (microstructures). Thus, means like, for example, the introduction of pin supports at the microstructures boundaries or the application of periodic boundary conditions have been proposed in order to relax such local stiffening effects [88]. The window method has a similar effect and for a constant number of foam cells one can find that the thicker the window the less the stiffening is pronounced. However, in the practical application of the resulting effective elasticity matrices to macroscopic problems the distance to the boundary is not known in advance and is, of course, also not constant within the macroscopic domain. Therefore, one has to find a compromise with respect to the choice of t_{win}. For the foam at hand we choose $t_{\text{win}} = 10 = l/20$.

Another observation is that the z-direction is more pronounced indicating anisotropy. This is not surprising since in the manufacturing process of foam materials there is a rise direction in which the cells are elongated [59, 61]. Normal to the rise direction the cells are nearly equiaxed and one can define $\mathcal{A} = h_1/h_2$ whereby h_1 is measured in the rise direction. In the foam at hand we have $\mathcal{A} \approx 1.5$ and as indicated above the rise direction coincides with $\underset{\sim}{E}_Z$, refer to Figure 5.81.

It is obvious that an equal number of foam cells in all coordinate directions is desirable. Thus,

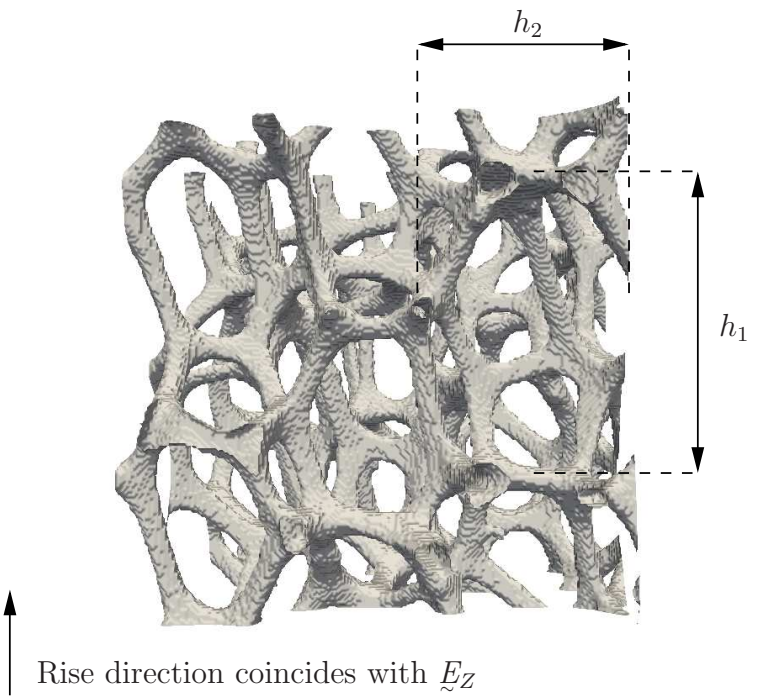

Figure 5.81: Illustration of rise direction and cell anisotropy

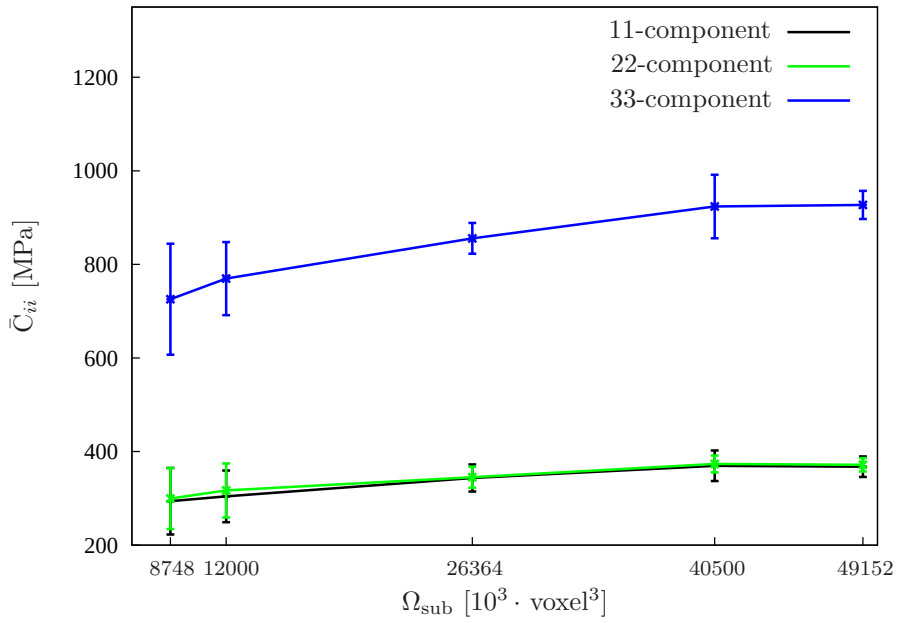

Figure 5.82: $\bar{C}_{ii}$ vs. Ω_{sub}. The errors bars indicate the standard deviation s_{ii} as defined in (5.5).

for the generation of subdomains $\mathcal{A}$ has to be taken into account. If we denote the subdomain's size in the xy-plane by l_{xy} then the size in rise direction emerges as $l_z = \mathcal{A} \cdot l_{xy}$ and the subdomain's volume is $\Omega_{\text{sub}} = l_{xy}^2 \cdot l_z = \mathcal{A} \cdot l_{xy}^3$. Consequently, for the window's thickness we have $l_{xy}/20$ and $l_z/20$, respectively.

Next we need to determine a representative subdomain. To this end, the subdomain's size and the starting positions are varied for statistical reasons. In particular, we propose $l_{xy} = \{\, 180, 200, 260, 300, 320 \,\}$ and for each size $n = 10$ samples with randomly distributed starting positions are chosen. In Figure 5.82 the arithmetic mean value

$$\bar{\mathrm{C}}_{ij} \;=\; \frac{1}{n} \sum_{k=1}^{n} \mathrm{C}_{ij}^{k} \tag{5.4}$$

is plotted against Ω_{sub} including error bars indicating the standard deviation

$$s_{ij} \;=\; \sqrt{\frac{1}{n-1} \sum_{k=1}^{n} \left(\bar{\mathrm{C}}_{ij} - \mathrm{C}_{ij}^{k} \right)^2}. \tag{5.5}$$

We notice that the mean values slightly increase as the subdomain's size grows. An explanation for this can be found in the extended probability of local stiffening effects like, for example, closed faces [61], compare with Figure 5.83.

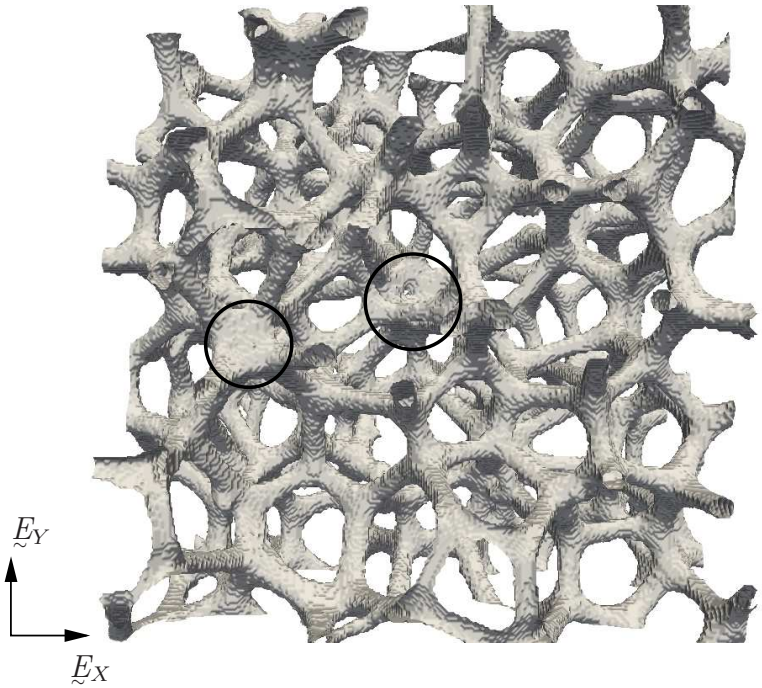

Figure 5.83: Two closed faces marked by circles

Almost converged values for $\bar{\mathrm{C}}_{ii}$ are obtained from $\Omega_{\text{sub}} = 40500 \cdot 10^3$ voxel on, resulting in $N \approx 1.9 \cdot 10^6$ degrees of freedom corresponding to $4 \times 4 \times 4$ foam cells. In Figure 5.85 the

corresponding subdomain's FCM mesh with 15153 cells is shown.

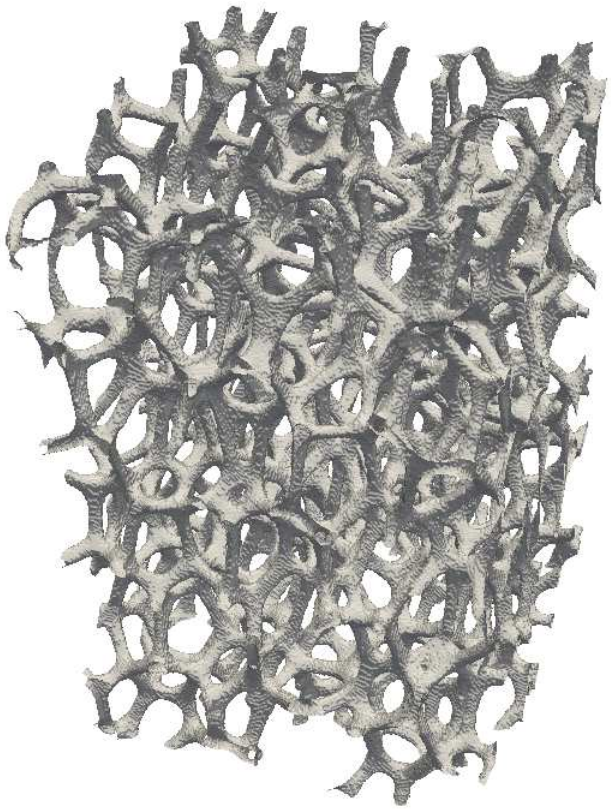

Figure 5.84: Subdomain $\Omega_{\text{sub}} = 40500 \cdot 10^3$ voxel

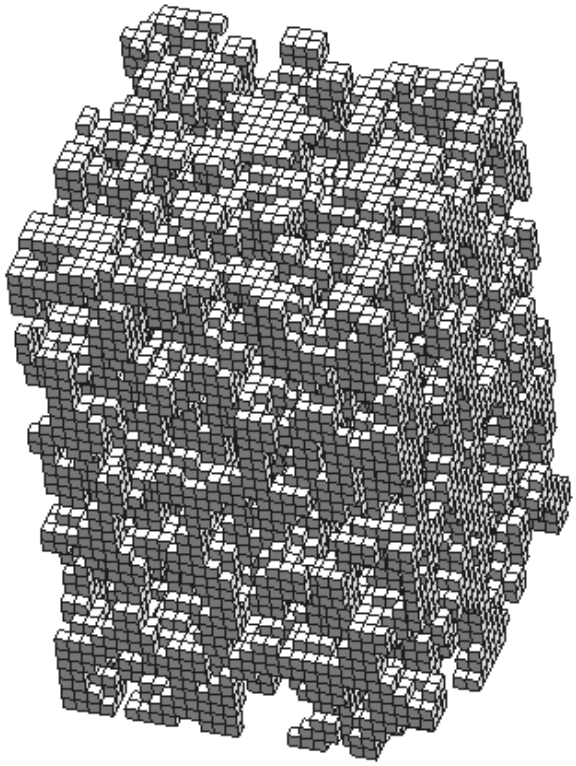

Figure 5.85: FCM mesh of subdomain $\Omega_{\text{sub}} = 40500 \cdot 10^3$ voxel

Note that in [99] a similar number of cells was identified for PMI foams. One additional remark: The computation time for this subdomain size, whereby 9 iteration steps have been performed in order to match the demanding tolerance of $e_{\text{Frob}} < 10^{-3}$, is about five hours. Hereby, a compute server with 48 cores (AMD Opteron 8425) has been used. For further discussions, it is of advantage to consider the mean effective elasticity matrix. To this end we show the one associated with $40500 \cdot 10^3$ voxel

$$\bar{\mathbf{C}}^{\,40500\cdot 10^3} = \begin{bmatrix} 367.606 & 120.665 & 221.621 & -0.965 & 6.136 & 23.670 \\ & 371.579 & 232.999 & -0.588 & 10.577 & 16.468 \\ & & 926.978 & 2.311 & 24.700 & 42.073 \\ & & & 117.069 & 3.565 & 2.402 \\ & & & & 155.743 & 3.622 \\ & & & & & 154.299 \end{bmatrix}.$$

Investigating the structure of $\bar{\mathbf{C}}^{40500\cdot 10^3}$ one may find similarities to an elasticity matrix of a transverse isotropic material

$$\mathbf{C}_{\text{trans-iso}} = \begin{bmatrix} \mathrm{C}_{11} & \mathrm{C}_{12} & \mathrm{C}_{13} & 0 & 0 & 0 \\ & \mathrm{C}_{11} & \mathrm{C}_{13} & 0 & 0 & 0 \\ & & \mathrm{C}_{33} & 0 & 0 & 0 \\ & & & \dfrac{(\mathrm{C}_{11}-\mathrm{C}_{12})}{2} & 0 & 0 \\ & & & & \mathrm{C}_{44} & 0 \\ \text{sym} & & & & & \mathrm{C}_{44} \end{bmatrix},$$

which is as mentioned above due to the fact that cells normal to the rise direction are nearly equiaxed. Referring to [9] Young's modulus can be computed for the transverse/rise direction by

$$E_{\text{trans/rise}} = \frac{(\mathrm{C}_{11}^2 \cdot \mathrm{C}_{33} + 2 \cdot \mathrm{C}_{13}^2 \cdot \mathrm{C}_{12} - 2 \cdot \mathrm{C}_{13}^2 \cdot \mathrm{C}_{11} - \mathrm{C}_{33} \cdot \mathrm{C}_{12}^2)}{(\mathrm{C}_{11}^2 - \mathrm{C}_{12}^2)} \tag{5.6}$$

and for the plane of isotropy by

$$E_{\text{plane}} = \frac{(\mathrm{C}_{11}^2 \cdot \mathrm{C}_{33} + 2 \cdot \mathrm{C}_{13}^2 \cdot \mathrm{C}_{12} - 2 \cdot \mathrm{C}_{13}^2 \cdot \mathrm{C}_{11} - \mathrm{C}_{33} \cdot \mathrm{C}_{12}^2)}{(\mathrm{C}_{11} \cdot \mathrm{C}_{33} - \mathrm{C}_{13}^2)}. \tag{5.7}$$

In our example we have $E_{\text{trans/rise}} \approx 725$ MPa and $E_{\text{plane}} \approx 300$ MPa which is in the same order of magnitude as the measurements reported by Jang [61] for an aluminum foam with 10 ppi, $\mathcal{A} \approx 1.3$, and $\varphi_V \approx 8.7\,\%$ with $E^{\mathrm{J}}_{\text{trans/rise}} \approx 585$ MPa and $E^{\mathrm{J}}_{\text{plane}} \approx 363$ MPa.

The main results obtained in this section can be summarized as follows:

- Provided a proper resolution of the individual cell walls by the CT-scan, 10 voxel per finite cell and $p = 5$ yields accurate results.
- For a representative subdomain $4 \times 4 \times 4$ foam cells should be included.
- It is known that the window's size influences the computation of the effective properties [46, 47]. For foamed materials this is even more pronounced due to size effects which can lead to stiffening. Therefore it is recommended to numerically investigate the influence of the window size for the foam at hand. It might be a good idea to compute effective material properties for different values of the window size and to apply the resulting elasticity matrices depending on the distance to the boundary of the macroscopic problem.

Figure 5.86: PU foams with different densities (10-30 ppi), taken from Saarschaum Saarbrücken, Germany - *www.saarschaum.de*

5.2.2.2.2 Effective material parameters of PU foams

In this paragraph we determine the effective material matrices for a specific PU foam. Three different densities with 10, 20, and 30 ppi are considered, compare with Figure 5.86, and the volume fraction is $\varphi_V \approx 2.3\,\%$.

For each density, three equidistant CT-Scans with approximately $700 \times 700 \times 700$ voxel on average have been generated. Hereby, the volume of the voxel V is related to the ppi-value in order to ensure an equal number of foam cells. More particularly, for 10 ppi we have $V_{10} = 62.697 \times 62.697 \times 62.697\,\mu m^3$, for 20 ppi $V_{20} = 43.766 \times 43.766 \times 43.766\,\mu m^3$, and for 30 ppi it is $V_{30} = 28.732 \times 28.732 \times 28.732\,\mu m^3$. The linear elastic parameters of the base material are assumed to be $E_{\mathrm{PU}} = 400$ MPa and $\nu_{\mathrm{PU}} = 0.49$ which is in accordance with the literature [6]. For the extraction of effective material parameters we make use of the suggestions concerning discretization and subdomain size as stated in paragraph 5.2.2.2.1. Consequently, we use $4 \times 4 \times 4$ foam cells, and in preliminary studies it has turned out that again $t_{\mathrm{win}} = l/20$ is a proper choice for the window's thickness. The number of samples per density is $n = 12$, i.e. four samples per scan are taken.

In Figure 5.87 selected entries of $\bar{\mathrm{C}}_{ii}$ are plotted against the ppi-values including error bars for the standard deviation[8]. One realizes that there is not that much difference between the entries of the 10 and 20 ppi foams and that the 30 ppi foam has lower stiffness.

Using equations (5.6) and (5.7) we can compute the effective moduli in transverse and plane direction as:

- 10 ppi: $E^{10}_{\mathrm{trans/rise}} \approx 187$ KPa and $E^{10}_{\mathrm{plane}} \approx 67$ KPa
- 20 ppi: $E^{20}_{\mathrm{trans/rise}} \approx 182$ KPa and $E^{20}_{\mathrm{plane}} \approx 70$ KPa
- 30 ppi: $E^{30}_{\mathrm{trans/rise}} \approx 144$ KPa and $E^{30}_{\mathrm{plane}} \approx 62$ KPa

These values confirm the statements with respect to the different foams, too.

[8]Note that in section B.1 the effective material matrices with standard deviation are shown explicitly.

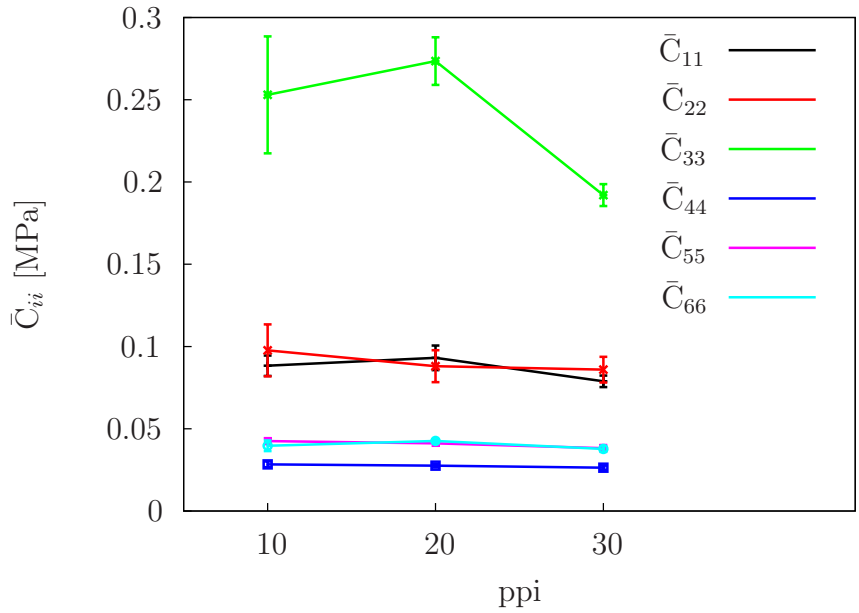

Figure 5.87: Selected entries of $\bar{C}_{ii}$ vs. ppi-values.

5.2.2.2.3 Validation

The effective material parameters of the PU foams presented in paragraph 5.2.2.2.2 shall be validated by mechanical experiments. To this end, we investigate different foams under uniaxial compression and simple shear, and in addition we perform three-point bending tests with sandwich plates. In all of the experiments the foam's rise direction coincides with $\underset{\sim}{E}_Z$.

Let us describe the experiments in more detail: In Figure 5.88 a sketch of the compression and the shear experiment is shown, and in Table 5.2 the corresponding geometric properties and boundary conditions can be found. Two remarks shall be given:

- In the compression experiment the specimen's lateral contraction at top and bottom was not restricted. Therefore, quarter symmetry and symmetry boundary conditions can be used. Consequently, only $A = B = 50\,mm$ is taken into account in the numerical model instead of the real dimensions $A = B = 100\,mm$.
- In the shear experiment the material is perfectly bonded to the shear plates at surface 1 and 6 and thus displacement boundary conditions are quite natural.

In the bending test, compare with Figures 5.77 and 5.89, the thin faceplates are made of aluminum ($E = 70$ GPa, $\nu = 0.3$). It is carried out for three different heights $H = \{40, 60, 80\}\ mm$. Due to symmetry only half of the system is taken into account.

In Figures 5.90 and 5.91 the corresponding p-FEM meshes are depicted. Note that the meshes are refined in order to account for possible singularities. In the bending test attention has been paid to accurately modeling the line load and the line support with solid elements. Numerical studies have shown that for $b \leq t/5$ the deviation of the solid-like line support from a real line

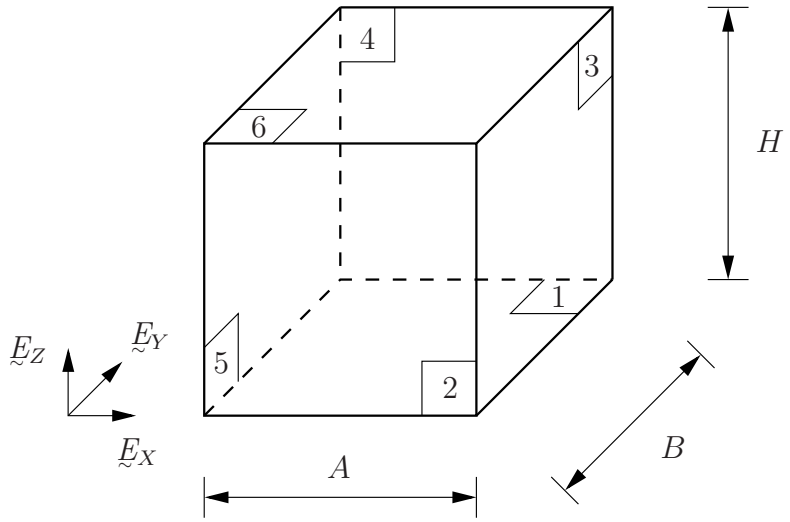

Figure 5.88: Geometric properties and surface indices of uniaxial compression and simple shear experiment

Table 5.2: Geometric properties and boundary conditions for uniaxial compression and simple shear experiment, refer to Figure 5.88. Note that $\bar{u} \propto H$.

Experiment	A $[mm]$	B $[mm]$	H $[mm]$	Surface 1	2	3	4	5	6
Uniaxial compression	50*	50*	$50, 100, 200$	$\bar{u}_z = 0$	free	free	$\bar{u}_y = 0$	$\bar{u}_x = 0$	$\bar{u}_z = \bar{u}$
Simple shear	200	60	$40, 60, 80$	$\bar{u}_x = 0$ $\bar{u}_y = 0$ $\bar{u}_z = 0$	free	free	free	free	$\bar{u}_x = \bar{u}$ $\bar{u}_y = 0$ $\bar{u}_z = 0$

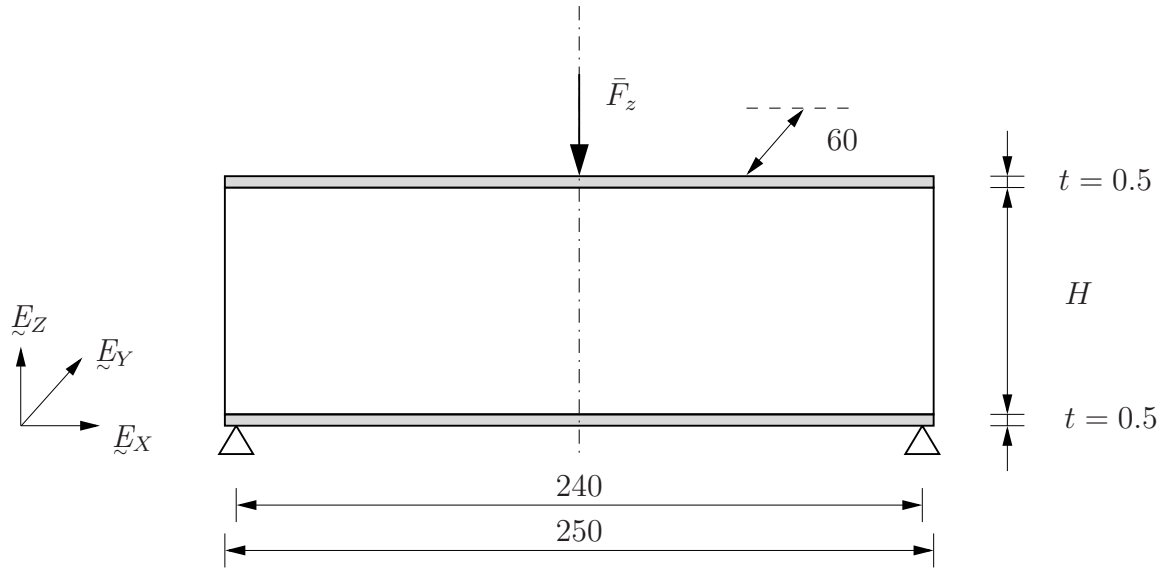

Figure 5.89: Geometric properties and boundary conditions for three-point bending experiment; all measures in mm.

support is negligible.

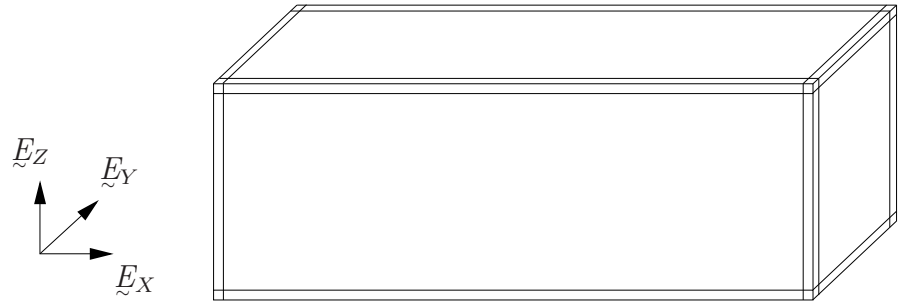

Figure 5.90: Compression / shear test: p-FEM mesh consisting of 27 hexahedrals

In all of the computations a polynomial degree $p = 8$ has been chosen which ensures accurate results. Now, let us discuss the experimental and numerical results in detail. Note that since the numerical approach is limited to small deformations, only a single point is computed at a certain state of deformation and no curve is plotted.

We start with the compression test, see Figures 5.92 to 5.94 where the reaction force F_z is plotted against the compressive strain ε_{zz}. First of all one realizes that the experiments indicate no distinct size effect. This is not surprising since the specimens include large numbers of foam cells in the z-direction, for which size effects are less pronounced, compare with section 5.1.2. To give an example the 10 ppi foam of $H = 50\ mm$ already has about 20 foam cells. Furthermore, one can state that the 10 ppi foam has the highest compression resistance which is in accordance to the fact that this foam exhibits the thickest ligaments. It is closely followed

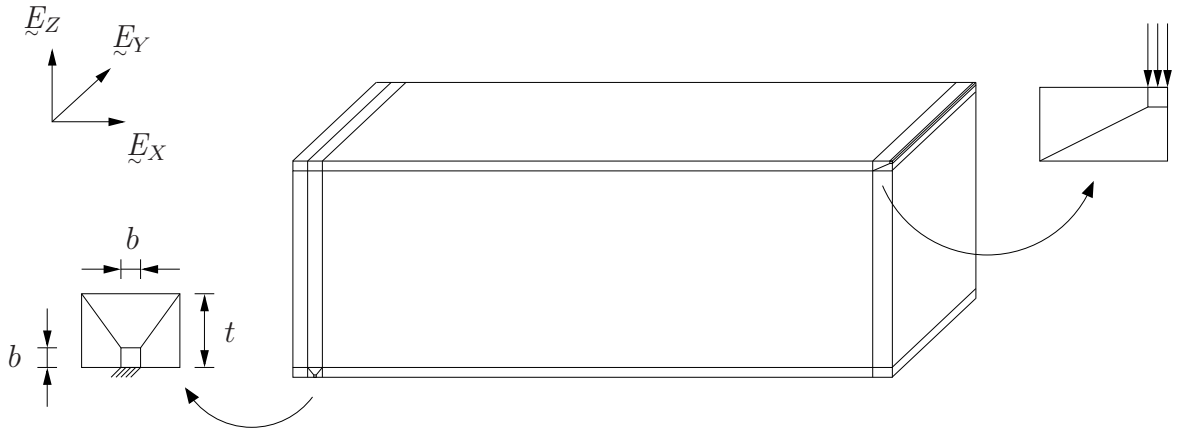

Figure 5.91: Bending test: p-FEM mesh consisting of 17 hexahedrals including refinements

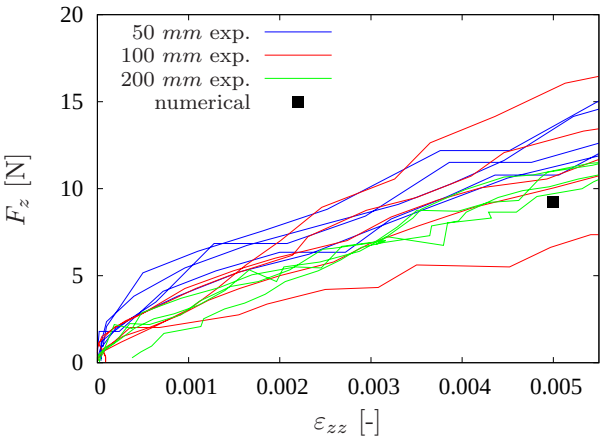

Figure 5.92: Uniaxial compression with 10 ppi: Reaction force F_z vs. ε_{zz} for $H = 50, \ldots, 200$.

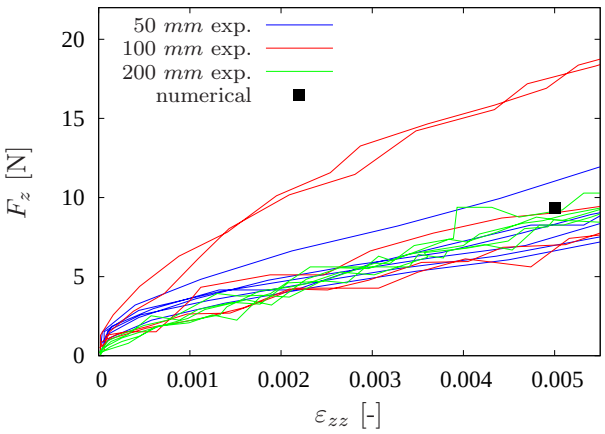

Figure 5.93: Uniaxial compression with 20 ppi: Reaction force F_z vs. ε_{zz} for $H = 50, \ldots, 200$.

by the 20 ppi foam. In the numerical computations the effective properties are constant over the macroscopic integration points and due to first-order homogenization there is no change in F_z if H is increased. Thus, one cannot distinguish between the different heights H. However, the numerical results are located within the experimental scatter band.

In the shear test, as plotted in Figures 5.95 to 5.97, size effects are present, i.e. the smaller specimens behave more stiffly than the larger ones. These effects are more pronounced for the 20 and 30 ppi foams. In addition, when comparing the absolute values, the 20 and 30 ppi foams are stiffer than the 10 ppi foams. The reason can be found in the different load carrying behavior under shear. Whereas larger cells are bending dominated over a longer range, smaller cells are tension dominated even for small deformations. The mismatching of the numerical results with the experiments for 20 and 30 ppi is therefore not astonishing. Note that the small scatter of the numerical reaction forces would vanish if periodic boundary conditions would have been applied which of course would not fit to the experiment.

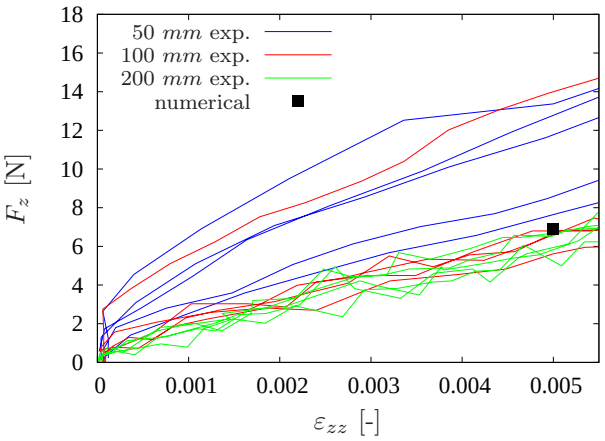

Figure 5.94: Uniaxial compression with 30 ppi: Reaction force F_z vs. ε_{zz} for $H = 50, \ldots, 200$.

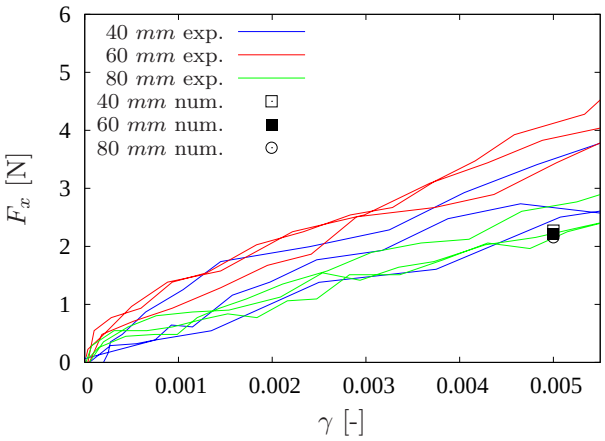

Figure 5.95: Simple shear with 10 ppi: Reaction force F_x vs. γ for $H = 40, \ldots, 80$.

Now, let us discuss the bending test, see Figures 5.98 to 5.100 where $\bar{F}_z$ is plotted against the u_z at the position of $\bar{F}_z$. In the experimental curves size effects are clearly visible. Let us give a brief mechanical explanation: As mentioned earlier bending is a combination of tension, compression and shear. The contribution of the individual stresses to the resulting state of stress depends on the aspect ratio between length and height (L/h): Whereas for slender beams with $L/h > 10$ the shear components become negligible, they may play an important role if thick beams with $L/h < 5$ are investigated. In the examples at hand we are dealing with beams where $L/h < 2.9$. Therefore, shear deformations /stresses are present and stronger size effects are expected.

Again, such size effects are not taken into account by the first-order homogenization scheme. However, the numerical results are not that far away from the experiments at least for $H = 60$ mm and $H = 80$ mm. Two explanations can be given: *Firstly*, as shown above, a state of compression can be modeled with sufficient accuracy. Dealing with small deformations we can

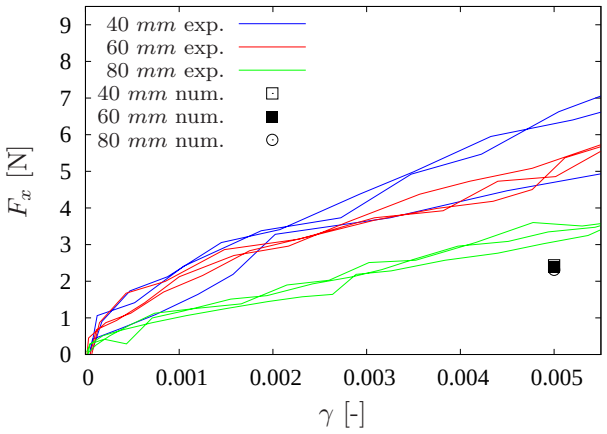

Figure 5.96: Simple shear with 20 ppi: Reaction force F_x vs. γ for $H = 40, \ldots, 80$.

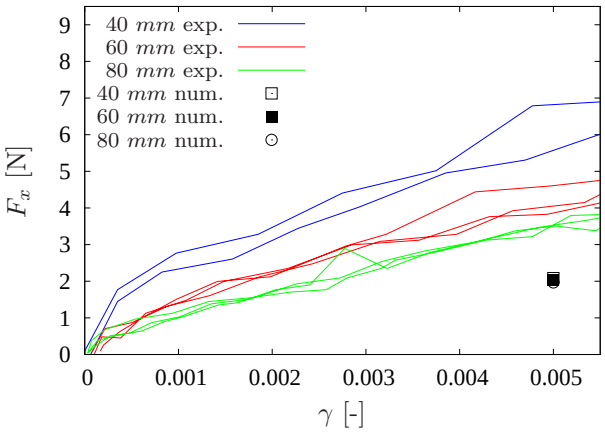

Figure 5.97: Simple shear with 30 ppi: Reaction force F_x vs. γ for $H = 40, \ldots, 80$.

assume that this is also true for tension. Thus, the compressive and tensile parts of the bending state can be represented by the numerical model. *Secondly*, the thin solid-like faceplates can be modeled with arbitrary accuracy by the p-version's elements.

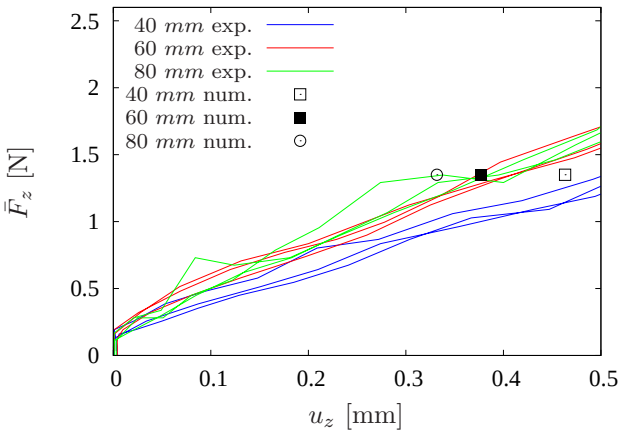

Figure 5.98: Three-point bending with 10 ppi: Tip force $\bar{F}_z$ vs. u_z for $H = 40, \ldots, 80$.

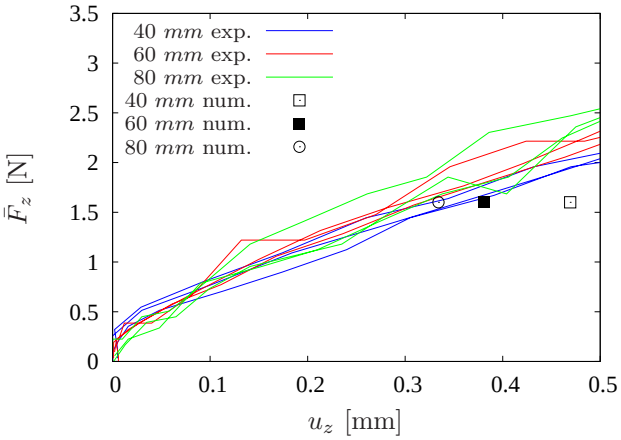

Figure 5.99: Three-point bending with 20 ppi: Tip force $\bar{F}_z$ vs. u_z for $H = 40, \ldots, 80$.

Finally, we assess our validation: Hereby, one has to take into account that there are uncertainties with respect to the micromechanical parameters and that the numerical computation is limited to small deformations, i.e. it is not possible to account for geometric effects like, for example, deformation-induced anisotropy. However, as long as size effects do not play a dominant role the numerical results are at least in moderate accordance with the experiments.

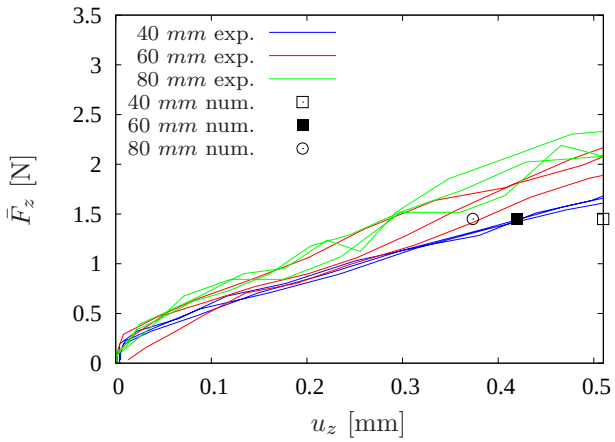

Figure 5.100: Three-point bending with 30 ppi: Tip force $\bar{F}_z$ vs. u_z for $H = 40, \ldots, 80$.

5.3 Microscopic approach - large strain compression

In this section we subject two- and three-dimensional foam-like structures to numerical large strain compression tests, whereby the focus lies on stability investigations due to cell buckling. The *microscopic* approach as introduced in section 1.2 is chosen since it allows for studying all mechanical effects in detail, but at high computational costs.

Referring to [105] the stability of a structure can be assessed in parallel to the FEA by:

- *Eigenvalue analysis*: In each converged step of the NEWTON-RAPHSON procedure an eigenvalue analysis of the global tangent matrix $\mathbf{k}_T$ is performed and the smallest eigenvalue $\omega_{\min}$ is extracted. In practical computations, a point of instability is detected if $\omega_{\min} < 10^{-5}$.
- *Analysis of the diagonal elements of* $\mathbf{k}_T$: During the triangularization of $\mathbf{k}_T = \mathbf{L}^{\mathrm{T}}\,\mathbf{D}\,\mathbf{L}$ the matrix $\mathbf{D}$ contains the diagonal elements D_{ii}. One can distinguish between three cases:

  $$\begin{aligned} \text{all } \mathrm{D}_{ii} > 0 \quad &\rightarrow \quad \text{point of stability} \\ \text{at least 1 } \mathrm{D}_{ii} = 0 \quad &\rightarrow \quad \text{indifferent point} \\ \text{at least 1 } \mathrm{D}_{ii} < 0 \quad &\rightarrow \quad \text{point of instability} \end{aligned}$$

  In our investigations the second case will not occur since we are applying small imperfections to our structures.

Note that eigenvalue analysis is computationally more expensive especially in 3D.

5.3.1 Preliminary study

Before analyzing foam-like structures a preliminary study is performed, where the classical EULER-case 1 is investigated. Figure 5.101 a) shows its geometry and boundary conditions.

The critical load can be computed analytically

$$F_{\text{crit}} \;=\; \frac{\pi^2 E I}{4 l^2}\,.$$

Assuming YOUNG's modulus as $E = 1000\,\text{GPa}$, $I = 83.\overline{3}\,mm^4$, and $l = 100\,mm$ yields $F_{\text{crit}} \approx 20561.7$ N. A small imperfection is chosen in order to trigger buckling, and a geometrically nonlinear FEA is performed. In Figure 5.101 b) the smallest eigenvalue $\omega_{\min}$ is plotted against the overall force. One observes that $\omega_{\min}$ tends to zero, when F tends to F_{crit}. The critical value obtained by the FEA is 20354.4 N, which is quite close to the analytical solution, i.e. the deviation is approximately 1%. Note that at this critical load level negative diagonal elements appear for the first time during the iterative solution process. More precisely, the maximum number of negative diagonal elements associated with this critical load level is two. From this simple example one may deduce that both approaches for investigating a structure's stability are reliable. This statement will be confirmed in the next section.

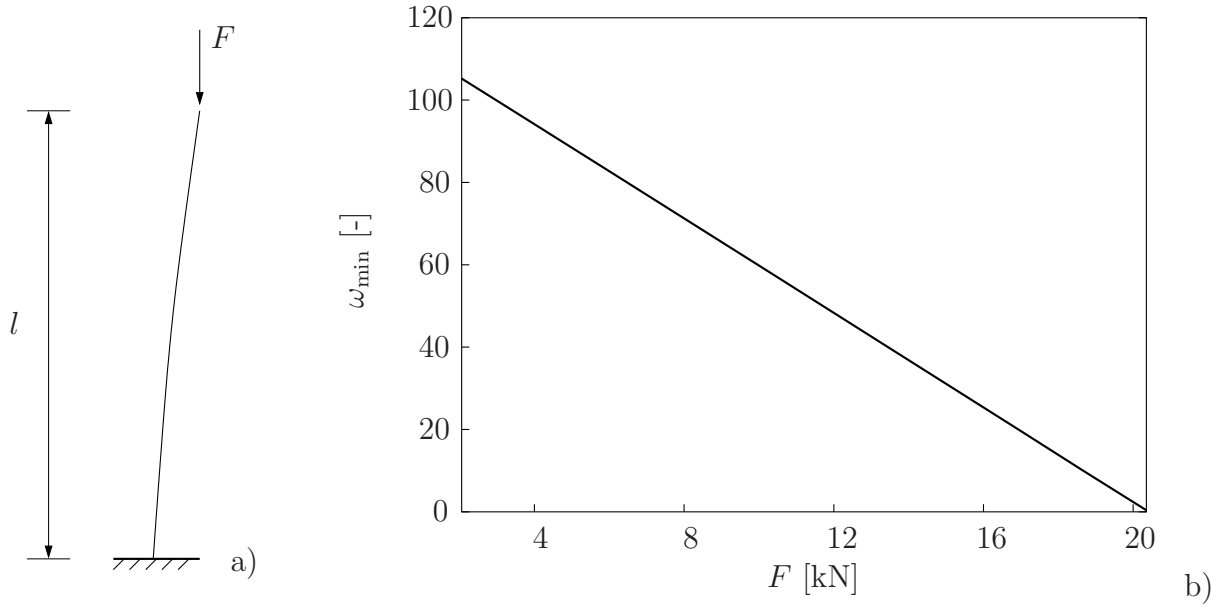

Figure 5.101: EULER-case 1: geometry, boundary conditions and smallest eigenvalue ($\omega_{\min}$) vs. overall force (F)

5.3.2 Two-dimensional analysis

We start with a numerical two-dimensional large strain compression test. The discretized structure of Figure 5.102 is loaded by a prescribed displacement. In order to ensure a more realistic modeling, the geometry is statistically disturbed.

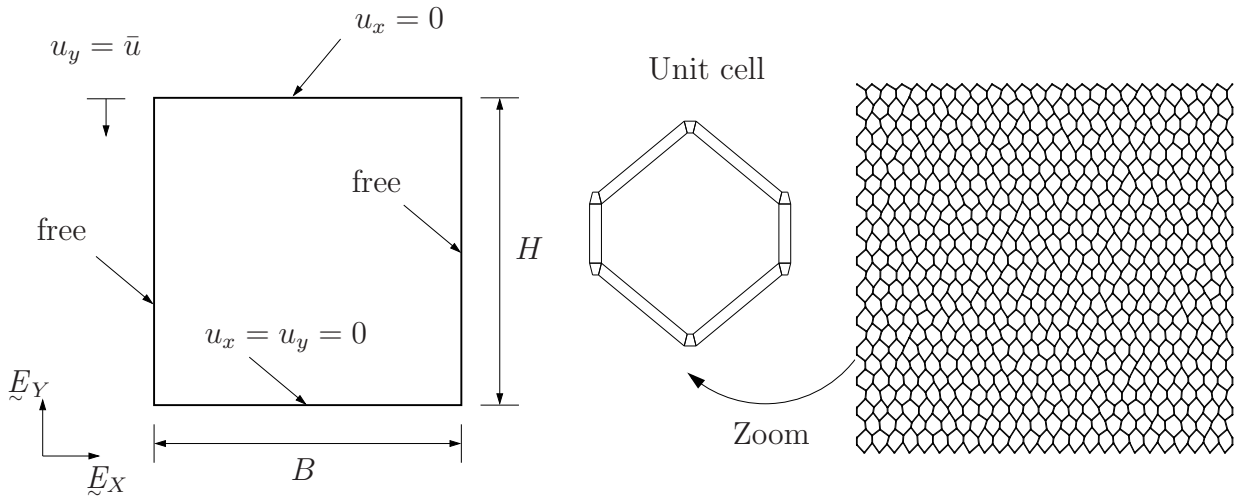

Figure 5.102: Foam-like two-dimensional structure: geometry, boundary conditions, unit cell, and discretization

Anisotropic finite elements of polynomial degrees $p = 6$ and $q = 3$ are applied to the beam-like cell components. The connecting trapezoidal elements are isotropic with $p = q = 3$, compare with section 5.1.1.1. As geometric parameters we have: $H \approx 50\,mm$, $B \approx 50\,mm$, the beam lengths are between $1.2, \ldots, 2\,mm$, and the thickness of the beams is $0.1\,mm$. The material pa-

rameters in the NEO-HOOKEAN material law are set to $\mu = 80.769\,\text{GPa}$ und $\Lambda = 121.15\,\text{GPa}$ assuming plane strain.

Firstly, the load-compression curve (F_y vs. ε_{yy}) is discussed, see Figure 5.103.

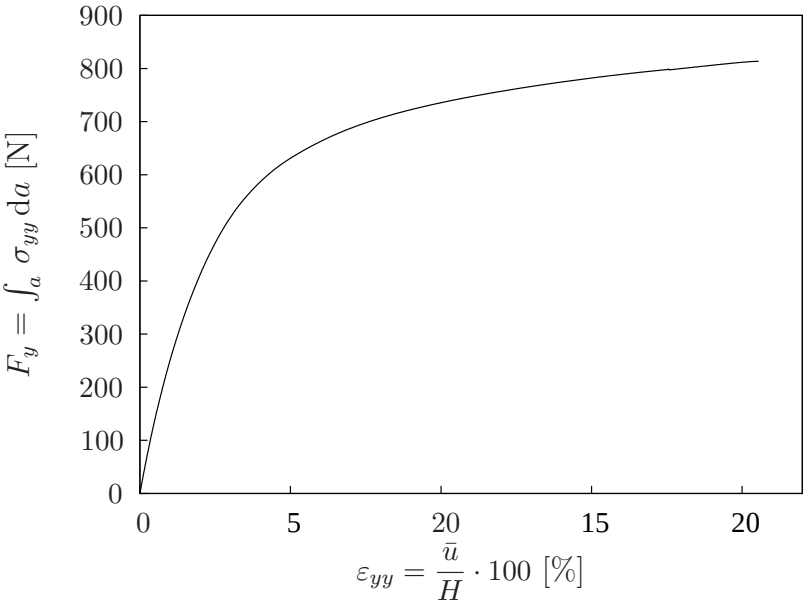

Figure 5.103: Foam-like two-dimensional structure: load-compression curve

The curve exhibits the characteristic behavior of foam-like materials under compression, see FÁTIMA VAZ and FORTES [31]. The curve can be divided into three regions:

- Until $\varepsilon_{yy} \approx 6\,\%$ the curve exhibits a steep slope. This is the bending dominated region.
- For $\varepsilon_{yy} > 6\,\%$ the slope flattens strongly, i.e. changes in F_y are small. Therefore, this region is termed as a *stress plateau* in the literature. The reason for the flattening is that more and more cells start to buckle.
- At $\varepsilon_{yy} \approx 20\,\%$ some cells come into contact with each other. This third region (crushing region) cannot be investigated since no contact formulation has been implemented, yet.

Although Figure 5.103 does not indicate any *global* point of instability, let us investigate the structure's stability by the help of the above mentioned methods in order to detect possible *local* instabilities. In Figure 5.104 $\omega_{\min}$ is shown as a function of ε_{yy}. We recognize two local minima located at $\varepsilon_{yy} \approx 17.5\,\%$ and $\varepsilon_{yy} \approx 20.6\,\%$. While the second point is associated with highly disturbed elements and the abort of the computation the first point might be a candidate for *local* instabilities.

In order to verify the results of the eigenvalue analysis, the development of negative diagonal elements is evaluated. To this end the maximum number of negative diagonal elements n_{neg} showing up during the NEWTON-RAPHSON iteration of a load step λ_{step} is plotted against

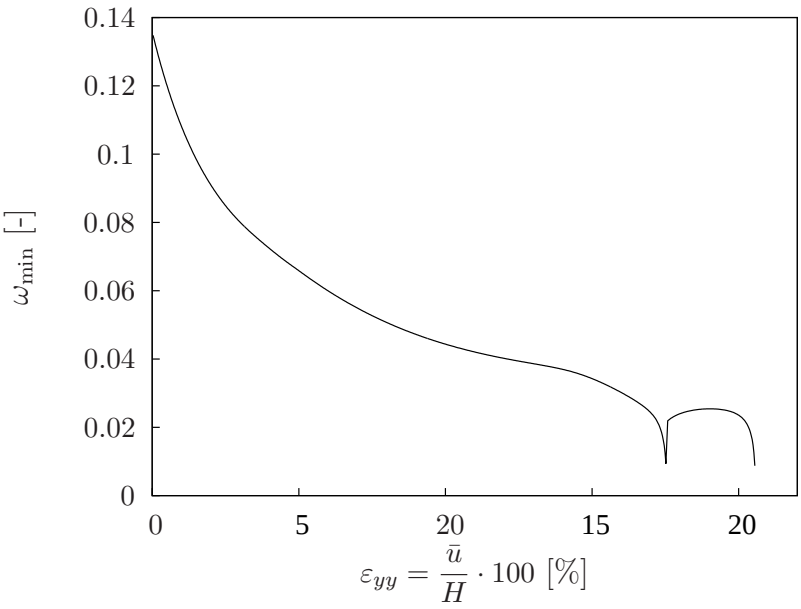

Figure 5.104: Foam-like two-dimensional structure: eigenvalue analysis

λ_{step}[9] in Figure 5.105, and for comparison $\omega_{\min}$ is included.

There are two clusters of n_{neg}, which coincide with $\omega_{\min}$, i.e. both methods again lead to the same results.

Finally, we zoom into the load-compression curve for $\varepsilon_{yy} = 17.2, \ldots, 18\,\%$, see Figure 5.106. The curve shows small oscillations which are located in the region close to the occurrence of the first negative eigenvalue respectively at the first clustering of n_{neg}.

5.3.3 Three-dimensional analysis

In this section we investigate a three-dimensional large strain compression test as depicted in Figure 5.107. The computation is force controlled by the load factor λ. Three-dimensional cellular structures can be modeled by combining polyhedron unit cells as shown by Ströhla, Winter and Kuhn [89]. The unit cell our computation is based on can be found in Figure 5.108 on the left hand side. It is already discretized and consists of 60 brick- and beam-like three-dimensional higher-order solid elements based on the *trunk space*. The bricks are isotropic with $p = q = 4$, and the beams are anisotropic with $p = 6$ and $q = 4$ resulting in 287,438 degrees of freedom. In Figure 5.108 on the right hand side the composed structure is depicted to which the boundary conditions of Figure 5.107 are applied. In each spatial direction four unit cells are used. In the interior the brick-like elements are statistically disturbed ensuring a more realistic modeling of the foam. The thickness of the beams is $1\,mm$, and the length has an average of approximately $10\,mm$. This leads to an equilateral cube

[9]Note that no negative diagonal elements have been detected for $\lambda_{\text{step}} < 585$.

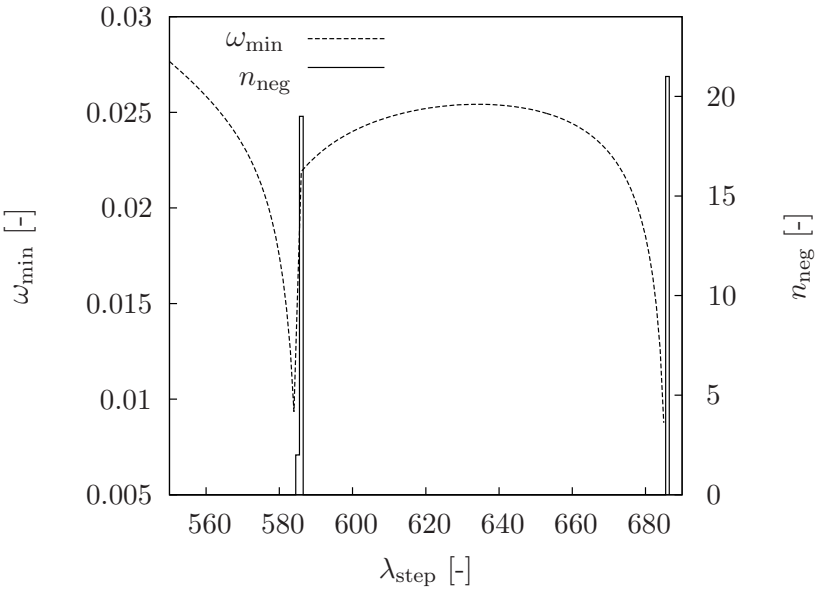

Figure 5.105: Foam-like two-dimensional structure: n_{neg} vs. λ_{step} and for comparison $\omega_{\min}$ vs. λ_{step}

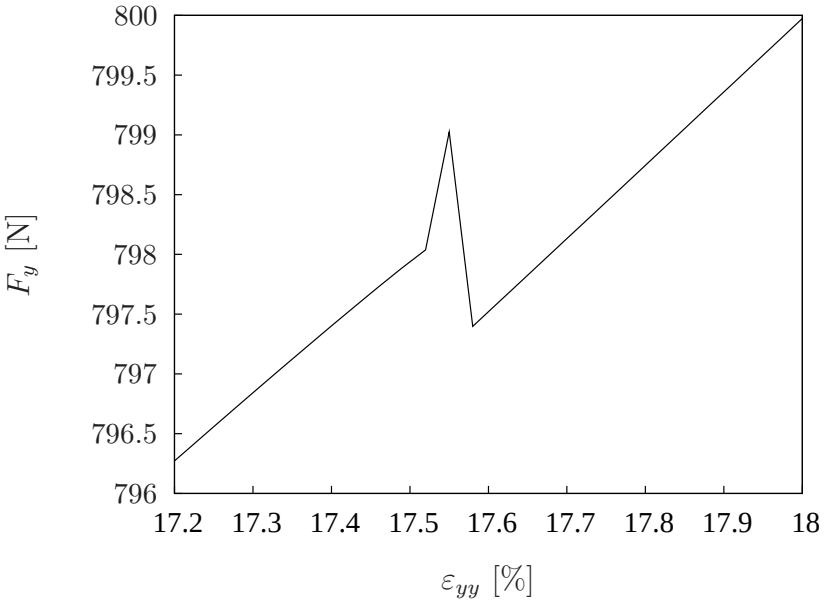

Figure 5.106: Foam-like two-dimensional structure: load-compression curve - zoom

with dimension $D = 113.13\,mm$. For the material constants in the NEO-HOOKEAN we choose $\mu = 26.923$ GPa and $\Lambda = 40.384$ GPa. The numerical simulation yields a load-compression curve (F_z vs. ε_{zz}), as plotted in Figure 5.109, which is, as in the two-dimensional case, in good agreement with experimentally obtained curves.

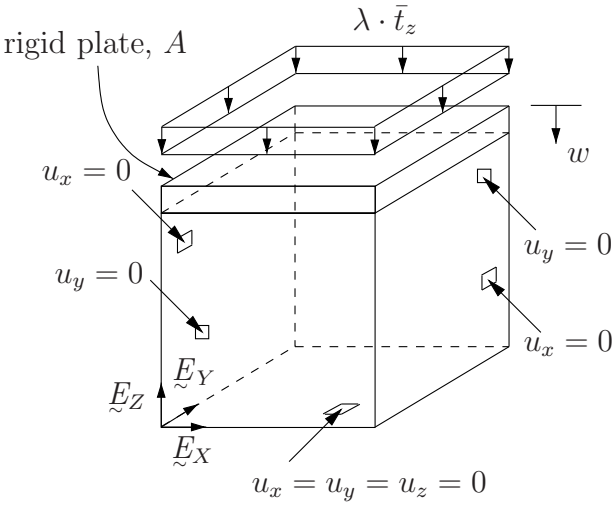

Figure 5.107: Three-dimensional cellular structure: boundary conditions

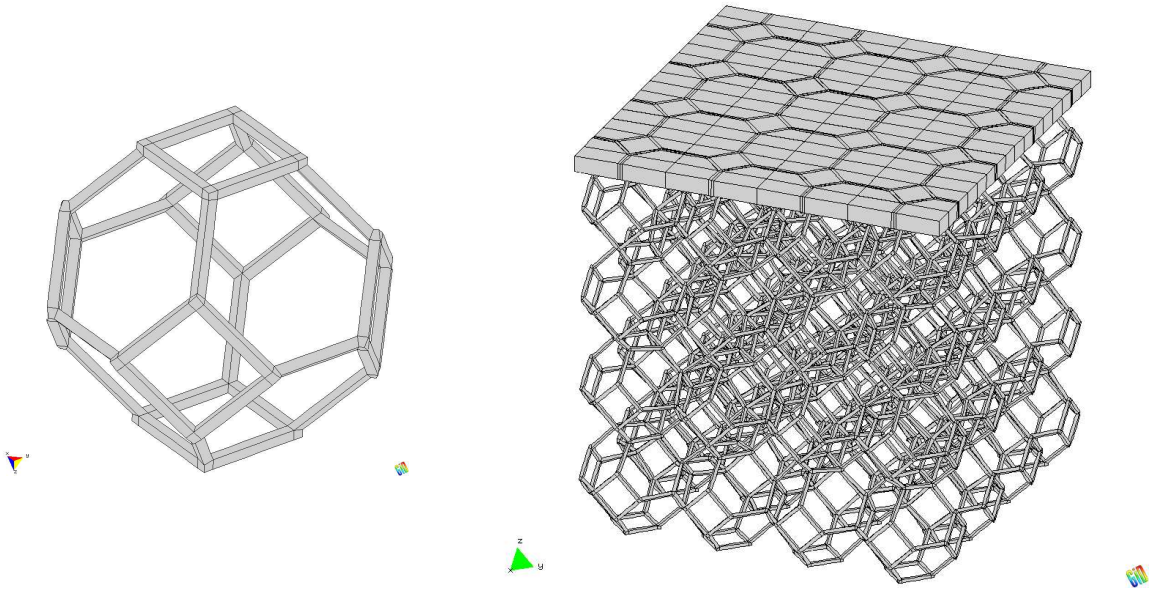

Figure 5.108: Three-dimensional cellular structure: composed out of unit cells

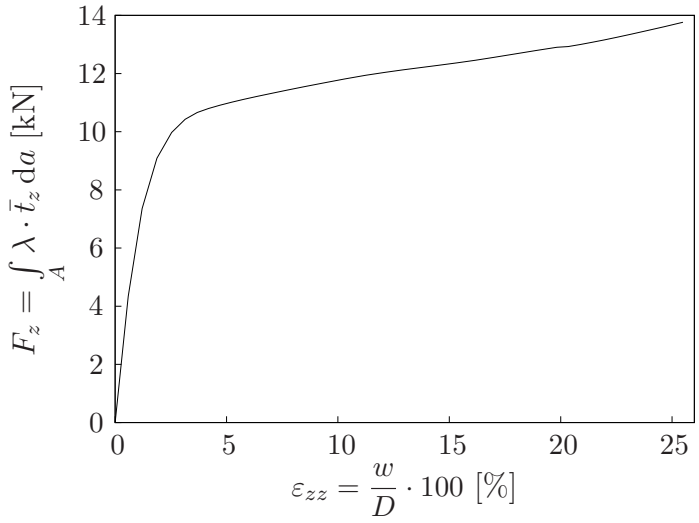

Figure 5.109: Three-dimensional cellular structure: load-compression curve

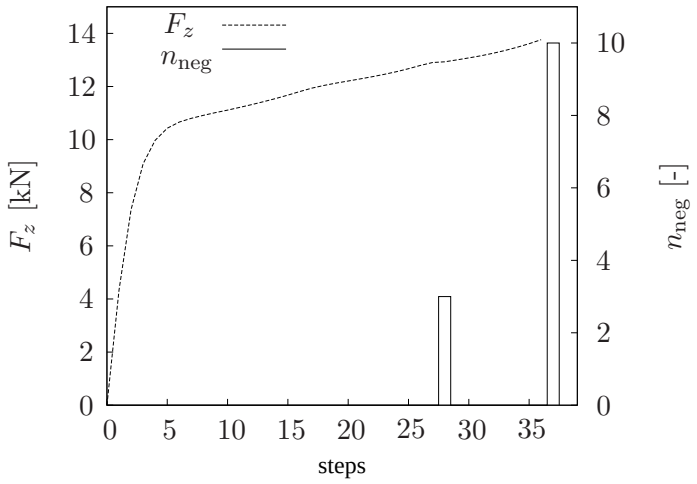

Figure 5.110: Three-dimensional cellular structure: n_{neg} vs. λ_{step} and for comparison F_z vs. λ_{step}

Finally, the structure's stability is discussed: Since an eigenvalue analysis, as demonstrated above, does not provide more information than the diagonal elements and would be computationally more expensive in 3D it is omitted here. Thus, only the development of the maximum number of negative diagonal elements n_{neg} is investigated, see Figure 5.110. We realize that during the computation negative elements occur at $\lambda_{\mathrm{step}} = 28$ for the first time and simultaneously F_z shows a small oscillation but no minimum. The clustering of negative elements at $\lambda_{\mathrm{step}} = 37$ is not surprising since during this step the computation aborted due to numerical problems, compare with the two-dimensional case.

Chapter 6

Summary and future research possibilities

The motivation of this work is the complex mechanical behavior of cellular materials governed by phenomena like, for example, size dependent boundary layer effects and deformation-induced anisotropy caused by reorientations and local cell buckling. In order to capture such phenomena numerical homogenization or FE^2 methods based on the principle of scale separation have been applied and further developed. In such methods, a distinction between at least a macro and micro scale coupled by projection and homogenization rules is made, resulting in a (possibly nonlinear) nested boundary value problem. In addition, a pure microscopic approach, where the structure is resolved on the microscopic level, was used for reference computations and stability investigations. For the discretization on the microlevel, i.e. of the individual cell walls, higher-order continuum finite element methods, which are known to be very robust, have been applied for the first time. The advantage of a continuum based approach is that no kinematic restrictions have to be taken into account and that the in-cooperation of nonlinear material laws is straightforward. More specifically, linear and nonlinear (hyperelastic) p-version solid finite elements were used for microstructures. In a preliminary step the efficiency of the nonlinear p-elements has been improved by introducing a *quasi-spatial* formulation based on spatial derivatives of the displacement field. In numerical studies it could be shown that the overall gain in efficiency was up to 60 % compared to a *material* formulation. In addition a higher-order fictitious domain method, namely the finite cell method (FCM), came into operation when discretizing microstructures stemming from micro tomography (CT-scans).

Let us summarize the three different homogenization schemes developed in this thesis whereby the corresponding numerical examples are discussed in detail:

- A two-dimensional hyperelastic first-order FE^2 (classical continua on both scales) has been implemented. It is based on a numerical tangent and its efficiency was improved by using distributed computing of the microscopic problems. In the numerical examples honeycomb microstructures including statistically distributed imperfections were focused on. Suitable boundary conditions have been proposed and verified by reference computations first and then applied to shear and bending multiscale computations. Here, the main focus was put on anisotropy and deformation-induced anisotropy which could be

captured by our methods. However, due to the nonlinear nested boundary value problem and despite the fact that distributed computing has been used, it turned out that the efficiency of a FE^2 is low even in two dimensions. This fact is in accordance with the literature.

- In order to avoid the nested boundary value problem the next FE^2 scheme, a higher-order scheme, was restricted to small deformations which allows for a tabulated solution of the microstructures. To be more specified the macroscale was equipped with the micromorphic continuum theory and its subcontinua allowing for size effects. Thus, the projection and homogenization rules become more involved, i.e. they include terms up to order three. Dealing with p-FEM on the micro scale special attention has been paid to the application of the cubic projection rule. To this end, inhomogeneous DIRICHLET boundary conditions described by polynomials have been derived, implemented and tested. Afterwards, size effects have been detected under shear in cross-like and honeycomb-like microstructured materials with the higher-order scheme. Herein, the relevance of the micromorphic continuum theory was outlined. In addition an application to sandwich materials was given, where a sandwich plate was subjected to three point bending. All of the FE^2 computations have been verified successfully whereby only small geometric disturbances could be admitted.

- For obtaining effective material properties of real-world three-dimensional microstructured materials a first-order homogenization approach with restriction to small deformations has been set up. The microstructure itself is embedded into a window of effective properties also referred to as window method. Since these properties are not known in advance they have to be determined iteratively. The key feature of this approach is a discretization strategy based on the FCM which allows for the fast and simple conversion of CT-data into numerical models. In a first numerical study the approach has been verified by computations with solid-like heterogeneous microstructures. Afterwards, general guidelines concerning discretization and a representative number of foam cells have been derived for cellular materials and compared to the literature. Equipped with these guidelines mechanical experiments with polymeric open-cell PU foams have been computed, whereby effective properties have been extracted first and then applied to macroscopic models of the corresponding experiments. The experiments cover compression and shear tests with the pure foam material on the one hand and bending of sandwich plates on the other hand. Despite the fact that there are uncertainties with respect to the micromechanical parameters and despite the limitation of the homogenization scheme to small deformations a good agreement with the experiments could be reached as long as size effects were not dominant like, for example, in the shear test.

- In the last part of the numerical examples two- and three-dimensional foam-like structures were subjected to large strain compressions test where no scale separation has been made. In an accompanying analysis where the eigenvalues were computed on the one hand and the diagonal elements of the factorized tangential stiffness matrix were observed on the other hand, it has been demonstrated that there is no global point of instability. This is typical for cellular materials under compression since buckling of the individual cell walls does not occur simultaneously.

In summary one can state that all of the above-mentioned mechanical phenomena associated with cellular materials could be investigated by the methods developed and implemented in this thesis. The results could be verified by reference computations. In the case of the open-cell PU foams a validation could be performed whereby size effects could not be taken into account due to the first-order homogenization. Note that at least for the three-dimensional homogenization approach, the applicability to real engineering problems is possible.

Now, let us look ahead to possible future research:

- The efficiency of the nonlinear (nested) first-order FE^2 scheme should be improved further. To this end, the numerical tangent should be replaced by a consistent tangent.
- Further developments of the higher-order FE^2 scheme is planned, in order to account for arbitrary irregular microstructures. To this end, the projection rule should be extended to the whole microstructure, i.e. it is not restricted to the boundary anymore, compare with [64].
- Since size effects cannot be captured by a first-order scheme, the focus of the three-dimensional homogenization approach should be applied to solid-like materials. Possible applications would be composite materials, where one could investigate the change in effective stiffness for different types of reinforcement. In addition damage could be included, whereby one has to set up corresponding functions that describe the damage process. Due to its generality the first-order homogenization approach could be adapted to commercial FE-software, too. Of course, its key feature, the FCM, would then be excluded. However, as indicated above there are several applications, which may be relevant in industry.

Appendix A

Some definitions

A.1 Elasticity matrix obtained via numerical differentiation

$$\mathbf{C}^{\text{eff}} \approx \tag{A.1}$$

$$\begin{bmatrix}
\frac{(\sigma^1_{xx}-\sigma^2_{xx})}{\Delta\varepsilon_{12}} & \frac{(\sigma^1_{xx}-\sigma^3_{xx})}{\Delta\varepsilon_{13}} & \frac{(\sigma^1_{xx}-\sigma^4_{xx})}{\Delta\varepsilon_{14}} & \frac{(\sigma^1_{xx}-\sigma^5_{xx})}{2\,\Delta\varepsilon_{15}} & \frac{(\sigma^1_{xx}-\sigma^6_{xx})}{2\,\Delta\varepsilon_{16}} & \frac{(\sigma^1_{xx}-\sigma^7_{xx})}{2\,\Delta\varepsilon_{17}} \\
 & \frac{(\sigma^1_{yy}-\sigma^3_{yy})}{\Delta\varepsilon_{13}} & \frac{(\sigma^1_{yy}-\sigma^4_{yy})}{\Delta\varepsilon_{14}} & \frac{(\sigma^1_{yy}-\sigma^5_{yy})}{2\,\Delta\varepsilon_{15}} & \frac{(\sigma^1_{yy}-\sigma^6_{yy})}{2\,\Delta\varepsilon_{16}} & \frac{(\sigma^1_{yy}-\sigma^7_{yy})}{2\,\Delta\varepsilon_{17}} \\
 & & \frac{(\sigma^1_{zz}-\sigma^4_{zz})}{\Delta\varepsilon_{14}} & \frac{(\sigma^1_{zz}-\sigma^5_{zz})}{2\,\Delta\varepsilon_{15}} & \frac{(\sigma^1_{zz}-\sigma^6_{zz})}{2\,\Delta\varepsilon_{16}} & \frac{(\sigma^1_{zz}-\sigma^7_{zz})}{2\,\Delta\varepsilon_{17}} \\
 & & & \frac{(\sigma^1_{xy}-\sigma^5_{xy})}{2\,\Delta\varepsilon_{15}} & \frac{(\sigma^1_{xy}-\sigma^6_{xy})}{2\,\Delta\varepsilon_{16}} & \frac{(\sigma^1_{xy}-\sigma^7_{xy})}{2\,\Delta\varepsilon_{17}} \\
 & & & & \frac{(\sigma^1_{yz}-\sigma^6_{yz})}{2\,\Delta\varepsilon_{16}} & \frac{(\sigma^1_{yz}-\sigma^7_{yz})}{2\,\Delta\varepsilon_{17}} \\
 & \text{sym} & & & & \frac{(\sigma^1_{xz}-\sigma^7_{xz})}{2\,\Delta\varepsilon_{17}}
\end{bmatrix}$$

with

$$\Delta\varepsilon_{1j} \;=\; \left\| \langle\tilde{\varepsilon}_1\rangle - \langle\tilde{\varepsilon}_j\rangle \right\|_{\mathrm{L}_2}$$

A.2 Babuška-Chen points

Table A.1: Babuška-Chen points for $p = 3, \ldots, 8$

p	abscissas ξ_i
3	-1.0
	-0.4177913013559897
	0.4177913013559897
	1.0
4	-1.0
	-0.6209113046899123
	0.0
	0.6209113046899123
	1.0
5	-1.0
	-0.7341266671891752
	-0.2689070447719729
	0.2689070447719729
	0.7341266671891752
	1.0
6	-1.0
	-0.8034402382691066
	-0.4461215299911067
	0.0
	0.4461215299911067
	0.8034402382691066
	1.0
7	-1.0
	-0.8488719610366557
	-0.5674306027472533
	-0.1992877299056662
	0.1992877299056662
	0.5674306027472533
	0.8488719610366557
	1.0
8	-1.0
	-0.8802308527184540
	-0.6535334790799030
	-0.3477879716116667
	0.0
	0.3477879716116667
	0.6535334790799030
	0.8802308527184540
	1.0

Appendix B

Results

B.1 Elasticity matrices of PU-foams with standard deviation

In this section the mean effective elasticity matrices $\bar{\mathbf{C}}$ and the corresponding standard deviations $\mathbf{s}$ for the PU-foams with 10, 20, and 30 ppi as discussed in paragraph 5.2.2.2.2 are shown explicitly whereby the unit of measurement is KPa.

$$\bar{\mathbf{C}}^{10} = \begin{bmatrix} 88.330871 & 34.482038 & 63.223237 & -2.387856 & -0.722179 & 1.595839 \\ & 97.643325 & 70.246279 & -1.162706 & 1.124662 & 1.100486 \\ & & 252.991139 & -2.783297 & -6.460592 & 2.742869 \\ & & & 28.380657 & 0.074728 & 0.18462 \\ & & & & 42.487579 & -0.448865 \\ \text{sym} & & & & & 39.681592 \end{bmatrix},$$

$$\mathbf{s}^{10} = \begin{bmatrix} 6.202562 & 6.089594 & 7.159217 & 5.564261 & 3.710578 & 10.212453 \\ & 15.793839 & 14.851017 & 5.35346 & 5.097533 & 6.821142 \\ & & 35.530756 & 6.066609 & 7.254909 & 12.071817 \\ & & & 1.739717 & 1.875266 & 1.294509 \\ & & & & 1.789284 & 1.677849 \\ \text{sym} & & & & & 3.226813 \end{bmatrix},$$

$$\bar{\mathbf{C}}^{20} = \begin{bmatrix} 93.108931 & 32.645311 & 75.677872 & -0.752524 & -1.986181 & 0.595599 \\ & 88.040143 & 71.1722 & -0.654592 & -3.925366 & -0.53431 \\ & & 273.472678 & -0.789421 & -6.127186 & -0.192003 \\ & & & 27.551906 & -0.070942 & -0.423725 \\ & & & & 41.109557 & 0.292451 \\ \text{sym} & & & & & 42.554927 \end{bmatrix},$$

$$\mathbf{s}^{20} = \begin{bmatrix} 7.464839 & 2.047713 & 5.77409 & 1.040966 & 2.204077 & 6.19197 \\ & 9.725039 & 7.408952 & 1.487821 & 3.435391 & 3.17859 \\ & & 14.474297 & 0.819548 & 6.537476 & 10.150542 \\ & & & 1.04077 & 1.277372 & 0.584515 \\ & & & & 1.448436 & 0.425118 \\ \text{sym} & & & & & 1.070789 \end{bmatrix},$$

$$\bar{\mathbf{C}}^{30} = \begin{bmatrix} 78.852291 & 26.615409 & 50.21248 & 0.589241 & -0.165197 & 1.272528 \\ & 85.937939 & 56.588212 & 0.324952 & 1.147256 & 0.766345 \\ & & 192.04502 & 0.803759 & 1.589134 & 3.84127 \\ & & & 26.345002 & 0.449321 & 0.134291 \\ & & & & 38.195485 & 0.372692 \\ \text{sym} & & & & & 37.729789 \end{bmatrix},$$

$$\mathbf{s}^{30} = \begin{bmatrix} 3.50764 & 2.425848 & 4.372923 & 2.003605 & 1.74434 & 4.338506 \\ & 7.817952 & 6.137127 & 1.892782 & 2.61316 & 3.869907 \\ & & 6.686588 & 1.197719 & 6.72161 & 7.426606 \\ & & & 1.232135 & 1.292385 & 0.934955 \\ & & & & 1.910475 & 0.708291 \\ \text{sym} & & & & & 1.784215 \end{bmatrix}.$$

Please note that the high standard deviation in the offdiagonal terms stems from the fact that the individual foams are not perfectly transversely isotropic.

Publications resulting from this work

Journals

[1] R. Jänicke, S. Diebels, H.-G. Sehlhorst, and A. Düster. Two-scale modelling of micromorphic continua. *Continuum Mechanics and Thermodynamics*, 12:297–315, 2009.

[2] H.-G. Sehlhorst, R. Jänicke, A. Düster, E. Rank, H. Steeb, and S. Diebels. Numerical investigations of foam-like materials by nested high-order finite element methods. *Computational Mechanics*, 45:45–59, 2009.

[3] R. Jänicke, H.-G. Sehlhorst, A. Düster, and S. Diebels. Micromorphic two-scale modelling of periodic grid structures. *International Journal for Multiscale Computational Engineering*, accepted for publication, 2011.

Proceedings

[1] R. Jänicke, H.-G. Sehlhorst, H. Steeb, S. Diebels, A. Düster, and E. Rank. Investigations on an elastic micropolar continuum model for large deformations. *Proceedings in Applied Mathematics and Mechanics*, 8(1):10549–10550, 2008.

[2] H.-G. Sehlhorst, A. Düster, R. Jänicke, and S. Diebels. On Dirichlet boundary conditions in second-order FE^2-schemes. *Proceedings in Applied Mathematics and Mechanics*, 10:423–424, 2010.

[3] H.-G. Sehlhorst, R. Jänicke, A. Düster, E. Rank, H. Steeb, and S. Diebels. Numerical homogenization of foam-like structures based on the FE^2 approach. *Proceedings in Applied Mathematics and Mechanics*, 8(1):10573–10574, 2008.

Submitted

[1] A. Düster, H.-G. Sehlhorst, and E. Rank. Numerical homogenization of heterogeneous and cellular materials utilizing the Finite Cell Method. *Computational Mechanics*, submitted.

[2] H.-G. Sehlhorst, A. Düster, R. Jänicke, S. Diebels, and E. Rank. Extraction of effective material parameters with application to sandwich structures. *Proceedings in Applied Mathematics and Mechanics*, submitted.

Bibliography

[1] A. Aşkar. *Lattice dynamical foundations of continuum theories*. World Scientific Publication, Singapore, 1986.

[2] H. Altenbach, J. Altenbach, and W. Kissing. *Mechanics of Composite Structural Elements*. Springer-Verlag, 2004.

[3] W. B. Anderson, C. P. Chen, and R. S. Lakes. Experimental study of size effects and surface damage in closed-cell polymethacrylimide and open-cell copper foams. *Cellular polymers*, 13(1):1–15, 1994.

[4] W. B. Anderson and R. S. Lakes. Size effects due to Cosserat elasticity and surface damage in closed-cell polymethacrylimide foam. *Journal of Material Sciences*, 29:6413–6419, 1994.

[5] Z. P. Bažant and M. Christensen. Analogy between micropolar continuum and grid frameworks under initial stress. *International Journal of Solids and Structures*, 8:327–346, 1972.

[6] G. W. Becker, D. Braun, and G. Oertel. *Polyurethane*. Hanser-Verlag, 1993.

[7] T. Belytschko, W.K. Liu, and B. Moran. *Nonlinear finite elements for continua and structures*. John Wiley & Sons, 2000.

[8] J. Bonet and R.D. Wood. *Nonlinear continuum mechanics for finite element analysis*. Cambridge University Press, New York, 2008.

[9] A.F. Bower. *Applied Mechanics of Solids*. CRC Press, 2009.

[10] R. Brezny and D. J. Green. Characterization of edge effects in cellular materials. *Journal of Material Sciences*, 25:4571–4578, 1990.

[11] H. Bröker. *Untersuchung von Flachdeckenauflagerungen mit einer Reissner-Mindlin Plattenformulierung*. Diploma thesis, Fach Numerische Methoden und Informationsverarbeitung, Universität Dortmund, 1997.

[12] G. Capriz. *Continua with Microstructures*, volume 35 of *Springer Tracts in Natural Philosophy*. Springer, New York, 1980.

[13] C. Chen and N. A. Fleck. Size effects in the constrained deformation of metallic foams. *Journal of the Mechanics and Physics of Solids*, 50:955–977, 2002.

[14] Q. Chen and I. Babuška. Approximate optimal points for polynomial interpolation of real functions in an interval and in a triangle. *Computer Methods in Applied Mechanics and Engineering*, 128:405–417, 1995.

[15] E. Cosserat and F. Cosserat. *Théorie des corps déformables*. A. Hermann et Fils, Paris, 1909.

[16] M. Di Sciuval and U. Icardi. On Modeling of Global and Local Response of Sandwich Plates with Laminated Faces. *Journal of Sandwich Structures and Materials*, 2:350–378, 2000.

[17] S. Diebels. Constitutive modelling of micropolar porous media. In J. F. Thimus et al., editor, *Poromechanics - A Tribute to Maurice A. Biot*, pages 71–76. A. A. Balkema, Rotterdam, 1998.

[18] S. Diebels. Ein mikropolares Materialgesetz für poröse Festkörper. *ZAMM-Zeitschrift für Angewandte Mathematik und Mechanik*, 79:533–534, 1999.

[19] S. Diebels and H. Steeb. The size effect in foams and its theoretical and numerical investigation. *Proceedings of the Royal Society London A*, 458:2869–2883, 2002.

[20] S. Diebels and H. Steeb. Stress and couple stress in foams. *Computational Material Science*, 28:714–722, 2003.

[21] A. Düster. *High order finite elements for three-dimensional, thin-walled nonlinear continua*. PhD thesis, Lehrstuhl für Bauinformatik, Fakultät für Bauingenieur- und Vermessungswesen, Technische Universität München, 2001.

[22] A. Düster, H. Bröker, and E. Rank. The p-version of the finite element method for three-dimensional curved thin walled structures. *International Journal for Numerical Methods in Engineering*, 52:673–703, 2001.

[23] A. Düster, S. Hartmann, and E. Rank. p-fem applied to finite isotropic hyperelastic bodies. *Computer Methods in Applied Mechanics and Engineering*, 192:5147–5166, 2003.

[24] A. Düster, J. Parvizian, Z. Yang, and E. Rank. The finite cell method for three-dimensional problems of solid mechanics. *Computer Methods in Applied Mechanics and Engineering*, 197:3768–3782, 2008.

[25] A. Düster and E. Rank. The p-version of the finite element method compared to an adaptive h-version for the deformation theory of plasticity. *Computer Methods in Applied Mechanics and Engineering*, 190:1925–1935, 2001.

[26] A. Düster and E. Rank. A p-version finite element approach for two- and three-dimensional problems of the J_2 flow theory with non-linear isotropic hardening. *International Journal for Numerical Methods in Engineering*, 53:49–63, 2002.

[27] A. Düster, D. Scholz, and E. Rank. *pq*-Adaptive solid finite elements for three-dimensional plates and shells. *Computer Methods in Applied Mechanics and Engineering*, 197:243–254, 2007.

[28] T. Ebinger, S. Diebels, and H. Steeb. Numerical homogenization techniques applied to growth and remodelling phenomena. *Computational Mechanics*, pages 815–830, 2007.

[29] A. C. Eringen and E. S. Suhubi. Nonlinear theory of simple micro-elastic solids - I. *International Journal of Engineering Sciences*, 2:189–203, 1964.

[30] C. Eringen. *Microcontinuum Field Theories, Vol. I: Foundations and Solids*. Springer Verlag, 1999.

[31] M. Fátima Vaz and M. A. Fortes. Characterization of deformation bands in the compression of cellular materials. *Journal of Materials Science Letters*, 12:1408–1410, 1993.

[32] C. Felippa, K. Park, and J. DeRuntz. Stabilization of staggered solution procedures for fluid-structure interaction analysis. In T. Belytschko and T. Geers, editors, *Computational Methods for Fluid-Structure Interaction Problems*, volume 26, pages 95–124. American Society of Mechanical Engineers, New York, 1977.

[33] F. Feyel. *Application du calcul parallèle aux modèles à grand nombre de variables internes*. Phd-thesis, Ecole National Supérieure des Mines de Paris, 1998.

[34] F. Feyel. A multilevel finite element method (FE^2) to describe the response of highly nonlinear structures using generalized continua. *Computer Methods in Applied Mechanics and Engineering*, 192:3233–3244, 2003.

[35] F. Feyel and J. L. Chaboche. FE^2 multiscale approach for modelling the elastoviscoplastic behaviour of long fiber SiC/Ti composite materials. *Computer Methods in Applied Mechanics and Engineering*, 183:309–330, 2000.

[36] S. Forest. Mechanics of generalized continua: Construction by homogenization. *Journal for Physics IV*, pages 39–48, 1998.

[37] S. Forest. Aufbau und Identifikation von Stoffgleichungen für höhere Kontinua mittels Homogenisierungsstrategien. *Technische Mechanik*, 19:297–306, 1999.

[38] S. Forest. Homogenization methods and the mechanics of generalized continua. In G. Maugin, editor, *Geometry, Continua and Microstructure*, Travaux en Cours, No. 60, pages 35–48. 1999.

[39] S. Forest. Nonlinear microstrain theories. *International Journal of Solids and Structures*, 135(3):117–131, 2006.

[40] S. Forest, J. M. Cardona, and R. Sievert. Thermoelasticity of second-grade media. In G. Maugin, R. Drouot, and F. Sidoroff, editors, *Continuum Thermomechanics, The Art and Science of Modelling Material Behaviour*, Paul Germain's Anniversary Volume, pages 163–176. 2000.

[41] L. J. Gibson and M. F. Ashby. *Cellular solids. Structure and properties*. Cambridge Solid State Science Series. Cambridge University Press, 1997.

[42] L. Gong and S. Kyriakides. Compressive response of open cell foams. part ii: Initiation and evolution of crushing. *International Journal of Solids and Structures*, 42:1381–1399, 2005.

[43] L. Gong, S. Kyriakides, and W.-Y. Jang. Compressive response of open-cell foams. Part i: Morphology and elastic properties. *International Journal of Solids and Structures*, 42:1355–1379, 2005.

[44] W.J. Gordon and Ch.A. Hall. Transfinite element methods: Blending function interpolation over arbitrary curved element domains. *Numerische Mathematik*, 21:109–129, 1973.

[45] D. Gross, P. Wriggers, and W. Ehlers. *Formeln und Aufgaben zur Technischen Mechanik 2*. Springer-Verlag, 2003.

[46] M. Hain. *Computational Homogenization of micro-structural Damage due to Frost in Hardened Cement Paste*. PhD thesis, Institut für Baumechanik und Numerische Mechanik, Leibniz-Universität Hannover, 2007.

[47] M. Hain and P. Wriggers. Numerical homogenization of hardened cement paste. *Computational Mechanics*, 42:197–212, 2008.

[48] S. Hartmann. *Finite-Elemente Berechnung inelastischer Kontinua - Interpretation als Algebro-Differentialgleichungssysteme*. Postdoctoral thesis, Institut für Mechanik, Universität Kassel, 2003.

[49] P. Haupt. *Continuum mechanics and theory of materials*. Springer, 2000.

[50] U. Heißerer. *High-order finite elements for material and geometric nonlinear finite strain problems*. PhD thesis, Chair for Computation in Engineering, Fakultät für Bauingenieur- und Vermessungswesen, Technische Universität München, 2008.

[51] U. Heißerer, S. Hartmann, A. Düster, W. Bier, Z. Yosibash, and E. Rank. *p*-fem for finite deformation powder compaction. *Computer Methods in Applied Mechanics and Engineering*, 197:727–740, 2008.

[52] R. Hill. Elastic properties of reinforced solids: Some theoretical principles. *Journal of the Mechanics and Physics of Solids*, 11:357–372, 1963.

[53] R. Hill. On constitutive macro-variables for heterogeneous solids at finite strain. *Proceedings of the Royal Society London A*, 326:131–147, 1972.

[54] J. Hohe and W. Becker. Effective stress-strain relations for two-dimensional cellular sandwich cores: Homogenization, material models and properties. *Applied Mechanics Reviews*, 55(1):61–87, 2002.

[55] J. Hohe and W. Becker. Effective mechanical behavior of hyperelastic honeycombs and two-dimensional model foams at finite strain. *International Journal of Mechanical Sciences*, 45:891–913, 2003.

[56] J. Hohe and L. Librescu. Advances in the Structural Modelling of Elastic Sandwich Panels. *Mechanics of Advanced Materials and Structures*, 11:395–424, 2004.

[57] H. Hu, S. Belouettar, E. M. Daya, and M. Potier-Ferry. Evaluation of Kinematic Formulations for Viscoelastically Damped Sandwich Beam Modeling. *Journal of Sandwich Structures and Materials*, 8:477–495, 2006.

[58] H. Hu, S. Belouettar, E. M. Daya, and M. Potier-Ferry. Modeling of Sandwich Structures and Localization of Three-dimensional Stress and Displacement Fields. *Journal of Sandwich Structures and Materials*, 10:161–188, 2008.

[59] A. T. Huber and L. J. Gibson. Anisotropy of foams. *Journal of Material Sciences*, 23:3031–3040, 1988.

[60] C. Huet. Coupled size and boundary-condition effects in viscoelastic heterogeneous and composite bodies. *Mechanics of Materials*, 31:787–829, 1999.

[61] W.-Y. Jang, A. M. Kraynik, and S. Kyriakides. On the microstructure of open-cell foams and its effect on elastic properties. *International Journal of Solids and Structures*, 45:1845–1875, 2008.

[62] R. Jänicke. *Micromorphic media: interpretation by homogenisation*. PhD thesis, Lehrstuhl für Technische Mechanik, Universität des Saarlandes, 2010.

[63] R. Jänicke, S. Diebels, H.-G. Sehlhorst, and A. Düster. Two-scale modelling of micromorphic continua. *Continuum Mechanics and Thermodynamics*, 12:297–315, 2009.

[64] R. Jänicke, H.-G. Sehlhorst, A. Düster, and S. Diebels. Micromorphic two-scale modelling of periodic grid structures. *International Journal for Multiscale Computational Engineering*, accepted for publication, 2011.

[65] C. B. Kafadar and C. Eringen. Micropolar media - I: The classical theory. *International Journal of Engineering Sciences*, 9:271–305, 1971.

[66] F. Koschnick. *Geometrische Locking-Effekte bei Finiten Elementen und ein allgemeines Konzept zu ihrer Vermeidung*. PhD thesis, Lehrstuhl für Statik, Technische Universität München, 2004.

[67] V. G. Kouznetsova. *Computational homogenization for the multi-scale analysis of multi-phase materials*. PhD thesis, Materials Technology, Eindhoven University of Technology, 2002.

[68] G. Kuhlmann and R. Rolfes. A hierarchic 3D finite element for laminated composites. *International Journal for Numerical Methods in Engineering*, 61:96–116, 2004.

[69] R. S. Lakes. Size effects and micromechanics of porous solids. *Journal of Material Sciences*, 18:2572–2580, 1983.

[70] R. S. Lakes. Experimental methods for study of Cosserat elastic solids and other generalized elastic continua. In H. B. Mühlhaus, editor, *Continuum methods for Materials with microstructures*, pages 1–25. John Wiley & Sons, Chichester, 1995.

[71] M. Laroussi, K. Sab, and A. Alaoui. Foam mechanics: nonlinear response of an elastic 3D-periodic microstructure. *International Journal of Solids and Structures*, 39:3599–3623, 2002.

[72] C. Miehe. Numerical computation of algorithmic (consistent) tangent moduli in large-strain computational inelasticity. *Computer Methods in Applied Mechanics and Engineering*, 134:223–240, 1996.

[73] C. Miehe and A. Koch. Computational micro-to-macro transitions of discretized microstructures undergoing small strains. *Archives of Applied Mechanics*, 72:300–317, 2002.

[74] P. Neff. On material constants for micromorphic continua. In K. Hutter and Y. Wang, editors, *Proceedings of 'International Symposium on Trends in Applications of Mathematics to Mechanics'*. Shaker, Aachen, 2004.

[75] S. Nemat-Nasser and M. Hori. *Micromechanics*. North Holland, Amsterdam, 1993.

[76] V. Nübel, A. Düster, and E. Rank. An *rp*-adaptive finite element method for elastoplastic problems. *Computational Mechanics*, 39:557–574, 2007.

[77] N. Ohno, D. Okumura, and H. Noguchi. Microscopic symmetric bifurcation condition of cellular solids based on a homogenization theory of finite deformation. *Journal of the Mechanics and Physics of Solids*, 50:1125–1153, 2002.

[78] P. R. Onck. Cosserat modeling of cellular solids. *C. R. Mecanique*, 330:717–722, 2002.

[79] A. Pantano and R. C. Averill. A 3d Zig-Zag Sublaminate Model for Analysis of Thermal Stresses in Laminated Composite and Sandwich Plates. *Journal of Sandwich Structures and Materials*, 2:288–312, 2000.

[80] J. Parvizian, A. Düster, and E. Rank. Finite cell method – h- and p-extension for embedded domain problems in solid mechanics. *Computational Mechanics*, 41:121–133, 2007.

[81] S. Reese. *Thermomechanische Modellierung gummiartiger Polymerstrukturen*. Postdoctoral thesis, Institut für Baumechanik und Numerische Mechanik, Universität Hannover, 2001.

[82] M. Rücker. *A parallel p-version finite element approach for civil engineering and structural mechanics problems*. PhD thesis, Lehrstuhl für Bauinformatik, Bauingenieur- und Vermessungswesen, Technische Universität München, 2000.

[83] K. Sab and F. Pradel. Homogenisation of periodic Cosserat media. *International Journal of Computer Applications in Technology*, 34(1):60–71, 2009.

[84] I. Saiki, K. Terada, K. Ikeda, and M. Hori. Appropriate number of unit cells in a representative volume element for micro-structural bifurcation encountered in a multi-scale modeling. *Computer Methods in Applied Mechanics and Engineering*, 191:2561–2585, 2002.

[85] O. Schenk, M. Bollhöfer, and R. A. Römer. On large scale diagonalization techniques for the Anderson model of localization. *SIAM Review*, 50(1):91–112, 2008. SIGEST Paper.

[86] O. Schenk, A. Wächter, and M. Hagemann. Matching-based preprocessing algorithms to the solution of saddle-point problems in large-scale nonconvex interior-point optimization. *Comput. Optim. Appl.*, 36(2-3):321–341, April 2007.

[87] J. Schröder. *Homogenisierungsmethoden der nichtlinearen Kontinuumsmechanik unter Beachtung von Stabilitätsproblemen.* Postdoctoral thesis, Institut für Mechanik (Bauwesen) Lehrstuhl I, Universität Stuttgart, 2000.

[88] H.-G. Sehlhorst, R. Jänicke, A. Düster, E. Rank, H. Steeb, and S. Diebels. Numerical investigations of foam-like materials by nested high-order finite element methods. *Computational Mechanics*, 45:45–59, 2009.

[89] S. Ströhla, W. Winter, and G. Kuhn. Numerische Ermittlung elastischer Eigenschaften von Metallschäumen mit Polyeder-Einheitszellen. *Materialwissenschaft und Werkstofftechnik*, 31:444–446, 2000.

[90] B.A. Szabó and I. Babuška. *Finite element analysis.* John Wiley & Sons, 1991.

[91] B.A. Szabó, A. Düster, and E. Rank. The p-version of the Finite Element Method. In E. Stein, R. de Borst, and T. J. R. Hughes, editors, *Encyclopedia of Computational Mechanics*, volume 1, chapter 5, pages 119–139. John Wiley & Sons, 2004.

[92] B.A. Szabó and G.J. Sahrmann. Hierarchic plate and shell models based on p-extension. *International Journal for Numerical Methods in Engineering*, 26:1855–1881, 1988.

[93] C. Tekoğlu. *Size effects in cellular solids.* PhD thesis, Rijksuniversiteit Groningen, 2007.

[94] C. Tekoğlu and P. R. Onck. Size effects in the mechanical behaviour of cellular materials. *Journal of Material Sciences*, 40:5911–3564, 2005.

[95] C. Tekoğlu and P. R. Onck. Size effects in two-dimensional Voronoi foams: A comparison between generalized continua and discrete models. *Journal of the Mechanics and Physics of Solids*, 56:3541–3564, 2008.

[96] A. Tessler, M. Di Sciuva, and M. Gherlone. A Refined Zigzag Beam Theory for Composite and Sandwich Beams. *Journal of Composite Materials*, 2009.

[97] N. Triantafyllidis and M. W. Schraad. Onset of failure in aluminum honeycombs under general in-plane loading. *Journal of the Mechanics and Physics of Solids*, 46:1089–1124, 1998.

[98] J. R. Vinson. Sandwich Structures. *Applied Mechanics Reviews*, 54(3):201–214, 2001.

[99] J. Wang, H. Wang, C. Xiuhua, and Y. Yin. Experimental and numerical study of the elastic properties of PMI. *Journal of Material Sciences*, 45:2688–2695, 2010.

[100] Y. Wang and A. M. Cuitiño. Three-dimensional nonlinear open-cell foams with large deformations. *Journal of the Mechanics and Physics of Solids*, 48:961–988, 2000.

[101] W. E. Warren and E. Byskov. Micropolar and Nonlocal Effects in Spatially Periodic, Two-Dimensional Structures. Department of Structural Engineering and Materials, Technical University of Denmark, Series R, No 37, 1997.

[102] W. E. Warren and A. M. Kraynik. The nonlinear elastic behavior of open-cell foams. *Journal of Applied Mechanics*, 58:376–381, 1991.

[103] J. Wiedemann. *Leichtbau: Elemente und Konstruktion*. Springer Verlag, 2006.

[104] J. G. F. Wismans, L. E. Govaert, and J. A. W. van Dommelen. X-ray computed tomography-based modeling of polymeric foams: the effect of finite element model size on the large strain response. *Journal of Polymer Science: Part B: Polymer Physics*, 48:1526–1534, 2010.

[105] P. Wriggers. *Nonlinear Finite-Element-Methods*. Springer-Verlag, 2009.

[106] J. Yvonnet, H. Zahrouni, and M. Potier-Ferry. A model reduction method for the post-buckling analysis of cellular microstructures. *Computer Methods in Applied Mechanics and Engineering*, 197:265–280, 2007.

[107] T.I. Zhodi and P. Wriggers. *Introduction to Computational Micromechanics*, volume 20 of *Lecture Notes in Applied and Computational Mechanics*. Springer, 2005.

[108] H. X. Zhu, N. J. Mills, and J. F. Knott. Analysis of the high strain compression of open-cell foams. *Journal of the Mechanics and Physics of Solids*, 45:1875–1904, 1997.